Project No. 09-835

Prediction and Monitoring Systems of Creep-Fracture Behavior of 9Cr-1Mo Steels for Reactor Pressure Vessels

Reactor Concepts RD&D

Dr. Gabriel Potirniche
University of Idaho

Sue Lesica, Federal POC
Richard Wright, Technical POC

NEUP Nuclear Energy University Programs
U.S. Department of Energy

PREDICTION AND MONITORING SYSTEMS OF CREEP-FRACTURE BEHAVIOR OF 9Cr-1Mo STEELS FOR REACTOR PRESSURE VESSELS

NEUP 2009 Project 09-835 (09-458)
Final Report

PI:
Gabriel Potirniche
gabrielp@uidaho.edu; tel.: 208-885-4049

Co-PIs:
Dr. Indrajit Charit,
Dr. Karl Rink,
Dr. Fred Barlow

Mechanical Engineering Department,
University of Idaho,
October 31, 2013

ABSTRACT

Modified 9Cr-1Mo (Grade 91) steel is currently considered as a candidate material for reactor pressure vessels (RPVs) and reactor internals for the Very High Temperature Reactor (VHTR) and in fossil-fuel fired power plants at higher temperatures and stresses. The goal of this project was to provide a fundamental understanding of the creep-fracture behavior of modified 9Cr-1Mo steel welds for RPVs through modeling and experimentation, and to recommend a design for a monitoring system for the structural health of RPVs. Several tasks were originally proposed and fully accomplished. A description of the project tasks, the main findings and conclusions are given next. A list of the publications and presentations resulted from this research are listed in the Appendix at the end of this report.

Task 1. Creep-fracture testing of base material and welds of Grade 91 steel specimens

Research activities

This task involed the manufacture of the base material testing specimens, the welded specimens, metallurgical characterization by means of optical, transmission and scanning electron microscopy, energy dispersive spectroscopy measurements, hardness measurements, characterization of the residual stress fields after welding process, and creep testing of base material specimens and of welded specimens. The tensile creep behavior of Grade 91 steel was studied in the temperature range of 600^{o}C to 750^{o}C and stresses between 35 MPa and 350 MPa. Heat treatment of Grade 91 steel was studied by normalizing and tempering the steel at various temperatures and times.

Thermo-Calc^{TM} calculations were used to predict the precipitate stability and their evolution, and construct carbon isopleths of Grade 91 steel. Residual stress distribution across gas tungsten arc welds (GTAW) in Grade 91 steel was measured by the time-of-flight neutron diffraction using the Spectrometer for Materials Research at Temperature and Stress (SMARTS) diffractometer at Lujan Neutron Scattering Center, Los Alamos National Laboratory, Los Alamos, NM, USA.

Findings and conclusions

Analysis of creep results yielded power stress exponents of n ~9-11 in the higher stress regime and n ~1 in the lower stress regime. The creep behavior of Grade 91 steel was described by the modified Bird-Mukherjee-Dorn relation. The rate-controlling creep deformation mechanism in the high stress regime was identified as the edge dislocation climb with a stress exponent of n = 5. On the other hand, the deformation mechanism in the Newtonian viscous creep regime (n = 1) was identified as the Nabarro-Herring creep. Creep rupture data were analyzed in terms of Monkman-Grant relation and Larson-Miller parameter. Creep damage tolerance factor and stress exponent were used to identify the cause of creep damage. The fracture surface morphology of the ruptured specimens was studied by scanning electron microscopy to elucidate the failure mechanisms. Fracture mechanism map for Grade 91 steel was developed based on the available material parameters and experimental observations. The microstructural evolution of heat treated steel was correlated with the differential scanning calorimetric study. The combination of microstructural studies with optical microscopy, scanning

and transmission electron microscopy, microhardness profiles, and calorimetric plots helped in the understanding of the evolution of microstructure and precipitates in Grade 91 steel. The residual stresses were determined at the mid-thickness of the Grade 91 steel plate, 4.35 mm and 2.35 mm below the surface of the as-welded and post-weld heat treated plate. The residual stresses of the as-welded plate were compared with the post-weld heat treated plate. The post-weld heat treatment significantly reduced the residual stress in the base metal, heat affected zone, and the weld zone. Vickers microhardness profiles of the as-welded, and post-weld heat treated specimens were also determined and correlated with the observed residual stress profile and microstructure. Finally, an extensive analysis of the creep rupture properties of the welded Grade 91 alloy (welded by the Gas Tungsten Arc Welding) alloy was carried out and presented in detail in this report.

Task 2: Testing of damage levels in aged pressure vessels with the leak rate method

Research activities

The objective of this task was to characterize the creep damage in welded pressure vessels by identifying the Rb deposition resulting from Kr-85 decay at damage sites and measure leak rates of Kr-85 from. The pressure vessels were manufactured by two welding methods, i.e. inertia welding and TIG welding. The main outcome of this task was to compare the creep damage reliability of the two welding processes.

Small Grade 91 pressure vessels were manufactured by the TIG and inertia welding techniques. The two halves of a cylindrical pressure vessel were machined out of a round bar of Grade 91 steel. Internal volumes in the two halves were formed by a simple boring process. Each vessel featured a specially-designed fill port through which gases could be introduced into the pressure vessels and then sealed using a ball weld process. The internal geometry of the inertia-welded units differed from that of the TIG welded specimens due to the nature of the weld process. The TIG welded parts were bored to an internal diameter and fillet welds preceded by the proper preheat treatment followed by adherence to the specified interpass and cooling temperatures.

Pressure vessels were first filled with a mixture of the Kr-85 and air (0.01% Kr-85, molar basis) at very low pressures (2.0 mm Hg) followed by a high pressure (approximately 6000 to 7500 psi) mixture of argon and helium (80% Ar / 20%He, molar basis). The weight of each pressure vessel was recorded after filling and an initial reading of the Kr-85 content was recorded. In this manner, leaks from the pressure vessel may be detected by mass loss (a gross or large leak check) or by reduction in Kr-85 greater than that expected by inherent radioactive decay. Leak detection by monitoring the reduction in Kr-85 content through gamma ray counting is considered the most sensitive leak detection technique available.

Hardness and microstructure were measured across the inertia weld zones of two specimens. Hardness values were measured using a Vickers indenter with a 500 gram load. Vickers Hardness values, HV, are noted in cross section views of the weld zones in the locations where they were measured. Microstructure photos were taken at various noted locations across the weld zones.

Findings and conclusions

Gaseous Kr-85 decays to form solid rubidium (Rb) as a decomposition product. From the EDS analysis, it was indeed found that the Kr-85 decays to Rb. Rb presence on the interior surface of the pressure vessels indicated the extent of gas penetration within the pressure vessels walls, and the possible evolution of damage (cracks, voids, porosity, etc.) within the parent materials.

EDS study was done on a control sample that was not subjected to radioactive Kr-85, and on samples that were subjected to radioactive Kr-85. In samples subjected to radioactive Kr-85, non-radioactive Rb was detected in cracks. Rb was detected mainly in cracks and voids on the inner face of the pressure vessels. However, Rb was not detected in the cracks of the control sample that was not subjected to radioactive Kr-85. The inertia welded specimens were found to be of better quality with no large crack present, and no significant localization of Rb at damage sites.

Kr-85 leaked out of the pressure vessels as a result of creep damage induced in the welds of the pressure vessels. Radiation readings of the TIG and inertia-welded pressure vessels fabricated were taken periodically. Results indicated that the reduction in gamma radiation from the pressure vessels manufactured by inertia welding over time agreed with the expected decay of Kr-85 over this time period. Thus, the leak rates from inertia welded pressure vessels appear to be in the range $1x10^{-10}$ atm cc/s and perhaps even lower. This indicates a good quality of the inertia welded in regard to the leak rates as a result of creep loading. The leak rates from the pressure vessels manufactured by TIG welding indicated leak rates slightly greater than those recorded from the inertia welded pressure vessels.

To measure such extremely fine leak rates, a novel calibration methodology was developed to better understand the limit of detectibility of gamma radiation using our experimental instrumentation for our geometries and materials. The activity of oil saturated with Kr-85 was first determined using the scintillation crystal detection equipment. The activity of the oil was determined on a mass basis in units of microcuries/gm of (vacuum pump) oil. Then known masses of the oil were carefully introduced in empty TIG and inertia welded specimens so that the attenuation of the gamma ray signal due to the wall thickness of the different test vessels could be determined. As a result, the quantity of Kr-85 in a vessel can be known very accurately - much more accuratley than using other calibration techniqies.

From the findings of this task, it was concluded that inertia welding is a much better welding technique compared to TIG welding for components that are intended to withstand creep conditions. The amount of damage in the inertia welded pressure vessles is much lower compared with than observed in the TIG welded vessels. Also, the leak rates from the TIG vessels were higher than those for inertial welded technique.

The Rb presence was observed mainly in the pressure vessels filled with gas containing Kr-85. Rb is found in high concentrations in voids and cracks nucleated during the welding process in the heat-affected zone or as a result of the creep conditions. Rb is highly corrosive, and it is believed that it leads to an acceleration of the creep damage. This technique can be used as a non-destructive evaluation method to assess the quality of the welds.

Task 3: Constitutive model for creep damage in modified 9Cr-1Mo steels

Research activities

A micromechanical model was developed for the simulation and evaluation of creep deformation and rupture times in Grade 91 steel specimens. Creep deformation in metals is generally induced by the dislocation generation, motion, and annihilation. To model the creep behavior of the modified 9Cr-1Mo steel the Orowan's equation was employed, which is valid for both glide and climb-controlled dislocation movement. The evolution of the dislocation density was modeled by considering the generation and annihilation of single and dipole dislocations. In addition to dislocation motion as a basis for creep deformation, there are several other factors which determine the creep resistance of this steel. Among these, the most significant are precipitate coarsening, solid solutions depletion, and void/crack nucleation and growth. The evolution of these mechanisms during creep deformation was accounted for by introducing specific continuum damage terms. Creep tests were also performed at several stress and temperature levels. The creep-damage model was implemented as a stand-alone material point simulator code in FORTRAN. Both explicit and implicit schemes were implemeneted for the integration of the differential equations governing the evolution of the creep strain and density of mobile dislocations.

Findings and conclusions

The material microstructure will degrade during creep deformation leading to accelerated creep deformation rates. The computational model was able to simulate all three stages of creep deformation. Simulations were performed and compared with the experimental results for the creep deformation and fracture of smooth unaxial non-welded specimens subjected to temperatures between 600-700 ˚C and stress ranges of 80-200 MPa. The results obtained from the model were in excellent agreement with the experimental data. The model is able to predict the service life of structural components manufactured of Grade 91 steels, which are subjected to elevated temperatures and a wide range of stress levels.

Task 4: Simulations of modified 9Cr-1Mo structures using polycrystal plasticity

Research activities

In this task a dislocation-based creep model combined with a continuum damage model for Grade 91 steels was developed and implemented as a User Material Subroutine (UMAT) in the finite element code ABAQUS. The model developed in Task 3 was adapted for finite element implementation. The evolution of dislocation structure has been considered as the driving creep mechanism. The effect of void growth and crack formation, precipitate coarsening, and solid solution depletion were considered as damage evolution phenomena. Experimental creep tensile tests and finite element simulations of welded specimens manufactured from modified 9Cr-1Mo were performed.

Findings and conclusions

The creep-fracture model implemented in the finite element code ABAQUS was able to predict well the behavior of non-welded and welded specimens made of Grade 91 steel. The creep behavior of specimens tested in Task 1 was simulated by taking into account the difference

in the creep strength of materials in the heat affected zone (HAZ) and the base material. The tensile creep tests were performed at a temperature range of 550-700 ˚C and stress level of 80-200 MPa. Numerical implementation considered both explicit and implicit schemes of integration for the set of differential equations governing the creep and fracture variables. While the explicit schemes we more straightforward to implement, they worked for small time steps. However, the explicit scheme was more time consuming and presenting convergence issues at times. The implicit scheme was very accurate, robust even for large time steps, and allowed for faster computation of longer creep life at low stress levels. The computational model was able to analyze three-dimensional geometries of both homogeneous and non-homogenous materials (i.e. welded specimens) subjected to complicated loading cases. To prove the applicability of the present model to complicated three-dimensional structural components, a simulation of creep-fracture for a three-dimensional flange joint with bolted connections was succesfully performed.

Task 5: Creep fracture simulations using FEM and strip yield modeling

Research activities

The failure process by creep crack growth in steels consists of crack incubation and growth. A numerical strip-yield model was developed to simulate creep crack incubation. The model is based on a strip-yield formulation originally proposed for fatigue crack growth under variable amplitude loading. The time evolution of the plastic deformation ahead of a crack loaded in tension was modeled using the Norton law for secondary creep stage, while the primary and tertiary creep stages were neglected. The model assumed a pre-existing crack in a specimen, and modeled the behavior of the material prior to the beginning of crack propagation due to creep loading. The evolution with time of the crack-tip plastic zone, crack-tip opening displacement and yield strength in the plastic zone were computed at constant temperature for center-cracked specimens. The method uses a critical crack-tip opening displacement (CTOD) approach, but other methods can be easily implemented in the model, such as K-based or C*-based laws for crack incubation. Given the large scale yielding conditions prevailing at the crack tip during creep deformation, the critical CTOD was used as a crack incubation criterion.

In addition to the strip-yield model, a combined plasticity-creep model was developed and implemented as a UMAT in the finitele element code ABAQUS. This model was applied to fracture problems by studying the crack tip behavior near the crack tip. It was necessary to combine plasticity and creep constitutive models because even though the remotely applied stresses were low, near the crack tip the stresses exceeded the yield strength of the material, thus leading to the development of instantaneous plastic strains in addition to the creep strains accumulated over time. Crack-tip opening displacement (CTOD), crack tip plastic zone sizes, and material relaxation in the crack tip plastic zone were simulated. Creep crack incubation times were predicted based on the critical CTOD criterion.

Findings and conclusions

Comparison with two previous strip-yield models and experimental data was performed, and excellent correlation was obtained for several Cr-Mo steels. This approach to modeling creep crack incubation has the potential to be applied to other types of cracked specimens under constant or variable amplitude loading. In general, the model developed in this task gives crack incubation times in agreement with the predictions provided by two other analytical strip-yield

models. Also, the model results compare well with experimental data for critical CTOD. The model accurately predicted the increase of the crack-tip plastic zone size, and increase of CTOD and a decrease of the stress at the crack tip with time. The two models (strip-yeild and finite element) can be used successfully to predict the initiation and incubation times for cracks in Grade 91 steels.

Task 6: Design of a device for damage detection using leak method

Research activities

A device for detection of Kr-85 radiation leaking out of containers was designed. Kr-85 content is commonly measured using gamma detectors that employ thallium-doped Sodium Iodide (NaI) crystals. These crystals are often manufactured using a Bridgman process and are formed in a wide variety of geometries depending on the nature of a specific application. Our research indicated that a small detector can be manufactured using low temperature co-fired ceramics (LTCC) which exhibit high degrees of hermeticity (with leak rates less than 10^{-10} atm cc/s). At the same time, conventional electrical interconnections (or "vias") can also be incorporated into LTCC products which also exhibit hermetic properties. This enables the possibility of manufacturing a new type of packaging for NaI scintillation detectors. Particularly intriguing is the possibility of producing scintillation detectors that could be place within pressure vessels, or possibly within the walls of pressure vessels and other containers, so that the emission process from a radioactive tracer can be monitored. The scintillation detector consists of four primary components and one soldered interface. The components are as follows: a scintillation crystal, a protective housing, a light pipe, and a photomultiplier.

Findings and conclusions

An LTCC-based scintillation detector was designed and built. The LTTC-based crystal can be further improved by linking the crystal to a photomultiplier and quantifying the data. Additionally, the use of LTCC in the design could open up the possibility to embed a method of wireless data transmission for relatively low manufacturing cost. The LTCC substrate offers the ideal system for incorporating additional components into the design with minimal change in tooling required for manufacturing. The application of LTCC for hermetic packaging could prove to be useful for customizing scintillation detector designs for each and every application.

.

Task 1: Creep fracture testing of base material and welds of Grade 91 steel specimens

1. Metallurgical Characterization of Grade 91 steel

1.1. Introduction

The Generation-IV reactors are expected to address the growing energy demand by producing electricity and at the same time mitigate greenhouse gas emissions. Various reactor types, such as Gas-Cooled Fast Reactor (GFR), Lead Cooled Reactor (LFR), Molten Salt Reactor (MSR), Sodium-Cooled Fast Reactor (SFR), Supercritical Water-Cooled Reactor (SCWR), and Very High Temperature Reactor (VHTR) are being considered. The VHTR is a Gen-IV reactor system at the heart of the so-called Next Generation Nuclear Plant (NGNP). VHTRs are designed to operate at temperatures much higher than those of currently operating reactors. Moreover, they are designed for longer service periods (60 years or more) compared to the current operating reactors [1]. Depending on the VHTR design, Prismatic Modular Reactor (PMR) or Pebble Bed Modular Reactor (PBMR), as shown in Figs. 1.1 (a) and (b), the operating temperature of the reactor pressure vessel (RPV) can vary between 300^{o}C and 650^{o}C.

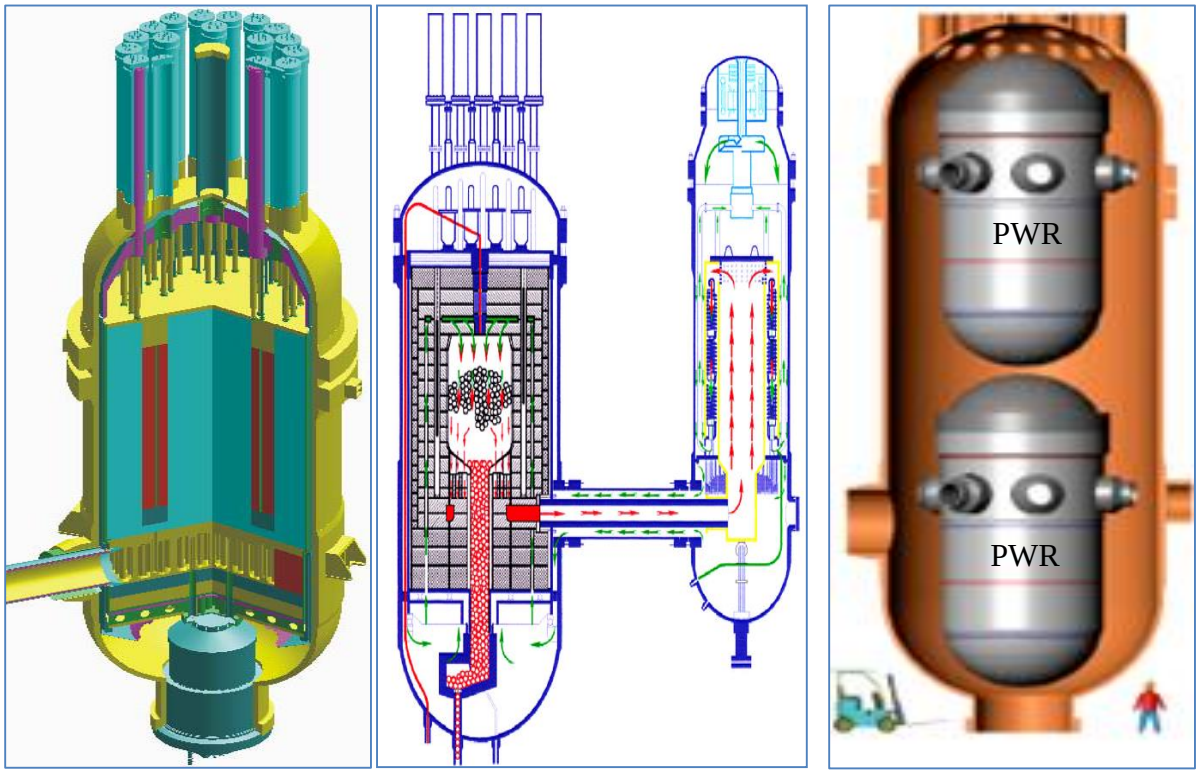

Fig. 1.1. (a) Prismatic reactor [2], (b) Pebble bed reactor [3], and (c) VHTR pressure vessel [4]

Furthermore, the RPV in the VHTR will be more than twice the size of a typical RPV in a Light Water Reactor (LWR) [4], as shown in Fig. 1.1 (c). Grade 91 steel is a material of choice

in fossil-fired power plants with increased efficiency, service life, and reduction in the greenhouse gas emissions of CO_2, NO_x, SO_2. The efficiency of fossil-fired power strongly depends on the temperature and pressure of steam, as shown in Fig. 1.2. One percent increase in the net efficiency can reduce the emission of CO_2, NO_x, SO_2, and particulates by 2.4 metric ton, 2000 ton, 2000 ton, and 500 ton, respectively, while reducing the fuel cost by 2.4% [5]. Steam in these advanced coal-fired power plants is expected to have temperatures in the range of 550 – 720^{o}C and pressures above 24 MPa [5-7].

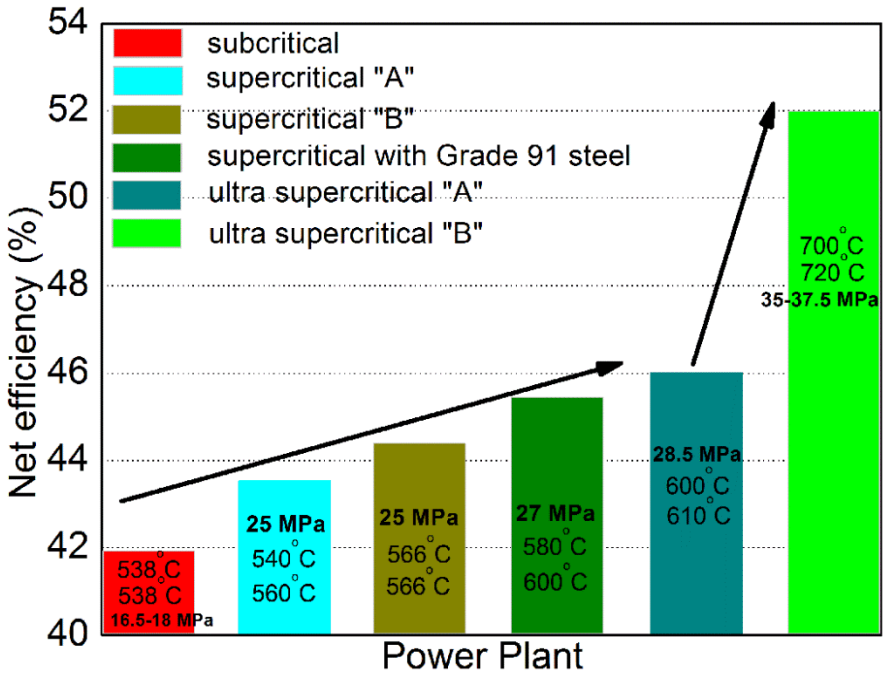

Fig. 1.2. Net efficiency of various power plants [5,7]

Since the introduction of Cr-Mo steels, significant progress has been made in the alloy design, and they have been the material of choice for use in the power plants. Low alloy ferritic steels (e.g. SA533) are generally used as the RPV material for the current LWRs [1]. However, because the RPV in the VHTR is expected to withstand higher temperatures for a longer service time, the material must have superior creep resistance. The current RPV steels cannot meet the creep strength required for the envisioned long term service conditions of VHTR pressure vessels operating at higher temperatures. Ferritic-martensitic (F-M) steels with 9-12 wt.% Cr were previously developed for fossil-fuel-fired power plants [1] in the 1960s, and later used as the boiler tube in the advanced gas-cooled reactors [8,9]. With the addition of Nb, V and other alloying elements, significant improvement in the creep rupture strength of F-M steels has been achieved over the years [9]. F-M steels have better void swelling resistance than austenitic steels [1], excellent thermo-physical properties, and are resistant to stress corrosion cracking in aqueous and chloride environment [10].

A potential candidate material for the VHTR pressure vessel is the Grade 91 F-M steel. It contains alloying elements like Nb and V, forming fine and stable carbides and carbonitrides, which help in improving its creep strength by disrupting the movement of dislocations, delaying the plastic deformation by inhibiting grain boundary sliding, retaining finer grains during austenitization [11], and delaying the onset of tertiary creep stage [12]. Creep strength depends

on various factors, such as temperature, applied stress, grain and subgrain sizes, precipitation at various creep stages, coarsening of precipitates and solute concentration. Presence of various precipitates with different characteristics and concomitant precipitation of particles during creep deformation make it challenging to explain the influence of precipitates on the creep deformation.

Evolution of various precipitates and microstructure can be understood from the heat treatment, differential scanning calorimetric (DSC) studies, and thermodynamic calculations using Thermo-Calc. The heat treatment studies of Grade 91 steel helps in understanding its microstructural evolution and mechanical properties as this material whether being used for a reactor pressure vessel or boiler component goes through a series of heating, cooling, and welding processes. Different types of carbides such as M_6C, $M_{23}C_6$, Laves phase, sigma phase, and Nb/V rich MX type carbide/carbonitride precipitate and evolves in Grade 91 steel. Ahn et al. [13] observed a decrease in the high temperature strength of Nb-free stainless steel, but over long aging period of Nb-added steel, the high temperature strength decreased due to coarsening of Nb rich precipitates. DSC was used to measure the heat absorbed or liberated during heating or cooling associated with carbide precipitation, phase change and chemical reactions. Ganesh et al. [14] were able to find the phase transformation temperatures.

RPV is considered an irreplaceable component of a nuclear power plant which dictates its useful service life. Hence, understanding the creep rupture properties of Grade 91 steel is important to predict the long term mechanical integrity of the plant. Service life is a major concern in VHTR RPVs, which have thickness in the range of 100-300 mm and are expected to operate for more than 60 years [4]. Welding is used in joining different parts of the RPV, but it has the potential of creating soft zones with lower strength in the welded specimens, leading to premature failure [15]. Residual stresses are present throughout the weldment as a result of intense localized heating and rapid cooling during solidification of the weld [16]. The residual stress resulting from welding can be both compressive and tensile. A compressive stress prevents crack propagation, while tensile stresses do the opposite, degrade the fatigue characteristics, lead to brittle fracture, and accelerate stress corrosion cracking [17]. Residual stresses can be measured by destructive techniques including the contour method, hole drilling, or by non-destructive techniques like X-ray and neutron diffraction techniques [18,19]. Because of higher depth of penetration, neutron diffraction has distinctive advantages over X-ray diffraction. Residual stress can be caused by machining of parts, phase transformation, dimensional change (thermal contraction) after weld cooling, and the chemical compositional gradient. In ferritic steels, the shrinkage effect is generated when a weld metal solidifies on a solid surface along all orthogonal directions. Residual stresses were measured using neutron diffraction technique in welded Grade 91 steel plates in the as-welded condition and after post-weld heat treatment. The reduction in the load bearing cross-section can be significant for specimens crept for extended period of time resulting in creep rupture. However, the significance of internal necking through the microstructural degradation, cavity formation, growth and coalescence must be taken into account to understand the final failure mechanism.

This project aimed to address various aspects of Grade 91 steel as a potential material for applications in a high temperature nuclear reactor. The overall theme of this work has been establishing the relationships between the mechanical properties and microstructural characteristics. The specific objectives of this dissertation are listed below.

1. Perform creep testing of Grade 91 steel in various temperatures and stress regions, and establish creep deformation mechanisms in the light of existing high temperature deformation theories.
2. Characterize the creep-rupture behavior of Grade 91 steel and identify the associated failure mechanisms.
3. Study the heat treatment behavior (normalizing and tempering) of Grade 91 steel using a combination of experimental and computational tools.
4. Characterize the fusion welded Grade 91 steel and study the residual stress distribution, microstructure, hardness and creep properties.

1.2. History of ferritic-martensitic steel development

Since the introduction of Cr-Mo steels, they have come a long way and have been a materials of choice in the power generation plants. At present, Grade 91 (*aka* modified 9Cr-1Mo steel) is being given active consideration for being used in Generation-IV reactors. Modified 9Cr-1Mo steel has different alloying elements alloyed in various quantities. T22 (Fe-0.15C-0.3Si-0.45Mn-2.25Cr-1.0Mo) and T9 (Fe-0.12C-0.6Si-0.45Mn-9.0Cr-1.0Mo) were first introduced in the 1940s. In both T22 and T9 steel, the percentage of ferrite stabilizers is higher than the austenite stabilizers, resulting in significant substitutional solid solution strengthening. For a test condition of 600^{o}C and 40 MPa, these steels had rupture lives up to10^5 hours. The developmental history of F-M steels is listed in Table 1.1. The first generation of F-M steels was made in 1960s by the addition of carbide formers, like V, to simpler Cr-Mo steel mainly for precipitation strengthening. Steels like EM-12, HCM9M, HT9, HT91 had a maximum operating temperature of 565^{o}C. These first generation steels were considered for fast reactors during 1970s. Addition of Nb and N, reduction of C content, and adjustment in the Cr content in first generation steel led to the development of the second generation of F-M steels. These steels could operate at higher stresses compared to the previous generation steels and have similar rupture strength. Additions of carbide formers like Nb and N aided in precipitation hardening because of the formation of fine carbides and carbonitrides. A reduction in the carbon content increased the corrosion resistance and ductility of the steels. The third generation steel, which had a maximum operation temperature of 620^{o}C, was made by lowering the Mo content, and adding W. Both Mo and W are ferrite stabilizers, and strongly contribute to the substitutional solid solution strengthening mechanism. Boron was added to aid the interstitial solid solution strengthening mechanism, and machinabilty of the steels. Though addition of W in the third generation steels decreases the creep life of the alloy, presence of B delays the coarsening of carbides. Finally, NF12 and SAVE12 are the fourth generation steels in which the amounts of W and Co are significantly increased. Cobalt is an austenite stabilizer, which reinforces the substitutional solid solution strengthening.

Table 1.1. Evolution of ferritic/martensitic steels for power generation industry [9]

Generation	Years	Steel modification	10^5 h rupture strength at 600°C, MPa	Steels	Maximum use of temperature, °C
0	1940-60		40	T22, T9	520-538
1	1960-70	Addition of V to simple Cr-Mo steels	60	EM-12, HCM9M, HT9, HT91	565
2	1970-85	Optimization of C, Nb, V, N	100	HCM12, T91, HCM2S	593
3	1985-95	Partial substitution of W for Mo and add Cu, N,B	140	NF616,E911, HCN12A	620
4	Future	Increase W and add Co	180	NF12,SAVE12	650

1.3. Metallurgy of Grade 91 steel

1.3.1. Microstructure

The as-received Grade 91 steels have a tempered martensitic microstructure. Precipitation hardening is one of the main strengthening mechanisms in highly alloyed steels like Grade 91. Alloying elements, such as C, N, Nb, V, Cr and Mo, promote the formation of precipitates like Cr-rich $M_{23}C_6$, and Nb or V-rich MX particles. In $M_{23}C_6$, 'M' stands for Cr and/or Mo whereas 'M' in MX stands for metals, such as Nb and/or V. The Cr-rich $M_{23}C_6$ precipitates are elongated rod-like or block-like particles, while Nb-rich and V-rich MX precipitates have nearly spherical shapes. The Cr-rich $M_{23}C_6$ type precipitates were mainly observed at the lath boundaries, prior austenite grain boundaries (PAGB). The dimensions of the elongated rod-like and block-like Cr-rich precipitates have an average length of 285±80 nm and width of 121±39 nm [20-22]. The average diameter of near-spherical MX-type precipitates are 37±15 nm [20,21,23]. These types of precipitates were mainly located in the inside PAGB and martensitic lath structure. Thermally stable fine MX type precipitates enhance the long term creep resistance. The addition of V and Nb increases the precipitation of MX particles, while 0.1 wt.% C limits the precipitation of large Cr-rich $M_{23}C_6$ carbides. The smaller interparticle spacing and increased volume fraction of the fine MX carbides generally help in enhancing the creep strength.

1.3.2. Precipitates

Precipitates present inside the grains tend to increase the strength of a material by increasing the stress required for dislocations to pass through the precipitates. The stress required to pass through incoherent precipitates is given by the following relationship:

$$\sigma_o = \frac{Gb}{\lambda} \quad (1)$$

where σ_o is the stress required to force the dislocation between the obstacles, G the shear modulus, and λ the inter-particle spacing. The spacing between two particles is given by the following equation:

$$\lambda = \left(\frac{0.5}{\sqrt{\left(\frac{6f}{\pi}\right)}} - \sqrt{\frac{2}{3}} \right) r \qquad (2)$$

where f is the volume fraction of precipitates, and r the average radius of spherical particle. It can be derived from Equation (1.1) that the stress required to force dislocation between the obstacles increases with decrease in the inter-particle spacing. Higher precipitate volume fraction also increases the strength of a material. In all above equation the particles are considered to be spherical. But stress required to force the dislocation between obstacles is higher for elongated precipitates [24]. Apart from the precipitates obstructing the movement of dislocations, each successful dislocation leaves a dislocation loop around the particle which decreases the distance between the particles.

Table 1.2. Different types of precipitates present in high chromium martensite steels [26].

Precipitate Phase	**Crystal Structure, Lattice Parameter**	**Typical Composition**	**Distribution of Precipitates**
$M_{23}C_6$	fcc, 1.066 nm	$(Cr_{16}Fe_6\ Mo)C_6$, $(Cr_4Fe_{12}Mo_4Si_2WV)C_6$	Coarse particles at prior austenite grain and martensite lath boundaries and fine intra-lath particles
MX	fcc, 0.444–0.447 nm	NbC,NbN, VN, (CrV)N, Nb(CN) and (NbV)C	Undissolved particles and fine precipitates at martensite lath boundaries
M_2X	Hexagonal, a = 0.478 nm, c = 0.444 nm	Cr_2N, Mo_2C and W_2C	Martensite lath boundaries (Cr_2N and Mo_2C); prior austenite grain boundaries (Mo_2C); intra-lath (Mo_2C and W_2C); δ-ferrite in duplex steel [$Cr_2(CN)$ and $(CrMo)_2$ and $(CrMo)_2(CN)$]
Z-phase	Tetragonal, a = 0.286 nm, c = 0.739 nm	(CrVNb)N	Large plate-like particles in the matrix after creep straining at 600°C.
η-carbide	Diamond cubic, 1.07-1.22 nm	M_6C, $(Fe_{39}Cr_6Mo_4Si_{10})C$	Prior austenite grain and martensite lath boundaries and intra-lath
Vanadium carbide	fcc, 0.420 nm	V_4C_3	Low number density in matrix
Laves phase	Hexagonal, a = 0.4744 nm, c = 0.7725 nm	Fe_2Mo, Fe_2W, and $Fe_2(MoW)$	Prior austenite grain and martensite lath boundries and intra-lath; δ-ferrite in duplex steels
Chi(χ)	bcc, 0.892 nm	$M_{18}C$ or $Fe_{35}Cr_{12}Mo_{10}C$	Intra-martensite lath; δ-ferrite in duplex steels

MX type precipitates are carbides and carbonitrides of niobium and vanadium which have a smaller lattice parameter than $M_{23}C_6$. The lattice parameter of $M_{23}C_6$ is about 2.4 times larger than that of MX type precipitates. The MX type precipitates are mainly seen within the grain boundary, and are able to restrict the dislocation movement, thus enhancing the precipitation strengthening. A list of various precipitates found in high chromium steels are shown in Table 1.2. Precipitates like $M_{23}C_6$, MX and vanadium carbide (V_4C_3) have fcc crystal structure, which is the same as that of γ-Fe; the coherency in the crystal structure of these carbides and γ-Fe aids in the even distribution of precipitates in the austenite phase. During creep tests, the size of precipitates increases, increasing the creep rate and leading to lower creep-rupture life. Laves phases are absent at the beginning but start forming during the creep in the solid solution matrix. In a TEM study by Hald [25], Laves phase was detected in a P92 steel after creep for 59,000h at 600^{o}C and 125 MPa. Laves phase lowers the strength of steel by pulling Mo out of solid solution, thus deteriorating the solid solution strengthening effect. Laves phase has hexagonal crystal structure (a = 0.4777 nm, c = 0.7725 nm) with a typical composition of Fe_2Mo, Fe_2W, and $Fe_2(MoW)$ [26].

1.3.3. Effect of constituent elements

Different elements are added to improve the strength of the steel, but one has to be careful in that adding alloying elements could lower the M_s-M_f temperature below the room temperature. An incomplete transformation of austenite phase to martensite phase would decrease the strength of material. Some elements are also reported to accelerate the creep rate of steels, promote coarsening of precipitates and increase subgrain sizes.

1.3.3.1. Chromium

Chromium improves hardenability, strength, wear resistance, and enhanced corrosion resistance at high concentrations. Chromium in Grade 91steel reacts with carbon to form coarse $M_{23}C_6$ and finer M_2X carbides. Most of the Grade 91 steels have nitrogen in about less than 0.05 wt.% which combines with chromium to form Cr_2N phases [9].

1.3.3.2. Vanadium

Vanadium increases strength, hardness, creep resistance and impact resistance due to formation of hard vanadium carbides, which limit grain growth. The amount of vanadium is generally limited to 0.2% as it deteriorates the creep strength over increased percentage. Vanadium addition increases the amount of ferrite [27] which leads to lower strength and fracture toughness [9]. The vanadium carbonitrides precipitate with niobium carbonitrides to form thermally stable V-wing [28]. The V-wing looks like a socket bone and is effective in the disruption of dislocation movement.

1.3.3.3. Niobium

Niobium has low neutron absorption cross-section (low activation). Like any other nitride/carbide former, niobium reacts with carbon and nitrogen to form Nb(CN), which removes

carbon from the matrix and enhances the corrosion property. Niobium carbides aid in the long term creep property of steels by pinning mobile dislocations. For short term creep (1000 h), the creep life of 20Cr-25Ni austenite steel was maximized using the Nb/C atomic ratio of 1:1 [29]. The amount of niobium carbide precipitates depends on the degree of deviation from the stoichiometry.

1.3.3.4. Molybdenum

Molybdenum increases hardenability and strength particularly at high temperature and under dynamic conditions. Mo is a ferrite stabilizer and is a potent solid solution strengthener. Mo can be present as a part of coarse $M_{23}C_6$ particles and fine grain MX precipitates. The bcc structures of Mo and α-ferrite have lattice constants (*a*) of 3.150 Å and 2.87 Å, respectively. Since the difference in the lattice parameter of both elements is about 10% and have same crystal structure, they form a strong substitutional solid solution. Tungsten is sometimes preferred over Mo because the precipitates containing W has slow response to creep over Mo. The amount of Mo is about 1.0% in P91 steel because increased Mo leads to formation of detrimental Laves phase [9].

1.3.3.5. Copper

Copper improves corrosion resistance and ductility in low carbon steel. But it causes irradiation embrittlement in structural steel of nuclear reactor [30]. Copper has also been to have contributed to the production of finer distribution and a faster growth of Laves phases [9].

1.3.3.6. Nickel, Manganese, Cobalt

Nickel, manganese and cobalt are austenite stabilizers which aid in solid solution strengthening. It increases impact strength and toughness, and impart corrosion resistance of steel in combination with other elements. Ni aids in hydrogen pick up. Nickel-containing alloys take longer time to deactivate. In Grade 91 steel, addition of nickel enhances the tensile properties but decreases the creep rupture time. Manganese improves hardenability, ductility and wear resistance of steel. It eliminates formation of harmful iron sulfides increasing strength at high temperature. Addition of Mn did not make significant change in tensile strength but generally decreases the creep rupture life [27].

1.3.3.7. Carbon, Nitrogen, and Sulfur

Carbon and nitrogen are strong austenite stabilizers which make the formation of carbides and carbonitrides possible. Even though lower amounts of carbon increase the ductility, the amount of carbon is kept low in most high strength steels as it compromises the weldability and corrosion resistance of the steels. Nitrogen contributes to the secondary hardening by aiding in the formation of hexagonal $Cr_2N(M_2X)$ phase precipitates [26]. Addition of nitrogen enhances the rupture strength significantly compared to Si. C. Riou et al. [31] have reported sulfur as a source of hot cracking. High manganese to sulfur ratio is favorable in avoiding hot cracking.

1.4. Creep

When a material deforms in an elastic region, the material regains its original state after the load is removed. The elastic deformation is a linear relationship in which stress is directly proportional to strain according to Hooke's law. Materials cannot retrieve their original state when it is deformed in the plastic region. Despite the material being deformed plastically at ambient temperature, work hardening increases the strength of the material. During work hardening, prior dislocations obstruct the passage of any new dislocations, thus increasing the strength of the material. But at elevated homologous temperatures due to thermal energy, the dislocations annihilate and the work hardening is weakened. Creep deformation and rupture of metals is of great concern for prolonged service life at elevated temperatures. For an engineering structure operating in ambient temperature, creep is not considered as a significant deformation mechanism. In a high temperature application, parameter like the duration of test, the grain size, subgrain size, precipitate size, effective stress all have a role in dictating the strength of the material.

A conventional creep curve consists of three distinct stages: primary, secondary and tertiary, as shown in Fig. 1.3a, and 1.3 b. In primary creep, the strain rate (or creep rate) decreases with time as work hardening takes the center stage. The secondary stage, also known as steady-state creep, is of vital importance as it sheds light on the creep deformation mechanism. In the secondary creep stage, the material is deformed plastically while there is a higher degree of strain hardening and increased dislocation density, resulting in a constant creep rate.

Strain rate increases as time increases in tertiary creep. Increased creep rate results in necking, crack, and void formation. Tertiary creep stage is very rapid so the materials in engineering structures are designed not to enter this stage.

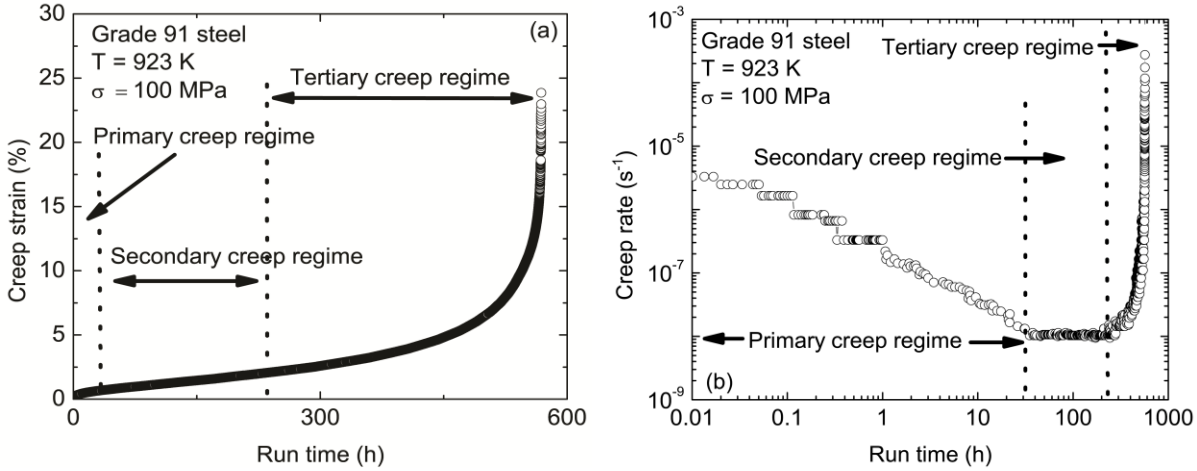

Fig. 1.3. (a) A typical creep curve, and (b) creep rate vs. time showing three distinct stages.

The operational life of a material can be predicted from the knowledge of creep deformation mechanism. Norton's and Bird-Mukherjee-Dorn (BMD) relations are used to describe creep mechanisms. Norton's equation is

$$\dot{\varepsilon}_s = k\sigma^n \ , \qquad (3)$$

where $\dot{\varepsilon}_s$ is the steady-state creep rate, σ the stress, k a constant based on material property and test condition, and n the stress exponent - a constant for a mechanism. A plot obtained by plotting creep rate (s^{-1}) against stress (MPa) generated high stress exponents of 13. The high stress exponent can be attributed to increased volume fraction of precipitates in the grain. The stress exponent value is influenced by the dynamics of precipitation [32]. Coarsening of precipitates occurs during the creep test. P92 steel when crept above 145 MPa at 600°C and above 110 MPa at 650°C, and at lower stresses, stress exponents were 16 and 6, respectively [33]. Kloc et al. [34] reported stress exponents ranging from 1 to 10 for modified 9Cr-1Mo steel crept in the temperature range of 600-650°C and stress range of 1-350 MPa. Stress exponent ranging from 1 to 15 was reported by Spigarelli et al. [28] for modified 9Cr-1Mo steel in the stress range of 160-225 MPa at 600°C. These changes in stress exponent direct to the change in the rate-controlling deformation mechanisms. Various deformation mechanisms are listed in Table 1.3.

Diffusional controlled processes dominate the high-temperature mechanical properties of metals especially above homologous temperatures of $0.4T_m$. The Bird-Mukherjee-Dorn (BMD) equation best describes the creep mechanism in this regime. BMD considers a wide range of parameters in determining the prevalent creep mechanism:

$$\frac{\dot{\varepsilon}kT}{DEb} = A\left(\frac{\sigma}{E}\right)^n\left(\frac{b}{d}\right)^p \tag{4}$$

where $\dot{\varepsilon}$ the steady state creep rate, A the microstructural mechanical constant, E the elastic modulus, b the burger vector, k the Boltzmann constant, T the absolute temperature, σ the applied stress, d the grain diameter, n the stress exponent, p the inverse grain size exponent, D the diffusivity. D is described by following relation:

$$D = D_o exp\left(\frac{-Q}{RT}\right) \tag{5}$$

where, D_o is the frequency factor, Q the activation energy for creep, and R the universal gas constant. Newtonian viscous mechanisms show stress exponent values of 1 as the material acts like Newtonian viscous fluid. There are three distinct creep mechanisms stress exponents of 1 (i.e., n = 1): Harper-Dorn (H-D), Nabarro-Herring (N-H) and Coble creep. The H-D creep was first observed in pure aluminum with large grain sizes at high homologous temperature (~ $0.99T_m$), with creep activation energy close to that of the lattice self-diffusion [35]. This creep mechanism is independent of grain size. Further, it involves subgrain formation, stress independent dislocation density, and distinctive primary creep stage [36], and significantly higher creep rates than those predicted by N-H, and may be for Coble if the test temperature is very low [37]. The constitutive equation for H-D creep is given by the following expression:

$$\dot{\varepsilon}_{HD} = A_{HD}\left(\frac{D_l Eb}{kT}\right)\left(\frac{\sigma}{E}\right)^1 \tag{6}$$

where A_{HD} ~3×10^{-10} [35], D_l is the lattice diffusivity, and $\dot{\varepsilon}_{HD}$ the steady state H-D creep rate.

In N-H and Coble creep mechanisms (collectively called diffusion creep), vacancies migrate through the lattice and grain boundary, respectively. In diffusion creep, excess vacancies are created at the grain boundaries experiencing tensile stress, and these vacancies

migrate to the boundaries in compression. So in essence, atoms move from the compressed grain boundaries to grain boundaries in tension. In the dispersion-hardened alloys, the matrix material free of dispersed precipitates is deposited at the transverse boundaries, while a high concentration of particles accumulates at the longitudinal boundaries [38]. In N-H creep, diffusion of vacancies takes place through the lattice and the corresponding constitutive model is described by the equation

$$\dot{\varepsilon}_{NH} = A'_{NH}\left(\frac{D_l Eb}{kT}\right)\left(\frac{b}{d}\right)^2\left(\frac{\sigma}{E}\right)^1 \tag{7}$$

where $A'_{NH} = 28$ [37], and $\dot{\varepsilon}_{NH}$ is the N-H creep rate. Coble creep model is described by the equation

$$\dot{\varepsilon}_C = A_C\left(\frac{D_b Eb}{kT}\right)\left(\frac{b}{d}\right)^3\left(\frac{\sigma}{E}\right)^1 \tag{8}$$

where A_C = 150 [39], D_b is the grain boundary diffusivity, and $\dot{\varepsilon}_C$ the Coble creep rate. Grain boundary diffusion is prominent in Coble creep mechanism and is grain size sensitive (p = 3). For high stress and low temperature regions, creep behavior is explained by the BMD equation (Eq.1.4). However, for particle-hardened alloys, the BMD equation tends to result in high activation energy and stress exponent. The deformation creep mechanism in a P92 steel (9.1Cr-0.5Mo-1.8W-0.2V-0.06Nb-0.04 N, wt.%) was found to be the power law creep with high stress exponents in the high stress, low temperature regime [34]. Ennis et al. [33] attributed the high stress exponents to precipitates that act as dislocation barriers. The high apparent stress exponents obtained necessitate the threshold stress to be considered in order to fully elucidate the true creep mechanisms in Grade 91 steel. The high stress exponent and activation energy make it difficult to elucidate the true deformation mechanisms. Hence, the BMD equation has to be modified for a particle hardened alloy by incorporating the stress imparted on the dislocations by the precipitates. The modified BMD equation incorporating threshold stress is described by the following equation:

$$\frac{\dot{\varepsilon}_{ss} kT}{DEb} = A\left(\frac{\sigma-\sigma_{th}}{E}\right)^n\left(\frac{b}{d}\right)^p \tag{9}$$

where σ_{th} is the threshold stress and all other terms have been defined previously. Threshold stress is generally defined as the stress below which no creep deformation occurs due to a specific creep mechanism. Thus, the effective stress, (σ - σ_{th}), is actually responsible for the creep deformation instead of the applied stress [40]. The true activation energy and stress exponent obtained from the modified BMD equation will be able to explain the creep deformation in the higher stress regime of Grade 91 steel. This type of behavior has been found to be prevalent in many particle-containing alloys. One of the theories of threshold stress is based on the local climb of particles by dislocations, while restricting the movement of dislocations via attractive interaction between the dislocations and incoherent particles resulting in departure side pinning [41]. Table 1.3 summarizes the parametric dependencies of various diffusion-controlled deformation mechanisms.

Table 1.3. Parametric dependence of various diffusion-controlled deformation mechanisms [42]

Mechanism	Q	n	p
Climb of Edge Dislocations	Q_L	5	0
Viscous Glide	Q_S	3	0
Grain Boundary Sliding (Superplasticity)	Q_B	2	2
Harper-Dorn	Q_L	1	0
Nabarro-Herring	Q_L	1	2
Coble	Q_B	1	3

Note. Q_L: lattice diffusion, Q_S: solute diffusion, Q_C: dislocation core diffusion, and Q_B: grain boundary diffusion

1.5. Strengthening mechanisms

Ferritic-martensitic steels like Grade 91 steels are strengthened by various strengthening mechanisms like solid solution hardening, precipitation hardening, strain hardening, and sub-grain size hardening.

1.5.1. Solid solution hardening

Various alloying elements get into the iron lattice to form a solid solution in Grade 91 steel. Each constituent element takes a spot in the solvent crystal while forming a solution. Based on the location of the solute element in the solvent crystal, solid solution is classified into substitutional solid solution and interstitial solid solution. In substitutional solid solution, the solute elements replace iron atoms in the lattice. These types of solute elements have atomic radii similar to that of iron (Fe), such as molybdenum (Mo), chromium (Cr), etc. In interstitial solid solutions, the solute elements occupy the interstitial spaces in the Fe crystal lattice. These types of solute elements (C and N) have atomic radii much smaller than that of Fe. The substitution of Fe atom or addition of other elements strain the Fe matrix, hindering the movement of dislocations through the crystal and lock the dislocations, thus resulting in increased strength.

1.5.2. Precipitation hardening

Precipitates formed in Grade 91 steel increase the strength of the alloys by disrupting the movement of dislocation. The disruption creates a strain field around the particle and in the lattice. The dislocation being pinned by precipitates have to cut through the precipitate, climb the dislocation, or move in between the precipitates. Grade 91 steel contains alloying elements like Nb, Ti and V, forming fine and stable carbides and carbonitrides, which help improve its creep strength by disrupting the movement of dislocations, delaying the plastic deformation by inhibiting grain boundary sliding, retaining finer grains during austenitization [11], and delaying the onset of tertiary creep stage [20].

Precipitation hardening in the low temperature and high temperature domains is controlled by different mechanisms. In low temperature, Orowan's repulsive dislocation-particle interaction is prevalent. In repulsive dislocation-particle interaction, a dislocation by-passes

precipitate by forming a dislocation loop around the particle. The climb of dislocation over the particle is possible at elevated temperature. The climb of dislocation over particle could be a general climb or local climb based on the dislocation energy between the matrix-particle interfaces. Based on the nature of interaction between precipitates and dislocation, various models explain the strengthening mechanism resulting from the precipitate-dislocation interaction. According to Srolovitz's model [43], when a dislocation enters the matrix-particle interface, there is relaxation of the dislocation core leading to the pinning of dislocation. Because of the reduced elastic energy of dislocation in the matrix-particle interface, the local climb of dislocation over a precipitate is dominant over the general climb. Artz et al. [44] proposed a model based on the attractive dislocation-particle interaction, in terms of the particle detachment stress as a description of threshold stress. The detachment threshold stress is independent of the mode of dislocation climb over particle. Hence, it is applicable for both local and general climb of dislocation over particle.

1.5.3. Strain hardening

Interactions of dislocations also known as forest of dislocations control the movement of dislocations through the lattice. These interactions create stress field in the grain disrupting the flow of dislocations. Ferritic-martensitic steels have dislocation density of about $4.5\pm1.9\times10^{14}$ m^{-2} [23]. Dislocation multiplication occurs via Frank-Read mechanisms, condensation of vacancies, multiple cross-slip mechanisms, and generation from high-angle grain boundaries. The stress (σ) can be related to average dislocation density (ρ) by following relation:

$$\sigma = \sigma_o + \alpha G b \rho^{\frac{1}{2}} \tag{10}$$

where σ_o is the stress required to move a dislocation in absence of other dislocations, α is a constant that varies from 0.3 to 0.6 for fcc and bcc metals, b is the Burgers vector, and G is the shear modulus.

1.5.4. Sub-grain hardening

With the increase in subgrain size, the strengthening mechanisms deteriorates over time during creep, and the material loses its inherent creep rupture strength. Panait et al. [23] assert that the growth of subgrains during creep contributes most to the decrease in long-term creep resistance. According to Qin et al. [45] the evolution of subgrain size is given by following relation:

$$log\lambda = log\lambda_s + \log\left(\frac{\lambda_0}{\lambda_s}\right) exp\left(\frac{-\varepsilon}{k_w}\right) \tag{11}$$

where, λ is the subgrain size, $\lambda_s = 10Gb/\sigma$ is the subgrain size in the steady state regime, λ_o is the subgrain size in as-received condition, ε is the creep strain, $k_w \approx 0.12$ is a growth constant, G is the shear modulus, b is the Burgers vector and σ is the applied stress. The mean subgrain size in 12Cr1MoV, P91 and P92 steel was 0.35-0.42 μm [46]. In P92 steel at 600°C and 160 MPa, the

subgrain size increases from 700 nm at 1.8% strain to 1400 nm at 22.8% strain [33]. In our study, the average size of subgrains in the as-received condition was 0.15-0.4 μm. In a test done at 650^{o}C and 200 MPa, the subgrain size in grip and gauge section of creep specimen was 0.5 μm and 0.7 μm, respectively.

1.6. Weldability characteristics of Grade 91 steel

Welding of Grade 91 steel creates a heat affected zone (HAZ) resulting in changes in microstructure because of the temperature gradient during welding. As-welded and post weld heat treated (PWHT) specimens have weld zone, unaffected base material (BM) and HAZ. HAZ has three distinct microstructures, i.e. coarse, fine grain and partially austenitized grain structures and an indistinctive columnar structure formed after directional solidification in the weld zone, as shown in Fig. 1.4.

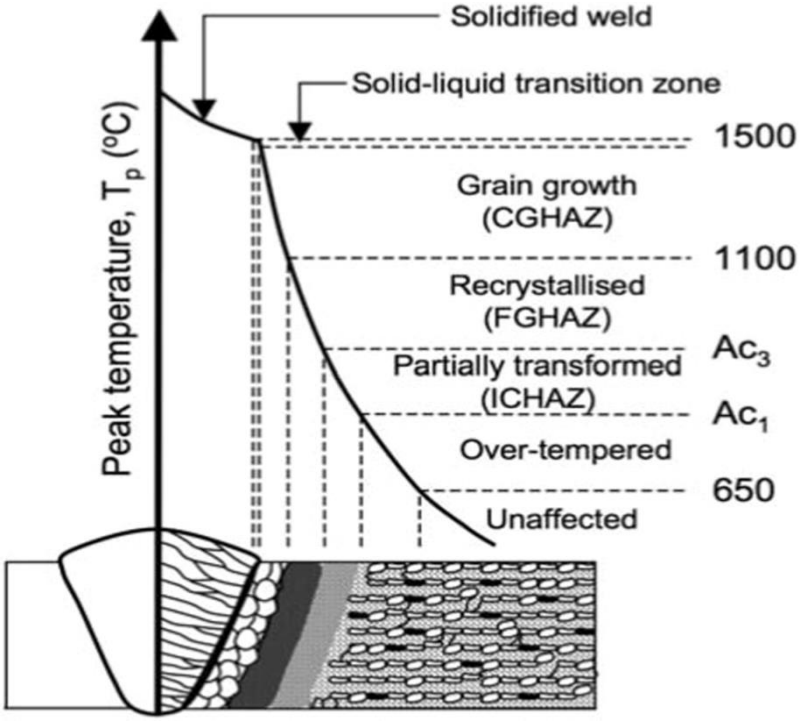

Fig. 1.4. Schematic representation of microstructures developed in welded 2.25Cr-1Mo steel specimen as approximate function of peak temperature during welding [47].

The weld zone in the as-welded material has martensitic lath structure, on post weld heat treatment the lath size increases. The HAZ is considered the most creep-prone zone and is susceptible to type IV cracking. It has been widely reported that type IV cracking is the point of initiation of cracks in the HAZ. During creep tests, materials undergo recovery, recrystallization and grain growth resulting in dynamic microstructure. The rate of transformation and localized concentration of δ-ferrite, austenite, α-ferrite, martensite and precipitates create intercritical heat affected zone (ICHAZ), fine grain heat affected zone (FGHAZ), and coarse grain heat affected zone (CGHAZ). ICHAZ is of greater concern as it is the initiation point for type IV cracking.

CGHAZ is next to fusion zone. It consists of austenite, martensite and δ-ferrite structure. As this region sees temperature above $A_{C3,}$ all of the carbides are dissolved increasing the austenite grain growth rate; thus, forming coarser austenite grains of about 80 μm size [10] and larger martensitic lath structure. In general, CGHAZ exhibits the same type of tempered martensitic microstructures as the base metal, with grains slightly larger. FGHAZ sees temperatures above A_{C3}, but lower than that of CGHAZ; thus, slowing the dissolution of carbides, which impedes the formation of austenite grain. The slower rate of austenite transformation results in finer austenite grain sizes of about 10 μm [10]. FGHAZ lies between CGHAZ and ICHAZ. FGHAZ had lower volume fraction of precipitates compared to CGHAZ. ICHAZ sees temperature between A_{C1} and A_{C3} resulting in partial transformation to austenite which limits the solid solution forming duration. ICHAZ lies next to the base metal. Klueh [9] has pointed out that ICHAZ is prone to type IV cracking due to preferential creep cavitation [10]. ICHAZ, a mixture of normalized and tempered martensite, acts as a nucleating site for voids and cracks.

References

[1] I. Charit, K. L. Murty, Structural materials issues for the next generation fission reactors, JOM 62 (9) (2010) 67-74.

[2] P. E. MacDonald, P. D. Bayless, H. D. Gougar, R. L. Moore, A. M. Ougouag, R. L. Sant, J.W. Sterbentz, W. K. Terry, The next generation nuclear plant insights gained from the INEEL point design studies, In: Proceedings International Congress on Advances in Nuclear Power Plants (ICAAP 04) Paper No. 3405, Pittsburgh, PA, June 13-14, 2004.

[3] H. Nabielek, Fuel for gas-cooled reactors mainly HTR, ATR NSUF Users Week 7-11, June 2010, Idaho Falls, ID, USA.

[4] K. L. Murty, I. Charit, Structural materials for Gen-IV reactors: challenges and opportunities, J. Nucl. Mater. 383 (2008) 189-195.

[5] D. Rojas, 9-12% Cr heat resistant steels: alloy design, TEM characterization of microstructure evolution and creep response at 650^{o}C, Doctoral dissertation, Ruhr-University Bochum, Bochum, Germany, 2011.

[6] R. Vishwanathan, W. T. Bakker, Materials for boilers in ultra-supercritical power plants, ASME, Proceedings of 2000 International Joint Power Generation Conference, Miami Beach, Florida, July 23-26 (2000) 1-22.

[7] B. J. P Buhre, R. Gupta, S. Richardson, A. Sharma, C. Spero, T. Wall, PF-Fired Supercitical Boilers: Operational Issues and Coal Quality Impacts, CCSD, March 2002.

[8] E. Barker, Creep fracture of a 9Cr-1Mo steel, Mater. Sci. Eng. 84 (1986) 49-64.

[9] R. L. Klueh, Elevated temperature ferritic and martensitic steels and their application to future nuclear reactors, Int. Mater. Rev. 50 (2005) 287-310.

[10] K. Laha, K. S. Chandravathi, P. Parameswaran, K. Bhanu Sankara Rao, S. L. Mannan, Characterization of microstructures across the heat-affected zone of the modified 9Cr-1Mo weld joint to understand its role in promoting type IV cracking, Metall. Mater. Trans. A 38 (2007) 58-68.

[11] Y. Z. Shen, S. H. Kim, H. D. Cho, C. H. Han, W. S. Ryu, Identification of precipitate phases in a 11Cr ferritic/martensitic steel using electron micro-diffraction, J. Nucl. Mater. 400 (2010) 64-68.

[12] M. Tanelke, F. Abe, K. Sawada, Creep-strengthening of steel at high temperatures using nano-sized carbonitride dispersions, Nature 424 (2003) 294-296.
[13] J. C. Ahn, G. M. Sim, K. S. Lee, Effect of aging treatment on high temperature strength of Nb added ferritic stainless steels, Mater. Sci. Forum 475-479 (2005) 191-194.
[14] B. J. Ganesh, S. Raju, A. K. Rai, E. Mohandas, M. Vijayalakshmi, K. B. S. Rao, B. Raj, Differential scanning calorimetry study of diffusional and martensitic phase transformations in some 9 wt.% Cr low carbon ferritic steels, Mater. Sci, Tech. 27 (2011) 500-5012.
[15] K. Laha, K. S. Chandravathi, P. Parameswaran, K. Bhanu Sankara Rao, S. L. Mannan, Metall. Mater. Trans. A 38 (2007) 58-68.
[16] S-H. Kim, J-B. Kim, W-J. Lee, Numerical Prediction and neutron diffraction measurement of the residual stresses for modified 9Cr-1Mo steel weld, J. Mater. Procs. Tech. 209 (2009) 3905-3913.
[17] G. E. Dieter, Mechanical Metallurgy, McGraw-Hill Book Company, New York, 1961.
[18] P. J. Withers, Residual stress and its role in failure, Rep. Prog. Phys. 70 (2007) 2211-2264.
[19] A. D. Krawitz, Introduction to diffraction in materials science and engineering, 1st eds. Wiley-Interscience Publication, New York, 2001.
[20] M. Tanelke, F. Abe, K. Sawada, Creep-strengthening of steel at high temperatures using nano-sized carbonitrides dispersions, Nature 424 (2003) 294-296.
[21] S. Spigarelli, E. Cerri, P. Bianchi, E. Evangelista, Interpretation of creep behavior of a 9Cr-Mo-Nb-V-N (T91) steel using threshold stress concept, Mater. Sci. Tech. 15 (1999) 1433-1440.
[22] P. Anderson, T. Bellgard, F. L. Jones, Creep deformation in a modified 9Cr-1Mo steel, Mater. Sci. Tech. 19 (2003) 207-213.
[23] C. G. Panait, A. Zielinska-Lipiec, T. Koziel, A. Czyrska-Filemonowicz, A-F. Gourgues-Lorenzon, W. Bendick, Evolution of dislocation density, size of subgrains and MX-type precipitates in a P91 steel during creep and during thermal ageing at 600^{o}C for more than 100,000 h, Mater. Sci Eng. A 527 (2010) 4062-4069.
[24] G. Dieter, Mechanical Metallurgy, 3rd Ed., McGraw Hill, Boston, p. 219.
[25] J. Hald, L. Karcokova, Precipitate stability in creep resistant ferritic steels - experimental investigations and modeling, ISIJ International 43 (2003) 420-427.
[26] R. L. Klueh, R. H. Donald, High-Chromium Ferritic and Martensitic Steels for Nuclear Applications, ASTM, Bridgeport, NJ, 2001, 28-39.
[27] Y. Tsuchida, K. Tokuno, K. Hashimoto, Nippon Steel Technical Report No. 58, July 1993.
[28] S. Spigarelli, E. Quadrini, Analysis of the creep behavior of modified P91 (9Cr-1Mo-NbV) welds, Materials and Design 23 (2002) 547-552.
[29] T. Sourmail, Precipitation in creep resistant austenitic stainless steels, Mat. Sci. Tech. 17 (2001) 1-14.
[30] J. B. Yang, T. Yamashita, N. Sano, M. Enomoto, Simulation of competitive Cu precipitation in steel during non-isothermal aging, Mat. Sci. Engr. A 487 (2008) 128-136.
[31] B. Riou, C. Escaravage, D. Hittner, D. Pierron, Issues in Reactor Pressure Vessel Materials, 2nd International Topical Meeting on High Temperature Technology, Beijing, China, September 22-24, 2004.
[32] J. R. Davis, ASM Specialty Handbook: Heat Resistant Materials, ASM International, 1997.

[33] P. J. Ennis, A. Zielinksa-Lipiec, O. Wachter, A. Czyrska-Filemonowicz, Microstructural stability and creep rupture strength of the martensitic steel P92 for advanced power plant, Acta Metall. 45 (1997) 4901-4907.
[34] L. Kloc, V. Sklenicka, A. Dlouhy and K. Kucharova, Microstructural Stability of Creep Resistant Alloys for High Temperature Plant Applications', Eds. A. Strang, J. Cawley and G. W. Greenwood), London Institute of Materials, London, 1998, p. 445.
[35] K. L. Murty, S. Gollapudi, I. Charit, Newtonian viscous creep in metals, Tans. Indian Inst. Met. 63 (2010) 85-91.
[36] M. E. Kassner, P. Kumar, W. Blum, Harper–Dorn creep, Int. J. Plast. 23 (2007) 980-1000.
[37] D. M. Owen, T. G. Langdon, Low stress creep behavior: an examination of Nabarro-Herring and Harper-Dorn creep, Mater. Sci. Eng. A 216 (1996) 20-29.
[38] F. R. N. Nabarro, H. L. deVilliers, The Physics of Creep: Creep and Creep-Resistant Alloys, Taylor & Francis Inc., Bristol, PA, 1995.
[39] S. Gollapudi, V. Bhosle, I. Charit, K. L. Murty, Newtonian viscous creep in Ti–3Al–2.5V, Philos. Mag. 88 (2008) 1357-1367.
[40] D. V. V. Satyanarayana, G. Malakondaiah, D.S. Sarma, Steady state creep behaviour of NiAl hardened austenitic steel, Mater. Sci. Eng. A 323 (2002) 119-128.
[41] S. C. Tjong, Z. Y. Ma, Creep behaviour of precipitation-hardened ferritic Fe–19Cr–4Ni–2Al alloy, Mater. Lett. 56 (2002) 59-64.
[42] I. Charit, K. L. Murty, Creep behavior of niobium-modified zirconium alloys, J. of Nucl. Mater. 374 (2008) 354-363.
[43] D. Srolovitz, R. Petkovic-Luton, M. J. Luton, Diffusional relaxation of the dislocation-inclusion repulsion, Philos. Mag. 48 (1983) 795-809.
[44] E. Artz, D. S. Wilkinson, Threshold stresses for dislocation climb over hard particles: the effect of an attractive interaction, Acta Metall. 34 (1986) 1893-1898.
[45] Y. Qin, G. Gotz, W. Blum, Subgrain structure during annealing and creep of the cast martensitic Cr-steel G-X12CrMoWVNbN 10-1-1, Mater. Sci. Engr. A 341 (2003) 211-215.
[46] P. J. Ennis, A. Zielinska-Lipiec, A. Czyrska-Filemonowicz, in: Microstructural stability of creep resistant alloys for high temperature plant applications. Strang A, Cawley J, Greenwood GW, (Eds.), London: Institute of Materials; 1998, p.135.
[47] S. L. Mannan and K. Laha, Creep behavior of Cr-Mo steel weldments, Trans. Ind. Inst. Met 49(4) (1996) 303-320.

2. Creep deformation mechanisms in modified 9Cr-1Mo steel

2.1. Introduction

Modified 9Cr-1Mo (Grade 91) steel is currently considered as a candidate material for reactor pressure vessels (RPVs) and reactor internals for the Very High Temperature Reactor (VHTR). The tensile creep behavior of modified 9Cr-1Mo steel (Grade 91) was studied in the temperature range of 873 K to 1023 K and stresses between 35 MPa and 350 MPa. Analysis of creep results yielded stress exponents of ~9-11 in the higher stress regime and ~1 in the lower stress regime. The high stress exponent in the power-law creep regime was rationalized by invoking the concept of threshold stress, which represents the lattice diffusion controlled dislocation climb process. Without threshold stress compensation, the activation energy was 510±51 kJ/mol, while after correcting for the threshold stress, the activation energy decreased to 225±24 kJ/mol. This value is close to the activation energy for lattice self-diffusion in α-Fe. Threshold stress calculations were performed for the high stress regime at all test temperatures. The calculated threshold stress showed a strong dependence on temperature. The creep behavior of Grade 91 steel was described by the modified Bird-Mukherjee-Dorn relation. The rate controlling creep deformation mechanism in the high stress regime was identified as the edge dislocation climb with a stress exponent of $n = 5$. On the other hand, the deformation mechanism in the Newtonian viscous creep regime (n = 1) was identified as the Nabarro-Herring creep.

The Next Generation Nuclear Plant (NGNP) is expected to address the growing energy demand by producing electricity and at the same time mitigate greenhouse gas emissions by co-producing hydrogen from the process heat. The Very High Temperature Reactor (VHTR) is a Gen-IV reactor system at the heart of the NGNP. VHTRs are designed to operate at temperatures much higher than those of currently operating reactors. Moreover, they are designed for longer service periods (60 years or more) compared to the current operating reactors [1]. Depending on the VHTR design, Prismatic Modular Reactor (PMR) or Pebble Bed Modular Reactor (PBMR), the operating temperature of the reactor pressure vessel (RPV) can vary between 573 K and 923 K. Furthermore, the RPV in the VHTR will be more than twice the size of a typical RPV in a Light Water Reactor (LWR) [2].

Since the introduction of Cr-Mo steels about a century ago, significant progress has been made in the alloy design, and they have been the material of choice for use in power generation plants. Low alloy ferritic steels (e.g. SA533) are generally used as the RPV material for the current LWRs [1]. However, because the RPV in the VHTR is expected to experience higher temperatures for a longer service time, the material must have superior creep properties. The current RPV steels cannot meet the creep strength required for the envisioned long term service conditions of VHTR pressure vessels. Ferritic-martensitic (F-M) steels with 9-12 wt.% Cr were previously developed for fossil-fuel-fired power plants [1] in the 1960s, and later used as boiler tube in the advanced gas-cooled reactors [3,4]. With the addition of Nb, V and other alloying elements, the creep rupture strength of F-M steels has gradually increased over the years [4]. F-M steels have better void swelling resistance than austenitic steels [1], excellent thermo-physical properties, and are resistant to stress corrosion cracking in aqueous and chloride environment [5].

A potential candidate material for the VHTR pressure vessel is the Grade 91 F-M steel. It contains alloying elements like Nb and V, forming fine and stable carbides and carbonitrides, which help improve its creep strength by disrupting the movement of dislocations, delaying the

plastic deformation by inhibiting grain boundary sliding, retaining finer grains during austenitization [6], and delaying the onset of tertiary creep stage [7]. Creep strength depends on various factors, such as temperature, applied stress, grain and subgrain sizes, precipitation at various creep stages, coarsening of precipitates and solute concentration. Presence of various precipitates with different characteristics and concomitant precipitation of particles during creep deformation make it challenging to explain the role of precipitates in creep deformation.

There are a number of studies on the creep properties of Grade 91 steel at various temperatures and stresses [8-12]. However, most of those studies are focused on the high stress regime. Understanding the creep mechanism at lower stress regimes is also important in determining the long term creep properties of Grade 91 steel since the real-world applications of these materials are mainly in the lower stress regimes. Hence, in this study creep tests were conducted in a wider stress regime (35-350 MPa) and in the temperature range of 873-1023 K. It is important to understand the creep mechanisms in order to better predict the creep behavior of this steel under different service conditions. Hence, creep deformation parameters (stress exponent and activation energy) were determined and detailed microstructural characterization was done in order to identify the operating creep mechanisms.

2.2. Experimental procedures

2.2.1. Material

The chemical composition of ASTM A387 Grade 91 CL2 steel (Grade 91) used in this study is shown in Table 2.1. The hot rolled Grade 91 plates were obtained from ArcelorMittal Plate LLC, in normalized and tempered condition (i.e., austenitized at 1311 K for 240 minutes followed by air cooling, and tempered at 1061 K for 43 minutes). The as-received plates had a dimension of 10.4 cm × 10.4 cm × 1.27 cm. Creep specimens with a gauge length of 2.54 cm and diameter of 0.635 cm were machined from the steel plates. At room temperature, the as-received Grade 91 steel exhibited yield strength of 533 MPa, ultimate tensile stress of 683 MPa and elongation to fracture of 26%.

2.2.2. Microstructural characterization

Optical microscopy was performed on both the as-received and creep tested specimens for easy characterization of the grain structure. Conventional metallographic procedures of cold mounting, grinding and polishing were followed to prepare the specimen surface to 0.5 μm finish before etching was carried out using Marble's reagent; a solution made of 50 ml distilled water, 50 ml hydrochloric acid and 10 g of copper sulfate. Subsequently, an Olympus light microscope was used to examine the metallographic specimens and an attached CCD camera was used to record the micrographs.

For a better detail on microstructure, some metallographic samples were examined using a Zeiss Supra 35 field emission gun scanning electron microscope (FEG-SEM) operated at an accelerating voltage of 10-20 kV under both secondary and backscattered electron imaging

modes. Energy dispersive spectroscopy (EDS) technique available in the SEM was used to estimate the relevant chemical compositions.

After the completion of the creep test, the furnace was removed from the load train and the specimen was immediately cooled under load by compressed air to preserve the final microstructural features. Samples were then sectioned from the gauge length of the specimen. For TEM study, the sectioned samples were mechanically polished down to ~120 μm thickness, and then 3 mm disks were punched out of the samples. Those disks were then jet polished in Fischione twin-jet polisher using a solution of 80 volume% methanol and 20 volume% nitric acid solution at a temperature of around 233 K. Dry ice bath was used to achieve low temperature. Philips CM200 and JEOL JEM-2010 TEM operated at an accelerating voltage of 200 kV were used to study in detail the grain and precipitate morphology of the material under both as-received and crept conditions. The EDS technique available in the same TEM was used to estimate the chemical composition of precipitates.

Table 2.1. Chemical composition (in wt.%) of Grade 91 steel

Element	Nominal	Measured
Cr	8.00 - 9.50	8.55
Mo	0.85 - 1.05	0.88
V	0.18 - 0.25	0.21
Nb	0.06 - 0.10	0.08
C	0.08 - 0.12	0.10
Mn	0.30 - 0.60	0.51
Cu	0.4 (max.)	0.18
Si	0.20 - 0.50	0.32
N	0.03 - 0.07	0.035
Ni	0.40 (max.)	0.15
P	0.02 (max.)	0.012
S	0.01 (max.)	0.005
Ti	0.01 (max.)	0.002
Al	0.02 (max.)	0.007
Zr	0.01 (max.)	0.001
Fe	Balance	Balance

2.2.3. Creep testing

Creep tests were performed at different temperatures between 873 and 1023 K and stresses between 35 and 350 MPa using an Applied Test Systems (ATS) lever arm (20:1) creep tester. The ATS creep tester is shown in Fig. 1.1 highlighting the location of the furnace, creep specimen and the linear variable displacement transformer (LVDT) used for displacement measurement.

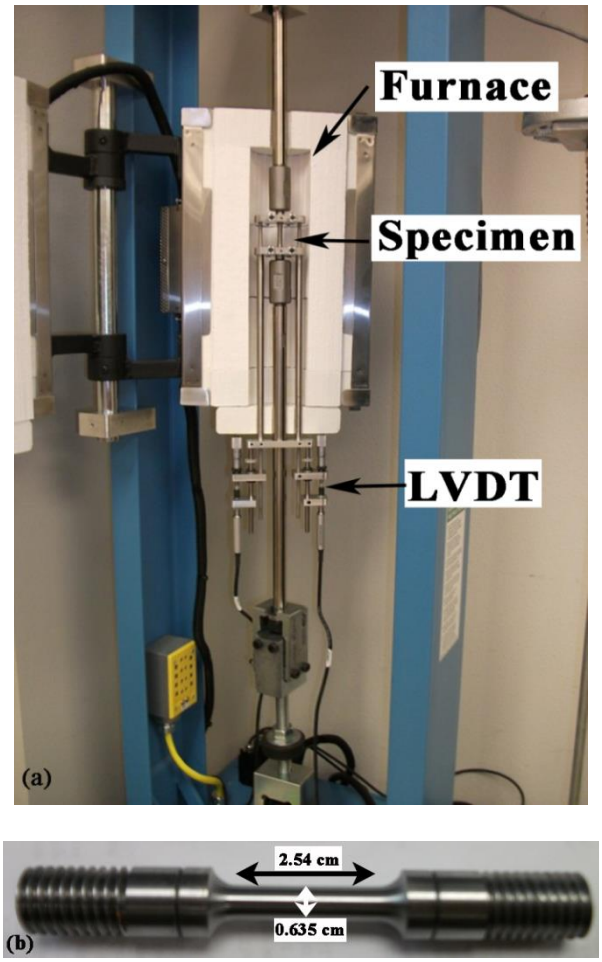

Fig. 2.1. (a) Uniaxial creep tester with LVDT axial extensometer, and (b) creep test specimen.

2.3. Results

2.3.1. Microstructural characteristics of the as-received material

The as-received Grade 91 steel had a tempered martensitic microstructure, as shown in Fig. 2.2a. Precipitation hardening is one of the main strengthening mechanisms in highly alloyed steels like Grade 91. Alloying elements, such as C, N, Nb, V, Cr and Mo, promote the formation of precipitates like Cr-rich $M_{23}C_6$, and Nb or V-rich MX particles, where M stands for metals, i.e. Cr, Mo, Nb or V. The Cr-rich $M_{23}C_6$ precipitates are elongated rod-like or block-like particles, while Nb-rich and V-rich MX precipitates have nearly spherical shapes. Cr-rich $M_{23}C_6$ type precipitates were mainly observed at the lath boundaries, prior austenite grain boundaries (PAGB), as shown in Fig. 2.2b. The dimensions of the elongated rod-like and block-like Cr-rich precipitates were measured, and found to have average length of 285±80 nm and width of 121±39 nm, which are similar to the ones reported by Shen et al. [6] in 11Cr F-M steel and Anderson et al. [13] in Grade 91 steel. The average diameter of near-spherical MX-type precipitates was 37±15 nm, similar to values reported by Shen et al. [6]. These types of precipitates were mainly located in the matrix and martensitic lath structure. These thermally

stable fine precipitates enhance the long term creep resistance. The TEM micrograph in Fig. 2.2c shows the morphology of the $M_{23}C_6$ and MX precipitates. Chemical composition of precipitates in the as-received condition was studied by EDS. The EDS spectra of these precipitates are shown in Fig. 2.2d, revealing that the main constituents of $M_{23}C_6$ precipitate were Cr and Mo, and those of MX type precipitates were V and Nb. The addition of V and Nb increases the precipitation of MX particles, while 0.1 wt.% C limits the precipitation of large Cr-rich $M_{23}C_6$ carbides. The smaller interparticle spacing and increased volume fraction of the fine MX carbides generally help in enhancing the creep strength.

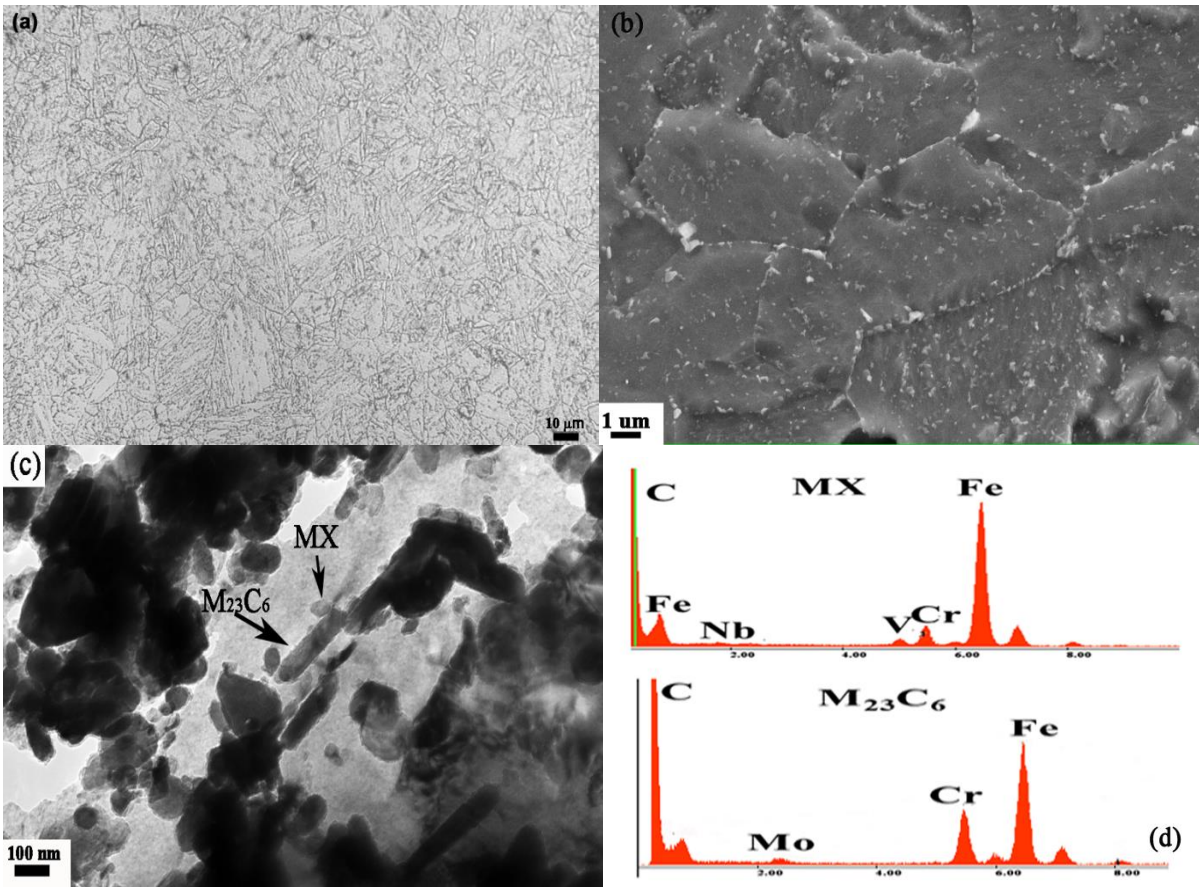

Fig. 2.2. (a) An optical micrograph showing the tempered microstructure, (b) an SEM image of the as-received material showing the presence of MX precipitates inside the grain and $M_{23}C_6$ carbides at the grain boundary, (c) a TEM micrograph of the $M_{23}C_6$ and MX particle, and (d) the EDS spectra of an MX particle revealed that its main constituents were V and Nb, while those of $M_{23}C_6$ were Cr and Mo.

2.3.2. Creep properties

Creep is time dependent plastic deformation in materials under constant load or stress, specifically observed at higher homologous temperatures. In the VHTRs, Grade 91 steels are likely to reach creep regime temperatures even under normal operating conditions. A typical example of a creep curve for a Grade 91 steel specimen tested at 923 K and 150 MPa is shown in Fig. 2.3a, and the corresponding variation of creep rate versus time is shown in Fig. 2.3b. All the

creep curves obtained in this study consisted of three distinct regimes: primary, secondary (steady state) and tertiary, as generally obtained in typical creep tests. Fig. 2.4 shows the steady state creep rates as a function of applied stress in a double logarithmic plot. There are two distinct creep deformation regimes: stage I – observed at lower stresses having a stress exponent (n) of ~1, and stage II – observed at higher stresses with high stress exponents ranging between of ~9-11, as shown in Fig. 2.4. Here it is relevant to note that no creep mechanism shown in Table 2.2 [14], which lists different creep mechanisms with corresponding parametric dependencies, has stress exponents as high as those obtained in Grade 91 steel. Fig. 2.5 shows the modulus compensated creep rate as a function of inverse temperature at a stress of 200 MPa. This analysis gives a creep activation energy of 510±51 kJ/mol in the higher stress regime. In the following section we will explain the discrepancy of higher stress exponents and activation energies than physically possible.

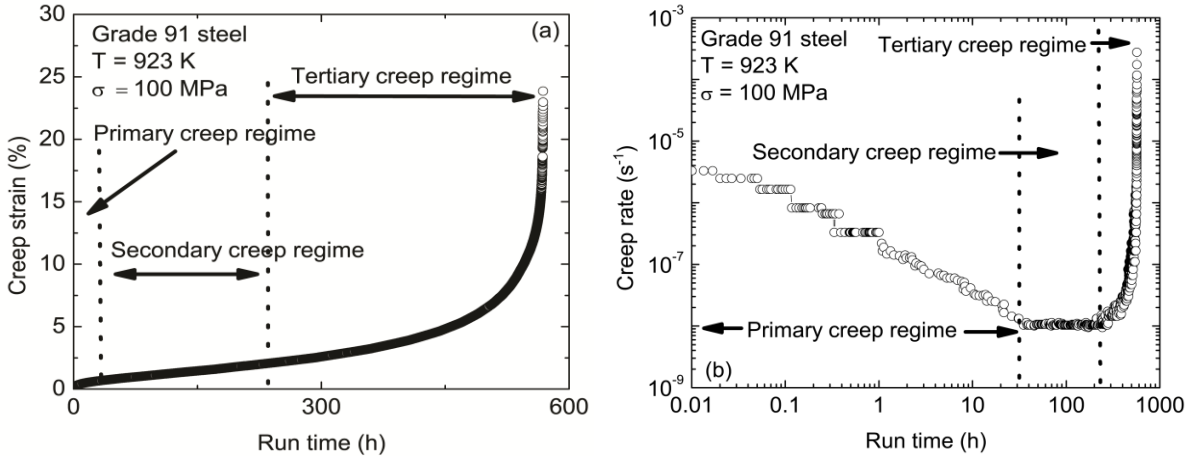

Fig. 2.3. (a) A creep curve and (b) the corresponding creep rate versus time plot at 923 K and 100 MPa for the as-received Grade 91 steel.

2.4. Discussion

2.4.1. Bird-Mukherjee-Dorn equation and its modified form

Creep, as a thermally activated diffusion-assisted deformation process, can be described by the Bird-Mukherjee-Dorn (BMD) equation [15]:

$$\frac{\dot{\varepsilon}_{ss} kT}{DEb} = A\left(\frac{\sigma}{E}\right)^{n}\left(\frac{b}{d}\right)^{p} \tag{1}$$

where A is a constant, $\dot{\varepsilon}_{ss}$ the steady state creep rate, E the elastic modulus, b the Burgers vector, k the Boltzmann constant, T the absolute temperature, σ the applied stress, d the grain diameter, p the inverse grain size exponent, and D the diffusivity which is described by the following relation:

$$D = D_o exp\left(\frac{-Q}{RT}\right) \tag{2}$$

where D_o is the frequency factor, Q the appropriate activation energy, and R the universal gas constant. The BMD equation is essentially an expanded form of the basic Norton equation. The creep parameters n, p and Q are often used to determine the operating creep mechanism. Different creep mechanisms with their representative diffusivity, stress exponent and inverse grain size exponent are listed in Table 2.2 [14].

For high stress and low temperature regime, creep behavior is explained by the simple BMD equation (Eq.2.1). However, for particle hardened alloys, the BMD equation tends to result in high activation energy and stress exponent. The deformation creep mechanism in a P92 steel (9.1Cr-0.5Mo-1.8W-0.2V-0.06Nb-0.04 N, wt.%) was found to be power law creep with high stress exponents in the high stress, low temperature regime [15]. Ennis et al. [9] attributed the high stress exponents to precipitates that act as dislocation barriers. The high apparent stress exponents obtained in Fig. 2.4 necessitate the threshold stress to be considered in order to fully elucidate the true creep mechanisms in Grade 91 steel. The high stress exponent and activation energy make it difficult to elucidate the true deformation mechanism. Hence, the BMD equation has to be modified for a particle hardened alloy by incorporating the stress imparted on the dislocations by the precipitates. The modified BMD equation incorporating threshold stress is described by the following equation:

$$\frac{\dot{\varepsilon}_{ss} kT}{DEb} = A\left(\frac{\sigma-\sigma_{th}}{E}\right)^{n}\left(\frac{b}{d}\right)^{p} \quad (3)$$

where σ_{th} is the threshold stress and all other terms have been defined before. Threshold stress is generally defined as the stress below which no creep deformation occurs due to a specific creep mechanism. Thus, the effective stress, (σ - σ_{th}), is actually responsible for the creep deformation instead of the applied stress [16]. The true activation energy and stress exponent obtained from the modified BMD equation will be able to explain the creep deformation in the higher tress regime of Grade 91 steel. This type of behavior has been found to be prevalent in many particle-containing alloys. One of the theories of threshold stress is based on the local climb of particles by dislocations, while restricting the movement of dislocations via attractive interaction between the dislocations and incoherent particles resulting in departure side pinning [17].

2.4.2. Threshold stress analysis

The stress exponent and activation energy vary for different creep deformation mechanisms as shown in Table 2.2. According to Ennis et al. [9], for creep tests performed on P92 steel at 873 K and above 150 MPa, and at 923 K and above 110 MPa, the stress exponent was 16; however, for tests performed below the mentioned stresses the stress exponent was 6. Further, Ennis et al. [9] attributed the high stress exponent in the high stress regime to the disruption of dislocation motion by carbides/nitrides, but did not provide any insight into the lower stress regime. Fig. 2.4 shows that for creep tests performed at various stresses and temperatures of 873 K, 923 K and 973 K, the apparent stress exponent ranged from n = 9 to 11. The apparent activation energy calculated from creep tests in the higher stress regime was found to be 510±51 kJ/mol as shown in Fig. 2.5. This value of the activation energy is much higher than that of the lattice self-diffusion, (Q_L = 250 kJ/mol) for α-iron [18], which is physically not possible. Solute diffusion of the major alloying elements, such as Cr, Mo etc. in Grade 91 steel)

etc. in α-Fe does not have such high activation energy either. Notably, higher creep activation energies for different high strength Cr-Mo steels have also been reported by different studies, and are compiled in Table 2.3 [8, 10-13, 17-21].

Higher than normal stress exponent and activation energy in the higher stress regime require incorporation of threshold stress in the creep data analysis of Grade 91 steel. The first step in that direction is to estimate threshold stresses. A standard method involving linear extrapolation as illustrated in the work by Mishra et al. [22] and Huang et al. [23] is used to determine threshold stresses. Possible true stress exponent values are chosen, and the creep rates raised to the power of the inverse stress exponent are plotted against the modulus compensated applied stresses on a linear scale. Only data from the same creep regime can be used for the calculation of threshold stress. The value of stress exponent was varied from 3 - 7 to achieve the best fit such that a correlation coefficient ≥ 0.98 was obtained for all temperatures. Though the data are best fitted with a correlation coefficient ≥ 0.98, the creep activation energy needs to be calculated, and finally all the normalized creep data, when plotted, should fall close to one another fulfilling the modified BMD equation.

To identify whether rate-controlling creep mechanism is viscous glide (n = 3) or dislocation climb (n = 4-7), the stress exponent was varied from 3 to 7, and a stress exponent of 5 gave the best fit. Fig. 2.6a shows the best fits for n = 3, in which the correlation coefficients for 973 K, 923 K and 873 K were 0.95, 0.96, and 0.94, respectively. Fig. 2.6b shows the best fit for n = 5, in which the correlation coefficients for 973 K, 923 K and 873 K were 0.99, 0.99, and 0.98, respectively. Threshold stress was calculated from the data that gave the best fit by extrapolating it to zero creep rate. The intersection of the extrapolated line with the X-axis gave the threshold stress at that particular temperature. Thus, threshold stresses were determined to be 136±13, 75±10, and 56±8 MPa at 873, 923, and 973 K, respectively. The calculated threshold stress decreased with increasing temperature. The high temperature climb of edge dislocations is the creep mechanism when n = 5 and the creep activation energy (225±24 kJ/mol) is consistent with that of lattice self-diffusion in α-Fe [24], as shown in Table 2.2. For n = 6, the correlation coefficient was the same as that of n = 5, but subsequent calculation of creep activation energy resulted in a much higher value (406±79 kJ/mol). Furthermore, using the data with n = 6 did not give a collinear fit when the $\left(\frac{\dot{\varepsilon}_{ss}kT}{DEb}\right)$ data were plotted against the normalized effective stresses, $\left(\frac{\sigma-\sigma_{th}}{E}\right)$.

In order to verify the correlation between the calculated threshold stress and the assumed stress exponent, creep rates are plotted against the corresponding effective stresses (σ- σ_{th}) on a double logarithmic plot as depicted in Fig. 2.7a. Thus, the plotted data reduce the stress exponents from the range of 9-11 to ~5. In order to calculate the true activation energy, steady state creep rates ($\dot{\varepsilon}_{ss}$) were plotted against the modulus compensated effective stress $\left(\frac{\sigma-\sigma_{th}}{E}\right)$, and the corresponding creep rate is obtained for each temperature at a constant modulus compensated effective stress of 7.9×10^{-4}. The slope obtained from the plot of $\dot{\varepsilon}_{ss}TE^{-1}$ against $10^3\mathrm{T}^{-1}$, shown in Fig. 2.7b, was multiplied by the gas constant R and 2.3, to obtain the true activation energy (Q_t = 225±24 kJ/mol). Thus, calculated activation energy is found to be close to the activation energy of lattice self-diffusion in α-iron (Q_L = 250 kJ/mol).

The validity of the obtained values of the threshold stress can be verified by calculating the creep activation energy and incorporating this value into the modified BMD equation. Using the modified BMD relation, $\left(\frac{\dot{\varepsilon}_{ss}kT}{DEb}\right)$ data were plotted against modulus-compensated effective

stress$\left(\frac{\sigma-\sigma_{th}}{E}\right)$, as shown in Fig. 2.8. The data points for different temperatures fall reasonably in a close proximity with a single stress exponent of ~5. The data merge well together with the correlation coefficient of 0.99. Hence, the rate-controlling mechanism in the high stress creep regime is unambiguously determined to be the high temperature climb of edge dislocations, which is the slowest process.

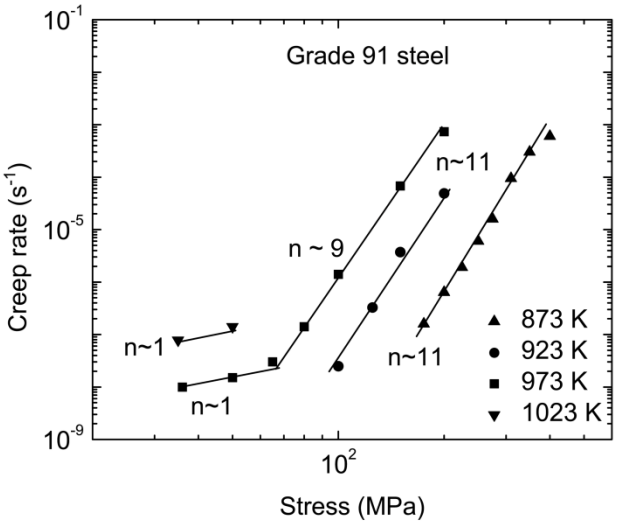

Fig. 2.4. Creep rate versus applied stress for Grade 91 steel at 873 K, 923 K and 973 K.

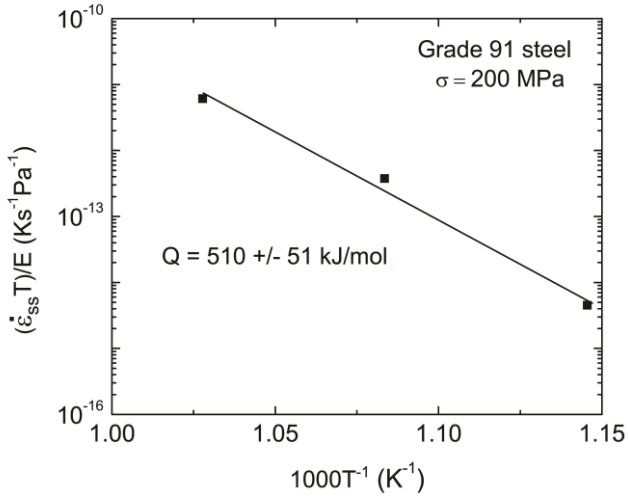

Fig. 2.5. Modulus compensated steady state creep rate versus inverse temperature plot. Apparent activation energy calculated for tests performed at 873 K, 923 K and 973 K, and 200 MPa.

Table 2.2. Parametric dependencies of different creep mechanisms [14]

Mechanism	Q	n	p
Climb of Edge Dislocations	Q_L	5	0
Viscous Glide	Q_S	3	0
Grain Boundary Sliding(Superplasticity)	Q_B	2	2
Low Temperature Climb	Q_C	7	0
Harper-Dorn	Q_L	1	0
Nabarro-Herring	Q_L	1	2
Coble	Q_B	1	3

Activation Energies: Lattice Diffusion (Q_L), Solute Diffusion (Q_S), Dislocation Core Diffusion (Q_c), Grain Boundary Diffusion (Q_B)

Table 2.3. Activation energy calculated in various Cr-Mo steels

Type of steel	Stress (MPa)	Activation energy (kJ/mol)	Stress exponent (n)	Reference
P91	50	600	-	[8]
P91	200	480	-	[8]
Grade 91	200	621	-	[10]
T91	200	680	-	[11]
T91	160	815	-	[11]
P91	125	545	-	[12]
P91	250	510	-	[12]
Grade 91	-	112	2	[13]
Grade 91	-	216	3.9	[13]
2.25Cr-1Mo	150	369	-	[17]
9Cr-1Mo	-	405 - 478	-	[18]
2.25Cr-Mo	+	420*	-	[19]
2.25Cr-Mo	+	370*	-	[19]
Grade 91	-	807	-	[20]
Grade 91	-	792	10-17	[21]
Grade 91	200	510±51	9-11	Present study

'*' Difference in heat treatment, '+' modulus compensated stress was used.

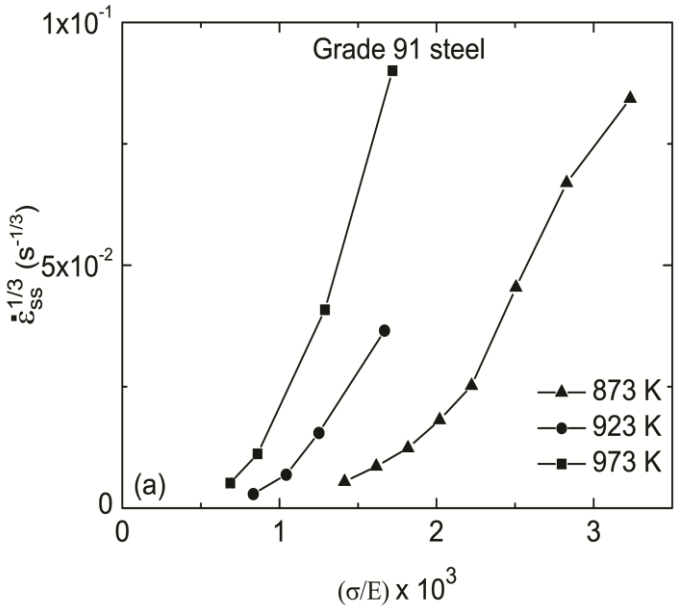

Fig. 2.6. Threshold stress calculation: (a) linear extrapolation for the viscous glide mechanism (n = 3), and (b) linear extrapolation for the dislocation climb controlled mechanism (n = 5).

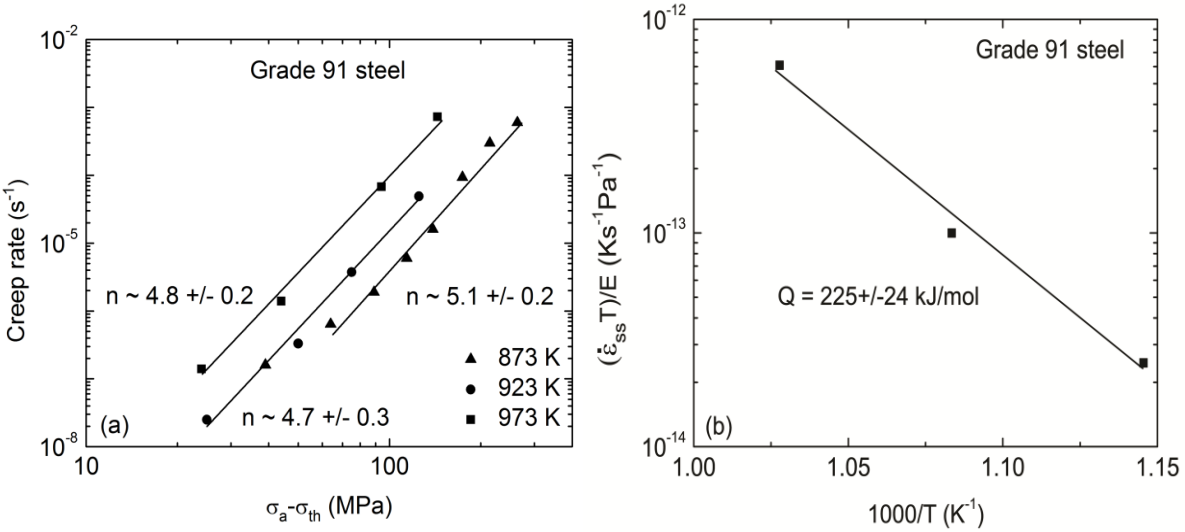

Fig. 2.7. Calculation of (a) true stress exponent, and (b) true activation energy. Note that the stress exponents have reduced to n ~ 5 and the activation energy has reduced from 510 kJ/mol to 225 kJ/mol.

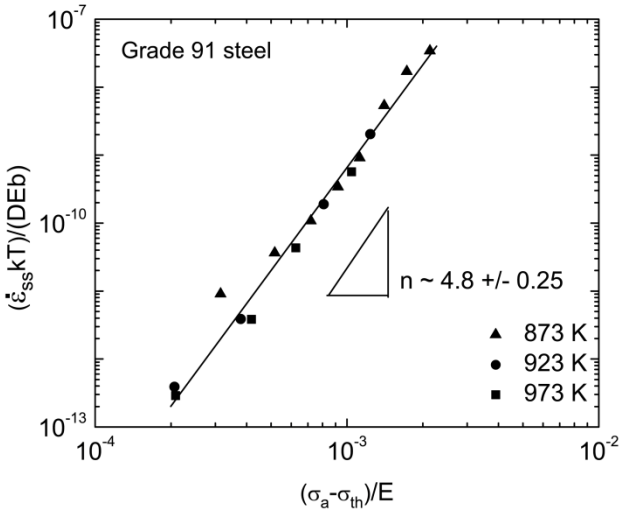

Fig. 2.8. A log-log plot of diffusion compensated creep rate versus modulus compensated effective stress. The data for 873 K, 923 K and 973 K are represented by a straight line with a slope of n ~5.

2.4.3. Theoretical prediction of threshold stress

Creep mechanisms depend on the threshold stress due to the dislocation-particle interactions. Particles that are responsible for the origin of threshold stress in this steel are MX type precipitates as they are finely dispersed inside the grains. However, $M_{23}C_6$ particles which are predominantly present on the boundaries may not contribute to the origin of threshold stress. Note that MX precipitates are incoherent particles. There are several models explaining the origin of threshold stress based on the attractive or repulsive dislocation-particle interaction [25-28]. These models are used to predict threshold stress in particle strengthened alloys. Threshold stress values predicted from the models are listed in Table 2.4 [25-28], and will be compared with the experimentally determined threshold stresses (i.e., 136±13, 75±10, and 56±8 MPa at 873, 923, and 973 K, respectively). All the parameters used in the calculation are listed below the table, where b is the Burgers vector, v the Poisson's ratio, G the shear modulus, r_o the dislocation core radius, r the average radius of the MX type precipitates, and λ is the interparticle spacing; k_A, B, and C are constants of their respective models. The interparticle spacing of the MX type particles was calculated using the following equation [29]:

$$\lambda = \left(\frac{0.5}{\sqrt{\left(\frac{6f}{\pi}\right)}} - \sqrt{\frac{2}{3}} \right) r \qquad (4)$$

where f is the volume fraction of particles. Considering the repulsive dislocation-particle interaction (Ashby's model based on Orowan model) [25], the threshold stresses were predicted to be 187, 181 and 176 MPa for 873, 923 and 973 K, respectively. In repulsive interaction, a dislocation by-pass particle by forming a dislocation loop around the particle. On the other hand, in Srolovitz's model [26] involving attractive interaction, when a dislocation enters the matrix-particle interface, there is relaxation of the dislocation core leading to the pinning of dislocation. Because of the reduced elastic energy of dislocation in the matrix-particle interface, the local

climb of dislocation over a precipitate is dominant over the general climb. However, the stress required to unpin the dislocation is close to Ashby-Orowan stress, as noted in Table 2.4.

Artz et al. [27] proposed a model based on the attractive dislocation-particle interaction, in terms of the particle detachment stress as a description of threshold stress. The detachment threshold stress is independent of the mode of dislocation climb over particle. Hence, it is applicable for both local and general climb of dislocation over particle. Based on Artz's detachment stress model, threshold stresses were calculated to be 130, 126 and 122 MPa for 873, 923 and 973 K, respectively, with the proper choice of the constant k_A (in this case, taken as 0.3). Thus, the threshold stress calculated for 873 K matches well with the experimentally determined threshold stress (136±13 MPa) for that temperature but not at other two temperatures.

According to Mishra's lattice dislocation dissociation model [28,30], the local climb process involves increase in the dislocation line length and reduced atomic diffusion during dislocation climb as a result of attractive dislocation-particle interaction. As shown in Table 2.4, the lattice dislocation dissociation model proposed underestimates the threshold stress since the threshold stresses at all three temperatures are found to be quite low (~5 MPa) at all three temperatures.

Threshold stresses predicted from the aforementioned models are not fully consistent with the threshold stresses determined experimentally. Artz's detachment model gives the best comparable results. Moreover, the threshold stresses predicted by the models do not show a strong temperature-dependence as observed experimentally. Certain microstructural processes like the role of boundary particles (like $M_{23}C_6$), subgrain coarsening, particle coarsening etc. which have not been taken into account in the mechanistic framework of the present study might have contributed to the deviation of the predicted threshold stresses from the experimental ones.

Table 2.4. Threshold stress values predicted from various models for 873 K, 923 K and 973 K

Model	Threshold stress (MPa)			Reference
	873 K	923 K	973 K	
$\sigma_{th} = \frac{2.73Gb}{2\pi(1-\nu)\lambda}\left(\ln(2) + \ln\left(\frac{r}{r_o}\right)\right)$	187	181	176	Ashby [25]
$\sigma_{th} = \frac{2.73Gb}{2\pi(1-\nu)\lambda}\left(\frac{\pi^2}{12} + ln\left(\frac{r}{r_o}\right)\right)$	191	185	180	Srolovitz et al. [26]
$\sigma_{th} = 2.73G\frac{b}{\lambda}\sqrt{1-k_A^2}$	130	126	122	Artz et al. [27]
$\sigma_{th} = 2.73GC\frac{b}{\lambda}exp\left(B\frac{r}{\lambda}\right)$	~5	~5	~5	Mishra et al. [28]
σ_{th}(Experimental)	136±13	75±10	56±8	Present study

Material constants: b = 0.248 nm; ν = 0.35; Microstructural parameters: $r_o = b$; r = 37 nm, λ = 237 nm; Model constants: (Artz) k_A = 0.3; (Mishra) C = 0.002, B = 20; Taylor factor was taken as 2.73.

2.4.4. Newtonian viscous creep regime

In the preceding sections, the rate-controlling creep mechanism in the high stress regime was identified. However, in the low stress regime as observed in Fig. 2.4, the stress exponent was found to be 1 which represents the Newtonian viscous creep regime. However, there are three distinct creep mechanisms that exhibit the stress exponent of 1 (i.e., n = 1): Harper-Dorn (H-D), Nabarro-Herring (N-H) and Coble creep as noted in Table 2.2. Creep tests performed at

973 K and 1023 K were only considered in this analysis, but the 873 K and 923 K tests were not performed because of time constraints as lower temperature tests take a longer period of time to reach the steady state. In the next section, the rate-controlling creep mechanism in the lower stress regime will be identified.

2.4.4.1. Harper-Dorn creep

The H-D creep was first observed in pure aluminum with large grain size at high homologous temperature (~ $0.99T_m$), with creep activation energy close to that of the lattice self-diffusivity [31]. This creep mechanism is independent of grain size. Further, it involves subgrain formation, stress independent dislocation density, and distinctive primary creep stage [24], and significantly higher creep rates than those predicted by N-H, and may be for Coble if test temperature is very low [32]. Fiala et al. [33] reported observing H-D creep in α-Fe in the temperature range of 0.4-0.54T_m. The constitutive equation for H-D creep is given by the following expression:

$$\dot{\varepsilon}_{HD} = A_{HD}\left(\frac{D_l E b}{kT}\right)\left(\frac{\sigma}{E}\right)^1 \tag{5}$$

where A_{HD} ~3×10^{-10} [31], D_l is the lattice diffusivity, and $\dot{\varepsilon}_{HD}$ the steady state H-D creep rate. Normalized experimental creep rates in the lower stress regime are compared with the normalized creep rates predicted by the H-D model in Fig. 2.9. It was found that the creep rates obtained from the H-D creep model were one order of magnitude lower than the experimental creep rates.

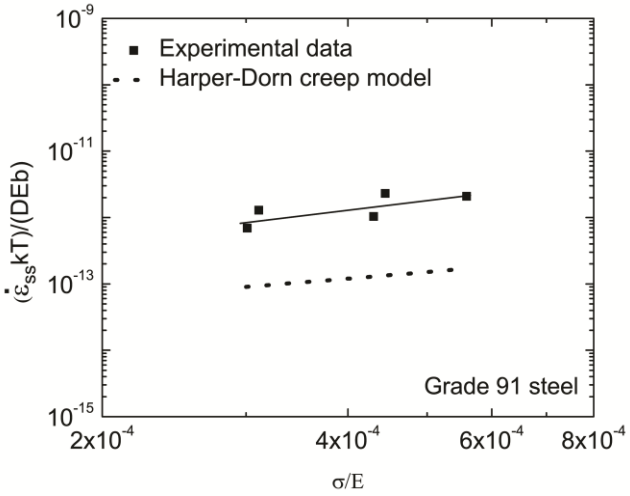

Fig. 2.9. Correlation of Newtonian viscous creep regime with the Harper-Dorn creep model.

2.4.4.2. Diffusion creep

In N-H and Coble creep mechanisms, vacancies migrate through the lattice and grain boundary, respectively. In diffusion creep, excess vacancies are created at the grain boundaries experiencing tensile stress, and these vacancies migrate to the boundaries in compression. So in essence, atoms move from the compressed grain boundaries to grain boundaries in tension. In dispersion-hardened alloys, matrix material free of dispersed precipitates is deposited at the

transverse boundaries, while a high concentration of particles accumulates at the longitudinal boundaries [34].

In N-H creep, diffusion of vacancies occur through the lattice and the corresponding constitutive model is described by the equation

$$\dot{\varepsilon}_{NH} = A'_{NH}\left(\frac{D_l E b}{kT}\right)\left(\frac{b}{d}\right)^2\left(\frac{\sigma}{E}\right)^1 \tag{6}$$

where $A'_{NH} = 28$ [32], and $\dot{\varepsilon}_{NH}$ is the N-H creep rate. Fig. 2.10 shows that the normalized creep rates are within one order of magnitude of those predicted by the N-H creep model. Both N-H and H-D creep models have activation energies consistent with lattice self-diffusivity. Hence for this calculation, the activation energy for lattice self-diffusion was taken as 250 kJ/mol [18]. H-D creep is a grain size independent process, while N-H creep model has an inverse grain size exponent of 2. For a test performed at 923 K and 59 MPa in T122 steel (12Cr-0.38Mo-1.85W-0.21V-0.06Nb-0.1C-0.3Si-0.5Mn-0.84Cu-0.06N, wt.%) [35], a dual phase material with coarse prior austenite grain size (55 μm) exhibited a better creep strength than that of a material with a fine prior austenite grain size (15 μm).

Coble creep model is described by the equation

$$\dot{\varepsilon}_C = A_C\left(\frac{D_b E b}{kT}\right)\left(\frac{b}{d}\right)^3\left(\frac{\sigma}{E}\right)^1 \tag{7}$$

where A_C = 150 [36], D_b is the grain boundary diffusivity, and $\dot{\varepsilon}_C$ the Coble creep rate. The creep rate predicted by the Coble creep model was about two orders of magnitude higher than the experimental creep rate, which is shown in Fig. 2.11. The higher predicted creep rate is due to the strong dependence of Coble creep model on the grain size. Kloc et al. [37] studied the creep behavior of P91 steel with a grain size of 55 μm, but could not ascertain whether Coble or H-D creep was the predominant creep mechanism in the lower stress regime. However, they did not investigate the possibility of N-H creep. But in this study, we find that the relative positions of normalized creep rates (experimental and predicted) as shown in Fig. 2.11 makes it highly unlikely that the Coble creep is a plausible creep mechanism for the Newtonian viscous creep regime.

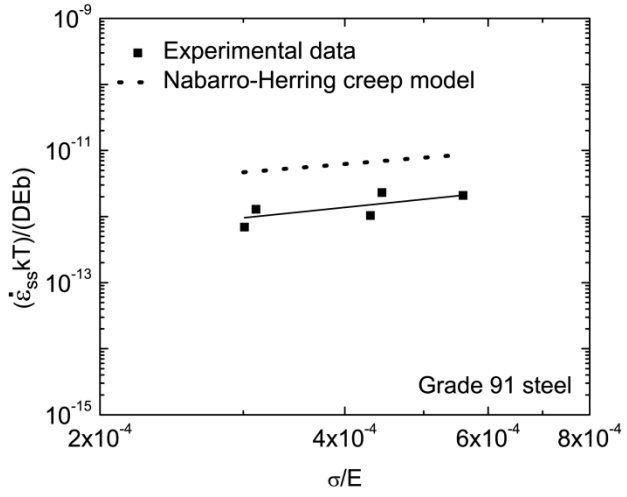

Fig. 2.10. Correlation of Newtonian viscous creep regime with Nabarro-Herring creep model.

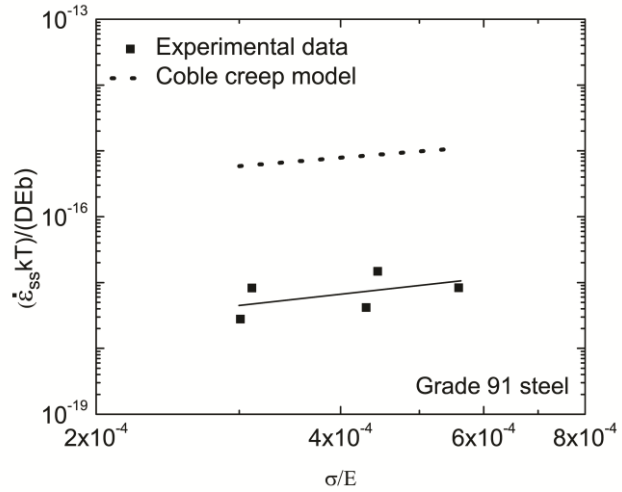

Fig. 2.11. Correlation of Newtonian viscous creep regime with Coble creep model.

2.4.5. Microstructural examination of the crept samples via TEM

2.4.5.1. Microstructural observation in the dislocation climb controlled creep regime

For the high stress regime with a stress exponent of 5 and activation energy of 225 kJ/mol, the creep deformation mechanism was predicted to be dislocation climb controlled. Presence of precipitates increases the strength of a material by disrupting the movement of dislocation. Fig. 2.12a shows the dislocation-particle interaction in a specimen crept at 873 K and 200 MPa. Previously, it was considered that the dislocation-particle interaction was repulsive in nature, and general climb of particle by dislocation was preferred over local climb because the sharp bend in local climb was unstable due to limited diffusion. Srolovitz et al. [26] suggested that the instability associated with local climb is relaxed by interfacial diffusion, while Mishra et al. [28] proposed the dissociation of lattice dislocations in the matrix-particle interface and their transformation to interfacial dislocation, thus lowering the matrix-particle interface energy. The departure side dislocation pinning is due to the attractive interaction between the dislocation and incoherent particle [38,39]. Departure side dislocation pinning was reported in a dispersion strengthened nickel based alloy [40]. The dislocation line cannot pass the precipitate unless it overcomes the departure side pinning by the particle. Fig. 2.12b shows an example of attractive interaction between a dislocation and MX type particle in a Grade 91 steel specimen crept at 973 K and 150 MPa. The climb of dislocation over the MX type precipitate was observed in a specimen crept at 973 K and 200 MPa as seen in Fig. 2.12c. Fig. 2.12d shows the presence of subgrain boundary formation in a specimen crept at 923 K and 200 MPa. This kind of microstructural evidence has, at times, been related to the dislocation climb controlled creep [41,42].

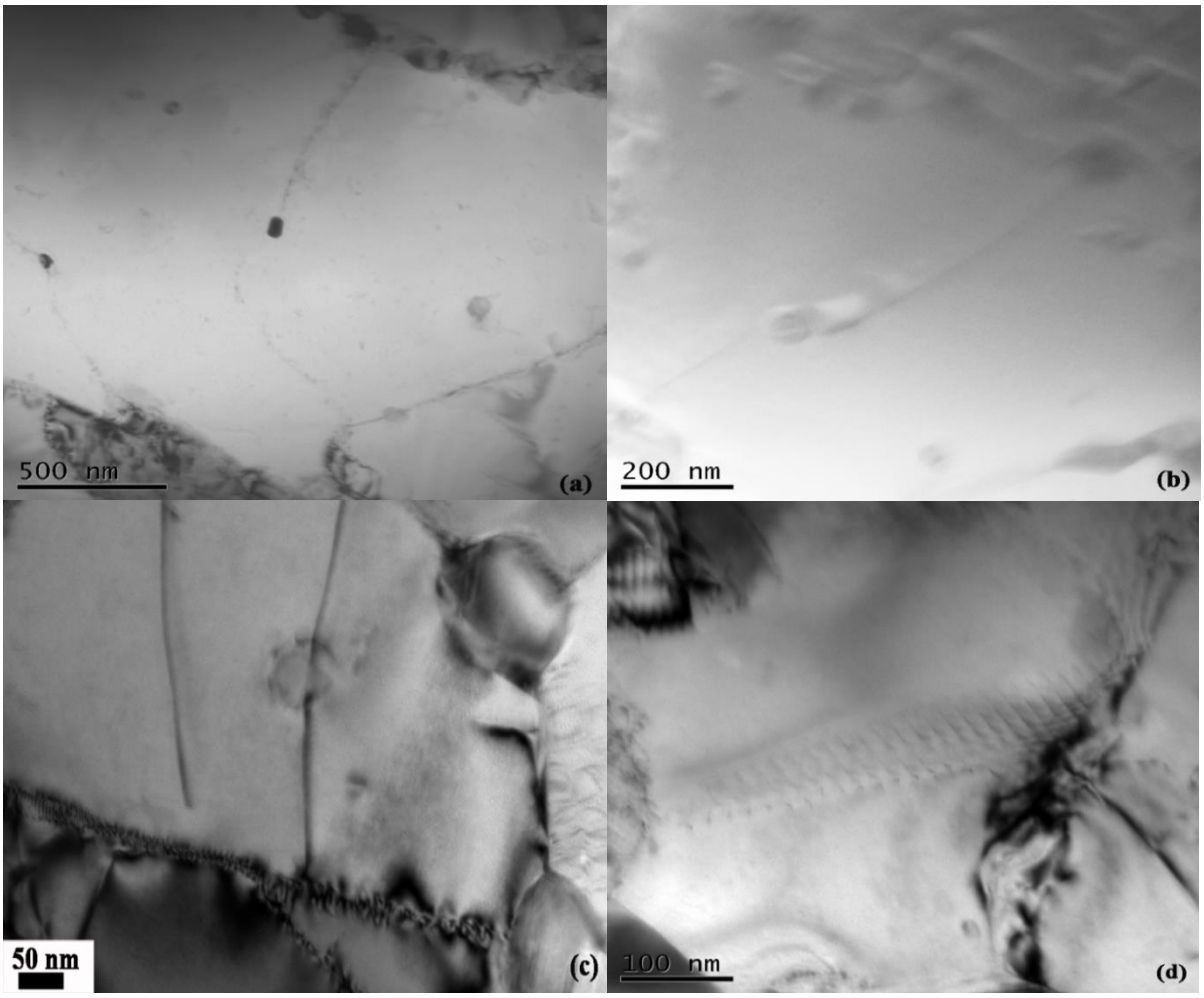

Fig. 2.12. (a) Pinning of dislocation by MX type carbide, (b) dislocation pinning on the departure side of the precipitate, (c) dislocation climbing the precipitate, and (d) subgrain boundary formation.

2.4.5.2. Microstructural observation in Newtonian viscous creep regime

Denuded zones, elongated grains and grain boundary grooves are some of the features that are representative of diffusion creep [31]. Denuded zones were first observed in hydrated magnesium - 0.55 at. % zirconium alloy tested at 673 K and 2.1 MPa [34]. Fig. 2.13a and b show the elongated grains and a denuded zone, respectively, in a Grade 91 steel specimen crept in the low stress regime. The specimen with elongated grains was crept at 973 K and 50 MPa, and the specimen with denuded zone was crept at 973 K and 35 MPa. Although the grain boundary grooves were not observed in the Grade 91 steel, the presence of denuded zone and elongated grain is likely the indication of diffusion creep. Under the applied stress, the iron atoms diffuse from the grain boundaries parallel to the applied stress to transverse grain boundaries. But since the precipitates do not diffuse like atoms, they form a zone devoid of precipitates along the transverse grain boundary. In Grade 91 steel which has the initial dislocation density in the range of 10^{13} –10^{14} /m^2, H-D creep is not expected as the material should have a low initial dislocation density in the order of 10^{6} –10^{8}/m^2 for H-D creep to be the rate-controlling mechanism [31]. Moreover, H-D creep has only been observed in high purity materials with large grain sizes. Thus, with the microstructural evidence and the predicted creep rates in strong favor of the N-H creep, the rate-controlling deformation mechanism in Grade 91 steel was identified as the N-H

creep. Because of the lack of Grade 91 steel with different grain sizes, the grain size dependency of the N-H creep regime could not be ascertained.

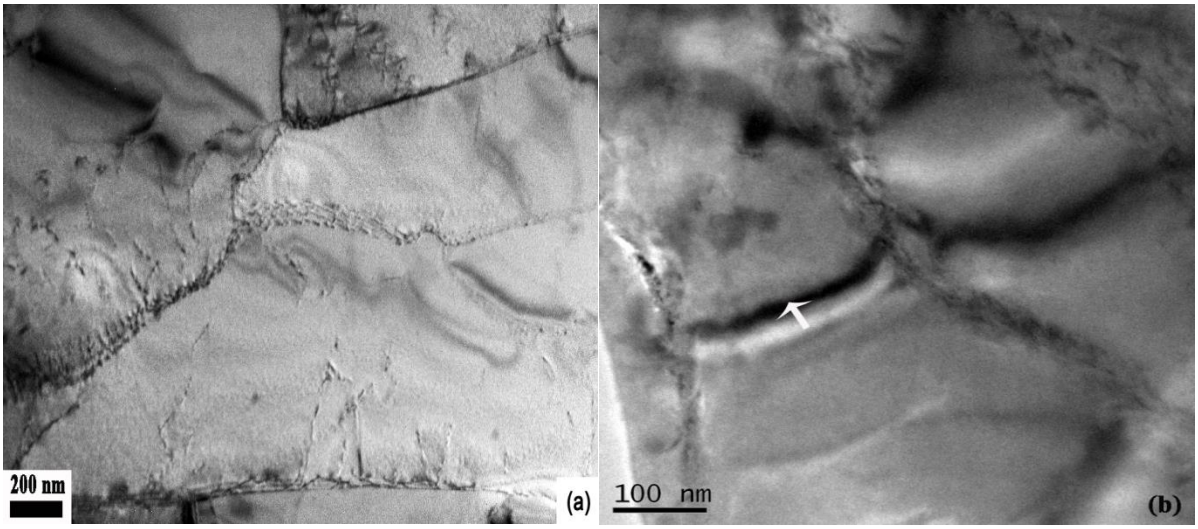

Fig. 2.13. (a) A TEM micrograph of a crept sample showing elongated grain structure, and (b) a TEM micrograph of denuded zones in a creep test performed at 700°C and 36 MPa.

2.5. Conclusions

Creep studies carried out in Grade 91 steel at the temperature range of 873 K–1023 K and under uniaxial tensile stress of 35–350 MPa yielded two distinct creep deformation mechanisms. Newtonian viscous creep was observed in the low stress regime with stress exponent of n ~1. The experimental creep rates were correlated with standard Newtonian viscous creep models: Harper-Dorn, Coble and Nabarro-Herring. Microstructural features and a comparison between the experimental and predicted creep rates indicated that the rate controlling creep mechanism was N-H creep in the low stress regime. The creep mechanism transitioned from the Newtonian viscous creep (n ~1) to a power-law creep with high stress exponent (n ~9–11) in the high stress regime. The high stress exponent was rationalized by incorporating threshold stress approach in the Bird-Mukherjee-Dorn equation resulting in the reduction of the stress exponent to ~5. The estimated threshold stress decreased with an increase in temperature. The rate-controlling creep mechanism in the high stress regime was identified as the dislocation climb (n ~5) involving attractive dislocation-particle interaction and departure side pinning, supported by relevant microstructural evidence.

References

[1] I. Charit, K. L. Murty, Structural materials issues for the next generation fission reactors, JOM 62 (9) (2010) 67-74.
[2] K. L. Murty, I. Charit, Structural materials for Gen-IV reactors: challenges and opportunities, J. Nucl. Mater. 383 (2008) 189-195.
[3] E. Barker, Creep fracture of a 9Cr-1Mo steel, Mater. Sci. Eng. 84 (1986) 49-64.

[4] R. L. Klueh, Elevated temperature ferritic and martensitic steels and their application to future nuclear reactors, Int. Mater. Rev. 50 (2005) 287-310.
[5] K. Laha, K. S. Chandravathi, P. Parameswaran, K. Bhanu Sankara Rao, S. L. Mannan, Characterization of microstructures across the heat-affected zone of the modified 9Cr-1Mo weld joint to understand its role in promoting type IV cracking, Metall. Mater. Trans. A 38 (2007) 58-68.
[6] Y. Z. Shen, S. H. Kim, H. D. Cho, C. H. Han, W. S. Ryu, Identification of precipitate phases in a 11Cr ferritic/martensitic steel using electron micro-diffraction, J. Nucl. Mater. 400 (2010) 64-68.
[7] M. Tanelke, F. Abe, K. Sawada, Creep-strengthening of steel at high temperatures using nano-sized carbonitride dispersions, Nature 424 (2003) 294-296.
[8] L. Kloc, V. Sklenicka, Transition from power-law to viscous creep behavior of P-91 type heat-resistant steel, Mater. Sci. Eng. A 234-236 (1997) 962-965.
[9] P. J. Ennis, A. Zielinska-Lipiec, O. Wachter, A. Czyrska-Filemonowicz, Microstructure, stability and creep rupture strength of the martensitic steel P92 for advanced power plant, Acta Mater. 45 (1997) 4901-4907.
[10] B. K. Choudhary, E. I. Samuel, Creep behavior of modified 9Cr–1Mo ferritic steel, J. Nucl. Mater. 412 (2011) 82-89.
[11] S. Spigarelli, E. Cerri, P. Bianchi, E. Evangelista, Interpretation of creep behaviour of a 9Cr–Mo–Nb–V–N (T91) steel using threshold stress concept, Mater. Sci. Tech. 15 (1999) 1433-1440.
[12] B. Ule, A. Nagode, A model based creep equation for 9Cr–1Mo–0.2V (P91 type) steel, Mater. Sci. Tech. 23 (2007) 1367-1374.
[13] P. Anderson, T. Bellgard, F. L. Jones, Creep deformation in a modified 9Cr-1 Mo steel, Mater. Sci. Tech. 19 (2003) 207-213.
[14] I. Charit, K. L. Murty. Creep behavior of niobium-modified zirconium alloys, J. Nucl. Mater. 374 (2008) 354-363.
[15] J. E. Bird, A. K. Mukherjee, J. E. Dorn, Quantitative relation between properties and microstructure, D. G. Brandon and A. Rosen (Eds.), Jerusalem University Press, 1969, pp. 255-342.
[16] D. V. V. Satyanarayana, G. Malakondaiah, D. S. Sarma, Steady state creep behaviour of NiAl hardened austenitic steel, Mater. Sci. Eng. A 323 (2002) 119-128.
[17] S. C. Tjong, Z. Y. Ma, Creep behaviour of precipitation-hardened ferritic Fe–19Cr–4Ni–2Al alloy, Mater. Lett. 56 (2002) 59-64.
[18] B. K. Choudhary, C. Phaniraj, K. Bhanu Sankara Rao, S. L. Mannan, Creep deformation behavior 9Cr-1Mo ferritic steel, ISIJ Int. 41 (2001) S73-S80.
[19] K. Maruyama, K. Sawada, J. Koike, H. Sato, K. Yagi, Examination of deformation mechanism maps in 2.25Cr-1Mo steel by creep tests at strain rates of 10^{-11} to 10^{-6} S^{-1}, Mater. Sci. Eng. A 224 (1997) 166-172.
[20] S. Spigarelli, E. Cerri, E. Evangelista, Proceedings of conference on creep and Fatigue-design and life assessment at high temperature, London, Institute of Mechanical Engineers,1996, p.1.
[21] V. Sklenica, K. Kucharova, A. Dlouhy, J. Krejci, Proceedings of conference on Materials for advanced power engineering, Liege, Belgium, 1994, p.435.
[22] R. S. Mishra, T. R. Bieler, A. K. Mukherjee, Superplasticity in powder metallurgy aluminum alloys and composites, Acta Metall. Mater. 43 (1995) 877-891.

[23] Y. Huang, T. G. Langdon, The creep behavior of discontinuously reinforced metal-matrix composites, JOM 55 (2003) 15-20.

[24] M. E. Kassner, P. Kumar, W. Blum, Harper–Dorn creep, Int. J. Plast. 23 (2007) 980-1000.

[25] M. F. Ashby, Results and consequences of a recalculation of the Frank-Read and the Orowan stress, Acta Metall. 14 (1966) 679-681.

[26] D. Srolovitz, R. Petkovic-Luton, M. J. Luton, Diffusional relaxation of the dislocation-inclusion repulsion, Philos. Mag. 48 (1983) 795-809.

[27] E. Artz, D. S. Wilkinson, Threshold stresses for dislocation climb over hard particles: the effect of an attractive interaction, Acta Metall. 34 (1986) 1893-1898.

[28] R. S. Mishra, T. K Nandy, G. W. Greenwood, The threshold stress for creep controlled by dislocation particle interaction, Philos. Mag. A 69 (1994) 1097-1109.

[29] J. W. Martin, Micromechanisms in particle-hardened alloys, Cambridge, Cambridge University Press, 1980, p. 41.

[30] R. S. Mishra, Dislocation-particle interaction at elevated temperatures, JOM 61 (2009) 52-55.

[31] K. L. Murty, S. Gollapudi, I. Charit, Newtonian viscous creep in metals, Trans. Indian Inst. Met. 63 (2010) 85-91.

[32] D. M. Owen, T. G. Langdon, Low stress creep behavior: an examination of Nabarro-Herring and Harper-Dorn creep, Mater. Sci. Eng. A 216 (1996) 20-29.

[33] J. Fiala, J. Novotny, J. Cadek, Coble and Harper-Dorn creep in iron at homologous temperatures T/T_m of 0.40-0.54, Mater. Sci. Eng. 60 (1983) 195-206.

[34] F. R. N. Nabarro, H. L. deVilliers, The Physics of Creep: Creep and Creep-Resistant Alloys, Taylor & Francis Inc., Bristol, PA, 1995.

[35] M. Yoshizawa, M. Igarashi, Long-term creep deformation characteristics of advanced ferritic steels for USC power plants, Int. J. Press. Vessel Pip. 84 (2007) 37-43.

[36] S. Gollapudi, V. Bhosle, I. Charit, K. L. Murty, Newtonian viscous creep in Ti–3Al–2.5V, Philos. Mag. 88 (2008) 1357-1367.

[37] L. Kloc, J. Fiala, On creep behaviour of several metallic materials at low stresses and elevated temperatures, Chem. Pap. 53 (1999) 155-164.

[38] E. Artz, M. F. Ashby, R. A. Verall, Interface controlled diffusional creep, Acta Metall. 31 (1983) 1977-1989.

[39] J. Rosler, R. Joos, E. Artz, Microstructure and creep properties of dispersion-strengthened aluminum alloys, Metall. Trans. A 23 (1992) 1521-1539.

[40] V. C. Nardone, J. K. Tien, Pinning of dislocations on the departure side of strengthening dispersoids, Scripta Metall. 17 (1983) 467-470.

[41] J. Weertman, Theory of steady-state creep based on dislocation climb, J. Appl. Phys. 26 (1955) 1213-1217.

[42] S. Gollapudi, I. Charit, K. L. Murty, Creep mechanisms in Ti–3Al–2.5V alloy tubing deformed under closed-end internal gas pressurization, Acta Mater. 56 (2008) 2406-2419.

3. Creep rupture behavior of Grade 91 steel

3.1. Introduction

Grade 91 steel is considered a potential structural material for advanced nuclear reactors. The creep deformation behavior of Grade 91 steel was studied in the temperature range of 600^{o}C to 700^{o}C and at stresses 35 MPa to 350 MPa. The data were analyzed in terms of Monkman-Grant relation and Larson-Miller parameter. Creep damage tolerance factor and stress exponent were used to identify the cause of creep damage. The fracture surface morphology of the ruptured specimens was studied by scanning electron microscopy to elucidate the failure mechanisms. Fracture mechanism map for Grade 91 steel was developed based on the available material parameters and experimental observations.

Since the introduction of Cr-Mo steels, they have been the material of choice for use in power generation plants. Ferritic-martensitic (F-M) steels with 9-12 wt.% Cr were developed for fossil-fuel-fired power plants [1] during 1960s, and later used as boiler tube in the advanced gas-cooled reactors [2,3]. With optimization of alloy compositions, the creep rupture strength of F-M steels has increased significantly over the years [3]. For example, the composition of the earlier version of 9Cr-1Mo (T9) F-M steel was modified by addition of Nb and V to enhance the creep properties. Nb and V form fine, stable carbides and carbonitrides, resulting in excellent creep strength. These precipitates improve creep strength of the steel by resisting the movement of dislocations, delaying the plastic deformation by inhibiting grain boundary sliding, retaining finer grains during austenitization [4], and delaying the onset of tertiary creep stage [5]. Compared to austenitic steels, F-M steels tend to have better radiation swelling resistance [1], excellent thermo-physical properties, resistance to stress corrosion cracking in aqueous and chloride environments, and are less expensive [6].

With the vision to enhance the efficiency of power production and lower the emission of greenhouse gases, the new generation nuclear power plants are expected to operate at higher temperatures and radiation doses for longer service life (60 years and beyond). Hence, the materials used in these power plants are required to have superior creep properties. For example, Grade 91 steel is seen as a potential candidate material for reactor pressure vessel (RPV) application in Gen-IV Very High Temperature Reactor (VHTR). In addition to that, Grade 91 steel (also called modified 9Cr-1Mo steel) is being considered as wrapper material for Fast Breeder Reactors (FBR) [7]. Depending on the VHTR design, Prismatic Modular Reactor (PMR) or Pebble Bed Modular Reactor (PBMR), the operating temperature of the reactor pressure vessel (RPV) can vary between 300^{o}C and 650^{o}C. Furthermore, the RPV in the VHTR will be more than twice the size of a typical RPV in a Light Water Reactor (LWR) [8]. The nuclear power plant with a VHTR design is expected to produce electricity and hydrogen (a clean source of energy) at the same time.

RPV is considered an irreplaceable component of a nuclear power plant which dictates its useful service life. Hence, understanding creep rupture properties of Grade 91 steel is important to predict the long term mechanical integrity of the plant. Detailed study of creep deformation mechanisms in Grade 91 steel can be found in Shrestha et al. [9]. Even though there are a number of other studies involving creep deformation mechanisms of as-received Grade 91 steels [10-14], there are very few studies [12,15] in the area of their creep rupture behavior. Generally, it is not clear how creep deformation mechanism affects the creep-rupture behavior which is

dominated by the tertiary stage of creep. The creep rupture characteristics of Grade 91 steel have been analyzed by linking them with the identified creep deformation mechanism, and in terms of the Monkman-Grant relation, creep damage tolerance and Larson-Miller parameter. The data analysis was supported by fractography, which is used to identify the cause of creep rupture failure.

3.2. Experimental Details

3.2.1. Material

The chemical composition of ASTM A387 Grade 91 CL2 steel (Grade 91) used in this study is shown in Table 3.1. The hot rolled Grade 91 plates were obtained from ArcelorMittal Plate LLC, in normalized and tempered condition (i.e., austenitized at 1040^{o}C for 240 minutes followed by air cooling, and tempered at 790^{o}C for 43 minutes). The as-received plates were 10.4 cm × 10.4 cm × 1.27 cm in size. Creep specimens with a gauge length of 2.54 cm and diameter of 0.635 cm were machined from the steel plates. At room temperature, the as-received Grade 91 steel exhibited yield strength of 533 MPa, ultimate tensile strength of 683 MPa and elongation to fracture of 19%.

Table 3.1. Chemical composition (in wt.%) of Grade 91 steel

Element	Nominal	Measured
Cr	8.00 - 9.50	8.55
Mo	0.85 - 1.05	0.88
V	0.18 - 0.25	0.21
Nb	0.06 - 0.10	0.08
C	0.08 - 0.12	0.10
Mn	0.30 - 0.60	0.51
Cu	0.4 (max.)	0.18
Si	0.20 - 0.50	0.32
N	0.03 - 0.07	0.035
Ni	0.40 (max.)	0.15
P	0.02 (max.)	0.012
S	0.01 (max.)	0.005
Ti	0.01 (max.)	0.002
Al	0.02 (max.)	0.007
Zr	0.01 (max.)	0.001
Fe	Balance	Balance

3.2.2. Microstructural characterization

Optical microscopy was performed on both the as-received and creep tested specimens for characterization of the grain structure. Conventional metallographic procedures of cold mounting, grinding and polishing were followed to prepare the specimen surface to 0.5 μm finish before etching was carried out using Marble's reagent; a solution made of 50 ml distilled water, 50 ml hydrochloric acid and 10 g of copper sulfate. Subsequently, an Olympus light microscope

was used to examine the metallographic specimens and an attached CCD camera was used to record the micrographs.

For detailed microstructural characterization, some metallographic samples were examined using a Zeiss Supra 35 field emission gun scanning electron microscope (FEG-SEM) operated at an accelerating voltage of 10-20 kV under both secondary and backscattered electron imaging modes. Energy dispersive spectroscopy (EDS) technique available in the SEM was used to estimate the relevant chemical compositions.

The ruptured samples were then sectioned from the gauge length of the specimen. For TEM study, the sectioned samples were mechanically polished down to ~120 μm thickness, and then 3 mm diameter disks were punched out of the samples. Those disks were then jet polished in Fischione twin-jet polisher using a solution of 80 volume% methanol and 20 volume% nitric acid solution at a temperature of ~-40^{o}C. Dry ice bath was used to achieve low temperature. Philips CM200 and JEOL JEM-2010 TEM operated at an accelerating voltage of 200 kV were used to study in detail the grain and precipitate morphology of the material under both as-received and crept conditions. Hardness was measured using Vickers microhardness tester – applied load was 500 g and the hold time was 15 s.

3.2.3. Creep testing

Creep tests were performed at different temperatures between 600^{o}C and 700^{o}C and stresses between 35 and 350 MPa using an Applied Test Systems (ATS) lever arm (20:1) creep tester. Though creep tests were intended for fracture, some tests in the lower stress regime were interrupted in the minimum creep stage due to time constrain.

3.3. Results and Discussion

3.3.1. Microstructural characteristics of as-received material

The as-received Grade 91 steel had a tempered martensitic microstructure as shown in Fig. 3.1a. Precipitation hardening is one of the main strengthening mechanisms in highly alloyed steels like Grade 91. Alloying elements, such as C, N, Nb, V, Cr and Mo, promote the formation of precipitates like Cr-rich $M_{23}C_6$, and Nb or V-rich MX particles, where M stands for metals, i.e., Cr, Mo, Nb or V, and X stands for C or N. The Cr-rich $M_{23}C_6$ precipitates are elongated rod-like or block-like particles, while Nb-rich and V-rich MX precipitates have nearly spherical shapes. The dimensions of the elongated rod-like and block-like Cr-rich precipitates were measured, and found to have an average length of 285±80 nm and width of 121±39 nm, which are similar to the ones reported in Grade 91 steel [5,13,16]. The average diameter of near-spherical MX-type precipitates was 37±15 nm, similar to the values reported in Grade 91 steel [5,13,17]. These thermally stable fine precipitates enhance the long term creep resistance. A SEM micrograph in Fig. 3.1b shows the distribution of precipitates in the alloy. Coarser $M_{23}C_6$ type precipitates were located on the grain boundaries, lath boundaries and prior austenite grain boundaries, while finer MX type precipitates were located inside the grain. The TEM micrograph in Fig. 3.1c shows the various precipitates including $M_{23}C_6$ and MX types. Morphology of the

$M_{23}C_6$ type precipitates was studied by EDS in SEM. The EDS line scan of these precipitates, as shown in Fig. 3.1d, revealed that the main constituents of $M_{23}C_6$ precipitate were Cr and plausibly Mo.

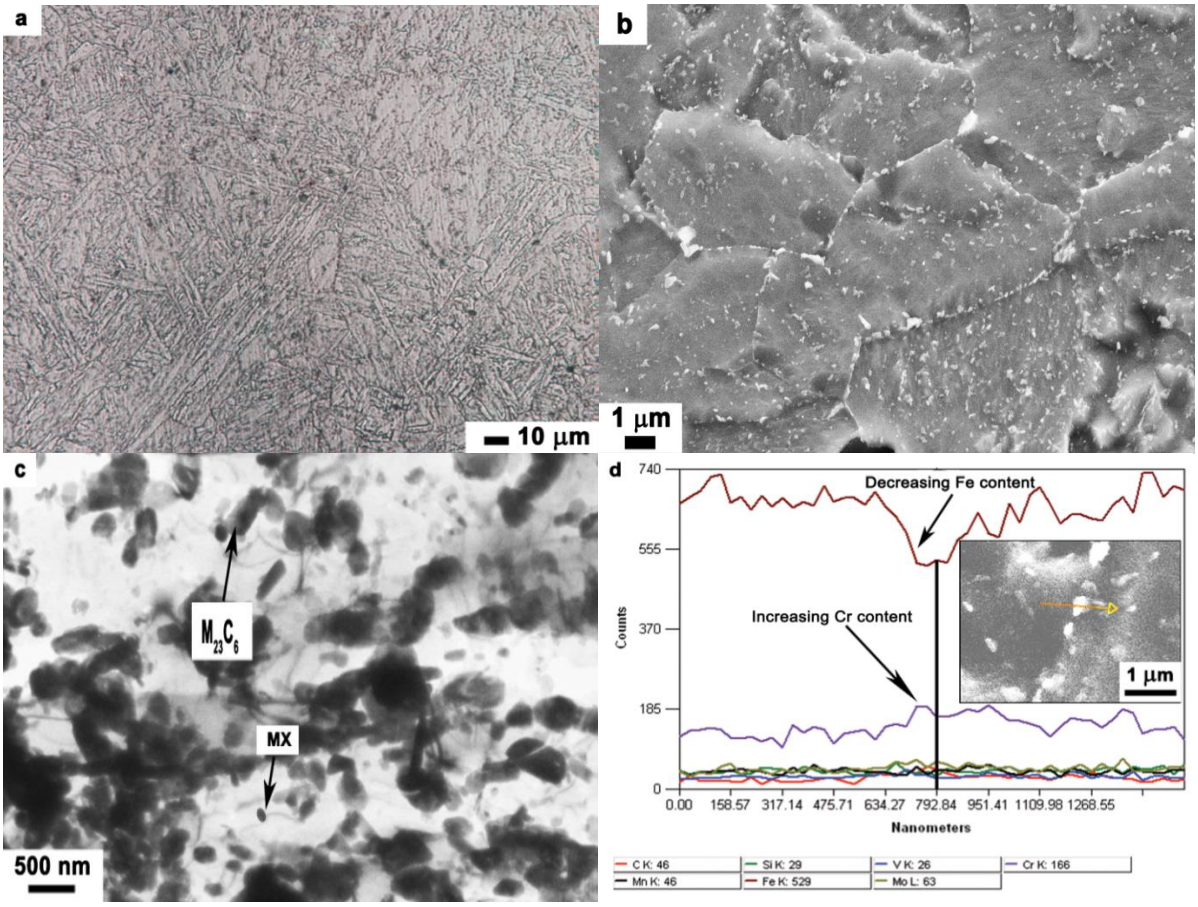

Fig. 3.1. Microstructure of Grade 91 steel: (a) optical micrograph showing the tempered martensitic structure, (b) a SEM micrograph showing the distribution of precipitates in the alloy, (c) a bright field TEM micrograph showing various particles, and (d) EDS line scan of $M_{23}C_6$ type particle.

3.3.2. Creep properties

During the primary creep, the creep rate decreases with increasing strain due to work hardening via dislocation multiplication and interactions. In the secondary stage, creep rate is stabilized as the work hardening effect is counterbalanced by the dislocation annihilation and rearrangement. Finally, the creep rate accelerates as cavities start growing leading to the tertiary stage. Most creep curves obtained in this study consisted of two distinct regimes: primary and tertiary, and a minimum creep rate regime in the transition. Fig. 3.2a shows the effect of applied stress on the creep rate at a temperature of 600°C. Minimum creep rates increased but rupture time decreased with increasing applied stress. Fig. 3.2b shows the effect of test temperature on creep rate at a stress of 100 MPa. The minimum creep rates increased but rupture time decreases with increasing temperature. Table 3.2 lists the summary of creep rupture data. All the data were obtained from power law creep regime.

The total creep rupture life is related to the duration of primary and secondary creep stage by the following relationship:

$$\frac{{t_R}^{\gamma}}{t_{ts}} = C, \tag{1}$$

where t_{ts} is the time to reach tertiary creep stage, t_R the rupture time, C and γ are constants. When t_{ts} data were plotted against t_R data in a double logarithmic scale, all the data fall on a straight line whose slope is the value of constant γ (~1.12) as shown in Fig. 3.3a. It is noted that the relation between the time to reach tertiary creep stage and the rupture time is independent of temperature. Creep rupture data for various temperatures are presented as stress versus rupture time as shown in Fig. 3.3b. Here straight lines were obtained for each temperature. No change in the slope was noted for any particular temperature implying that the creep damage mechanism remained the same. Nevertheless, the knowledge of such microstructural instabilities is important since they could lead to significant errors in extrapolation of the data to longer time [18].

Table 3.2. Summary of creep rupture data.

Sample	Temp. (°C)	Stress (MPa)	Fracture elongation (%)	Reduction in area (%)	True fracture strain
1	600	200	21	87	2
2	600	225	21	87	2
3	600	250	19	85	1.9
4	600	275	24	85	1.9
5	600	310	26	85	1.9
6	650	100	24	85	1.9
7	650	125	21	90	2.3
8	650	150	30	92	2.5
9	650	200	16	90	2.2
10	700	80	20	94	2.9
11	700	100	23	93	2.7
12	700	200	27	97	3.4

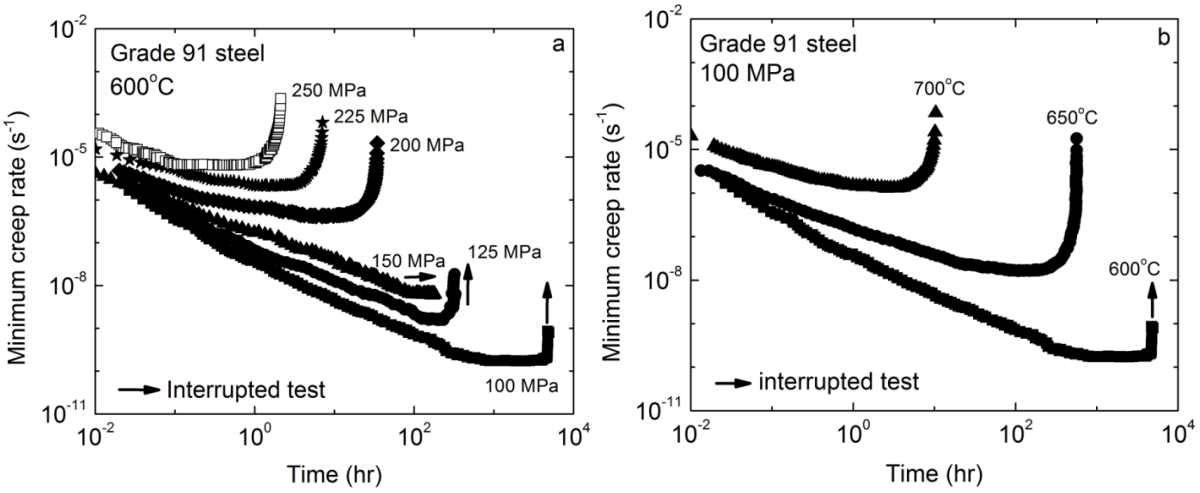

Fig. 3.2. (a). The variation of creep rates as a function of stress at 600°C, and (b) the variation of creep rates with temperature at 100 MPa.

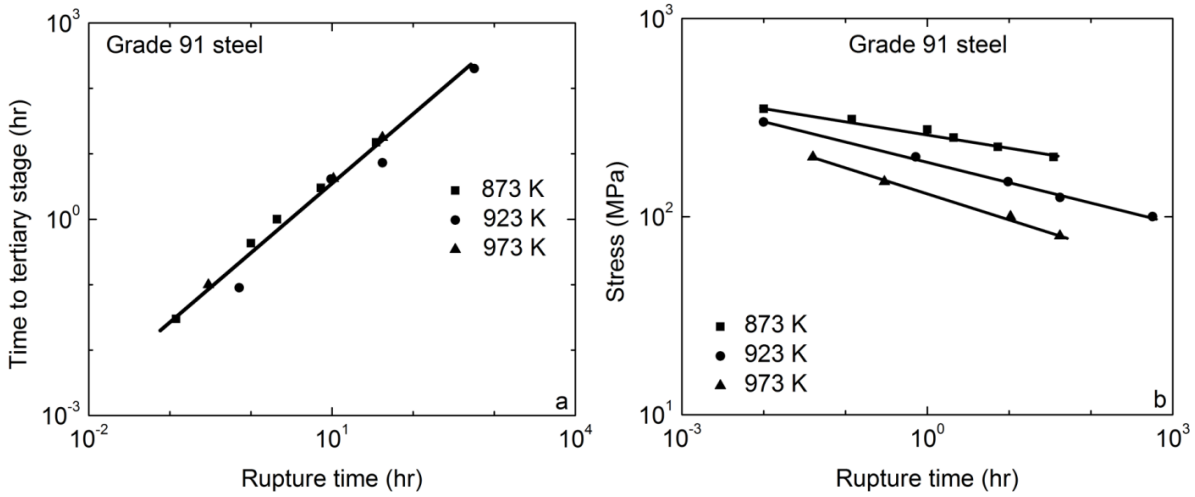

Fig. 3.3. (a) Relation between the creep rupture life and the time to get to tertiary creep stage, and (b) stress and temperature dependency of creep rupture life.

3.3.2.1. Creep Deformation Mechanism

Here creep deformation mechanism in the higher stress regime was analyzed based on the minimum creep rates using the Bird-Mukherjee-Dorn (BMD) equation [19]:

$$\frac{\dot{\varepsilon}_m kT}{DEb} = A\left(\frac{\sigma}{E}\right)^n \left(\frac{b}{d}\right)^p, \tag{2}$$

where A is a constant, $\dot{\varepsilon}_m$ the minimum creep rate, E the modulus of elasticity, b the Burgers vector, k the Boltzmann constant, T the absolute temperature, σ the applied stress, d the grain diameter, p the inverse grain size exponent, n the stress exponent, and D the diffusivity which is described by the following relation:

$$D = D_o exp\left(\frac{-Q}{RT}\right), \quad (3)$$

where D_o is the frequency factor, Q the appropriate activation energy, and R the universal gas constant. However, for particle hardened alloys like Grade 91 steel, the BMD equation tends to result in higher activation energy and stress exponent [9]. In this study, the apparent stress exponents of 11 and 9, and high activation energy of 510 kJ/mol were obtained. The BMD equation was modified to incorporate the threshold stress (σ_{th}). The threshold stress compensated constitutive equation can then be described by

$$\frac{\dot{\varepsilon}_m kT}{DEb} = A\left(\frac{\sigma-\sigma_{th}}{E}\right)^n \left(\frac{b}{d}\right)^p, \quad (4)$$

where (σ - σ_{th}) is the effective stress. Even though the above equations are used to describe the creep deformation behavior in the minimum creep regime, they do provide insights into the failure mechanisms that occur during the tertiary stage of creep. After incorporating the threshold stress, the rate controlling creep deformation mechanism in the high stress regime was identified as climb of edge dislocations, the high apparent stress exponents of 11 and 9 were reduced to 5 (true stress exponent), and the creep activation energy was reduced from 510 kJ/mol to 225 kJ/mol, which is close to the activation energy of lattice self-diffusion in α-iron. Fig. 3.4 shows the normalized $\left(\frac{\dot{\varepsilon}_m kT}{DEb}\right)$ data plotted against modulus-compensated effective stress$\left(\frac{\sigma-\sigma_{th}}{E}\right)$. Here compilation of data from other studies [10,12,13,20] were superimposed on the $\left(\frac{\dot{\varepsilon}_m kT}{DEb}\right)$ vs. $\left(\frac{\sigma-\sigma_{th}}{E}\right)$ plot. Based on the plot shown in Fig. 3.4, the constant A was calculated to be 7.3×10^5. Though most of the compiled and present study data are within a band, some data are sparse.

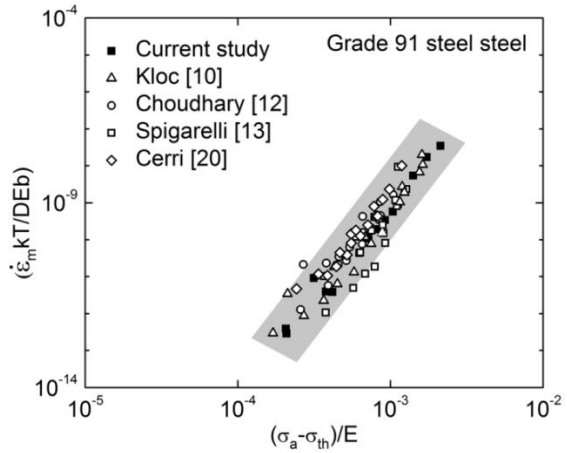

Fig. 3.4. Modified BMD plot involving normalized creep data for various Grade 91 steels

3.3.2.2. Microstructural characteristics of crept specimen

The solid solution strengthening, fine substructure, dense dislocation network and precipitates increase the creep resistance of Grade 91 steel. These strengthening mechanisms deteriorate over time during creep, and the material loses its inherent creep rupture strength. The microstructural studies of specimen crept at 650°C and 200 MPa, as shown in Fig. 3.5a, showed

decrease in the dislocation and precipitate density. Creep strength is reduced in precipitate-free matrix as there are no obstacles for the movement of dislocations. Apart from deterioration of above mentioned strengthening mechanisms, precipitation of Laves phase (Fe_2Mo) weakens the creep strength by removing Mo from solid solution. The creep strength of an alloy depends on its ability to withstand temperature and stress for prolonged period of time and maintain its as-received microstructure. Degradation of creep strength has been correlated with changes in microstructure [17,21-23]. Polygonized microstructure can be seen in the gauge section of crept specimen, as shown in Fig. 3.5a, but in contrast, martensitic lath structure can still be seen in the grip section, as shown in Fig. 3.5b, which does not experience stress, just the temperature. The TEM studies revealed a decrease in the dislocation and precipitate density, and an increase in the subgrain size. Panait et al. [17] assert that the growth of subgrains during creep contributes most to the decrease in long-term creep resistance. According to Qin et al. [24] the evolution of subgrain size is given by following relation:

$$log\lambda = log\lambda_s + \log\left(\frac{\lambda_0}{\lambda_s}\right) exp\left(\frac{-\varepsilon}{k_w}\right) \quad (5)$$

where, λ is the subgrain size, $\lambda_s = 10Gb/\sigma$ is the subgrain size in the steady state regime, λ_o is the subgrain size in as-received condition, ε is the creep strain, $k_w \approx 0.12$ is a growth constant, G is the shear modulus, b is the Burgers vector and σ is the applied stress. The mean subgrain size in 12Cr1MoV, P91 and P92 steel was 0.35-0.42 μm [25]. In P92 steel at 600ºC and 160 MPa, the subgrain size increases from 700 nm at 1.8% strain to 1400 nm at 22.8% strain [11]. In our study, the average size of subgrains in the as-received condition was 0.15-0.4 μm. In a test done at 650ºC and 200 MPa, the subgrain size in grip and gauge section of creep specimen was 0.5 μm and 0.7 μm, respectively.

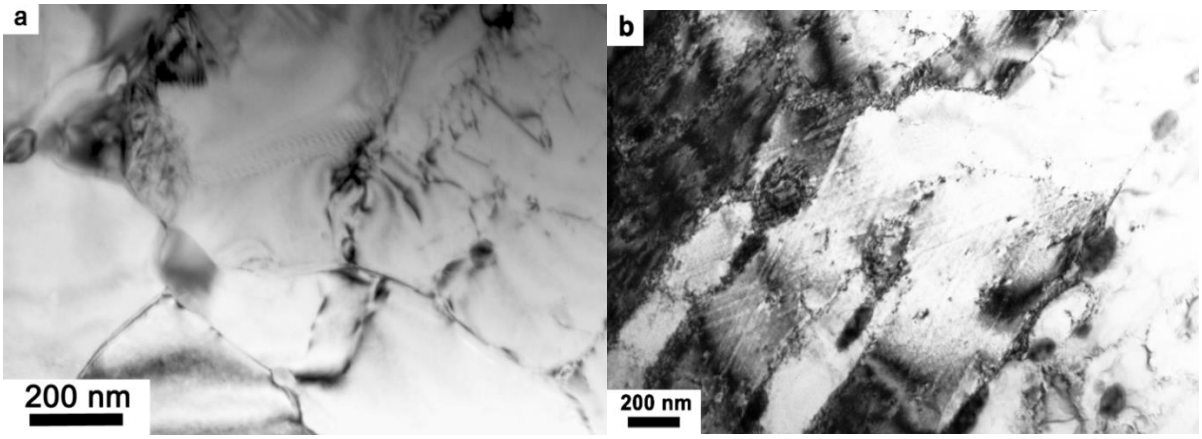

Fig. 3.5. Bright field TEM micrographs of a specimen crept at 200 MPa and 650ºC: (a) microstructure of the gauge section showing polygonized structure, and (b) martensitic lath structure in grip section, which does not experience stress.

3.3.3 Fractography

The creep specimens ruptured with external necking and the associated percentage reduction in area, in many cases, was ~90% as shown in Table 3.2. The reduction in area percent

increased with increase in temperature. In addition to the microstructural instability, the reduction in load bearing cross section is a result of Fe-Cr oxides, which corresponds to ~2% decrease in load-bearing cross-section for a Grade 91 steel crept at 650^{o}C and 155 MPa for 31 h [15]. The reduction in load bearing cross-section can be significant for specimens crept for extended period of time. However, the significance of internal necking through the microstructural degradation, cavity formation, growth and coalescence must be taken into account to understand the final failure mechanism. It is important to note that none of the specimens failed through necking down to a point implying that internal damage processes had a significant bearing on their failure. Generally, cavities form throughout the creep deformation; however, in the tertiary stage nucleation and growth of cavities take place at an accelerated pace.

SEM study of fracture surface of the crept specimens revealed dominant dimple features, as shown in Fig. 3.6. These features are characteristic of transgranular mode of fracture. Similar fracture morphology was also reported by Yurechko et al. [15] in Grade 91 steel. Fig. 3.6a shows the fracture surface of a specimen crept at 650^{o}C and 100 MPa, while Fig. 3.6b shows the fracture surface of a specimen crept at 700^{o}C and 80 MPa. Transgranular fracture mode was also observed in a sample crept at 700^{o}C and 200 MPa, but the number density of cavities was lower while the average size was larger. For creep-enhanced diffusive cavity growth, increasing stress leads to greater cavity growth rates and coalescence resulting in a smaller number density and larger dimple size.

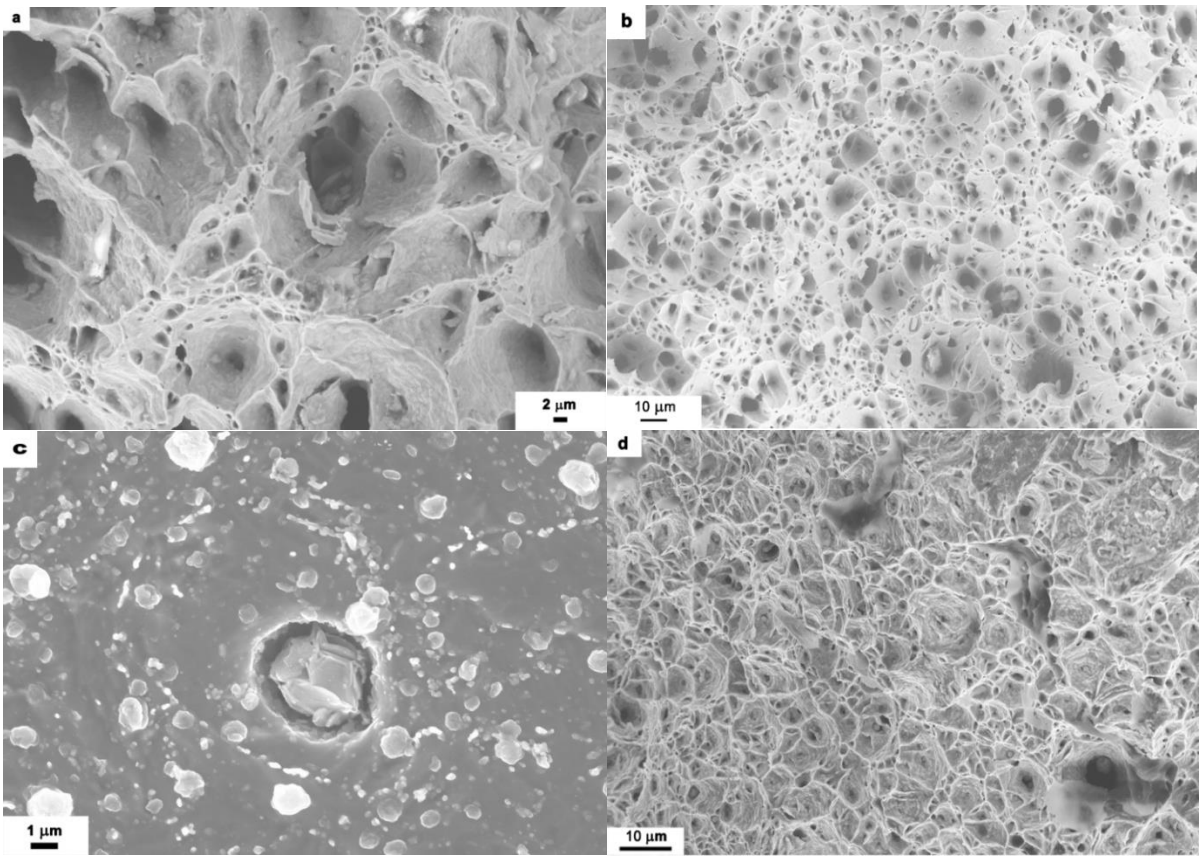

Fig. 3.6. (a) Dimpled fracture surface in specimen crept at 100 MPa and 650^{o}C, (b) ductile dimple fracture in specimen crept at 80 MPa and 700^{o}C, (c) cavity formation around a particle (600^{o}C and 200 MPa), and (d) dimpled fracture surface in specimen crept at 200 MPa and and 650^{o}C.

While precipitates increase the creep strength of materials by impeding the dislocation motion, they act as the stress concentration sites for cavity nucleation during creep deformation. Creep damage in general is due to the combined effect of cavity nucleation, growth and coalescence. The cavities act as a stress raiser where the localized stress exceeds the applied stress. Because of some ductility of the steel, the stress concentration site undergoes plastic deformation. Ultimately, excessive plastic strain at the particle-matrix interface will lead to decohesion. That phenomenon can be further exacerbated via grain boundary sliding if the particle is located at the grain boundary [26]. Fig. 3.6c shows the cavity formation around a carbide precipitate in a specimen crept at 200 MPa and 600^{o}C. Precipitates were seen in the dimpled fracture surface, which suggests that the carbides aided in the cavity formation.

SEM was used to do the cavitation study on the necked area of the fractured specimens. Fig. 3.7a shows a low magnification SEM image of the cavities present in the necked region of a specimen crept at 200 MPa and 700^{o}C, which was taken ~5 mm away from the fractured surface. From the SEM image in Fig. 3.7a and also images of higher magnification, no significant cavitation was observed. At this region on the gauge section, the local reduction in area was only ~0.5. The percentage reduction in area and the corresponding true fracture strain are listed in Table 3.2. The extent of cavitation depends on the amount of local strain. Fig. 3.7b shows the variation of true local strain and Vickers microhardness with the position on the gauge length of the aforementioned crept specimen. The fracture point is indicated as '0' which has the highest true strain of 3.4. True local strain decreases as we move away from the fracture point. The region where the creep damage is concentrated and has high true strain undergoes true tertiary stage, while other parts on the gauge showing little true strain have not reached the tertiary creep stage. However, the gauge section undergoing tertiary creep is so dominant that it becomes responsible to the final failure of the specimen. Further evidence of that is noted in the microhardness data shown in Fig. 3.7b. The microhardness increased as we moved away from the point of fracture. The point of fracture showed drastic decrease in hardness of 29VHN compared to 231VHN at the grip section and 248VHN of the as-received material. The hardness decreased with increasing number of cavities.

For a creep test performed at 100 MPa and 650^{o}C, localized creep cavitation at ~ 5 mm away from fracture tip can be seen in Fig. 3.7c. These creep cavities are found to be aligned along a more or less straight path and are round or elliptical shaped (*r*-type crack). This is likely due to the propensity of cavities forming on the straighter lath boundaries. Growth of incipient *r*-type crack is controlled by diffusion but as the cavity size increases they grow by power law creep, and in transition they grow as a coupled effect of diffusion and power law creep [27]. Another example of damage initiation is noted in Fig. 3.7d where it shows a triple–point crack, ~ 7 mm away from the fracture tip, in a creep specimen tested at 150 MPa and 650^{o}C. These types of cracks are known as wedge shaped cracks (*w*-type cracks). Because of tensile stress, the grain boundaries which have precipitates and are normal to the applied stress are activated and the cavity grows as a result of the sliding of grains. In this study, all specimens failed predominantly in transgranular mode, but there was limited evidence of wedge cracks. The EDS line scan of fracture surface along the grain boundary shows the presence of Cr containing precipitate, as shown in Fig. 3.7e.

Apart from the $M_{23}C_6$ and MX type carbides, the manganese sulfide particles may also act as cavity nucleation site in Grade 91 steel. With the help of scanning auger microprobe, Hippsley et al. [28] reported observing segregation of sulfur along the crack tip. Choudhary et al. [29] reported observing wedge crack in plain 9Cr-1Mo steel which is due to the split in the lath

boundaries. The split in the lath boundaries was promoted by the presence of silicon and phosphorous. Grade 91 steel has 0.02 wt.% phosphorus, which is higher than 0.007 wt.% in 9Cr-1Mo steel. The higher phosphorous content makes the Grade 91 steel susceptible to phosphorous embrittlement [7].

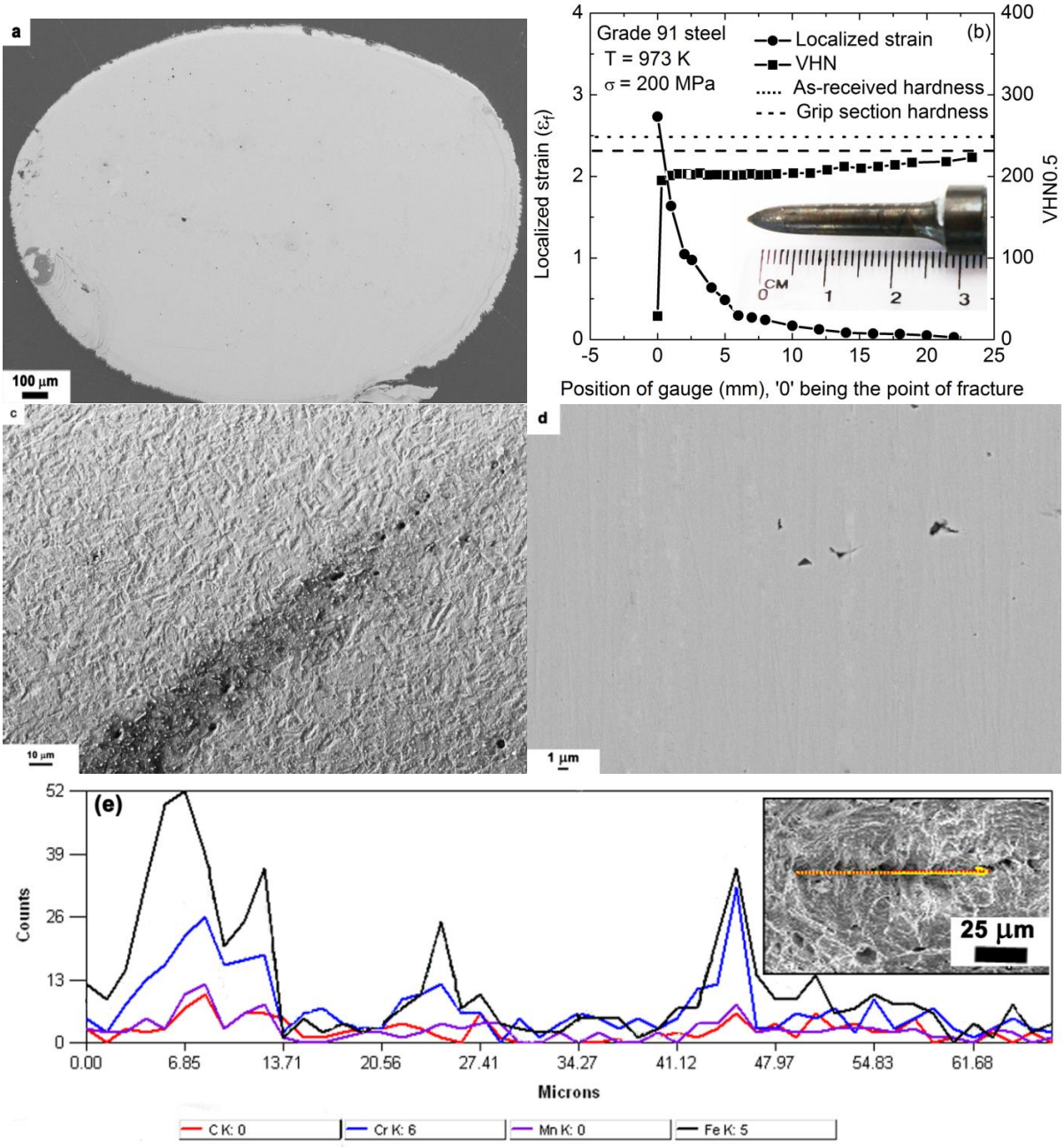

Fig. 3.7. (a) Necked area of a creep ruptured specimen (700°C and 200 MPa), (b) variation of true local strain and microhardness with position in a specimen fractured at 700°C and 200 MPa, (c) nucleation of voids along a straight line in a specimen crept at 650°C and 100 MPa, (d) wedge cracks seen in a specimen crept at 150 MPa and 650°C, and (e) EDS line scan along grain boundary.

3.3.4. Creep rupture data analysis and life prediction

The relationship between minimum creep rate and rupture life is given by the Monkman-Grant equation [30]

$$\dot{\varepsilon}_m{}^m t_R = K_1, \tag{6}$$

where $\dot{\varepsilon}_m$ is the minimum creep rate, t_R the rupture time, m and K_1 are constants. The value of $K_1 = 0.04$ was obtained from straight line fit of the logarithmic relation deduced from Equation 6. Nabarro [31] noted that for better prediction of creep rupture life m needs to be less than 1. In this study, the m was calculated to be ~0.9. Thus, using the above relationship creep rupture life was predicted based on the experimentally determined minimum creep rate. From Eq. 3.6 and creep deformation plot reported by Shrestha et al. [9], the stresses for creep rupture life of 10^5 h in Grade 91 steel are predicted to be 87 MPa and 54 MPa at 600°C and 650°C, respectively. The creep life prediction for 600°C is similar to one reported by Srinivasan et al. [32] using various creep life prediction methods.

Monkman and Grant [30] and Evans [33] found that the value of K_1 was 0.04 for ferritic steel and 0.08 for austenitic steel, and predicted that the K_1 to be less than n^{-1}, meaning that the data from Newtonian viscous creep regime were not included. Shrestha et al. [9] have calculated the stress exponent of ~10 in the higher stress regime before the incorporation of threshold stress in BMD equation. Stress exponent higher than 9 is common in engineering alloys like Grade 91 steel. The inverse of the calculated stress exponent (n) was ~0.1. The fit in Fig. 3.8a resulted in K_1 to be 0.04. For a material to fail by complete necking, K_1 has to be equal to n^{-1} [33]. Thus, necking is not the dominant fracture mode in the creep rupture tests reported in this study. With regards to engineering alloys like Grade 91 steel, Dobes et al. [34] modified the aforementioned Monkman-Grant relation to obtain better correlation of the rupture time with the minimum creep rate by an equation

$$\dot{\varepsilon}_m{}^{m'} \frac{t_R}{\varepsilon_f} = K_2, \tag{7}$$

where ε_f is the strain at fracture (based on elongation to fracture), K_2 and m' are constants. The value of $K_2 = 0.26$ was found from the fitting of logarithmic plot deduced from Equation 3.7, as shown in Fig. 3.8b. Eq. 3.7 was used to calculate the creep damage tolerance factor, λ. For $m' = 1$, λ is given by inverse of K_2 [35,36]. The creep damage tolerance factor is used as a measure to identify the creep rupture mode whose value for engineering alloys range from 1 to 20 [36]. For $\lambda = 1$, materials have low creep strain, and brittle fracture mode is detected as they fracture without any significant plastic deformation, while large values indicate that the material can withstand strain concentration without local cracking and the fracture is ductile [31,36]. Ashby and Dyson [36] suggested that λ in the range of 1.5 and 2.5 indicates that damage is due to the cavity growth resulting from combined effect of power law and diffusion creep. Incipient cavities grow by diffusion, but power law creep takes over as they become larger [27]. For tests performed in higher stress regime (125-275 MPa) and at temperatures of 550°C, 575°C and 600°C, Choudhary et al. [12] reported observing high λ close to 5. High λ value was attributed to the absence of intergranular cracks, absence of wedge shaped cracks, and the microstructural

degradation like precipitate coarsening. Dominant creep damage mechanism is necking for λ higher than 2.5 [36], while coarsening of precipitates and subgrains, and decrease in dislocation density are the dominant creep damage mechanism when λ is 5 or higher [36,37]. Creep damage tolerance λ of 1.5 was observed in MA957, an yttrium bearing oxide dispersion strengthened (ODS) ferritic alloy, which fractured with little evidence of neck formation [38]. In this study, creep damage tolerance factor of ~4 was observed. The λ of ~4 indicates that the creep damage is due to the cavity growth resulting from combined effect of power law and diffusion creep, necking and microstructural degradation. Sometimes precipitates act as cavity nucleation sites, that is why some wedge type cracks and intergranular fracture mode was observed in this study, as shown in Fig. 3.7d. The reduction in area as indicated in Table 3.2 was similar to the one reported in [39]. Creep deformation mechanism of Grade 91 steel in high stress regime is controlled by power law creep [9,13,14]. Coarsening of precipitates and subgrains which were observed in Grade 91 steel [17,21-23] can decrease the creep strength as they become less effective in disrupting the movement of mobile dislocations [9, 40]. The creep damage tolerance is expected to be ~5 when coarsening of precipitates and subgrains are the dominant failure mechanism [36]. But the values of K_1 (~ 0.04), which is less than n^{-1} (~0.1), and the creep damage tolerance higher than 2.5 indicate that the dominant failure mechanism in Grade 91 steel is microstructural degradation with limited contribution from necking, and void growth. This is illustrated in diagnostic diagram for creep failure as shown in Fig. 3.9 [36]. The figure shows that all the creep fracture data reported in this study fell on the microstructural degradation domain, except for the test done at 700ºC and 200 MPa. Data from aforementioned test fell on the loss of section and necking domain. The same test showed significant necking, and had the highest true fracture strain of 3.4 as listed in Table 3.2. Note that the Ashby's diagnostic diagram for creep failure map uses the apparent stress exponent (as obtained from Norton's law), not the true stress exponent (as obtained from modified BMD equation). Details of constructing such maps are given in the work of Ashby and Dyson [36]. Moreover, the creep rupture data of precipitation strengthened Grade 91 steel were compared with that of iron. The dominant creep fracture mechanism in iron is void growth, while Grade 91 steel with more complex microstructure (as show in Fig. 3.1) exhibits microstructural degradation as the most dominant creep fracture mechanism.

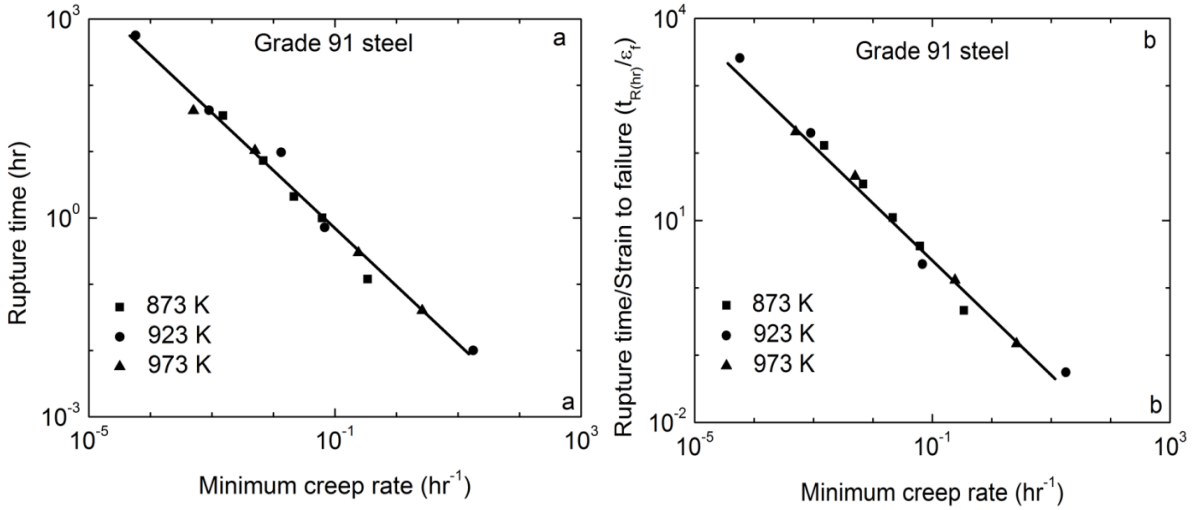

Fig. 3.8. (a) Monkman-Grant relation, and (b) modified Monkman-Grant relation

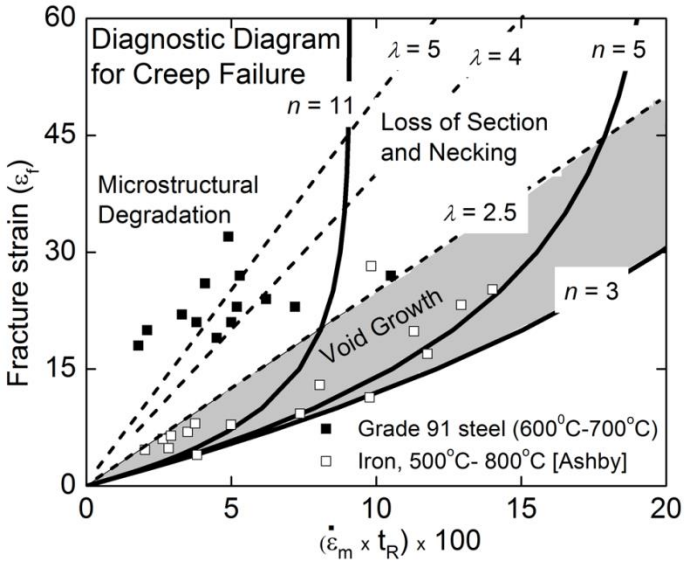

Fig. 3.9. A diagnostic diagram for creep failure of Grade 91 steel and iron

Another way of presenting creep rupture data for creep life prediction is through Larson-Miller parameter (LMP). LMP can be expressed in terms of rupture time and temperature as

$$LMP = T(logt_R + C), \tag{8}$$

where T is the temperature (K), t_R the rupture time (h), and C the Larson-Miller constant, typically taken as 33. LMP values of Grade 91 steel decrease with increased stress, and the data obtained in the present study remain within the ambit of the data band obtained from other studies, as shown in Fig. 3.10. A best fit polynomial equation for stress versus LMP plot, Fig. 3.10, was used to predict the creep life of Grade 91 steel in the 500-700°C temperature range. Table 3.3 lists the creep life prediction of Grade 91 steel. Thus, predicted creep life for 10^5 h rupture life is similar to the ones predicted by Srinivasan et al. [32] and Wilshire et al. [41] using various creep life prediction techniques. Klueh noted that the LMP plots for creep rupture tests of various steel types showed greater data scatter at low temperatures and high stresses than for the high temperatures and low stresses [3]. Even though the Monkman-Grant relation and LMP can be used to predict rupture life, it does not provide us with insights of the creep failure mechanisms. These approaches are empirically based, so their use may not lead to the precise estimation of the creep rupture life. Detailed study of temperature dependence on creep life prediction can be found in Srinivasan et al. [32] and Wilshire et al. [41].

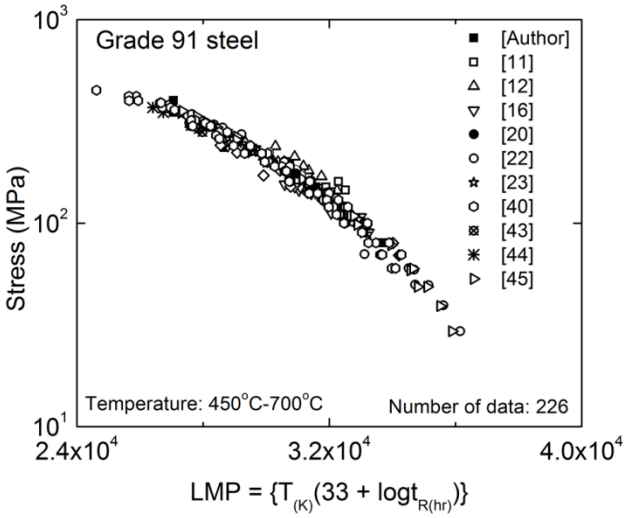

Fig. 3.10. Larson-Miller parameter plot of Grade 91 steel

Table 3.3. Creep life prediction of Grade 91 steel by LMP

Temp. (°C)	Rupture life (h)	Predicted allowable stress (MPa)
500	10^5	241
525	10^5	199
550	10^5	161
575	10^5	123
600	10^5	91
625	10^5	68
650	10^5	47
675	10^5	33
700	10^5	21

3.3.5. Fracture mechanism map of Grade 91 steel

Fracture mechanism map of Grade 91 steel was constructed in two-dimensional space of normalized stress and homologous temperature using relevant constitutive equations, tensile data, and fracture data from current study and literature [12,15]. Five fracture mechanisms have been identified as shown in Fig. 3.11. Since this study is mainly focused on the creep rupture behavior of Grade 91 steel, the low temperature cleavage fracture is not included in this map. Each fracture regime was obtained from relevant models and supported by the fractographic observation. Material parameters obtained from reference 47 were for F82H F-M steel similar to Grade 91 steel. The major alloying elements in F82H steel are 8 wt.% Cr and 2 wt.%W, instead of 9 wt.% Cr and 1 wt.% Mo. Due to limited fractographic observations, variation in test condition, variation in grain size, lack of material parameters, and because of the fact that some of the models are not well-established, the map presented here is the best approximate mechanistic representation of the fracture behavior of Grade 91 steel under different test conditions. Material parameters used for construction of this fracture mechanism map are listed in Table 3.4.

Fracture at the ideal strength is defined as [18]

$$\sigma_{ideal} \approx \frac{E(T)}{10}, \tag{9}$$

where *E(T)* is the temperature dependent modulus of elasticity. The dynamic fracture is the region in between the ideal strength fracture and ductile fracture regimes. Dynamic fracture is observed in a material when it is loaded at high strain rates. Grade 91 steel fractures by plastic deformation resulting in necking, which is the localized reduction in diameter of the test specimen. Necking introduces triaxiality of stress in the radial, transverse and longitudinal directions. The average true stress increases with decreasing cross-sectional area. Ductile fracture is observed in materials that have large strains in the range of 10-100% [45]. The ductile fracture domain was determined from the data obtained from tensile test performed at various temperatures. The higher domain of ductile fracture is the true fracture stress [46]

$$\sigma_{FS} = \sigma_{TTS}(1 + \varepsilon_f - \varepsilon_u), \tag{10}$$

where ε_f is the true fracture strain, ε_u the strain at uniform elongation, σ_{FS} the true fracture stress, and σ_{TTS} the true ultimate tensile stress given by [46]

$$\sigma_{TTS} = \sigma_{TS}\exp(\varepsilon_u), \tag{11}$$

where σ_{TS} is the engineering ultimate tensile stress. The true tensile stress is the lower domain of the ductile fracture. At temperatures higher than 0.4 $T_{m,}$ creep becomes dominant deformation mechanism. In creep regime, Grade 91 steel deforms by transgranular and intergranular creep fracture. Transgranular creep fracture (TCF) is observed in high stress regime, while intergranular creep fracture (ICF) is observed at low stresses. Dominant failure mechanism in TCF is the microstructural degradation, nucleation, growth and coalescence of cavities. The fracture surface of transgranular creep is similar to that of low temperature ductile fracture (*r*-type cracking), but the rate-controlling deformation mechanism is the high temperature dislocation climb instead of low temperature dislocation glide in low temperature ductile fracture [9,46]. Transgranular creep fracture regime was identified by coupled Monkman-Grant equation (Eq. 3.6) and modified BMD equation (Eq. 3.4). After using these equations, the fractographic observation from various studies and tensile data were used to better delineate the domain of TCF. The shaded region indicates the transition between the TCF and ICF. ICF is characterized by *w*-type cracks, which nucleate and grow on grain boundaries. *W*-type cracks seen in the present study were mainly located away from necked region, the region which has not reached the minimum creep stage, but they were not observed in the necked region. ICF domain was calculated by Hull and Rimmer cavity growth rate equation [47] as mentioned in Li and Zinkle [46]

$$t_R = B.\frac{kTa^3}{(D_{gb}\delta)\sigma\Omega}, \tag{12}$$

where *B* is the constant based on the spatial distribution of cavities, *k* the Boltzmann's constant, *T* the absolute temperature, *a* the mean cavity spacing, D_{gb} the grain boundary diffusivity, δ the grain boundary thickness, σ the applied stress, and Ω the atomic volume. The shaded region represents the variation in creep rupture life in the range of 10^4 hr to 10^5 hr. To the best of our knowledge, Fig. 3.11 presents the first attempt at constructing the fracture mechanism map of

Grade 91 steel. This could potentially lead to the development of fracture mechanism maps of other 9-12 wt.% Cr F-M steels.

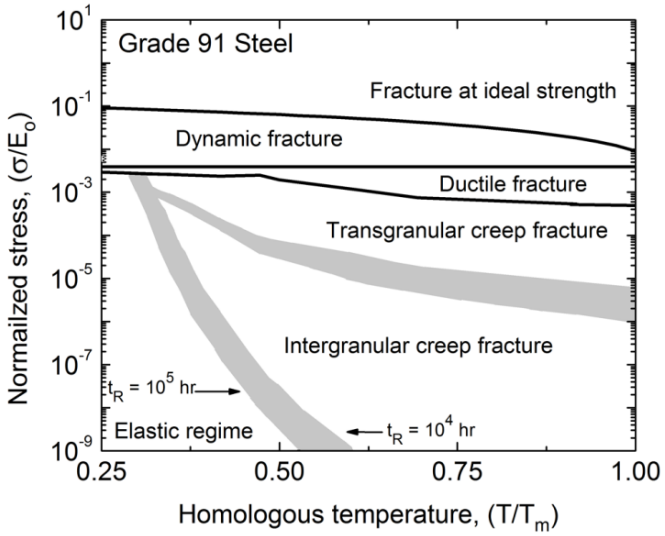

Fig. 3.11. Fracture mechanism map of Grade 91 steel

Table 3.4. Material parameters used in this study.

Parameter	Value	Reference
T_m (K)	1800	[47]
b (nm)	0.248	[47]
Ω (m^3)	1.38×10^{-29}	[47]
E_o (GPa)	223	
$\frac{T_m d\mu}{\mu_o dT}$	-1.09	[49]
Q_{gb} (kJ/mol)	150	[47]
A	7.3×10^5	
B	0.05	
a (μm)	1	[47]
δD_o^{gb}	1.0×10^{-13}	[47]
ν	0.3	

3.4. Conclusions

The creep deformation and fracture behavior of Grade 91 steel was studied in the temperature range of 600°C to 700°C and at stresses 35 MPa to 350 MPa. Creep deformation mechanisms in higher and lower stress regimes were identified as dislocation climb and Nabarro-Herring creep, respectively. The fractography of creep ruptured specimens revealed dominant dimpled fracture surfaces (transgranular fracture mode), but some wedge type cavities were also observed. With the help of stress exponent and creep damage tolerance factor obtained, the dominant creep rupture mechanism was identified as microstructural degradation. The creep

rupture data were analyzed in terms of Monkman-Grant relation, modified Monkman-Grant relation and Larson-Miller parameter. Fracture mechanism map of Grade 91 steel was constructed based on the available data.

References

[1] I. Charit, K.L. Murty, JOM 62 (2010) 67-74.
[2] E. Barker, Mater. Sci. Eng. 84 (1986) 49-64.
[3] R. L. Klueh, Int. Mater. Rev. 50 (2005) 287-310.
[4] Y. Z. Shen, S. H. Kim, H. D. Cho, C. H. Han, and W. S. Ryu, J. Nucl. Mater. 400 (2010) 64-68.
[5] M. Tanelke, F. Abe, K. Sawada, Nature 424 (2003) 294-296.
[6] K. Laha, K. S. Chandravathi, P. Parameswaran, K. Bhanu Sankara Rao, and S. L. Mannan, Metall. Mater. Trans. A 38 (2007) 58-68.
[7] S. Sathyanarayanan, A. Moitra, K. G. Samuel, G. Sasikala, S. K. Ray, and V. Singh: Mater. Sci. Engr. A 488 (2008) 519-528.
[8] K. L. Murty, I. Charit, J. Nucl. Mater. 383 (2008) 189-195
[9] T. Shrestha, M. Basirat, I. Charit, G. P. Potirniche, K. K. Rink, J. Nucl. Mater. 423 (2012) 110-119.
[10] L. Kloc, V. Sklenicka, Mater. Sci. Eng. A 234-236 (1997) 962-965.
[11] P. J. Ennis, A. Zielinska-Lipiec, O. Wachter, and A. Czyrska-Filemonowicz, Acta Mater. 45 (1997) 4901-4907.
[12] B. K. Choudhary, E. I. Samuel, J. Nucl. Mater. 412 (2011) 82-89.
[13] S. Spigarelli, E. Cerri, P. Bianchi, E. Evangelista, Mater. Sci. Tech. 15 (1999) 1433-1440.
[14] B. Ule, A. Nagode, Mater. Sci. Tech. 23 (2007) 1367-1374.
[15] M. Yurechko, C. Schroer, O. Wedemeyer, A. Skrypnik, J. Konys, J. Nucl. Mater. 419 (2011) 320-328.
[16] P. Anderson, T. Bellgard, F. L. Jones, Mater. Sci. Tech. 19 (2003) 207-213.
[17] C. G. Panait, A. Zielinska-Lipiec, T. Koziel, A. Czyrska-Filemonowicz, A-F. Gourgues-Lorenzon, W. Bendick, Mater. Sci Eng A 527 (2010) 4062-4069.
[18] G.E. Dieter, Mechanical Metallurgy, 3rd ed., McGraw-Hill, Boston, MA, 1986.
[19] J. E. Bird, A. K. Mukherjee, J. E. Dorn, in: D. G. Brandon and A. Rosen (Eds.), Quantitative relation between properties and microstructure, Israel Universities Press, Jerusalem, Israel, 1969, pp. 255-342.
[20] E. Cerri, E. Evangelista, S. Spigarelli, P. Bianchi, Mater. Sci. Eng. A 245 (1998) 285-292.
[21] K. Sawada, H. Kushima, M. Tabuchi, K. Kimura, Mater. Sci. Eng. A 528 (2011) 5511-5518.
[22] V. Sklenicka, K. Kucharova, M. Svoboda, L. Kloc, J. Bursik, A. Kroupa: Mater. Charact. 51 (2003) 35-48.
[23] J. Hald, Int. J. Pressure Vessels Piping 85 (2008) 30-37.
[24] Y. Qin, G. Gotz, W. Blum, Mater. Sci. Engr. A 341 (2003) 211-215.
[25] P. J. Ennis, A. Zielinska-Lipiec, A. Czyrska-Filemonowicz, in: Microstructural stability of creep resistant alloys for high temperature plant applications. (Eds.) A. Strang, J. Cawley, Greenwood GW, London: Institute of Materials;1998, p.135.
[26] H. Riedel, Fracture at High Temperatures, Springer-Verlag Berlin, Heidelberg, Germany, 1987, pp. 215-24.
[27] A. C. F. Cocks, M. F. Ashby, Prog. Mater. Sci. 27 (1982) 189-244.

[28] C. A. Hippsley, Acta Metall. 35 (1987) 2399-2416.
[29] B. K. Choudhary, K. B. S. Rao, S. L. Mannan, B. P. Kashyap: J. Nucl. Mater. 273 (1999) 315-325.
[30] F. C. Monkman, N. J. Grant Proc. ASTM 56 (1956) 593-620.
[31] F. R. N. Nabarro, H. L. de Villiers, The Physics of Creep, Taylor & Francis, London, 1995, pp. 22-25.
[32] V. S. Srinivasan, B. K. Choudhary, M. D. Mathew, T. Jayakumar, Mater. High Temp. 29 (2012) 41-48.
[33] H. E. Evans: Mechanics of Creep Fracture, Elsevier Applied Science Publishers, New York, NY, 1984, pp. 18-22.
[34] F. Dobes, K. Milicka, Metal Sci. 10 (1976) 382-384.
[35] F. A. Leckie, D. R. Hayhurst, Acta Metall. 25 (1977) 1059-1070.
[36] M. F. Ashby, B. F. Dyson: in Advances in Fracture Research, Eds. S. R. Valluri et al. Vol. 1, Pergamon Press, Oxford, 1984, pp. 3-30.
[37] B. K. Choudhary, C. Phaniraj, B. Raj, Trans. Indian Inst. Met. 63 (2010) 675-680.
[38] B. Wilshire, H. Burt, Z. Metallkd. 96 (2005) 552-557.
[39] National Research Institute for Metals Creep Data Sheet, No. 43, Tokyo, 1996.
[40] M. Basirat, T. Shrestha, G. P. Potirniche, I. Charit, K. K. Rink, Int. J. Plast. 37 (2012) 95-107.
[41] B. Wilshire, P. J. Scharning, Int. Mater. Rev. 53 (2008) 91-104.
[42] F. Vivier, J. Besson, A. F. Gourgues, Y. Lejeail, Y. de Carlan, and S. Dubiez, in: Creep behavior and life prediction of ASME Gr. 91 steel welded joints for nuclear power plants, eds. Le Goff et al., Mines-Paris Tech, France, 2008, pp. 1-2.
[43] E. M. Haney, F. Dalle, M. Sauzay, L. Vincent, I. Tournie, L. Allais, B. Fournier, Mater. Sci. Eng. A 510-511 (2009) 99-103.
[44] K. Kimura, H. Kushima, K. Sawada, Mater. Sci. Eng. A 510-511 (2009) 58-63.
[45] C. Gandhi, M. F. Ashby, Acta Metall. 27 (1979) 1565-1602.
[46] M. Li, S. J. Zinkle, J. Nucl. Mater. 361 (2007) 192-205.
[47] D. Hull, D. E. Rimmer, Philos. Mag. 4 (1959) 673-687.
[48] H. J. Frost, M. F. Ashby, Deformation Mechanism Maps, Pergamon Press, New York, NY, pp. 61-70.

4. Effect of heat treatment on modified 9Cr-1Mo steel mechanical properties

4.1. Introduction

The modified 9Cr-1Mo steel (Grade 91) is a material of choice in fossil-fuel-fired power plants with increased efficiency, service life, and reduction in emission of CO_2, NO_x, and SO_2. It is also considered as a prospective material for the Next Generation Nuclear Power Plant for application in reactor pressure vessels at temperatures up to 650°C. In this work, heat treatment of the modified 9Cr-1Mo steel was studied by normalizing and tempering the steel at various temperatures and times, with the ultimate goal of improving its creep resistance and optimizing material hardness. The microstructural evolution of the heat treated steels was correlated with the differential scanning calorimetric results. Optical microscopy, scanning and transmission electron microscopy in conjunction with microhardness profiles and calorimetric plots were used to understand the evolution of microstructure including precipitate structures in modified 9Cr-1Mo steel and relate it to the mechanical behavior of the steel. Thermo-Calc^{TM} calculations were used to support experimental work and provide guidance in terms of the precipitate stability and microstructural evolution. Furthermore, the carbon isopleth and temperature dependencies of the volume fraction of different precipitates were constructed. The predicted and experimentally observed results were found to be in good agreement.

The Next Generation Nuclear Plant (NGNP) is expected to address the growing energy demand by producing electricity and at the same time mitigate greenhouse gas emissions by co-producing hydrogen from the process heat. The Very High Temperature Reactor (VHTR) is a Gen-IV reactor system at the heart of the NGNP. VHTRs are designed to operate at temperatures much higher than those of currently operating reactors. Moreover, they are designed for longer service periods (60 years or more) compared to the current operating reactors [1]. The operating temperature of the reactor pressure vessel (RPV) in VHTR can vary between 300^{o}C and 650^{o}C. Furthermore, the RPVs will be more than double the size of a typical RPV as found in a Light Water Reactor (LWR) [2].

The modified 9Cr-1Mo steel (Grade 91) is a material of choice in fossil-fuel-fired power plants with increased efficiency, service life, and reduction in emission of CO_2, NO_x, and SO_2. The efficiency of fossil-fired power strongly depends on the temperature and pressure of steam. One percent increase in net efficiency reduced the emission of CO_2, NO_x, SO_2, and particulates by 2.4 metric ton, 2000 ton, 2000 ton, and 500 ton, respectively, furthermore reduces fuel cost by 2.4% [3]. Temperature of steam in coal-fired power plant is expected to be in the range of 550^{o}C – 720^{o}C and pressure above 24 MPa [3-5].

Grade 91 steels are a ferritic-martensitic (F-M) class of steel with superior creep properties [6,7]. The addition of strong carbide and carbonitride formers like vanadium (V), niobium (Nb), and titanium (Ti) lead to the precipitation of various particles, such as $M_{23}C_6$, and MX type precipitates – (Ti,Nb)(N,C), (Nb,V)(C,N), and (V,Nb)(N,C). The smaller interparticle spacing and increased volume fraction of the fine MX carbides enhance the alloy strength. These precipitates obstruct the movement of dislocations, refine grains during normalizing, and delay plastic deformation [6,8]. However, precipitates like Z-phase and Laves phase may lead to a decrease in the strength of the alloy by weakening the solid solution.

Evolution of various precipitates and microstructure can be understood from the heat treatment, differential scanning calorimetric (DSC) studies, and thermodynamic calculations

using Thermo-Calc. The heat treatment study of Grade 91 steel helps in understanding its microstructural evolution and mechanical properties; as this material whether being used for a reactor pressure vessel or boiler component goes through a series of heating, cooling, and welding processes. With the change in normalizing and tempering temperatures, different types of carbides such as $M_{23}C_6$, Z-phase, Ti/Nb/V rich MX type carbide/carbonitride precipitate and coarsen in Grade 91 steel resulting in change in the creep strength, ductility, hardness, and microstructure. Ahn et al. [9] observed a decrease in the high temperature strength of a Nb containing steel due to coarsening of Nb-rich precipitates. DSC was used to measure the heat absorbed or liberated during heating or cooling associated with carbide precipitation and other phase changes. Ganesh et al. [10] were able to find the phase transformation temperatures including temperature ranges for dissolution of various precipitates in different low carbon steels.

The present article aims to elucidate the effects of various heat treatment conditions (normalizing and tempering) on Grade 91 steel. There are numerous studies on the normalizing/tempering of Grade 91 steel [11-15], but these studies are limited to few temperatures and times. Thus, this research has taken about 50 normalizing and tempering conditions to study the relevant microstructural evolution. To that end, a combination of optical microscopy, scanning electron microscopy (SEM), transmission electron microscopy (TEM)-(EDS), and microhardness measurements were performed. Findings were discussed with the help of DSC study and finally Thermo-Calc was used to understand the microstructural evolution and precipitate stability.

4.2. Experimental Details

4.2.1. Material

The chemical composition of ASTM A387 Grade 91 CL2 steel used in this study is shown in Table 4.1. The hot rolled Grade 91 plates were obtained from ArcelorMittal Plate LLC, in a normalized and tempered condition (i.e., austenitized at 1040^{o}C for 240 minutes followed by air cooling, and tempered at 790^{o}C for 43 minutes). The as-received plates were 10.4 cm × 10.4 cm × 1.27 cm in size. Heat treatment specimens were cut out from these plates using a diamond wafering blade. At room temperature, the as-received Grade 91 steel had yield strength of 533 MPa, ultimate tensile strength of 683 MPa and elongation to fracture of 19%.

4.2.2. Heat treatment

Heat treatment was performed using an electric resistance furnace, capable of reaching a temperature exceeding 1200°C. Normalizing was first done on each sample within a temperature range of 1020-1100°C for 2, 4, and 8 h. Normalizing temperature and time were so chosen that austenitization had been complete before tempering was carried out. Normalized samples were cooled down to room temperature before tempered at various temperature and times. Samples that have been normalized at 1040°C for 2, 4 and 8 h were tempered at 690, 725, 745 and 790°C for 2, 8 and 20 h. Tempering of samples normalized at 1040^{o}C for 2 h was expanded to include

temperatures in the range of 635ºC to 850ºC. This created a matrix of close to 50 possible combinations of normalizing and tempering scenarios, which provided an adequate sequence to reveal the microstructural changes during heat treatment.

Table 4.1. Chemical composition (in wt.%) of Grade 91 steel

Element	Nominal	Measured
Cr	8.00 - 9.50	8.55
Mo	0.85 - 1.05	0.88
V	0.18 - 0.25	0.21
Nb	0.06 - 0.10	0.08
C	0.08 - 0.12	0.10
Mn	0.30 - 0.60	0.51
Cu	0.4 (max.)	0.18
Si	0.20 - 0.50	0.32
N	0.03 - 0.07	0.035
Ni	0.40 (max.)	0.15
P	0.02 (max.)	0.012
S	0.01 (max.)	0.005
Ti	0.01 (max.)	0.002
Al	0.02 (max.)	0.007
Zr	0.01 (max.)	0.001
Fe	Balance	Balance

4.2.3. Microstructural characterization

Optical microscopy was performed on both the as-received and heat treated specimens for characterization of the grain structure. Optical micrographs were taken for each sample and provided visual representation of the changing phases and microstructural features. TEM studies were done on selected samples. Conventional metallographic procedures of cold mounting, grinding and polishing were followed to prepare the specimen surface to 0.5 μm finish before etching was carried out using Marble's reagent; a solution made of 50 ml distilled water, 50 ml hydrochloric acid and 10 g of copper sulfate. Subsequently, an Olympus light microscope was used to examine the metallographic specimens and an attached CCD camera was used to record the images.

For TEM study, the sectioned samples were mechanically polished down to ~120 μm thickness, and then 3 mm diameter disks were punched out of the samples. Those disks were then jet polished in Fischione twin-jet polisher using a solution of 80 volume% methanol and 20 volume% nitric acid solution at a temperature of about -40ºC. Dry ice bath was used to achieve low temperature. Philips CM200 and JEOL JEM-2010 TEM operated at an accelerating voltage of 200 kV were used to study in detail the grain and precipitate morphology of the material under both as-received and heat treated conditions. The EDS system available in the same TEMs was used to estimate the chemical composition of precipitates. Hardness was measured using a Vickers microhardness tester; the applied load was 500 g-f and the hold time was 15 s.

4.2.4. Thermodynamic modeling

The calculations of thermodynamic equilibrium in Grade 91 steel and construction of C-isopleths were done with the help of Thermo-Calc AB software (Thermo-Calc Classic Version S). Thermo-Calc TCFE6 database for iron-based alloys was used to conduct all the equilibrium calculations. Due to the significant complexity of the Grade 91 steel (iron plus 13 alloying elements), impurities such as S or P were excluded from the thermodynamic calculations.

4.2.5. Differential scanning calorimetry

Differential scanning calorimetric study of Grade 91 steel was done using a Netzsch STA 409 PC calorimeter. The DSC chamber was evacuated and purged several times with the argon gas of high purity (99.999%), and the flow rate of argon was maintained at 85 cm^3/min. The sample mass ranging between 50 and 60 mg was found suitable for an acceptable signal to noise ratio. The sensitivity curves for scan rate of 20 ^oC/min were calibrated using the melting point of pure indium, tin, zinc, aluminum and gold under research grade argon atmosphere. Baseline calibrations were performed by using a pair of empty crucibles corresponding to the heating rate of 20^oC/min. Non-isothermal DSC measurements were done by heating the sample from 25 to 1400^oC and then cooling at the same rate down to 200^oC.

4.3. Results

4.3.1 Microstructural characteristics

The as-received Grade 91 steel had a tempered martensitic microstructure with a lot of precipitates, as shown in Fig. 4.1(a) and (b). Precipitation hardening is one of the main strengthening mechanisms in highly alloyed steels like Grade 91. Alloying elements, such as C, N, Ti, Nb, V, Cr and Mo, promote the formation of precipitates like Cr-rich $M_{23}C_6$, and Ti or Nb or V-rich MX particles, where M stands for metals, i.e. Cr, Mo, Ti, Nb or V. The Cr-rich $M_{23}C_6$ precipitates were elongated rod-like or block-like particles, while Ti-rich, Nb-rich and V-rich MX precipitates had nearly spherical shape. The Cr-rich $M_{23}C_6$ type precipitates were mainly observed at the lath boundaries and prior austenite grain boundaries (PAGB). The dimension of the elongated rod-like and block-like Cr-rich precipitates was measured, and found to have an average length of 285±80 nm and width of 121±39 nm, which are similar to the ones reported by Shen et al. [16] in 11Cr F-M steel and Anderson et al. [17] in Grade 91 steel. The average diameter of near-spherical MX-type precipitates was 37±15 nm, similar to values reported in literature [3,16]. These types of precipitates were mainly located in the matrix and martensitic lath structure. These thermally stable fine precipitates enhance the long term creep resistance by impeding movement of mobile dislocations, prior austenite grain boundaries, martensite lath and subgrain boundaries, and restrict fine grain structure from recrystallization. For a constant normalizing time of 2 h, prior austenite grain size and martensite lath size increased with increasing normalizing temperatures of 1020^oC – 1100^oC, as shown in Fig. 4.2 (a)-(d). The as-normalized (1040^oC for 2 h) microstructure had hard martensitic lath structures with high

dislocation density, as observed in Figs. 4.2(c) and (d). Similarly for constant normalizing temperature of 1040^{o}C, martensite lath size and prior austenite grain size increased with increasing normalizing time of 2, 4 and 8 h. Fig. 4.2 (e) and (f) shows the optical and TEM micrograph of sample normalized at 1040^{o}C for 8 h, respectively.

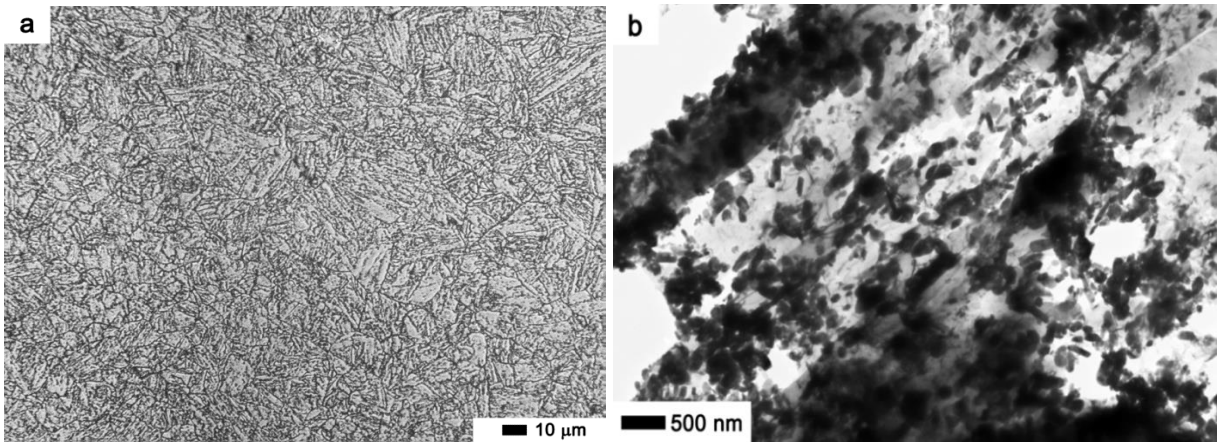

Fig. 4.1. As-received microstructure (a) optical and (b) TEM micrograph

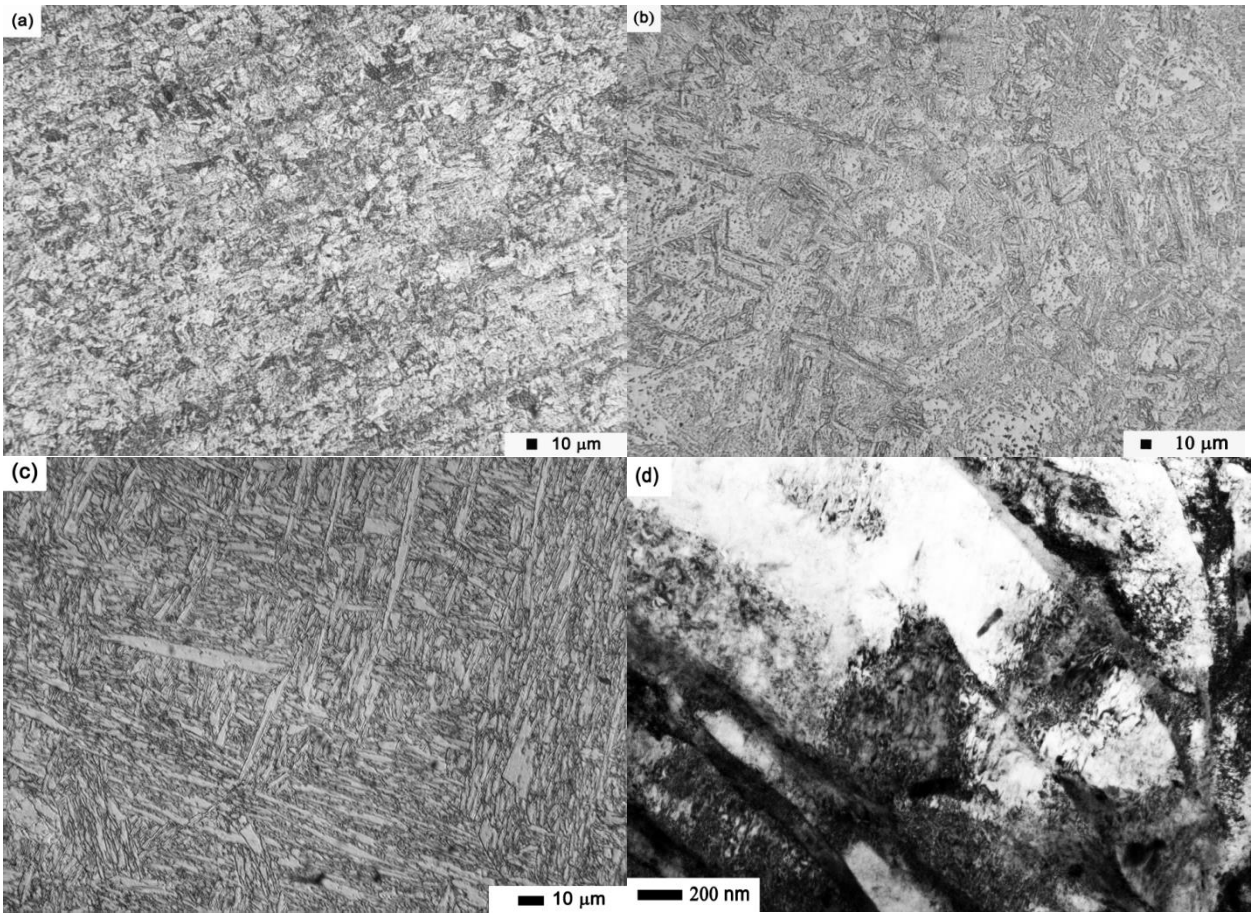

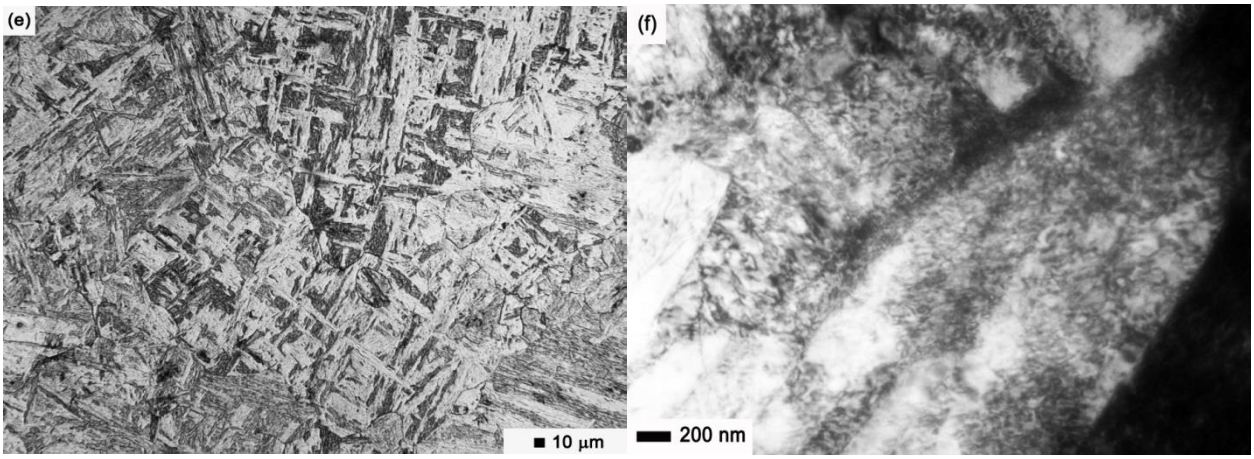

Fig. 4.2. As-normalized. Optical micrograph (a) normalized at 1020°C for 2 h (b) normalized at 1100°C for 2 h, (c) normalized at 1040°C for 2 h (d) TEM micrograph of sample normalized at 1040°C for 2 h, (e) optical micrograph of sample normalized at 1040°C for 8 h, and (f) TEM micrograph of a sample normalized at 1040°C for 8 h.

The tempered microstructure of Grade 91 steel is shown in Fig. 4.3. Fig. 4.3(a) shows fine microstructure of sample normalized at 1040°C for 2 h and tempered for 690°C. Fig. 4.3(b) shows coarse martensitic microstructure of sample normalized at 1040°C for 2 h tempered at 745°C for 8 h. Fig. 4.3 (c) and (d) show the martensitic lath structure of sample normalized at 1040°C for 2 h and tempered at 790°C for 2 h. Grain size increased with increasing normalizing time, and tempering time. The sample normalized at 1040°C for 2 h and tempered at 790°C for 2 h has grain size of ~11 μm, while the sample normalized at 1040°C for 8 h and tempered at 790°C for 20 h resulted in a grain size of ~17 μm. Fig. 4.3 (e) shows tempered martensitic structure of sample normalized at 1040°C for 4 h and tempered at 725°C for 2 h. The sample normalized at 1040°C for 8 h and tempered at 790°C for 20 h had a coarse grain structure, as shown in Fig. 4.3 (f).

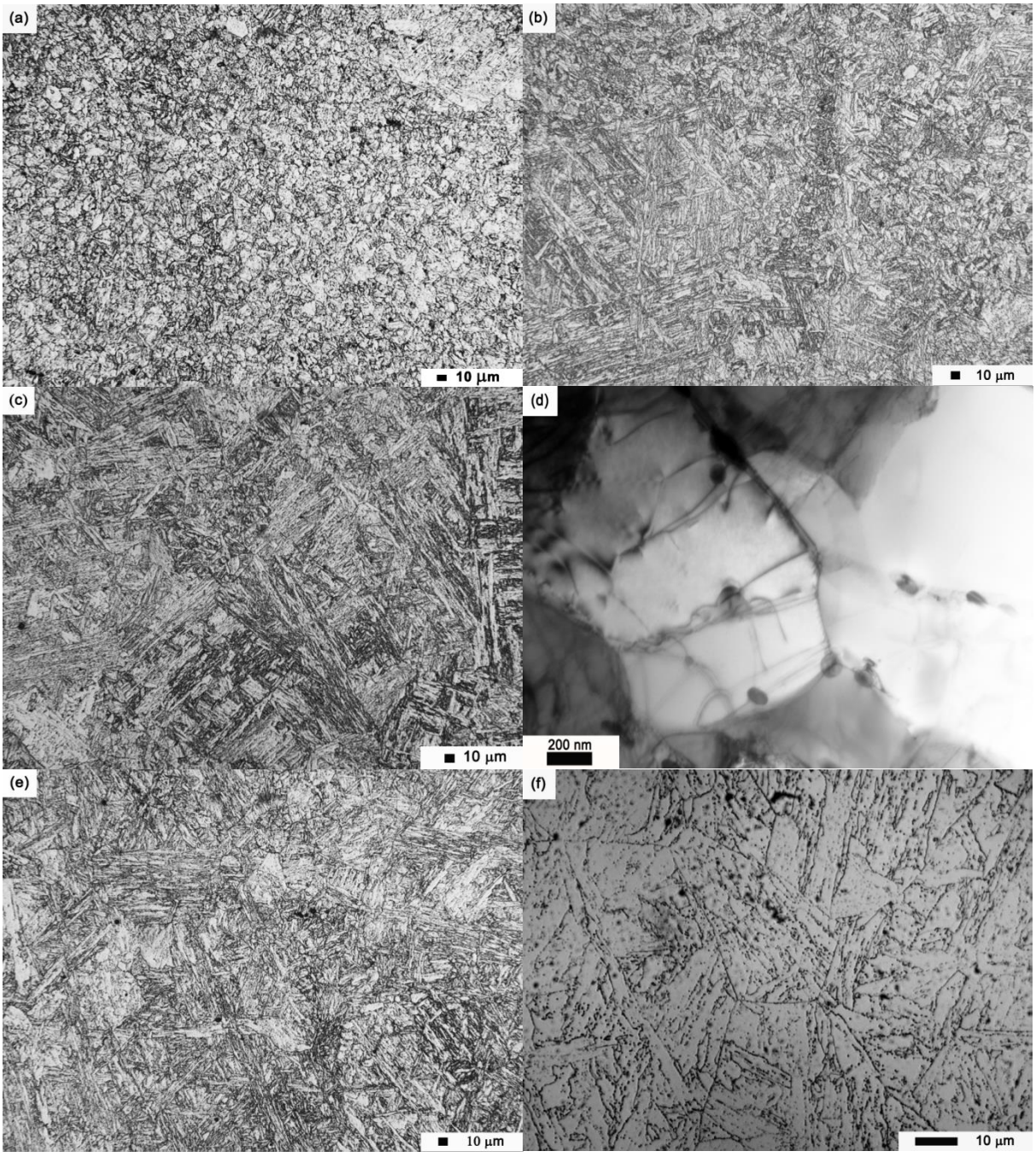

Fig. 4.3. Optical micrographs of tempered microstructures: (a) normalized at 1040°C for 2 h and tempered at 690°C for 2 h, (b) normalized at 1040°C for 2 h and tempered at 745°C for 8 h, (c) normalized at 1040°C for 2 h and tempered at 790°C for 2 h, (d) TEM micrograph of sample normalized at 1040°C for 2 h and tempered at 790°C for 2 h; optical micrographs (e) normalized at 1040°C for 4 h and tempered at 725°C for 2 h, and (f) normalized at 1040°C for 8 h and tempered at 790°C for 20 h.

4.3.2. Hardness of heat treated steel

Normalizing treatment is intended for austenitization and homogenization of the solid solution. However, the right combination of normalizing temperature and time has to be found to optimize the material mechanical properties. Hardness measurements were performed on the alloy samples normalized at 1020^{o}C, 1040^{o}C, 1050^{o}C, 1060^{o}C, 1080^{o}C and 1100^{o}C while keeping the time constant at 2 h. The hardness decreased with increasing normalizing temperature, as shown in Fig. 4.4(a). The hardness value was about the same for normalizing carried out at 1020^{o}C and 1040^{o}C, but after that the hardness gradually decreased till 1100^{o}C. The effect of change in normalizing time was studied by heat treating Grade 91 steel at 1040^{o}C for 2 h, 4 h and 8 h. The hardness of the alloy decreased with increasing normalizing time, as shown in Fig. 4.4(b). Alloy normalized at 1040^{o}C for 2 h was tempered at 690^{o}C, 725^{o}C, 745^{o}C and 790^{o}C for 2 h , 8 h and 20 h. Hardness of the alloy decreased with increasing tempering temperature and time, as shown in Fig. 4.4(c). Alloy tempered at 690^{o}C and 725^{o}C showed significant drop in hardness with increasing tempering time, but for 745^{o}C and 790^{o}C the decrease in hardness was gradual. Similar, profiles were observed for samples normalized at 1040^{o}C for 4 h then tempered, and samples normalized at 1040^{o}C for 8 h then tempered at aforementioned temperatures, as shown in Fig. 4.4 (d) and (e), respectively. Fig. 4.4 (g) shows the hardness of all tempered samples. Among all samples normalized at 1040^{o}C and tempered, samples normalized for 2 h and tempered at 690^{o}C for 2 h had the highest hardness, while sample normalized for 8 h and tempered at 790^{o}C for 20 h had the lowest hardness. The tempering temperature of sample normalized at 1040^{o}C for 2 h was expanded to temperatures slightly above A_{C1} temperatures. Hardness of the alloy normalized at 1040^{o}C for 2 h and tempered for 2 h decreased with increasing tempering temperature up to 745^{o}C, stabilized till 820^{o}C, then increased, as shown in Fig. 4.4 (f). Tempering above A_{C1} temperature was done to study the role of re-precipitation in Grade 91 steel.

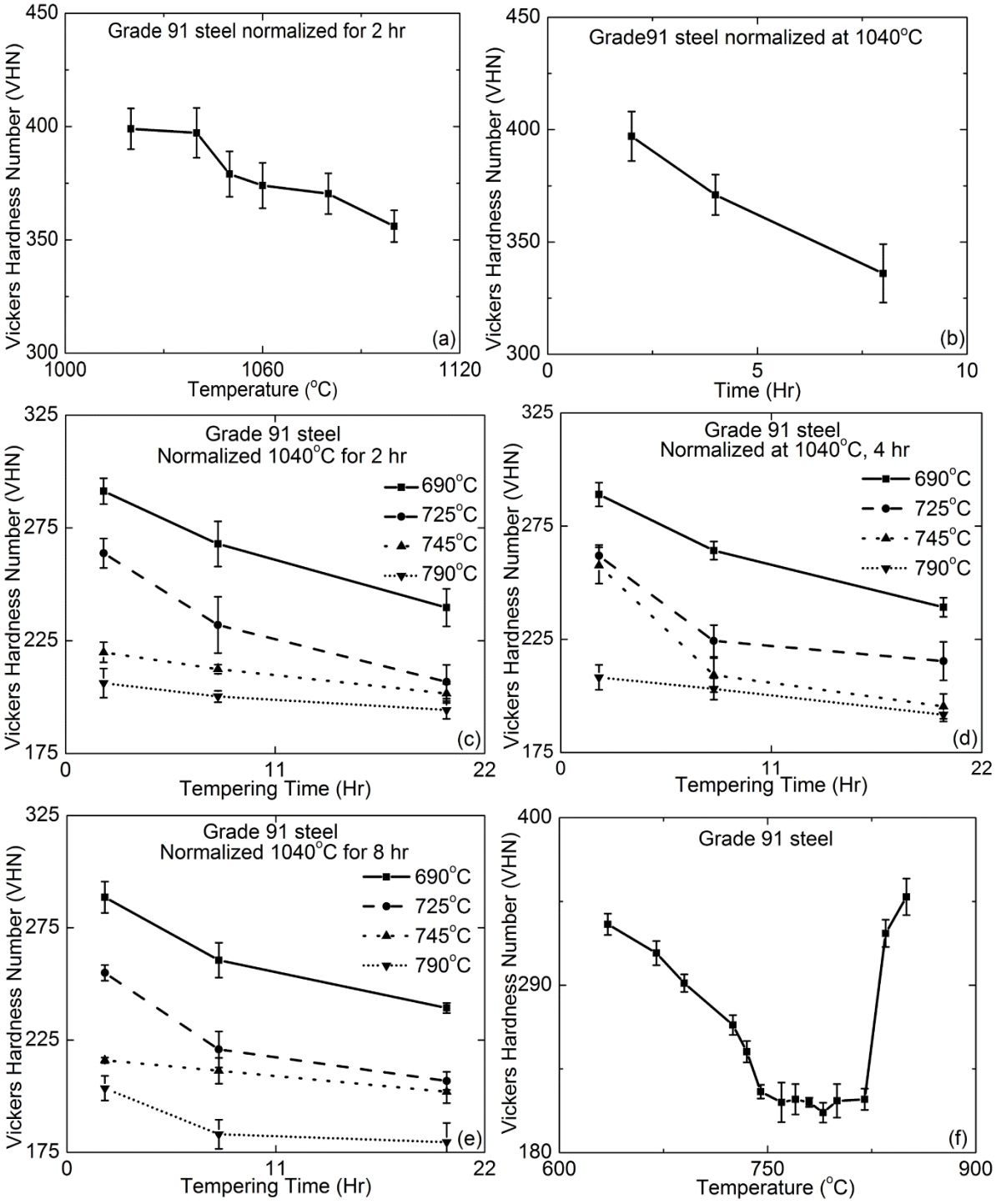
Grade 91 steel normalized for 2 hr
Vickers Hardness Number (VHN)
Temperature (°C)
(a)
Grade91 steel normalized at 1040°C
Time (Hr)
(b)
Grade 91 steel
Normalized 1040°C for 2 hr
690°C
725°C
745°C
790°C
Tempering Time (Hr)
(c)
Grade 91 steel
Normalized at 1040°C, 4 hr
(d)
Grade 91 steel
Normalized 1040°C for 8 hr
(e)
Grade 91 steel
(f)

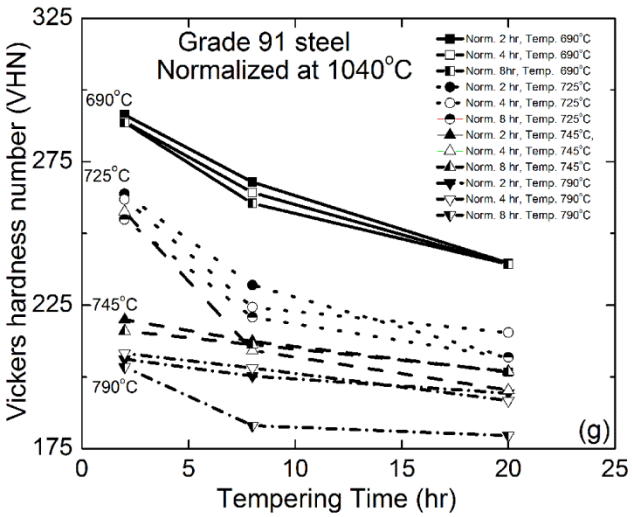

Fig. 4.4. Variation in Vickers microhardness for various heat treatment condition (a) variation in normalizing temperature (b) samples normalized at 1040°C for various times, (c) variation with tempering temperature and time for sample normalized at 1040°C for 2 h, (d) variation with tempering temperature and time for sample normalized at 1040°C for 4 h, (e) variation with tempering temperature and time for sample normalized at 1040°C for 8 h, (f) sample normalized at 1040°C for 2 h and tempered at various temperatures for 2 h, and (g) normalized at 1040°C and tempered samples.

4.3.3. Differential scanning calorimetry

Phase transformations of as-received (normalized and tempered) Grade 91 steel were studied using DSC. The phase transformations and reactions associated with heating and cooling of the alloy, as shown in Fig. 4.5, are listed in Table 4.2. The transformation of martensite to ferrite started at 550°C, and the change in magnetism of the alloy, the Curie temperature (T_c) was observed at 741°C. The austenite phase started to form at 820°C (Ac_1), peaked at 848°C (Ac_p), and the transformation was complete at 870°C (Ac_3), which was confirmed by differential thermal analysis (DTA) and the results of our thermodynamic calculations. The dissolution of $M_{23}C_6$ precipitate was complete at 870°C. Dissolution of (V,Nb)(N,C) type precipitates bottomed at 998°C, but beyond that temperature they re-precipitated out. With the help of the first derivative of the heating curve, the onset of the second dissolution reaction of fine (V,Nb)(N,C) type precipitates was found to be at ~1140°C. From cooling curve and its first derivative, the martensite start temperature (M_s) was calculated as 380°C. Using A_{C1} as the onset temperature and A_{C3} as the end temperature, the DSC plot was used to calculate the enthalpy associated with the $\alpha\text{-}ferrite \rightarrow austenite$ phase transformation. The phase transformation enthalpy ($\Delta^o H^{\alpha \rightarrow \gamma}$) of 10 J/g was calculated.

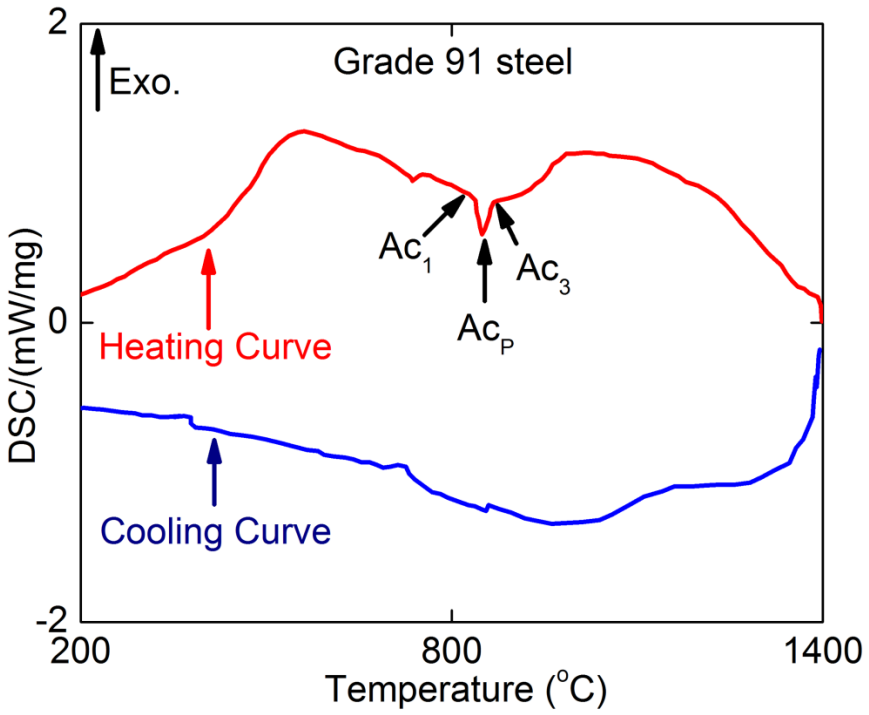

Fig. 4.5. Differential scanning calorimetric plot of as-received Grade 91 steel

Table 4.2. Various transformation temperatures of Grade 91 steel

Description of phase change	Transformation temperature (°C)
$\alpha' + M_{23}C_6 + (V,Nb)(N,C) + Z\text{-phase} \longrightarrow \alpha + M_{23}C_6 + (V,Nb)(N,C) + Z\text{-phase}$	550
T_c (Curie Temperature)	741
$\alpha + M_{23}C_6 + (V,Nb)(N,C) + Z\text{-phase} \longrightarrow \alpha + M_{23}C_6 + (V,Nb)(N,C) + (Nb,V)(C,N)$	770
$\alpha + M_{23}C_6 + (V,Nb)(N,C) + (Nb,V)(C,N) \longrightarrow \alpha + \Upsilon + (V,Nb)(N,C) + (Nb,V)(C,N) + M_{23}C_6$	820 (A_{c1})
$\alpha + \Upsilon + (V,Nb)(N,C) + (Nb,V)(C,N) + M_{23}C_6 \longrightarrow \Upsilon + (V,Nb)(N,C) + (Nb,V)(C,N)$	870 (A_{c3})
$\Upsilon + (V,Nb)(N,C) + (Nb,V)(C,N) \longrightarrow \Upsilon + (Ti,Nb)(N,C) + (Nb,V)(C,N)$	1045
$\Upsilon + (Ti,Nb)(N,C) + (Nb,V)(C,N) \longrightarrow \delta + \Upsilon + (Ti,Nb)(N,C)$	1270
$\delta + \Upsilon + (Ti,Nb)(N,C) \longrightarrow \Upsilon + \delta$	1397
M_s	380

4.3.4. Thermo-Calc calculations

The carbon isopleth for the Fe-Cr-Mn-Mo-Nb-Ni-Ti-V-N-C full system is shown in Fig. 4.6 (a). It is a property diagram, which represents the analog of the binary Fe-C phase diagram, but constructed for the full alloy system. It was calculated using the previously mentioned TCFE6 thermodynamic database. The bcc ferrite phase starts dissolving at ~810°C and exists up to ~855°C and then reappears above 1270°C, as noted in Table 2. In between 850°C and 1270°C, the fcc austenite phase becomes stable. Other phases that are featured in the diagram in Figs. 4.6 (a), (b), and (c), are the Z-phase; the $M_{23}C_6$-phase; (with metal M being mostly Cr); the Ti-rich

(Ti,Nb)(N,C) precipitates; the Nb-rich and the Nb-poor (Nb,V)(C,N) precipitates; and the V-rich (V,Nb)(N,C) precipitates. All of the four phases have variable compositions but the same fcc crystalline lattice. The following notation was adopted for the latter four phases: in those cases when there was more carbon than nitrogen on a particular sublattice, the (C,N) notation was used; in the opposite case – (N,C). Similarly, the first position on the metal sublattice is assigned to a chemical element the concentration of which is the highest, e.g. (Nb,V); in the opposite case the (V,Nb) notation was used.

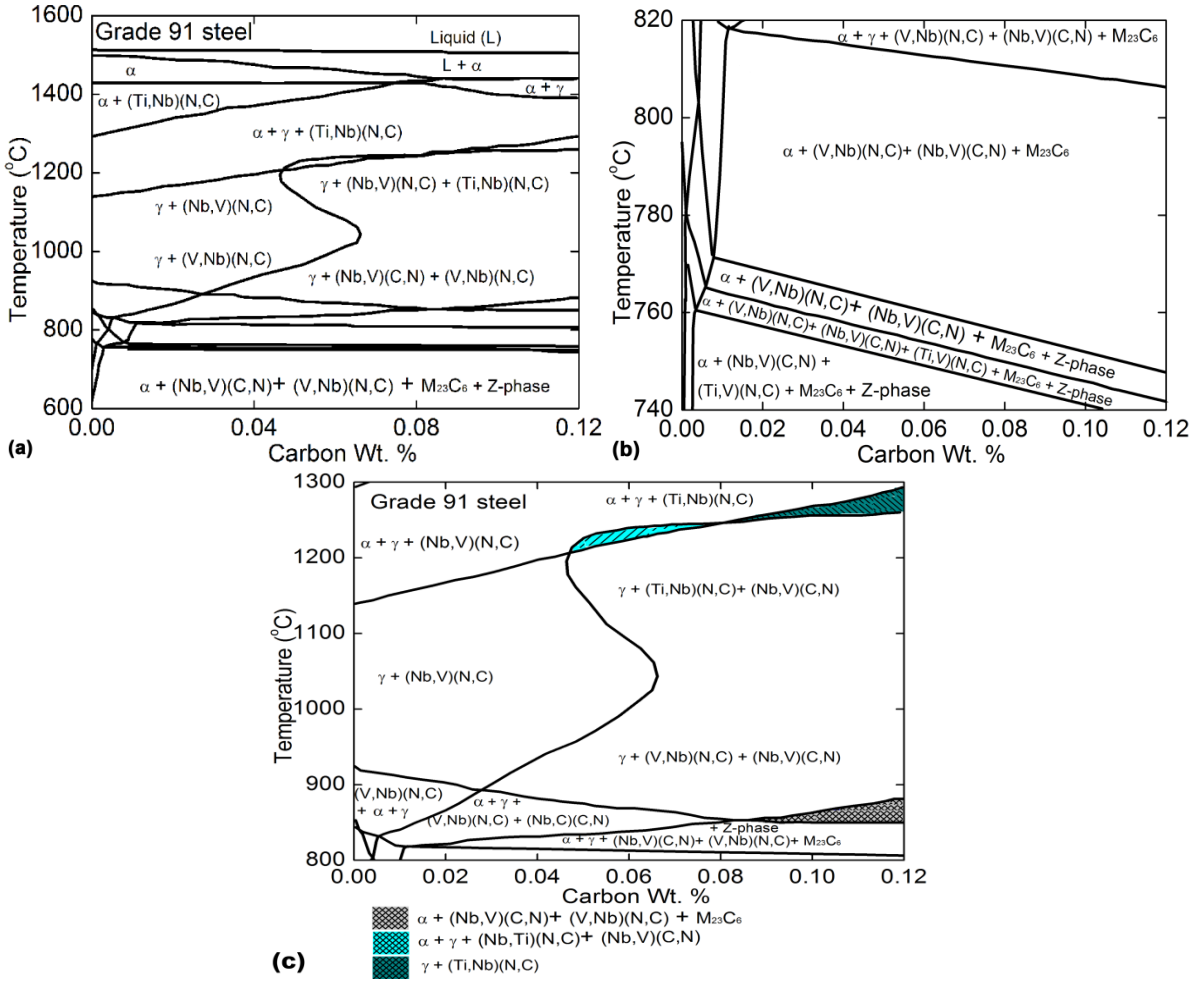

Fig. 4.6. Carbon isopleth for Grade 91 steel (a) complete diagram: 600°C – 1600°C, (b) 740°C – 820°C, (c) 800°C – 1300°C.

It was established that the Ti-bearing precipitates (Ti, Nb)(C, N) were more stable than the (Nb,V)(C,N), and (V,Nb)(N,C) precipitates in the higher temperature range. Fig. 4.7(a) shows a TEM micrograph of the as-normalized (normalized at 1040°C for 2 h) sample with Ti-rich MX precipitates. The EDS spectrum of the Ti-MX is shown in Fig. 4.7(b). This example clearly demonstrates the significance of simulations for the computational thermodynamics driven alloy design.

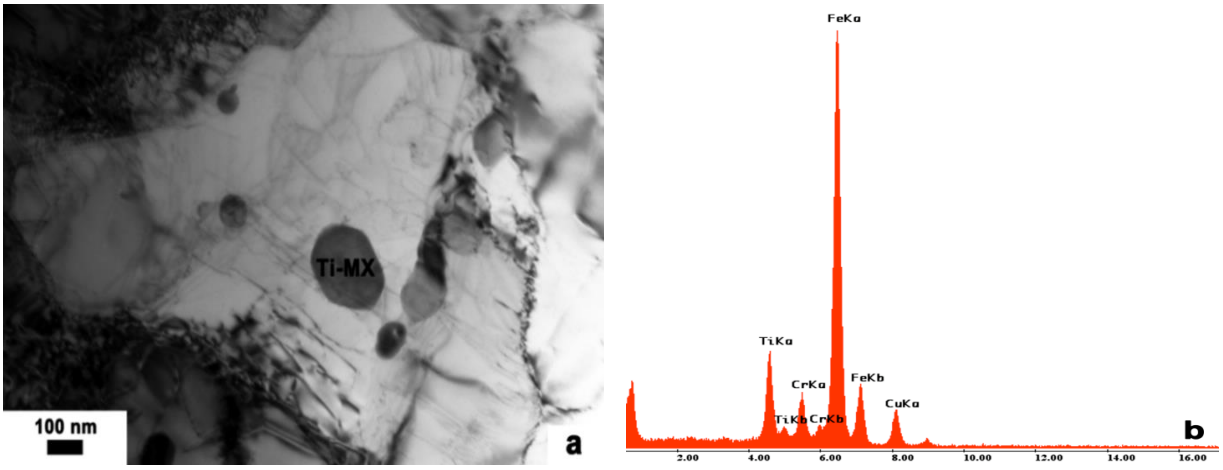

Fig. 4.7. (a) A TEM micrograph of as-normalized (at 1040ºC for 2 h) sample, and (b) EDS of a Ti-rich MX precipitate

The evolution of the ferrite phase and its volume fraction with respect to temperature is shown in Fig. 4.8(a), and the evolution of $M_{23}C_6$ precipitate is shown in Fig. 4.8(b). The volume fraction of Z-phase, (Nb,V)(N,C) + (Ti,Nb)(N,C), and (V,Nb)(N,C) precipitates are illustrated by Fig. 4.8(c). Thermo-Calc calculations predicted that the volume fraction of $M_{23}C_6$ precipitate was higher than that of V-rich and Nb-rich MX type precipitates, owing to the higher wt.% of Cr and Mo compared to Nb and V. Higher resolution plot of the evolution of (V,Nb)(N,C) precipitate is shown in the inset of Fig. 4.8(c). Special attention was paid to the possibility of a phase separation and/or atomic clustering. Indeed, phase separation reaction and the miscibility gap were observed for the Fe-Cr system, so this possibility could not be excluded for the Fe-9Cr-1Mo steel.

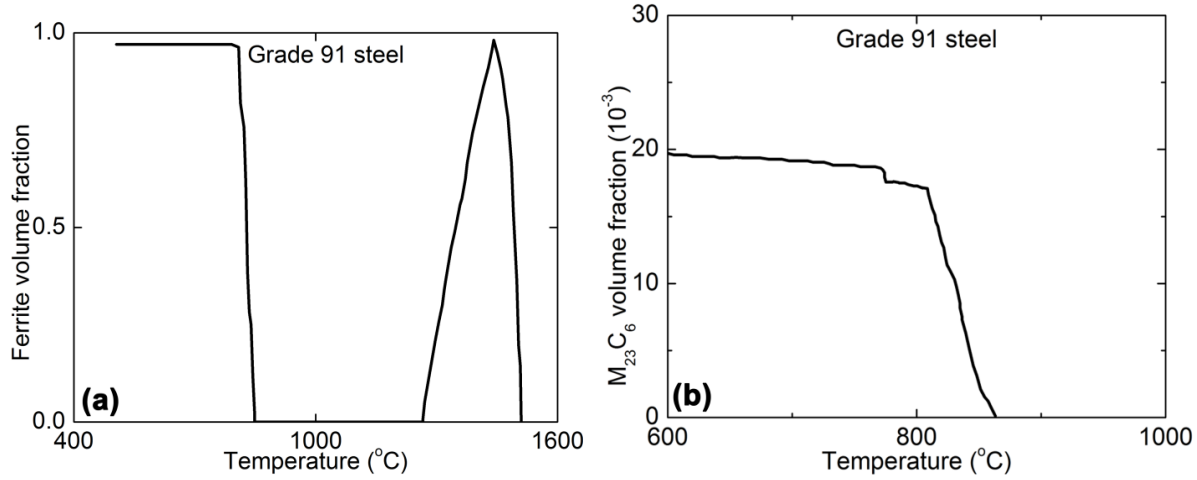

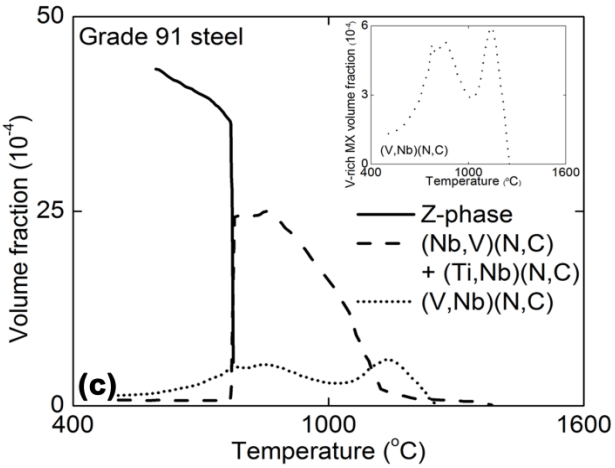

Fig. 4.8. Evolutions of (a) the ferrite phase, (b) $M_{23}C_6$ precipitate, (c) Z-phase, Nb-rich MX, V-rich MX, and Ti-rich MX precipitates as a function of temperature.

4.4. Discussion

4.4.1. As-normalized microstructure

Hardness of the Grade 91 steel normalized for 2 h at 1020, 1040, 1050, 1060, 1080 and 1100^{o}C decreased with increasing temperature. Similarly, hardness of the as-normalized sample at 1040^{o}C decreased with increasing normalizing time. As-normalized microstructure had hard martensitic lath structures with high dislocation density and M_6C type precipitates in it, as shown in Fig. 4.2(d). Yoshino et al. [11], and Das et al. [18] reported increase in the prior austenite grain size with increase in normalizing temperatures from 1050^{o}C to 1250^{o}C. But hardness remained constant for same temperature range. However, in the current study, for normalizing carried out for 2 h in the temperature range of 1020^{o}C to 1100^{o}C, hardness decreased with increasing normalizing temperature. The decrease in hardness value and increase in prior austenite grain size was due to decrease in the volume fraction of precipitates with increased normalizing temperature and time. Average diameter of MX precipitates increased from 35 nm after normalizing at 1050^{o}C to 315 nm after normalizing at 1200^{o}C [11], leading to a decrease in the number density of precipitates.

Given the higher carbon solubility in austenite than in alpha ferrite, carbide precipitates dissolve in austenite. With increased diffusion at higher temperature and long time, the precipitates coarsen while the lath size and grain size also increase. Grade 91 steel normalized at 1040^{o}C for 8 h had a martensitic lath width of 473±105 nm, and the size of the needle shaped $M_{23}C_6$ precipitates was 136±75 nm in length and 28±20 nm in width. While the sample normalized at 1040^{o}C for 2 h had a martensitic lath size of 335±115 nm, while the $M_{23}C_6$ precipitates were 78±15 nm in length and 13±4 nm in width. At higher normalizing temperature, considerable grain growth occurred, but at lower normalizing temperature the austenite grain structure was finer. Moreover, normalizing below 900^{o}C resulted in partially transformed ferrite with patches of martensitic structure [12]. However, the change in the normalizing temperature in the range of 1020°C to 1100°C can result in different precipitate size distribution(s) that could possibly affect the mechanical behavior of the alloys.

4.4.2. Tempered microstructure

The as-normalized hard martensitic lath structure with high dislocation density changed to stress-free, relaxed tempered martensitic structure upon tempering. Upon tempering, the normalized steel is reheated to a temperature just below Ac_1, which relieves stress in martensitic structure via carbon diffusion and carbide formation. With increased tempering time, the diffusion of carbon is increased and simultaneously got stress relieved. For example, a P92 steel normalized at 1050°C showed a decrease in hardness with increasing tempering temperature from 525 up to 720°C. Similarly, the tensile strength and yield strength decreased with increasing tempering temperature [13]. Moreover, for Grade 91 steel tempered at 765, 730, and 680°C, specimens tempered at lowest temperature had the highest creep strength at 600°C, as shown by Sawada et al. [14]. Tempering above Ac_1 temperature decreased the toughness of the material due to the formation of fresh martensites as found by Silwal et al. [19]. In the present work, the hardness decreased with increasing tempering temperature till Ac_1 temperature (820°C). The decrease in hardness, as seen in Fig. 4.4(g), is due to the coarsening of precipitates, dissolution of $M_{23}C_6$ carbides, and breakdown of martensitic lath structure.

Coarser precipitates are not effective in impeding the mobility of dislocations, and affect the strength of the steel [6]. Decrease in hardness with increased temperature can also in part be associated with the increased molybdenum in carbides. In Fe-Mo-C steels tempered at 700°C, Shtansky and Inden [20] observed 4% increase in the molybdenum content in $M_{23}C_6$ precipitates after increasing the tempering time from 25 h to 500 h. Increased molybdenum content in precipitates means leaching of Mo from the matrix, thus weakening the solid solution. Moreover, the $M_{23}C_6$ precipitates located on the prior austenite grain boundaries penetrate into the grains with increasing tempering time. Removal of these precipitates from the grain boundary could result in grain boundary sliding. The stability of hardness at temperatures around 800°C reflects the maximum precipitation rate for 0.1 wt.% C in the alloy. But after 820°C, the hardness increased because of secondary hardening resulting from increased volume fraction of (V,Nb)(N,C) and (Nb,V)(N,C) precipitates, as seen in Fig. 4.8(c) for respective precipitates. Tempered martensitic structure had precipitates, subgrain structures, but reduced dislocation density, as seen in Fig. 4.3(d). MX type precipitates were observed inside the subgrain structure and martensite lath structure. $M_{23}C_6$ precipitates were mainly located on the prior austenite grain boundaries and martensitic lath boundaries. The microstructure of Grade 91 steel tempered at the lowest temperature had much finer martensite lath size and higher dislocation density. The as-received material had grain size of ~11 μm, while that of the sample normalized at 1040°C for 8 h and tempered at 790°C for 20 h was 17 μm. The martensitic lath size increased and dislocation density decreased upon tempering. Dudko et al. [13] noted that when tempered at 720°C for 3 h, the lath size increased to 300 nm from 250 nm, and the dislocation density decreased to 6.2×10^{14} m^{-2} from 7.0×10^{14} m^{-2} compared to as-normalized microstructure. In 9-12% Cr heat resistant steels, the dislocation density, hardness, and creep rupture life generally get decreased, but ductility and subgrain size increases with increasing tempering temperature [3].

The transformation of martensite to alpha-ferrite, and stress relief is dependent on the tempering temperature and holding time. The tempering temperature and holding time of tempering can be described by a single empirical parameter known as the Holloman-Jaffe parameter (P)

$$P = T(C + logt) \quad (1)$$

where T (K) is temperature, C (40) constant, and t (s) time. Generally in the Holloman-Jaffe parameter 20 is used as the constant (C), but in this study C (40) gave the best fit. Fig. 4.9 shows the Holloman-Jaffe parameter for Grade 91 steel normalized at 1040°C/ 2 h, and tempered in the temperature range of 635°C-820°C for 2, 8 and 20 h. The polynomial fit shown in Fig. 4.9 can be used to describe the hardness of the tempered Grade 91 steel.

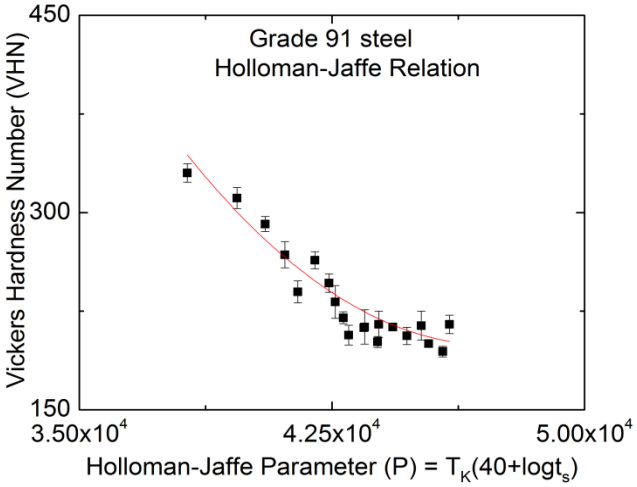

Fig. 4.9. Holloman-Jaffe relation of Grade 91 steel normalized at 1040°C for 2 h and tempered at various temperatures and times.

4.4.3. DSC study

DSC plot presented in this study tracked the phase changes and reactions happening during heating and cooling of Grade 91 steel. Various temperatures associated with phase changes and reactions are listed in Table 4.2. DSC plot can slightly change depending on the heat treatment history of the material. Masuyama [15] reported that for various tempering temperatures Ac_1 temperature was between 820–851°C and the martensite transformation was ~400°C. In this study, the Ac_1 temperature was 820°C and the M_s temperature was 380°C. DSC study of Grade 91 steel showed the change in the enthalpy associated with α-ferrite to austenite phase transformation is dependent on the starting microstructure produced by thermal aging [21]. A list of enthalpy change associated with α-ferrite to austenite phase transformation ($\Delta^o H^{\alpha \rightarrow \gamma}$) is included in Table 4.3. The $\Delta^o H^{\alpha \rightarrow \gamma}$ for pure iron was 16 Jg^{-1}, but decreased with increased addition of alloying elements. The volume fraction of (V,Nb)(C,N) precipitates peaked initially at 790°C and 850°C, then started to dissolve in the matrix with the dissolution bottoming out at ~1000°C and then peaked at ~1140°C; these temperature were captured with the help of the first derivative of the DSC heating curve. Furthermore, these temperatures were predicted by the Thermo-Calc calculations as shown in Fig. 4.8(c). The activation energy of Nb diffusion in the alpha-iron lattice is larger than those of Mo and Cr diffusion, and self-diffusion of iron [22]. Thus, the dissolution of Nb rich precipitates takes place at a higher temperature compared to the $M_{23}C_6$ precipitates. The MX type precipitates rich in V dissolve in the matrix before Nb, given the smaller atomic radius of V compared to Nb.

Table 4.3. Comparison of enthalpy associated with $\alpha \rightarrow \gamma$ phase change

Steel Composition (wt.%)	$\Delta^o H^{\alpha \rightarrow \gamma}$ (Jg^{-1})	Reference
Pure Iron	16	[21]
9Cr-1Mo	15	[10]
9Cr-1Mo-0.001V-0.1C	15	[21]
9Cr-1Mo-0.1C-0.42Si	13	[10]
9Cr-1W-0.23V-0.06Ta-0.1C	12	[23]
9Cr-1Mo-0.21V-0.08Nb-0.1C-.002Ti	10	Present study

4.4.4. Thermo-Calc calculations

In the present study, the normalizing temperatures (1020^{o}C, 1040^{o}C, 1050^{o}C, 1060^{o}C, 1080^{o}C, and 1100°C) and the temperature range of the subsequent tempering (690°C, 725°C, 745°C, and 790°C) were of most interest. Figs. 4.6 and 4.8 show the evolution of various phases as a function of temperature. These phase and precipitates play an important role in the formation of microstructure and strength of the heat treated alloy. The Thermo-Calc calculations predicted the existence of the Z-phase, but it was not observed in the TEM studies. During cooling, the austenite phase undergoes partial dissolution (the onset of transformation) at temperature ~850°C and disappears completely at ~810°C, in almost complete agreement with the findings of the DSC experiments (temperatures 870°C and 820°C, respectively). The Thermo-Calc does not make any distinction between α-ferrite and the δ-ferrite because they have the same bcc lattice. It would be appropriate to say that the α-ferrite dissolved at ~850^{o}C, but the δ-ferrite appeared at ~1270^{o}C peaked at ~1440^{o}C and then gradually dissolved as seen in Fig. 4.8(a).

The mass fraction of $M_{23}C_6$ precipitates remained constant up to the Ac_1 temperature but decreased drastically as austenite phase started forming. Given that austenite has higher affinity for C than α-ferrite, the $M_{23}C_6$ precipitates exist up to 865°C, and then dissolve into the austenitic matrix. The mass fraction of MX type precipitates was constant till Ac_3 temperature, but then gradually decreased with increased temperature and totally dissolved at ~1200^{o}C [24]. In the present study, the volume fraction of Nb-rich MX increased at ~770^{o}C, started to decrease rapidly after ~850^{o}C, then gradually at ~1120^{o}C till 1260^{o}C. Since there was no clear distinction between the evolution of (Ti,Nb)(N,C) precipitate and (Nb,V)(N,C) precipitate, one could speculate that 1120^{o}C marks the onset of the phase separation reaction. As indicated in Fig. 4.8(c), the line indicating both (Nb,V)(N,C) and (Ti,Nb)(N,C) precipitates has a tail to it. The tail indicates the presence of Ti-rich MX which is stable up to ~1400^{o}C, as shown in Fig. 4.6(a). At around 470°C, the dissolution of the M_6C precipitates was observed in the Thermo-Calc calculations, not the Laves phase (absent at any temperature for x(C)=0.001 wt.%). Laves phase was not observed in the as-received 9%Cr alloys containing 0.1% and 0.05% C with 0.03% Ti [3]. The Z-phase disappeared as the Nb-rich MX precipitates started to form. It remains to be established whether at such a low temperature there is enough time for the formation of such precipitates (M_6C). However, they were identified in the computed phase diagram quite reliably for different alloy compositions.

The temperature of 1045°C corresponded to the terminus of the carbon solubility in the V-MX + Nb-MX phase field, as shown in Fig. 4.6(a). At this temperature range, a phase transformation reaction accompanied by the formation of the three types of Nb-bearing FCC

precipitates: Nb-rich, V-rich and Ti-rich was obtained. Whether this could be considered as a transformation of the V-rich precipitates of the V-MX type (containing ~47 wt.% V and ~32% of Nb) into a new FCC phase in which the amounts of Nb and V are practically reversed, and the evolution of Ti-rich precipitate remains to be studied. Hong et al. [25] reported dendritic Nb-rich carbonitrides in high strength low alloy steel. On reheating the HSLA steel from 1050^{o}C to 1400^{o}C, the Nb content decreased with increasing temperature till 1250^{o}C. But eventually, Ti started to dissolve into the austenite phase after 1300^{o}C. Similar observation was made in Grade 91 steel where the (Ti,Nb)(N,C) precipitate was stable at higher temperature compared to (Nb,V)(C,N) and (V,Nb)(N,C) precipitates. The solubility of (V,Nb)(C,N) was higher than that of (Ti,Nb)(C,N) and (Nb,Ti)(C,N) in both ferrite and austenite phases [26].

5. Conclusions

The heat treatment study of Grade 91 steel was performed, and Thermo-Calc calculations were used to predict the stability of various phases and provide guidance for future research in this direction. The hardness of the alloy decreased with increasing normalizing and tempering temperatures and times. The decrease in hardness was attributed to increase in the grain size, martensite lath size, and decrease in dislocation density. Differential scanning calorimetry indicated the various phase changes and precipitate reactions taking place during heating and cooling of Grade 91 steel. The Thermo-Calc predicted the evolution of ferrite and austenite phases, and various precipitates. With the help of differential scanning calorimetry study and Thermo-Calc, various temperatures important to heat treatment of Grade 91 steel were identified.

References

[1] I. Charit and K.L. Murty: JOM, 2010, vol. 62, pp. 67-74.
[2] K.L. Murty and I. Charit: J. Nucl. Mater., 2008, vol. 383, pp. 189-195.
[3] D. Rojas: 9-12% Cr heat resistant steels: alloy design, TEM characterization of microstructure evolution and creep response at 650^{o}C, PhD dissertation, Ruhr-University Bochum, Bochum, Germany, 2011.
[4] R. Vishwanathan, and W.T. Bakker: ASME, Proceedings of 2000 International Joint Power Generation Conference, Miami Beach, Florida, July 23-26, 2000, pp. 1-22.
[5] B. J. P. Buhre, R. Gupta, S. Richardson, A. Sharma, C. Spero, and T. Wall: PF-Fired Supercitical Boilers: Operational Issues and Coal Quality Impacts, CCSD, March, 2002.
[6] T. Shrestha, M. Basirat, I. Charit, G. P. Potirniche, and K. K. Rink: J. Nucl. Mater., 2012, vol. 423, pp. 110-19.
[7] M. Basirat, T. Shrestha, G. P. Potirniche, I. Charit, and K. Rink: Int. J. Plast., 2012, vol. 37, pp. 95-107.
[8] T. Shrestha, M. Basirat, I. Charit, G. P. Potirniche, and K. K. Rink: Mater. Sci. Engr. A: 2013, vol. 565, pp. 382-91.
[9] J. C. Ahn, G. M. Sim, and K. S. Lee: Mater. Sci. Forum, 2005, vol. 475-479, pp. 191-94.
[10] B. J. Ganesh, S. Raju, A. K. Rai, E. Mohandas, M. Vijayalakshmi, K. B. S. Rao, and B. Raj: Mater. Sci. Technol., 2011, vol. 27, pp. 500-12.

[11] M. Yoshino, Y. Mishima, Y. Toda, H. Kushima, K. Sawada, and K. Kimura: Mater. High Temp., 2008, vol. 25, pp. 149-58.
[12] T. C. Totemeier, H. Tian, and J. A. Simpson: Metall. Trans., 2005, vol. 37A, pp. 1519-25.
[13] V. Dudko, A. Delyakov, and R. Kaibyshev: Mater Sci. Forum, 2012, vol. 706-709, pp. 841-46.
[14] K. Sawada, K. Suzuki, H. Kushima, M. Tabuchi, and K. Kimura: Mater. Sci. Eng. A, 2008, vol. 480, pp. 558-63.
[15] F. Masuyama and N. Nishimura: Proceedings: ASME/JSME Pressure Vessels and Piping Conference, San Diego, CA, USA, ASME, 2004, vol. 476, pp. 85-92.
[16] Y. Z. Shen, S. H. Kim, H. D. Cho, C. H. Han, and W. S. Ryu: J. Nucl. Mater., 2010, vol. 400, pp. 64-8.
[17] P. Anderson, T. Bellgard, and F.L. Jones: Mater. Sci. Technol., 2003, vol. 19, pp. 207-13.
[18] C. R. Das, S. K. Albert, A. K. Bhaduri, G. Srinivasan, and B. S. Murty: Mater. Sci. Engr. A, 2008, vol. 477, pp. 185-92.
[19] B. Silwal, L. Li, A. Deceuster, and B. Griffiths: Weld. J., 2013, vol. 92, pp. 80s-87s.
[20] D. V. Shtansky and G. Inden: Acta Mater., 1997, vol. 45, pp. 2879-95.
[21] B. J. Ganesh, S. Raju, E. Mohandas, and M. Vijayalakshmi: Diffus. Defect Forum, 2008, vol. 279, pp. 85-90.
[22] N. Oono, H. Nitta, and Y. Iijima: Mater. Trans., 2003, vol. 44, pp. 2078-83.
[23] S. Raju, B. J. Ganesh, A. K. Rai, S. Saroja, E. Mohandas, M. Vijayalakshmi, and B. Raj: Int. J. Thermophys, 2010, vol. 31, pp. 399-415.
[24] J. Hald, L. Korcakova, H.K. Danielsen, and K.V. Dahl: Mater. Sci. and Technol., 2009, vol. 24, pp. 149-58.
[25] S. G. Hong, H. J. Jun, K. B. Kang, and C. G. Park: Scr. Mater., 2003, vol. 48, pp. 1201-06.
[26] K. A. Taylor: Scr. Mater., 1995, vol. 32, pp. 7-12.

5. Residual stress measurement by neutron diffraction in modified 9Cr-1Mo Steel weldments

5.1. Introduction

Residual stress distribution across gas tungsten arc welds in modified 9Cr-1Mo (Grade 91) steel were measured by the time-of-flight neutron diffraction using the SMARTS diffractometer at Lujan Neutron Scattering Center, Los Alamos National Laboratory. Rectangular plates of dimensions 104 mm×104 mm×12.7mm were welded using the gas tungsten arc welding (GTAW) technique. The residual stresses were determined at the mid-thickness, 4.35 mm and 2.35 mm below the surface of both the as-welded and post-weld heat treated plates. The residual stresses of the as-welded plates were compared with those of the post-weld heat treated plates. The post-weld heat treatment significantly reduced the residual stress level in the base metal, heat affected zone and the weld zone. Vickers microhardness of the as-welded and post-weld heat treated specimens was also mapped and correlated with the observed residual stress profile and microstructure.

Since the introduction of Cr-Mo steels about a century ago, significant progress has been made in the alloy design, and they have been the material of choice for use in power generation plants. Ferritic-martensitic (F-M) steels with 9-12 wt.% Cr were developed for fossil-fuel-fired power plants [1] during the 1960's, and later used as boiler tubes in the advanced gas-cooled reactors [2,3]. The addition of Nb and V, which form fine, stable carbides and carbonitrides, has enhanced the mechanical properties of advanced F-M steels. Modified 9Cr-1Mo steel, also known as Grade 91 steel, is an important member of F-M class of steels.

With the vision to enhance the efficiency of power production and lower the emission of greenhouse gases, the new generation nuclear power plants are expected to operate at higher temperatures and radiation doses for longer service life than their predecessors. Hence, the structural materials used in these power plants are required to have superior creep properties, corrosion and radiation damage resistance. For example, Grade 91 steel is being considered a potential candidate material for reactor pressure vessel (RPV) application in Gen-IV Very High Temperature Reactor (VHTR). In addition to that, Grade 91 steel has found use as wrapper materials in Fast Breeder Reactors (FBR) [4].

RPV is considered an irreplaceable component of a nuclear power plant which dictates its useful service life. This is a major concern in VHTR RPVs, which have thickness in the range of 100-300 mm and are expected to operate for more than 60 years [5]. Welding is used in joining different parts of the RPV, but it has the potential of creating soft zones with lower strength in the welded specimens, leading to premature failure [6]. Residual stresses are present throughout the weldment as a result of intense localized heating and rapid cooling during solidification of the weld [7]. The residual stress resulting from welding is both compressive and tensile. A compressive stress prevents crack propagation, while tensile stresses do the opposite, degrade the fatigue characteristics, lead to brittle fracture, and accelerate stress corrosion cracking [8]. Residual stresses can be measured by destructive techniques including the contour method, hole drilling, or by non-destructive techniques like X-ray and neutron diffraction techniques [9, 10]. Because of higher depth of penetration, neutron diffraction has distinctive advantages over X-ray diffraction.

Residual stress can be caused by machining of parts, phase transformation, dimensional change (thermal contraction) after weld cooling, and the chemical compositional gradient. In ferritic steels, the shrinkage effect is generated when a weld metal solidifies on a solid surface along all orthogonal directions. In this study, residual stresses were measured using neutron diffraction technique in welded Grade 91 steel plates in the as-welded condition and after post-weld heat treatment. Vickers microhardness was used to measure the resistance to plastic deformation of the base metal and weldment, and microstructural characteristics were studied using optical and scanning electron microscope.

5.2. Experimental

5.2.1. Material and welding procedure

The chemical composition of ASTM A387 Grade 91 CL2 steel (Grade 91) used in this study is given in Table 5.1. The hot rolled Grade 91 plates were obtained from ArcelorMittal Plate LLC, in normalized and tempered condition (i.e., austenitized at 1038 K for 240 min. followed by air cooling, and tempered at 789 K for 43 min.). The as-received plates had dimensions of 104 mm×104 mm×12.7 mm. At room temperature, the as-received Grade 91 steel exhibited yield strength of 533 MPa, ultimate tensile strength of 683 MPa and elongation to fracture of 26%. The plates of aforementioned dimensions were cut into two halves and tapered on one side at 30^{o} to make a V-butt end. The double V-butt weld specimens were made by welding these two V-butt end halves together, as shown in Fig. 5.1, where Long. is the longitudinal stress, Trans. the transverse stress, and TT the through-thickness stress. Metrode 2.4 mm diameter 9CrMoV-N TIG filler wire having low residual elements were used for welding. The plates were preheated to 260^{o}C before welding. The steel plates were placed on an aluminum plate to prevent overheating during welding. Three successive passes were used to create the complete weld using a current of 130 A and voltage of 15 V. PWHT of the welded plates were carried out at 750^{o}C for 2 hr.

Table 5.1. Chemical composition (in wt.%) of Grade 91 steel

Element	Nominal	Measured
Cr	8.00 - 9.50	8.55
Mo	0.85 - 1.05	0.88
V	0.18 - 0.25	0.21
Nb	0.06 - 0.10	0.08
C	0.08 - 0.12	0.10
Mn	0.30 - 0.60	0.51
Cu	0.4 (max.)	0.18
Si	0.20 - 0.50	0.32
N	0.03 - 0.07	0.035
Ni	0.40 (max.)	0.15
P	0.02 (max.)	0.012
S	0.01 (max.)	0.005
Ti	0.01 (max.)	0.002
Al	0.02 (max.)	0.007
Zr	0.01 (max.)	0.001
Fe	Balance	Balance

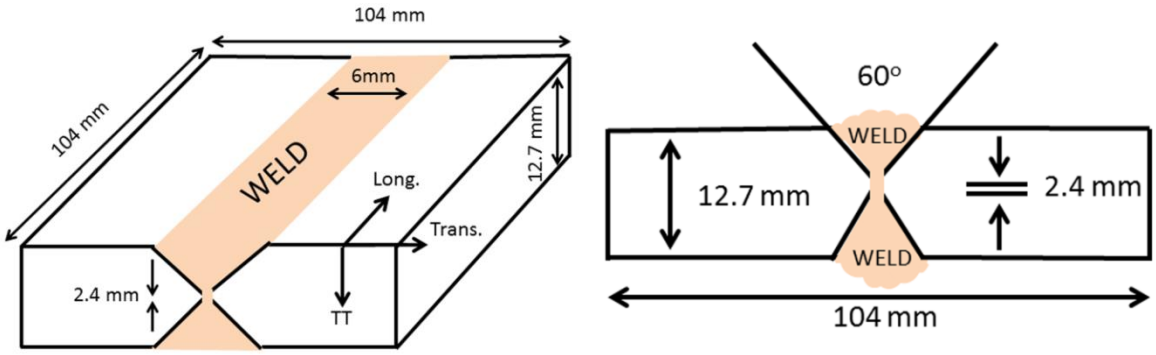

Fig. 5.1. Schematic representation of the double V-butt welded plate (not up to scale).

5.2.2. Residual Stress Measurement

The residual stress measurement in the welded plates was conducted by time-of-flight neutron diffraction on the 'Spectrometer for Materials Research at Temperature and Stress (SMARTS)' diffractometer at Lujan Neutron Scattering Center, Los Alamos National Laboratory, Los Alamos, New Mexico, USA. Residual strains were measured at the mid-thickness, 4.35 mm and 2.35 mm below the surface of 12.7 mm thick plate. The positioning of the sample in the neutron beam was accomplished with a precision sample stage which can move in three orthogonal directions with an accuracy of 0.01 mm in translation and 0.1^o in rotational angle. Two computer controlled theodolites were used to position the sample on the stage at the goniometer center. The SMARTS instrument receives a moderated "white" neutron beam (λ = 0.5 – 4 Å) from the tungsten spallation target. The sample position is 30 m from the moderator. Boron nitride slits define the incident beam size (2 mm x 2 mm in this case) that impinges on the sample and gets diffracted. Radial collimators focus the view of the two detector banks situated 1.5 m away from the sample position at ±90^o orientation with respect to the incident beam. The cross section of the defined incident beam with the field of view of the detectors creates a 2 mm x 2 mm x 2 mm integration volume (gauge volume) within the sample. A computer controlled motion table then moves the sample with respect to the gauge volume in order to obtain a spatial resolved profile of the lattice parameter, which is used to determine the strain. The residual stress at any point in a component is represented by a stress tensor (σ_{ij}) [11]. At least six measurements of strain are necessary to completely define an arbitrary stress tensor. We only measure 3 orthogonal components and assume they are the principal components. This is usually done by rotating the sample with respect to the probe volume and the acceptance volume of the radial collimators [12]. The Trans. and TT strain components were measured by positioning the weld vertical. The Long. and TT strain components were measured by positioning the transverse direction vertical.

A representative diffraction pattern from Grade 91 steel with distinctive peaks measured for the entire range of d-spacing and its respective (*hkl*) orientation is shown in Fig. 5.2. The General Structure Analysis System (GSAS) program [13] calculates an entire diffraction pattern based on assumptions of the crystal structure and microstructure, and compares it to the observed diffraction pattern. Linear least-squares fitting was used to refine lattice parameter making the

calculated diffraction pattern best fit that observed. The lattice strain averaged over the gauge volume was then calculated as

$$\varepsilon_i = \frac{a^i - a_0^i}{a_0^i} \text{ , } i = \text{Long., Trans., TT} \quad (1)$$

where a_0 is the unstressed lattice parameter for the specified *hkl* plane.

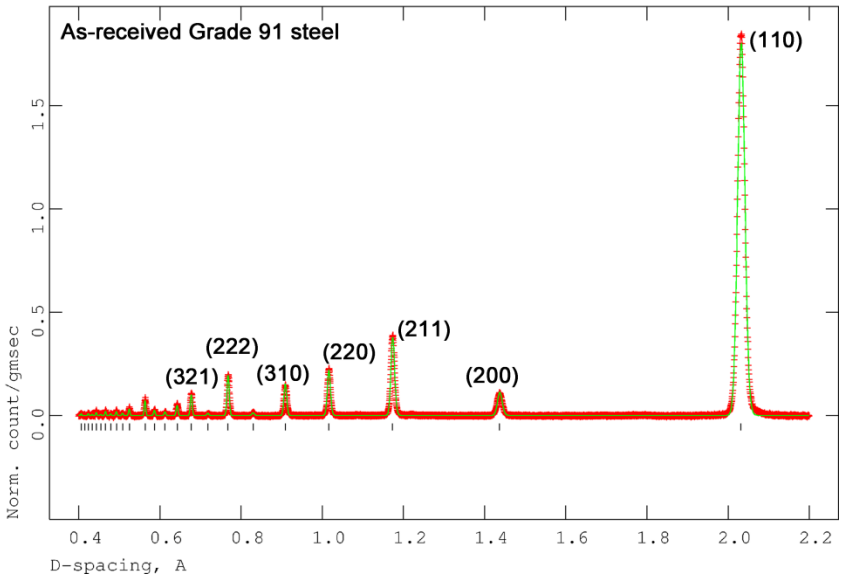

Fig. 5.2. Diffraction pattern of Grade 91 steel after Rietveld refinement

Residual stresses were measured by the peak shift method, in which the lattice parameter of the region of interest (a) is compared to the lattice parameter of the stress-free sample (a_0). The uncertainty in the strain was calculated from the estimated standard deviation in the lattice parameter determined by the fitting routine for the case of the intact weld and the reference coupons. The unstressed lattice parameter (a_0) were determined by taking stress-free 3.5×3.5×3.5 mm^3 cubes from the base material (BM), heat affected zone (HAZ) and the weld. Cutting such small dimension relieves any residual stress while the microstructure and chemical composition stay the same [12].

Using the generalized Hooke's law, the residual stress profiles along the BM, HAZ and weld were computed for the Long., Trans. and TT orientations, such that the principal stress/strain axes coincided with these directions

$$\sigma_{Long.} = \frac{E}{(1+\nu)(1-2\nu)}\left[(1-\nu)\varepsilon_{Long} + \nu(\varepsilon_{Trans.} + \varepsilon_{TT})\right], \quad (2)$$

where E is the Young's modulus, $\sigma_{Long.}$ the stress in longitudinal direction, ε_{Long} strain in longitudinal direction, $\varepsilon_{Trans.}$strain in transverse direction, ε_{TT} strain in through-thickness direction and υ the Poisson's ratio. We have assumed Long., Trans. and TT to be the principal axes, and are indicated in Fig. 5.1. The a_0 was measured in the weld, the HAZ and the base metal. No variation of a_0 was noted in the HAZ and base metal so the average value was used. A small variation of a_0 was seen in the HAZ and base metal, thus a linear correction to a_0 was used for the residual strain calculation.

5.2.3. Microstructural characterization and hardness measurement

Optical microscopy was performed on as-welded and PWHT specimens for characterization of the grain structure. Conventional metallographic procedures of cold mounting, grinding and polishing were performed to prepare the specimen surface to 0.5 µm finish before etching was carried out using Marble's reagent (a solution made of 50 ml distilled water, 50 ml hydrochloric acid and 10 g of copper sulfate). Subsequently, an Olympus light microscope was used to examine the metallographic specimens, and an attached CCD camera was used to record the micrographs. Microhardness tests were performed on the as-welded and PWHT samples using a Vickers indenter under a load of 0.5 kgf and loading time of 15 s.

5.3. Results

5.3.1. Metallographic examinations

As-welded and PWHT microstructural features of the unaffected BM, HAZ, and weld are shown in Figs. 5.3 and 5.4, respectively. Two distinct heat affected zone microstructure, i.e. coarse and fine grain structures, and an indistinctive columnar structure formed after directional solidification was observed in weld. As-welded base material, fine grained, coarse grained, and weld microstructure are shown in Fig. 5.3a, b, c, and d, respectively. PWHT base material, fine grained, coarse grained, and weld microstructure are shown in Fig. 5.4a, b, c, and d, respectively. As-welded weld zone has martensitic lath structure, on post weld heat treatment the lath size increases. The base materials in the as-welded and PWHT conditions had similar coarse and fine grain microstructures as these regions were not affected by the thermal cycle.

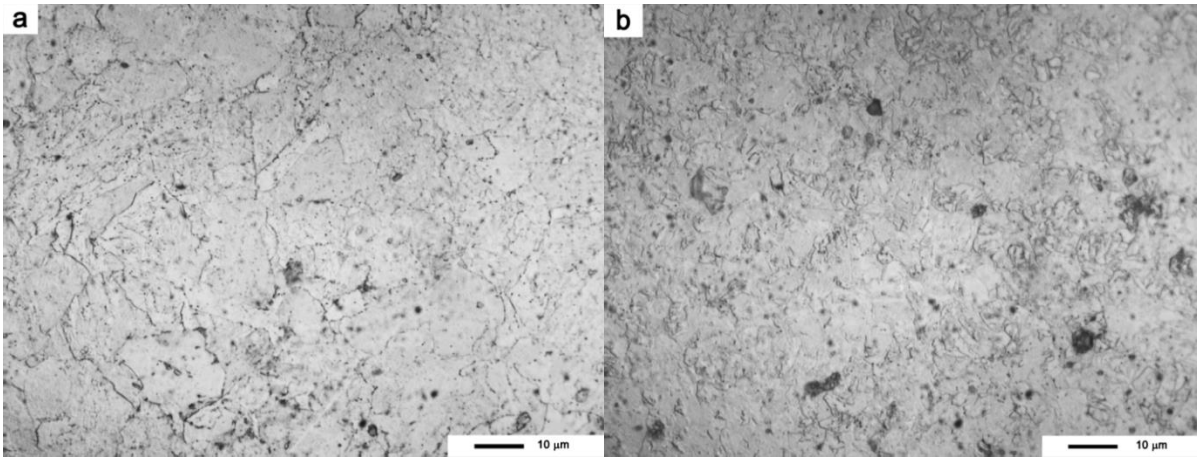

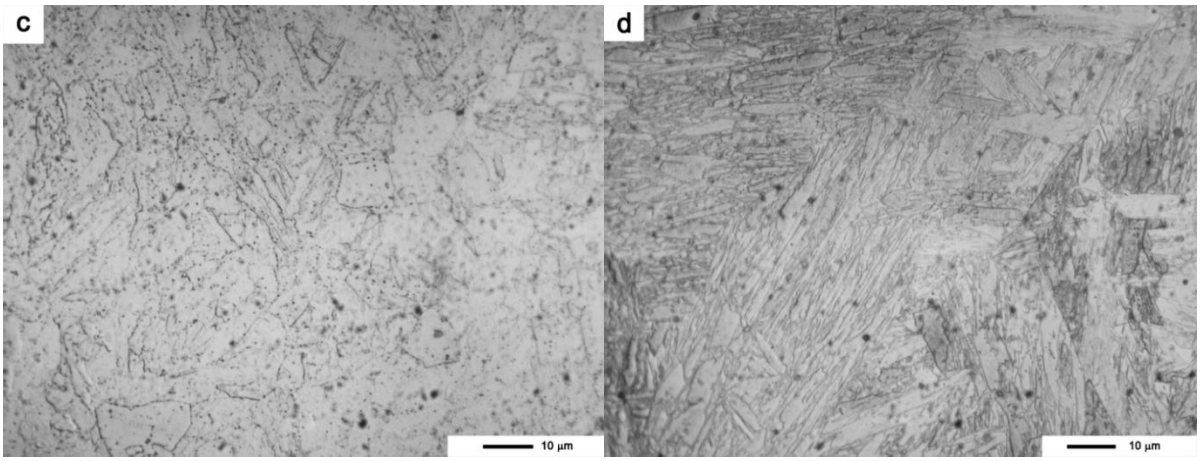

Fig. 5.3. Optical micrograph of as-welded microstructures, (a) base metal, (b) fine grain, (c) coarse grain, and (d) weld zone

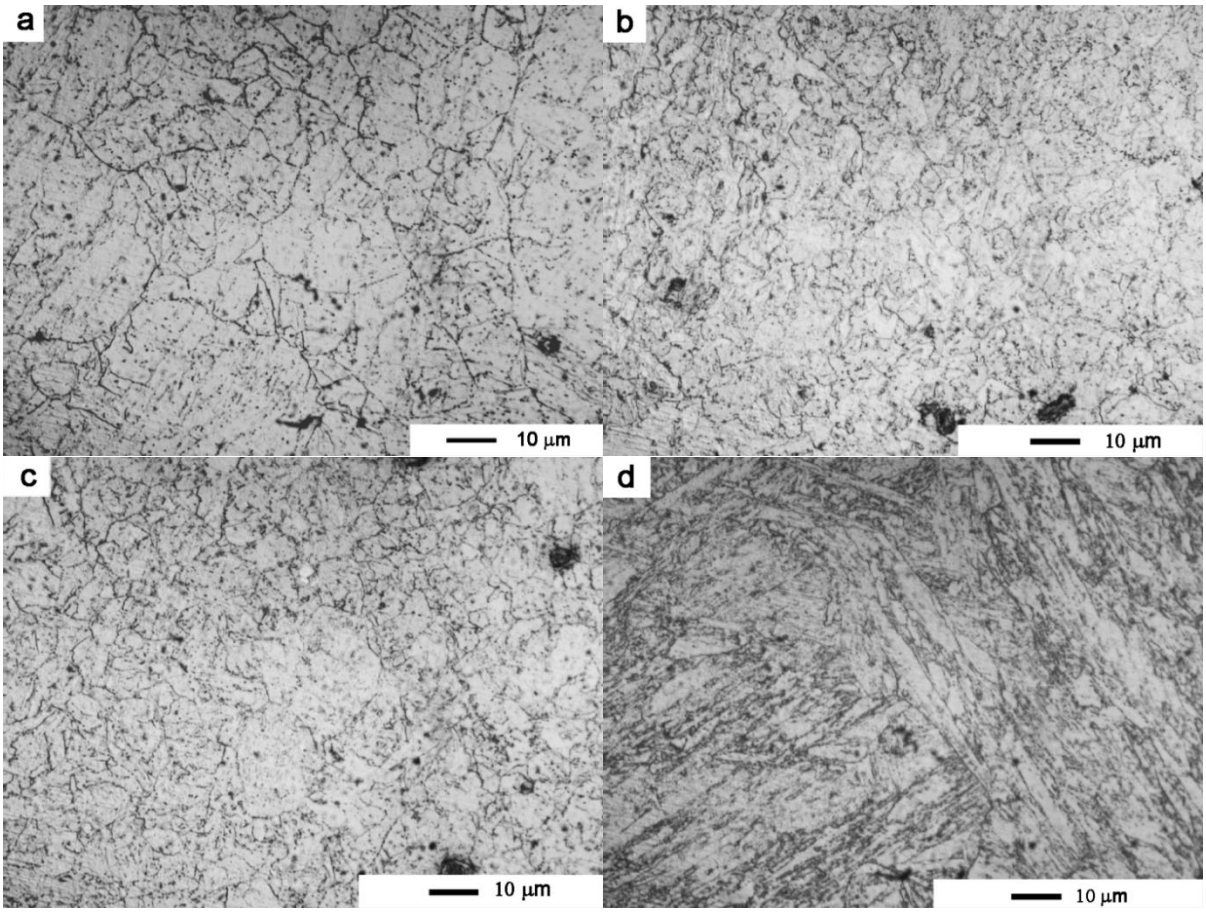

Fig. 5.4. Optical micrograph of PWHTed microstructure (a) base material, (b) fine grain HAZ, (c) coarse grain HAZ, and (d) weld zone after post-weld heat treatment

5.3.2. Residual stress of as-welded Grade 91 steel plate

The variation of lattice parameter (a_0) in longitudinal orientation associated with welding as a function of location across the weld and the depth of the measurement is shown in Fig. 5.5.

The center of the weld is marked as 0 mm, as shown in Fig. 5.5. At the mid-thickness and 4.35 mm below the surface, the lattice parameter in the weld is higher than that of 2.35 mm below the surface. However, in the HAZ the lattice parameters at all three depths are similar. The variation in lattice parameter reflects the changes in residual strains. Residual strains were measured over 90 mm across the weld, '0' being the center of the weld. Fig. 5.6 shows the distribution of the residual strain across the weldment at 2.35 mm below the surface. The Long. residual strain is compressive at the weld, while tensile in the HAZ. The Trans. residual strain is slightly compressive at the weld, which is less than the Long. strain, but tensile at the HAZ. However, the TT strain is mostly compressive throughout the weld and HAZ.

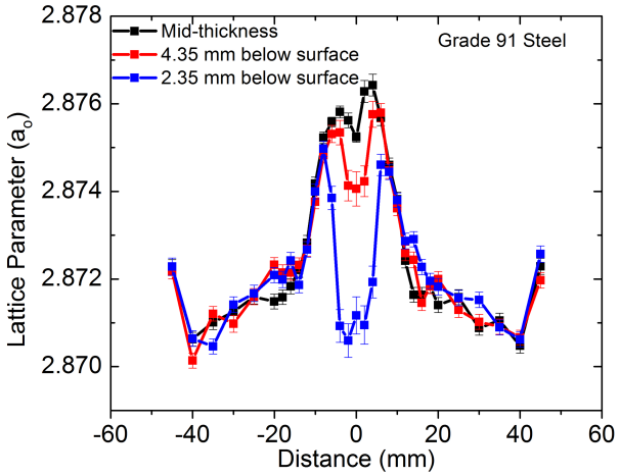

Fig. 5.5. Variation of lattice parameter in the longitudinal orientation at various depths of the welded plate, '0' being the center of the weld

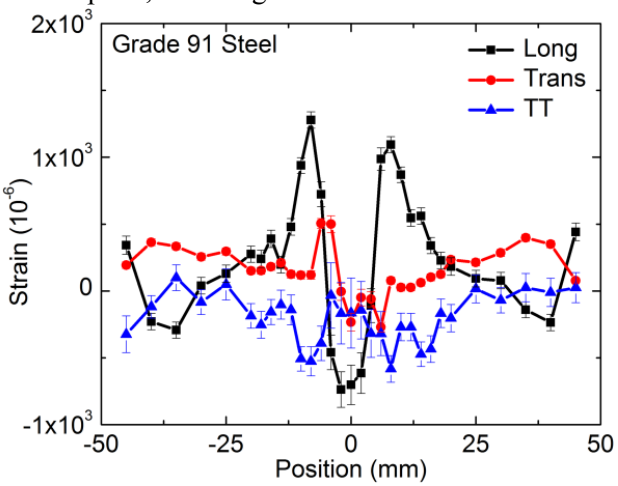

Fig. 5.6. Variation of residual strain across the weldment, 2.35 mm below the surface

The variation of residual stress across the weldment in three orthogonal directions as a function of depth of measurement is shown in Fig. 5.7. Fig. 5.7a shows the variation in the residual stress at the mid-thickness of the plate. Residual stresses in the Long. and Trans. orientations are tensile in the weld and HAZ, while the one in the TT orientation is compressive in the weld zone. The longitudinal residual stress has the maximum compressive stress of –71±18 MPa at 40 mm away from the center of the weld and maximum tensile stress of +351±14 MPa at 8 mm away from the center of the weld, which is ~66% of the yield strength of the base

material. The highest Trans. tensile residual stress of 286±20 MPa, measured at the center of the weld, is ~54% of the yield strength of the base material. The through-thickness residual stress is mostly negligible, except at the center of the weld where it reaches a maximum compressive value of –132±11 MPa. A similar stress distribution was found 4.35 mm below the surface as shown in Fig. 5.7b. Fig. 5.7c shows the variation in the residual stress along the weldment at 2.35 mm below the surface. The residual stresses in the Long., Trans. and TT orientations are compressive in the weld and tensile in the heat affected zone. Maximum compressive Long., Trans. and TT stresses at the center of the weld were found to be –252±54 MPa, –172±41 MPa and –159±79 MPa, respectively. The maximum tensile Long. and Trans. stresses were +325±22 MPa and +187±22 MPa in the HAZ, respectively, while a maximum TT stress of +69±34 MPa was observed in the BM.

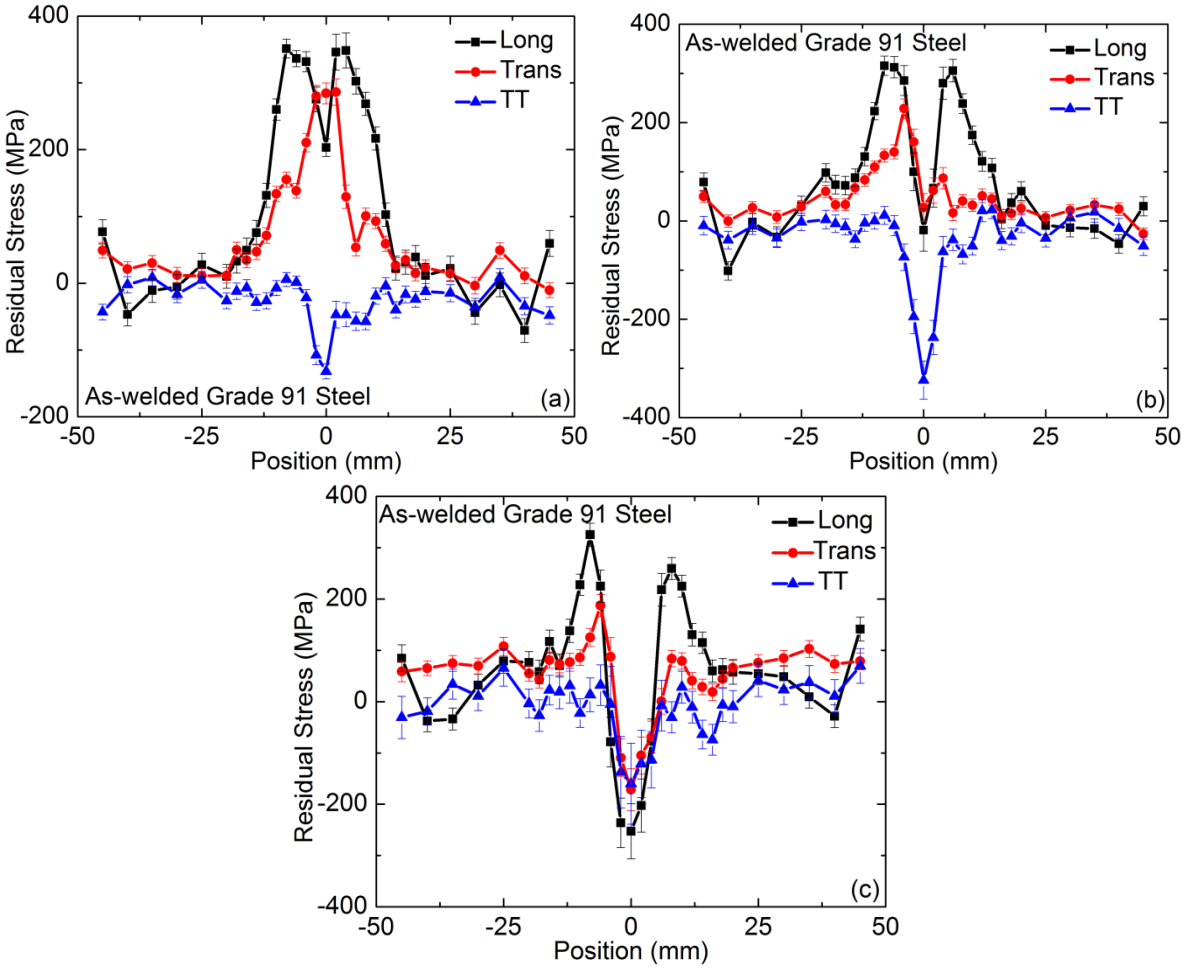

Fig. 5.7. Variation of the residual stress across the weldment: (a) at mid-thickness, (b) 4.35 mm below the surface, (c) 2.35 mm below the surface.

5.3.3. Residual stress after post-weld heat treatment

Heat treatment carried out after welding significantly lowered the residual stress as shown in Fig. 5.8a and b. These figures show the residual stresses measured at mid-thickness and 2.35 mm below surface of the weldment, respectively, after PWHT. For the measurement carried

out at the mid-thickness of the weld plate, maximum tensile residual stress of +90±18 MPa was observed in Long. orientation at HAZ, while maximum compressive stress of -112±15 MPa was observed in the TT orientation in the weld. For the measurement carried at 2.35 mm below the surface, maximum tensile residual stress of +111±15 MPa was observed in the Trans. orientation at HAZ, while maximum compressive stress of -147±33 MPa was observed in the TT orientation in the weld. The PWHT reduced the residual stress significantly, but some still exist.

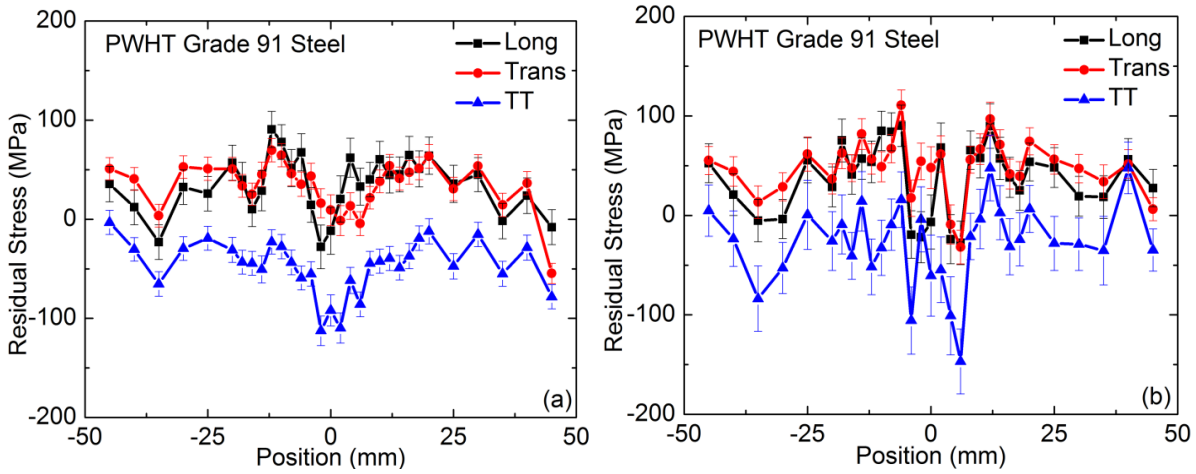

Fig. 5.8. Residual stress profile after PWHT (a) at mid-thickness and (b) 2.35 mm below the surface

5.3.4. Microhardness

Vickers microhardness tester was used to measure the hardness of Grade 91 steel in as-received and PWHT condition. The hardness of the as-welded material increased across the weld but decreased at HAZ, as shown in Fig. 5.9a. As-welded specimen had maximum hardness of 474 VHN at the weld, while HAZ had the lowest hardness of 200 VHN. The as-welded base material had hardness of ~225 VHN, and the HAZ was symmetric on either side of the weld. The hardness profile of specimen PWHT at 750^{o}C for 2 hours was similar to the as-welded specimen, but the hardness magnitudes were lower. The maximum hardness of 304 VHN was observed at the weld, while the lowest hardness of 174 VHN was observed at HAZ. Pavlina et al. [14] have correlated the hardness of steels with the yield strength (*YS*) as follows:

$$YS = -90.7 + 2.876H_v \tag{3}$$

where H_v is Vickers microhardness. The yield strength profile of as-welded and PWHT specimen looks similar to the hardness profile, as noted in Fig. 5.9b. The yield strength profile shows the localized yield strength of the material obtained from Equation 5.3.

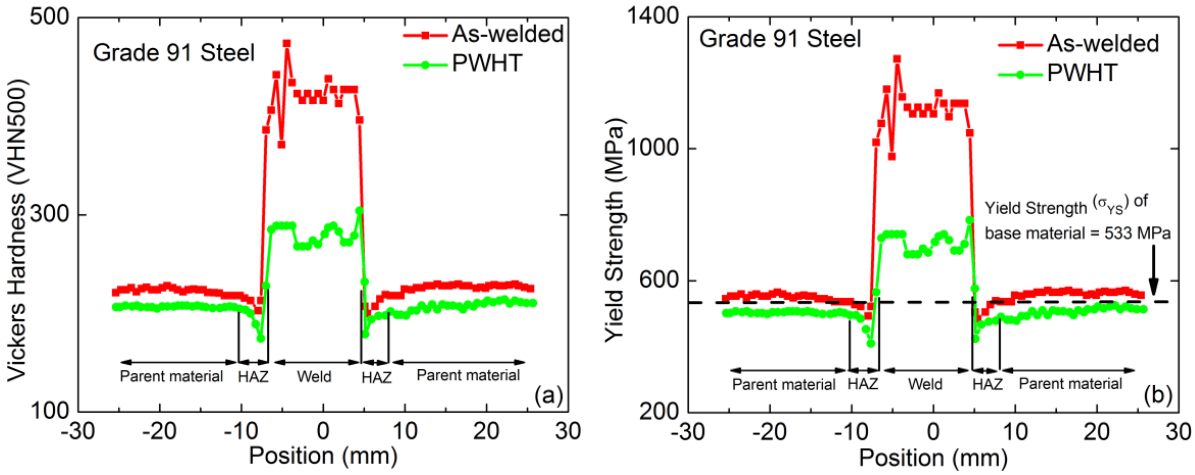

Fig. 5.9. Vickers microhardness (a) and yield strength profile (b) of the welded Grade 91 steel, '0' being the center of the weld.

5.4. Discussion

5.4.1. Residual stress

Welding creates thermal gradient across the weld which alters the microstructure and leads to the development of residual stresses. During welding, the material close to the weld zone experiences temperatures high enough to form the austenite phase. As the material starts to cool down after welding, the face-centered cubic (fcc) crystal structure of austenite phase transforms to body centered tetragonal (bct) structure of martensite in a diffusionless manner, thus increasing the volume. In Grade 91 steel which is an alloy steel does not need water quenching to form martensite; martensite can form under slower cooling rate during the weld solidification itself. This change in volume in martensitic transformation is associated with the change of the tensile residual stress to compressive stress. For the Grade 91 steel containing 0.1 wt.% carbon, the austenite to martensite phase transformation results in 4.56% volume increase [15].

During welding, the weld plate experiences a thermal gradient ranging from melting temperature at the weld to room temperature at the base material, which constrains the thermal shrinkage during solidification of the weld. This alters the lattice parameter of the material. In a multipass weld, like this one, where the thermal gradient varies for each subsequent pass, the variation of lattice parameter changes with the thickness of the weld. The distribution of Long. residual strain 2.35 mm below the surface was compressive at the center of the weld and tensile in the HAZ, as shown in Fig. 5.6. The variation of longitudinal strain reflects the thermal gradient and phase transformation during welding. The strain decreases as we move away from the HAZ, eventually becoming compressive as a result of shrinkage, but then increases to become tensile at the farthest point from HAZ. The residual strain distribution in the single V-butt GTA welded 2.25Cr-1Mo ferritic steel was attributed to the thermal contraction of the weld zone and the individual passes, and the through-thickness temperature gradient during cooling [16]. However, Pyzalla [15] asserted that the strains induced by volume increase during austenite to martensite phase transformation are larger than the strains induced by thermal gradient during cooling.

For measurement carried out at the mid-thickness, tensile Long. and Trans. residual stresses were observed at the weld and HAZ, while the residual stress in TT orientation was compressive in weld zone, as shown in Fig. 5.7a. Maximum tensile Long. residual stress of +351±14 MPa was at the HAZ, while maximum tensile Trans. residual stress of +286±20 MPa was at the weld. Kim et al. [7] measured maximum tensile Long. and Trans. residual stresses of +705 MPa and +304 MPa at 5 mm away from the weld centerline in a GTA welded modified 9Cr-1Mo steel, respectively. The tensile residual stresses in the BM below the weld nugget is due to the fact that phase transformation takes place at higher temperature compared to the nugget [16].

The residual stresses 2.35 mm below the surface in the Long., Trans. and TT orientations were compressive in the weld and tensile in the heat affected zone, as shown in Fig. 5.7c. Similarly, compressive residual stresses were observed by Paddea et al. [17] and Yaghi et al. [18] on the surface of ferritic-martensitic P91 steel weld. However, Residual stress measurement carried out 1.5 mm below the top surface of a metal inert gas (MIG) welded low carbon steel, which was unrestrained while welding had tensile longitudinal stress at the weld, and the stress dropped gradually and became compressive away from the center of the weld [19]. In contrast, the Trans. and TT stresses were compressive at the weld, but gradually increased to be tensile while moving away from the center of the weld. The compressive stresses were due to the martensitic transformation as confirmed by diffraction peak asymmetry measurements [16, 20]. The tensile residual stresses in the HAZ was due to the compressive residual stresses in the weld, which self-equilibrates the tensile stresses when there is no thermal gradient or external forces acting on it. The TT stress is lower than the Trans. and Long. stresses because of the thickness is much smaller than the length and width of the welded plate.

Smith et al. [21] observed the maximum surface tensile residual stresses in the last weld bead in a submerged-arc welded C-Mn ferritic steel BS1501. However, McDonald et al. [22] reported the highest tensile Trans. residual stress of ~+700 MPa at the HAZ in manual metallic arc (MMA) welded low alloy ferritic CrMoV steel plate, as listed in Table 5.2. Table 5.2 lists the residual stresses measured on ferritic steel plate weldments from various sources. The locations of the observed highest residual stresses are mentioned in the discussion. Ficquet et al. [23] reported highest Long. and Trans. residual stress of ~1000 MPa and ~800 MPa, respectively at the mid-thickness of the weld zone of A533B ferritic steel plate, as listed in Table 5.2. For measurement carried out on surface, Kim et al. [7] measured the highest tensile Long. residual stress of +718 MPa and tensile Trans. residual stress of +365 MPa in the HAZ, at 10 mm from the center of the GTA welded modified 9Cr-1Mo steel. For measurement carried out at the mid-thickness, Kim et al. [7] reported highest Long. stress of +705 MPa and Trans. stress of 304 MPa. Residual stresses of +705 MPa at mid-thickness and +718 MPa at surface are ~119% and ~121% higher than the yield strength of the base material, respectively. In general, the residual stresses are elastic stress and expected to be lower than the yield strength [8]. When the residual stress is higher than the yield strength, the material will undergo plastic deformation which can lead to significant warping. Paddea et al. [17] observed the maximum tensile residual stresses in GTA welded P91steel pipe at the HAZ, which is prone to type IV cracking.

The fact that the residual stresses were tensile at mid-thickness and compressive at 2.35 mm below the surface, as shown in Fig. 5.7 a and c, was due to the differential cooling rates of the surface and center, which is constrained by already hardened cold surfaces . Since thermal contraction along the Long. was more constrained compared to Trans., it has the highest residual stresses across the weldment. The dimensions of the sample along the Long. and Trans.

direction are both long compared to the size of the weld. The difference is the direction of the thermal gradient, which is from the weld outward along the Trans. direction. When the hot material contracts in the Trans., it is not so self-constrained because the gradient is along the Trans. direction, in contrast, the contraction along the Long. direction is much more constrained.

Table 5.2. Residual stresses in various steels

Ferritic Steel plate	Welding Technique	Measurement		Highest Residual Stresses (MPa)					Ref.
		Technique	Location	As-welded			PWHT		
				Long	Trans	TT	Long	Trans	
BS1501	SAW[b]	RSG[a]	Surface	+580	+450	NA	+90	+90	30
Grade 91	GTAW*	ND[c]	surface	+718	+365	NA	NA	NA	7
Grade 91	GTAW*	ND[c]	mid-thickness	+705	+304	NA	NA	NA	7
Ducol	MMA[f]	XRD[d]	surface	NA	~+700	NA	NA	NA	31
Ducol	MMA[f]	RSG[a]	surface	NA	~+700	NA	NA	NA	31
A533B	Not reported	ND[c]	mid-thickness	+1000	+797	NA	NA	NA	32
A533B	Not reported	DHD[e]	surface	+650	+410	NA	NA	NA	32
A533B	Not reported	ND[c]	surface	+609	+378	NA	NA	NA	32
Grade 91	GTAW	ND[c]	Mid-thickness	+351	+286	-132	+90	+70	PS[g]
Grade 91	GTAW	ND[c]	4.35 mm deep	+315	+228	-324	+107	+93	PS[g]
Grade 91	GTAW	ND[c]	2.35 mm deep	+259	+187	-160	+90	+111	PS[g]

[a]Rosetta strain gauge, [b] Submerged arc weld, [c]Neutron diffraction, [d]Xray diffraction, [e]Deep hole drill, *Gas tungsten arc welding, [f]Manual metal arc, [g]Present study

This change in volume is associated with changing of the residual stress from tensile to compressive [15, 16]. Thus the increase in hardness values at the weld is related to martensitic transformation which leads to compressive residual stress in the weld as seen in Fig. 5.7c. The decrease in microhardness at the HAZ reflects the presence of over-tempered martensite along with α-ferrite phase and formation of soft zone. The ferrite and austenite phases are more prone to plastic deformation compared to martensite phase [29].

PWHT carried out at 750^{o}C for 2 hr lowered the hardness across weldment by transforming tempered martensite structure (consisting of α-ferrite with other carbides) and causing a strain relief in the process. Welding leads to the migration of carbon creating soft areas in the HAZ, which are likely the initiation sites of type IV cracking. The lowest hardness was measured in the HAZ because of the reduction in dislocation density, coarsening of precipitation, formation of polygonized structure, break-up of martensitic lath structure, and reduction in solid solution strengthening due to precipitation [30, 31]. A similar hardness profile was reported by Sato et al. [32] across the welded joint of modified 9Cr-1Mo steel. The decrease in hardness reflects the diminished yield strength at the HAZ, which results in premature failure of the weldment [6]. HAZ having low yield strength is considered the soft zone in the weldment which

leads to preferential plastic deformation. Higher yield strength in the weld is due to the martensitic lath structure resulting in higher residual stresses in as-welded condition [33]. Even after PWHT, the gradient in hardness and yield strength, as shown in Fig. 5.9, and residual stress, as shown in Fig. 5.8 still exist. This may require performing PWHT at higher temperature and/or for longer time, which can increase the toughness of the steel [34]. However, based on the differential scanning calorimetry (DSC) study, the austenitization start temperature (A_{c1}) for Grade 91 steel is 853^{o}C. PWHT carried out at temperatures above austenitization start temperature (A_{c1}) modifies the martensitic lath structure, reducing the strength of the steel. Hence the PWHT treatment of the welded plate must be carried out below that temperature to restrict the formation of austenite.

5.5. Conclusions

Neutron diffraction technique was used to measure the residual stresses in a gas tungsten arc welded Grade 91 steel plate in the as-welded and post-weld heat treated conditions. The residual stress distribution was measured at the mid-thickness, 4.35 mm and 2.35 mm below the surface of weld plate. At mid-thickness and 4.35 mm below surface, tensile longitudinal and transverse residual stresses were observed in the weld zone and the HAZ. At 2.35 mm below the surface, compressive longitudinal, transverse and through-thickness residual stresses were observed in the weld. Post weld heat treatment resulted in significant reduction of residual stress. Vickers microhardness measurement done to understand the resistance of HAZ and weld to plastic deformation showed lower hardness in the HAZ and higher values in the weld compared to the parent material. The microhardness values were correlated to obtain the localized yield strength of the weldment. HAZ had a lower yield strength compared to the base material and the weld zone.

References

[1] I. Charit, K. L. Murty, JOM 62 (2010) 67-74.
[2] E. Barker, Mater. Sci. Eng. 84 (1986) 49-64.
[3] R. L. Klueh, Int. Mater. Rev. 50 (2005) 287-310.
[4] S. Sathyanarayanan, A. Moitra, K. G. Samuel, G. Sasikala, S. K. Ray, V. Singh, Mater. Sci. Engr. A 488 (2008) 519-528.
[5] K. L. Murty, I. Charit, J. Nucl. Mater. 383 (2008) 189-95
[6] K. Laha, K. S. Chandravathi, P. Parameswaran, K. Bhanu Sankara Rao, S. L. Mannan, Metall. Mater. Trans. A 38 (2007) 58-68.
[7] S-H. Kim, J-B. Kim, W-J. Lee, J. Mater. Procs. Tech. 209 (2009) 3905-3913.
[8] George E. Dieter, Mechanical Metallurgy, McGraw-Hill Book Company, New York, 1961.
[9] P. J. Withers, Rep. Prog. Phys. 70 (2007) 2211-2264.
[10] A. D. Krawitz, Introduction to diffraction in materials science and engineering, 1st eds. Wiley-Interscience Publication, New York, 2001.
[11] L. Pintschovius, Macrostresses, microstresses and stress tensors, in: M. T. Hutchings, A. D. Krawitz (Eds.), Measurement of Residual and Applied Stress Using Neutron Diffraction, Kluwer Academics Publishers, Boston, 1992, pp. 115-130.
[12] B. Clausen, D. W. Brown, I. C. Noyan, JOM 64(1) (2012) 117-126.

[13] H. M. Rietveld, J. Appl. Cryst. 2 (1969) 65-71.
[14] E. L. Pavlina, C. J. Van Tune, J. Mater. Engr. Perf. 17(6) (2008) 888-893.
[15] A. R. Pyzalla, Internal stresses in engineering materials, in: W. Reimers, A. R. Pyazalla, A. Schreyer, H. Clemens (Eds.), Neutrons and Synchrotron Radiation in Engineering Materials Science, Wiley-VCH, Weinheim, 2008, pp. 21-56.
[16] H. Dai, J. A. Francis, H. J. Stone, H. K. D. H Bhadeshia, P. J. Withers, Met. Mater. Trans. A 39 (2008) 3070-3078.
[17] S. Paddea, J. A. Francis, A. M. Paradowska, P. J. Bouchard, I. A. Shibi, Mater. Sci. Engr. A 534 (2012) 663-672.
[18] A. H. Yaghi, T. H. Hyde, A. A. Becker, W. Sun, Sci. Tech. Weld. Join. 16(3) (2011) 232-238.
[19] J. W. H. Price, A. Paradowska, S. Joshi, T. Finlayson, Int. J. Press. Vessel. Pip. 83 (2006) 381–387.
[20] R. J. Moat, D. J. Hughes, A. Steuwer, N. Iqbal, M. Preuss, S. E. Bray, M. Rawson, Metall. Mater. Trans. A 40 (2009) 2098-2108.
[21] D. J. Smith, S. J. Garwood, Int. J. Press. Vessel. Pip. 51 (1992) 241-256.
[22] E. J. McDonald, L. F. Exworthy, P. E. J. Flewitt, K. Hallam, W. Bell, Mater. Sci. Forum 347-349 (2000) 664-669.
[23] X. Ficquet, C. E. Truman, D. J. Smith, Mater. Sci. Forum 524-525 (2006) 653-658.
[24] M. Turski, A. H. Sherry, P. J. Bouchard, P. J. Withers, J. Neutron Res. 12(1-3) (2004) 45-49.
[25] P. J. Bouchard, P. J. Withers, S. A. McDonald, R. K. Heenan, Acta Mater. 52(1) (2004) 23-34.
[26] S. K. Albert, M. Matsui, H. Hongo, T. Watanabe, K. Kubo, M. Tabuchi, Int. J. Press. Vess. Pip. 81 (2004) 221–234.
[27] D. Li, K. Shinozaki, Sci. Technol. Weld. Join. 10(5) (2005) 544–549.
[28] T. Watanabe, M. Yamazaki, H. Hongo, M. Tabuchi, T. Tanabe, Int. J. Press. Vess. Pip. 81 (2004) 279–284.
[29] Y. Tomota, H. Tokuda, Y. Adachi, M.Wakita, N.Minakawa, A.Moriai, Y.Morii, Acta Mater. 52 (2004) 5737-5745.
[30] S. A. David, T. Debroy, Sci. 257 (1992) 497-502.
[31] M. Regev, S. Berger, B. Z. Weiss, Weld. J. 75 (1996) 261s-268s.
[32] T. Sato, K. Tamura, Advances in Materials Technology for Fossil Power Plants: Proceedings of the 5th International Conference, Oct. 3-5, 2007, Marco Island, FL, USA, ASM Int., 2008, pp. 874-883.
[33] D. Dean, M. Hidekazu, Comput. Mater. Sci. 37 (2006) 209-219.
[34] M. Sireesha, S. K. Albert, S. Sundaresan, J. Mater. Eng. Perform. 10(3) (2001) 320-330.

Chapter 6. Creep rupture behavior of welded Grade 91 steel

6.1. Introduction

Creep rupture behavior of welded Grade 91 steel was studied in the temperature range of 600-700^{o}C and at stresses of 50 – 200 MPa. The creep data were analyzed in terms of Monkman-Grant relation and Larson-Miller parameter. Creep damage tolerance factor was used to identify the cause of creep damage. The creep damage was identified as the void growth in combination with microstructural degradation. The fracture surface morphology of the ruptured specimens was studied by scanning electron microscopy to elucidate the failure mechanisms.

Generation-IV nuclear reactors are expected to address the growing energy demand by producing electricity and at the same time mitigate greenhouse gas emissions. Various reactor types, such as Gas-Cooled Fast Reactor (GFR), Lead Cooled Reactor (LFR), Molten Salt Reactor (MSR), Sodium-Cooled Fast Reactor (SFR), Supercritical Water-Cooled Reactor (SCWR), and Very High Temperature Reactor (VHTR) are being considered. The VHTR is a Gen-IV reactor system at the heart of the so-called Next Generation Nuclear Plant (NGNP). VHTRs are designed to operate at temperatures much higher than those of currently operating reactors. Moreover, they are designed for longer service periods (60 years or more) compared to the current operating reactors [1]. Depending on the VHTR design, Prismatic Modular Reactor (PMR) or Pebble Bed Modular Reactor (PBMR), the operating temperature of the reactor pressure vessel (RPV) can vary between 300^{o}C and 650^{o}C. Furthermore, the RPV in the VHTR will be more than twice the size of a typical RPV in a Light Water Reactor (LWR) [2]. Grade 91 steel is a material of choice in fossil-fired power plants with increased efficiency, service life, and reduction in the greenhouse gas emissions of CO_2, NO_x, SO_2. The efficiency of fossil-fired power strongly depends on the temperature and pressure of steam. One percent increase in the net efficiency can reduce the emission of CO_2, NO_x, SO_2, and particulates by 2.4 metric ton, 2000 ton, 2000 ton, and 500 ton, respectively, while reducing the fuel cost by 2.4% [3]. Steam in these advanced coal-fired power plants is expected to have temperatures in the range of 550 – 720^{o}C and pressures above 24 MPa [3-5].

Understanding the creep rupture properties of Grade 91 steel is important in predicting the long term mechanical integrity of a power plant. Although there are some studies on the creep-rupture properties of monolithic Grade 91 steel, there is a limited number of studies on the creep properties of welded Grade 91 steel. Monolithic Grade 91 steel had two different rate-controlling creep deformation mechanisms in lower stress regime and higher stress regime. The creep deformation mechanism in lower stress regime was identified as Nabarro-Herring creep, while that in higher stress regime was identified as the edge dislocation climb controlled [6]. Higher stress regime showed an apparent stress exponent of ~11, which was reduced to ~5 by invoking the concept of threshold stress. Diagnostic diagram for creep failure showed the dominant creep rupture mechanism was microstructural degradation [7-11]. The fracture mechanism map of Grade 91 steel developed by Shrestha et al. [7] indicated that the monolithic sample ruptured in transgranular mode.

Use of Grade 91 steel in power plants involves some sort of fusion welding. Welding destroys the microstructural homogeneity of the material creating carbon denuded soft zones and residual stresses. The inhomogeneity of microstructure mainly in the heat affected zone (HAZ)

has led to type IV cracking [12,13], and low creep strength in fine grain HAZ (FGHAZ) [14-18]. The exact location of type IV cracking whether in over tempered martensite, FGHAZ, or inter critical HAZ (ICHAZ) is still up for discussion. Partial transformation of austenite to martensitic, resulting in presence of retained austenite [19], formation of delta ferrite [20-24], and differential migration of interstitial and precipitation forming elements [25, 26] across the weldment create a complex microstructure prone to failure. In nuclear power plants, reactor pressure vessel is considered an irreplaceable component of a nuclear power plant which dictates its useful service life. The creep rupture characteristics of Grade 91 steel have been analyzed in terms of Monkman-Grant relation and Larson-Miller parameter. The data analysis was supported by fractography, which is used to identify the cause of creep rupture failure.

6.2. Experimental details

6.2.1. Material and welding procedure

The chemical composition of ASTM A387 Grade 91 CL2 steel (Grade 91) used in this study can be found elsewhere [6]. The hot rolled Grade 91 plates were obtained from ArcelorMittal Plate LLC, in normalized and tempered condition (i.e., austenitized at 1038 K for 240 min. followed by air cooling, and tempered at 789 K for 43 min.). The as-received plates had dimensions of 104 mm×104 mm×12.7 mm. At room temperature, the as-received Grade 91 steel exhibited yield strength of 533 MPa, ultimate tensile strength of 683 MPa and elongation to fracture of 26%. The plates of aforementioned dimensions were cut into two halves and tapered on one side at 30^{o} to make a V-butt end. The double V-butt weld specimens were made by welding these two V-butt end halves together. Metrode 2.4 mm diameter 9CrMoV-N TIG filler wire having low residual elements were used for welding. The plates were preheated to 260^{o}C before welding. The steel plates were placed on an aluminum plate to prevent overheating during welding. Three successive passes were used to create the complete weld using a current of 130 A and voltage of 15 V. PWHT of the welded plates were carried out at 750^{o}C for 2 hr.

6.2.2. Microstructural characterization

Optical microscopy was performed on both the as-received and creep tested specimens for characterization of the grain structure. Conventional metallographic procedures of cold mounting, grinding and polishing were followed to prepare the specimen surface to 0.5 μm finish before etching was carried out using Marble's reagent; a solution made of 50 ml distilled water, 50 ml hydrochloric acid and 10 g of copper sulfate. Subsequently, an Olympus light microscope was used to examine the metallographic specimens and an attached CCD camera was used to record the micrographs.

For detailed microstructural characterization, some metallographic samples were examined using a Zeiss Supra 35VP field emission gun scanning electron microscope (FEG-SEM) operated at an accelerating voltage of 10-20 kV under both secondary and backscattered electron imaging modes. Energy dispersive spectroscopy (EDS) technique available in the SEM was used to estimate the relevant chemical compositions.

The ruptured samples were then sectioned from the gauge length of the specimen. For TEM study, the sectioned samples were mechanically polished down to ~120 μm thickness, and then 3 mm diameter disks were punched out of the samples. Those disks were then jet polished in Fischione twin-jet polisher using a solution of 80 volume% methanol and 20 volume% nitric acid solution at a temperature of ~-40^{o}C. Dry ice bath was used to achieve low temperature. Philips CM200 and JEOL JEM-2010 TEM operated at an accelerating voltage of 200 kV were used to study in detail the grain and precipitate morphology of the material under both as-received and crept conditions. Hardness was measured using Vickers microhardness tester – applied load was 500 g and the hold time was 15 s.

6.2.3. Creep testing

Creep tests were performed at different temperatures between 600^{o}C and 700^{o}C and stresses between 35 and 350 MPa using an Applied Test Systems (ATS) lever arm (20:1) creep tester. Though creep tests were intended for fracture, some tests in the lower stress regime were interrupted in the minimum creep stage due to time constrain.

6.3. Results and Discussion

6.3.1. Microstructural characteristics of as-received and as-welded material

The as-received Grade 91 steel had a tempered martensitic microstructure as shown in Fig. 6.1(a). Precipitation hardening is one of the main strengthening mechanisms in highly alloyed steels like Grade 91. Alloying elements, such as C, N, Nb, V, Cr and Mo, promote the formation of precipitates like Cr-rich $M_{23}C_6$, and Nb or V-rich MX particles, where M stands for metals, i.e., Cr, Mo, Nb or V, and X stands for C or N. The Cr-rich $M_{23}C_6$ precipitates are elongated rod-like or block-like particles, while Nb-rich and V-rich MX precipitates have nearly spherical shapes. These thermally stable fine precipitates enhance the long term creep resistance. A SEM micrograph in Fig. 6.1(b) shows the distribution of precipitates in the alloy. Coarser $M_{23}C_6$ type precipitates were located on the grain boundaries, lath boundaries and prior austenite grain boundaries, while finer MX type precipitates were located inside the grain. Microstructural features of welded specimen: the unaffected base material (BM), HAZ, and weld are shown in Fig. 6.2. Two distinct heat affected zone microstructure, i.e. coarse and fine grain structures, and an indistinctive columnar structure formed after directional solidification was observed in the weld, BM, fine grained, coarse grained, and weld microstructure are shown in Fig. 6.2(a), (b), (c), and (d), respectively.

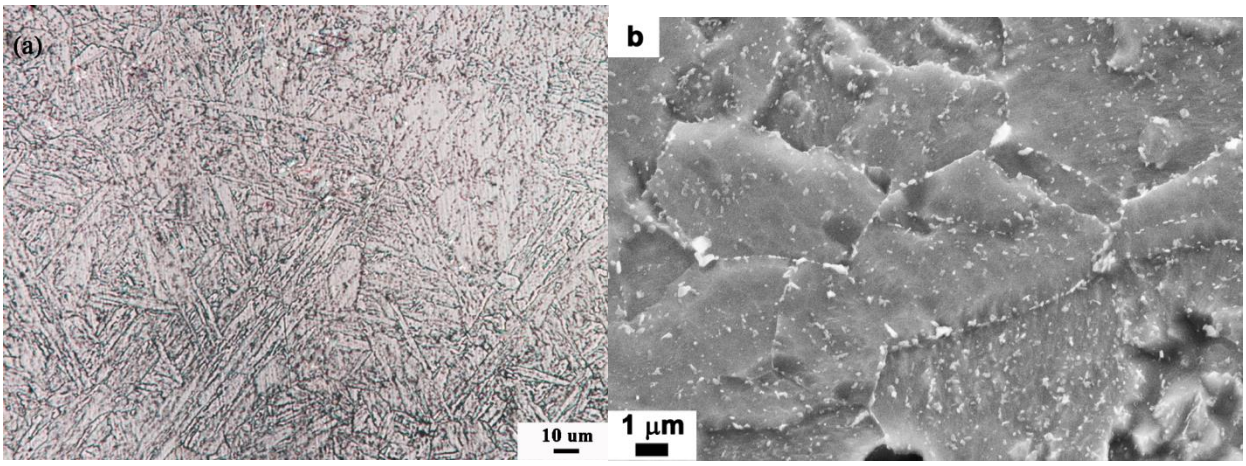

Fig. 6.1. Microstructure of as-received Grade 91 steel: (a) optical micrograph showing the tempered martensitic structure, and (b) SEM micrograph showing the distribution of precipitates.

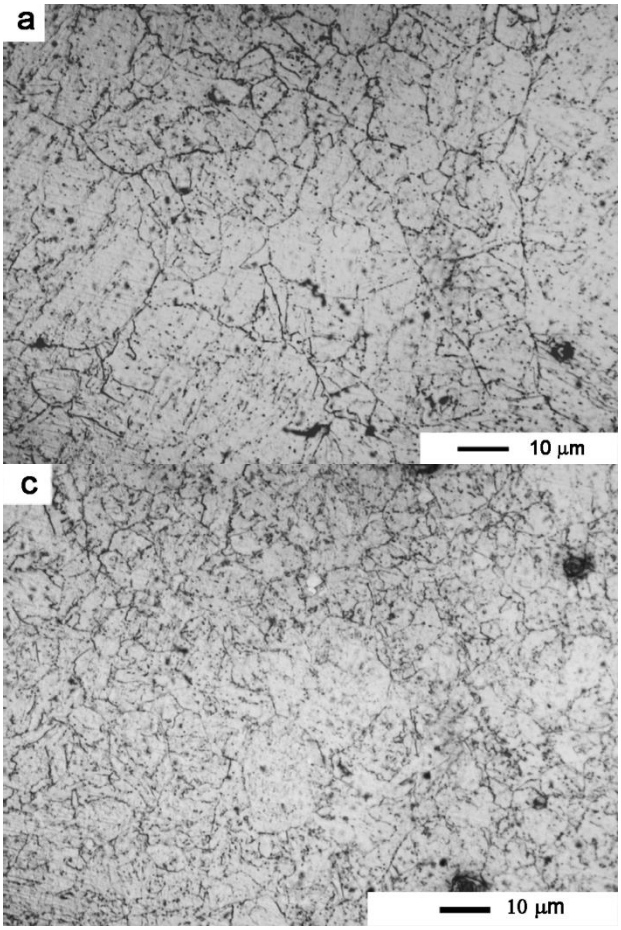

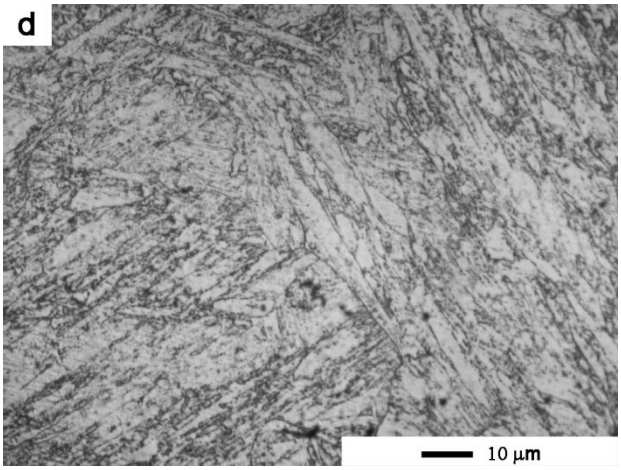

Fig. 6.2. Optical micrograph of welded microstructure (a) base material, (b) fine grain HAZ, (c) coarse grain HAZ, and (d) weld zone after post-weld heat treatment.

6.3.2. Creep properties

During the primary creep, the creep rate decreases with increasing strain due to work hardening via dislocation multiplication and interactions. In the secondary stage, creep rate is stabilized as the work hardening effect is counterbalanced by the dislocation annihilation and rearrangement. Finally, the creep rate accelerates as cavities start growing leading to the tertiary stage. Most creep curves obtained in this study consisted of two distinct regimes: primary and tertiary, and a minimum creep rate regime in the transition. Fig. 6.3a shows the effect of applied stress on the creep rate at a temperature of 600°C. Minimum creep rates increased but rupture time decreased with increasing applied stress. Fig. 6.3(b) shows the effect of test temperature on creep rate at a stress of 100 MPa. The minimum creep rates increased but rupture time decreases with increasing temperature. Table 6.1 lists the summary of creep rupture data.

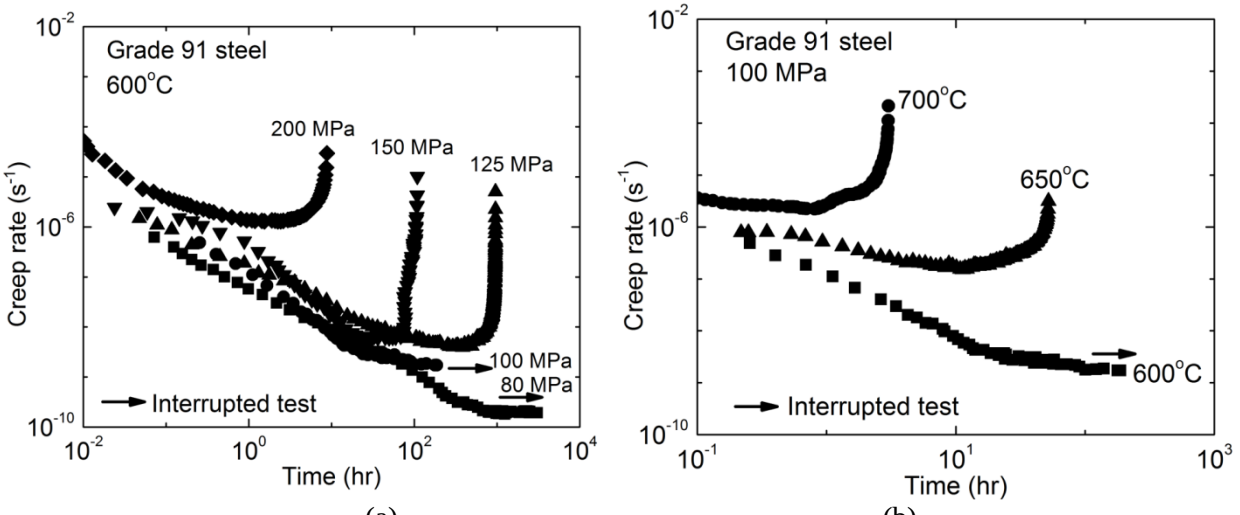

(a) (b)

Fig. 6.3. (a) The variation of creep rates as a function of stress at 600°C, and (b) the variation of creep rates with temperature at 100 MPa.

Table 6.1. Summary of creep rupture data of the welded Grade 91 steel

Temp. (oC)	Stress (MPa)	Fracture elongation (%)	Reduction in area (%)	True fracture Strain (ε_f)
(W7) 600	125	6	43	0.6
(W3) 600	150	8	74	1.4
(W4) 600	200	11	85	1.9
(W17)650	50	4	40	0.5
(W11) 650	80	6	48	0.7
(W2) 650	100	8	58	0.9
(W8) 650	125	9	73	1.3
(W1) 650	150	10	91	2.4
(W9) 700	50	7	52	0.7
(W13) 700	80	8	62	0.9
(W14) 700	100	10	80	1.6
(W15) 700	150	10	93	2.8
(W16)700	200	14	92	2.5

The total creep rupture life is related to the duration of primary and secondary creep stage by the following relationship

$$\frac{t_R{}^{\gamma}}{t_{ts}} = C, \tag{1}$$

where t_{ts} is the time to reach tertiary creep stage, t_R the rupture time, C and γ are constants. When t_{ts} data were plotted against t_R data in a double logarithmic scale, all the data fall on a straight line whose slope is the value of constant γ (~1.0) as shown in Fig. 6.4(a). It is noted that the relation between the time to reach tertiary creep stage and the rupture time is independent of temperature. Creep rupture data of monolithic and welded samples for various temperatures are presented as stress versus rupture time as shown in Fig. 6.4(b). The monolithic samples have better creep strength compared to welded ones. Here straight lines were obtained for each temperature. No change in the slope was noted for any particular temperature implying that the creep damage mechanism remained the same. Nevertheless, the knowledge of such microstructural instabilities is important since they could lead to significant errors in extrapolation of the data to longer time [27].

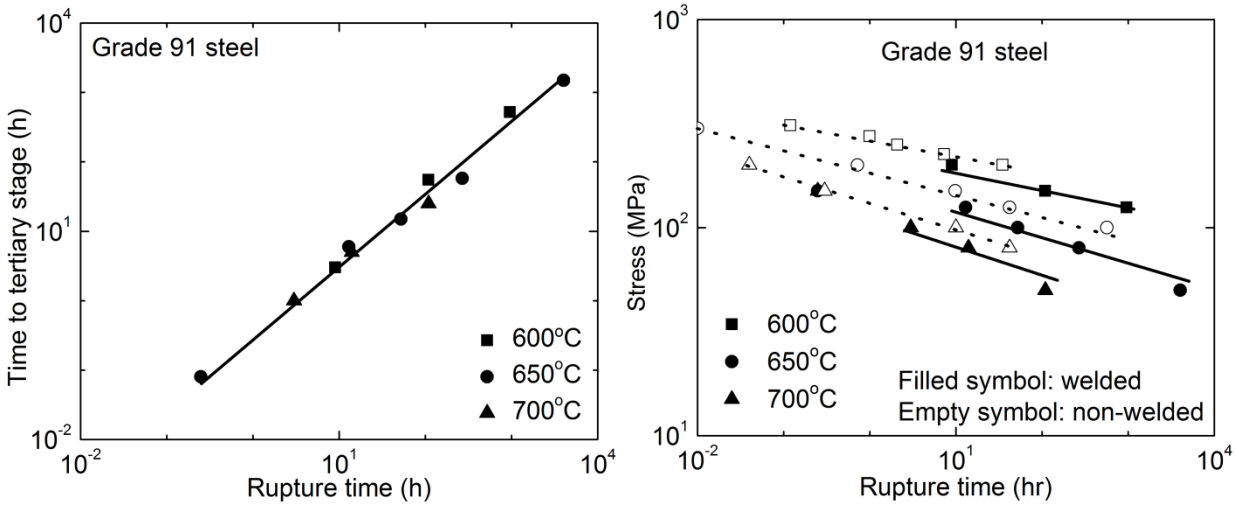

Fig. 6.4. (a) Relation between the creep rupture life and the time to get to tertiary creep stage, and (b) stress and temperature dependence of creep rupture life.

6.3.3. Microstructural and microhardness characteristics of crept specimen

Vickers microhardness tester was used to measure the hardness of Grade 91 steel before the creep test, as shown in Fig. 6.5. The hardness of weldment increased across the weld but decreased at HAZ. Hardness is the measure of resistance to plastic deformation that provides the microstructural information about the phases present. Due to the variation of microstructure and the gradient in thermal history of weldment, residual stresses reduce the creep life of the material by early onset of creep damage [28,29]. The presence of tensile residual stress in HAZ, as a result of heat treatment, accelerates the carbide coarsening, which enhances the formation of voids [12, 30-32] leading to creation of a soft zone. The hardness of the material increased across the weld, but decreased at HAZ as a result of the dissolution and coarsening of strength enhancing carbides. Moreover, as the material starts to cool down after welding, the FCC crystal structure of austenite phase undergoes diffusionless transformation to a BCT crystal structure, with an accompanying volume increase. This change in volume is associated with changing of the residual stress from tensile to compressive [33,34]. Thus, the increase in hardness values at the weld is related to martensitic transformation which leads to compressive residual stress in the weld. The decrease in microhardness at the HAZ reflects the presence of over-tempered martensite along with α-ferrite phase and retained austenite with dislocation and precipitates free microstructure. The ferrite and austenite phases are more prone to plastic deformation compared to the martensite phase [35]. Welding leads to the migration of carbon creating soft areas in the HAZ, which are likely the initiation sites of type IV cracking. The lowest hardness was measured in the HAZ because of the reduction in dislocation density, coarsening of precipitation, formation of polygonized structure, break-up of martensitic lath structure, and reduction in solid solution strengthening due to precipitation [36,37]. A similar hardness profile was reported by Sato et al. [38] across the welded joint of modified 9Cr-1Mo steel. The decrease in hardness reflects the diminished yield strength at the HAZ, which results in premature failure of the weldment [12]. HAZ having low yield strength is considered the soft zone in the weldment

which leads to preferential plastic deformation. Higher yield strength in the weld is due to the martensitic lath structure resulting in higher residual stresses in as-welded condition [39].

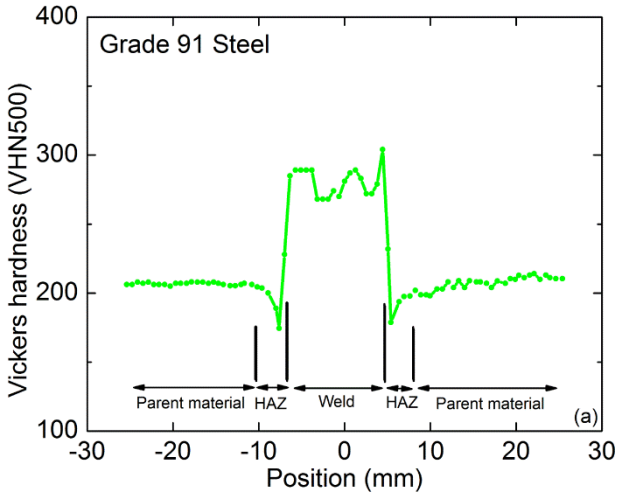

Fig. 6.5. Microhardness profile of specimen prior to creep test

6.3.4 Fractography

The creep specimens ruptured with limited external necking and the associated percentage reduction in area. The reduction in area (≥ 40%) of a welded sample was not as significant as in monolithic samples, which had reduction in area of ≥ 85%. For a particular temperature, reduction in area decreased with decrease in applied stress. Similarly true fracture strains of welded sample were ~0.7 in lower stress regime and ~2 in higher stress regime. This is distinctly differently compared to monolithic samples, which had true fracture strain of ≥ 2 in all stress regimes [7]. Heterogeneous microstructure across the weldment and limited reduction in load bearing cross-section is the cause for creep rupture. However, the significance of internal of internal necking through microstructural degradation, cavity formation, growth and coalescence must be taken into account to understand the final failure mechanisms. Laha et al. [12] and Albert et al. [15, 16] have reported increase in cavity density in HAZ. Furthermore, creep cavities and cracks starts from inside of a sample [40], and the cavity density was higher mid-thickness of the HAZ compared to outer or inner surface [16]. It is important to note that welded samples did not fail by complete necking implying that the internal damage processes had a significant bearing on their failure. Generally, cavities from throughout the creep deformation; however, in the tertiary stage nucleation and growth of cavities take place at an accelerated pace. Moreover, the grain size gradient, and presence of dislocation and precipitate free microstructure in the weldment makes it easier for cavities to form in welded samples.

SEM study of fracture surface of crept specimens revealed dominant dimple features, as shown in Fig. 6.6. These features are characteristic of transgranular mode of fracture. Similar fracture morphology was also reported by Laha et al. [12] in welded Grade 91 steel. Fig. 6.6 shows the SEM micrograph of ruptured sample crept at 600^{o}C and 125 MPa: (a) Low magnification fracture surface and (b) high magnification micrograph showing dimpled fracture surface. Fig. 6.6 (c) show the SEM micrograph of ruptured surface crept at 600^{o}C and 125 MPa, and Fig. 6.6 (d) shows SEM micrograph of ruptured surface crept at 700^{o}C and 200 MPa.

Sample crept at 700°C and 200 MPa had the transgranular fracture mode, but the number density of cavities was lower while the average size was larger. For creep-enhanced diffusive cavity growth, increasing stress leads to greater cavity growth rates and coalescence resulting in a smaller number density and larger dimple size. Please note that, sample crept at 600°C and 125 MPa had reduction in area of about 43% and true fracture strain of about 0.6, while sample crept at 700°C and 200 MPa had reduction in area of about 92% and true fracture strain of about 2.5. The entire creep specimen dominantly failed in transgranular mode. Creep cavities observed were found to be round or elliptical shaped (*r*-type crack). Growth of incipient *r*-type crack is controlled by diffusion but as the cavity size increases they grow by power law creep, and in transition they grow as a coupled effect of diffusion and power law creep [41]. While precipitates increase the creep strength of materials by impeding the dislocation motion, they act as the stress concentration sites for cavity nucleation during creep deformation. Creep damage in general is due to the combined effect of cavity nucleation, growth and coalescence. The cavities act as a stress raiser where the localized stress exceeds the applied stress. Because of some ductility of the steel, the stress concentration site undergoes plastic deformation. Ultimately, excessive plastic strain at the particle-matrix interface will lead to decohesion. That phenomenon can be further exacerbated via grain boundary sliding if the particle is located at the grain boundary [42].

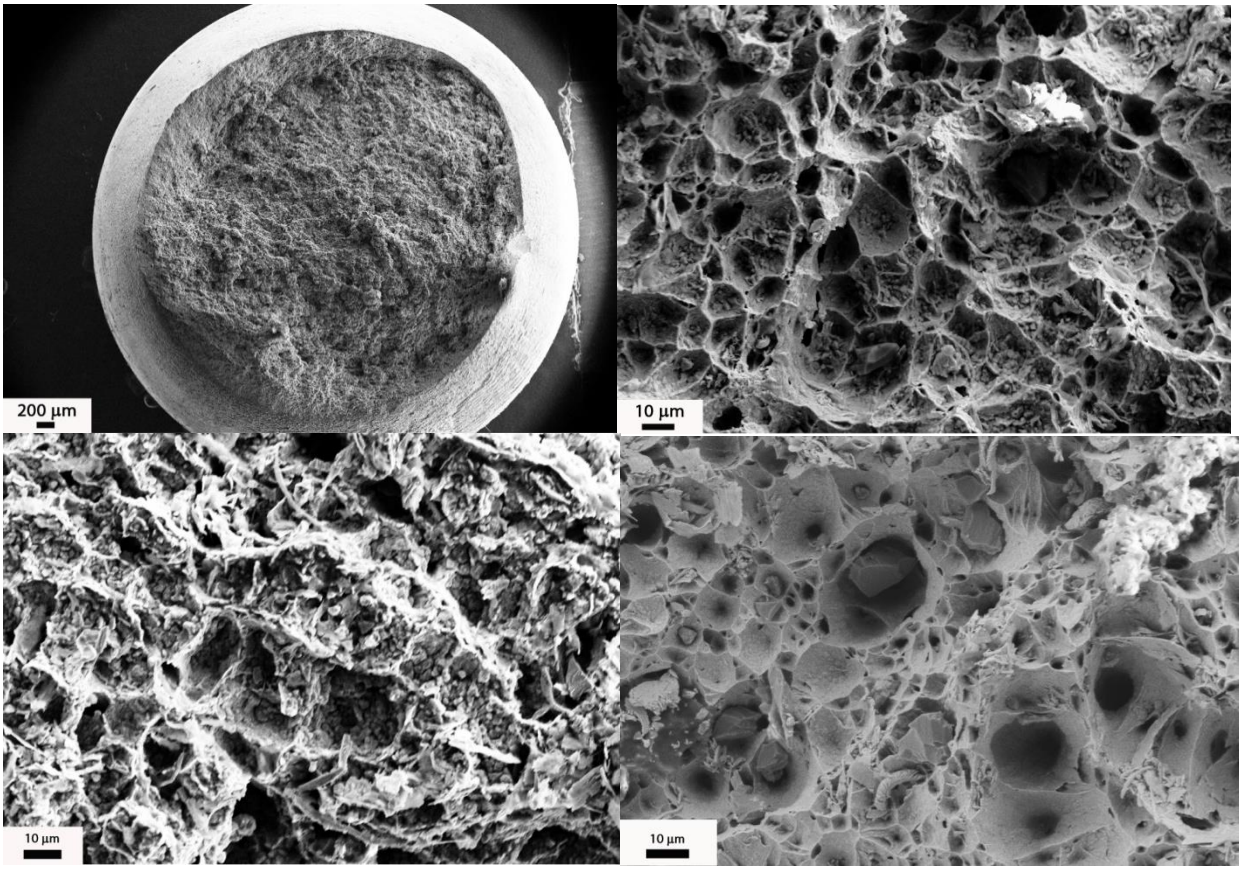

Fig. 6.6. SEM micrograph of ruptured sample crept at 600°C and 125 MPa: (a) Low magnification fracture surface and (b) high magnification micrograph showing dimpled fracture surface, (c) SEM micrograph of ruptured surface crept at 600°C and 125 MPa, and (d) SEM micrograph of ruptured surface crept at 700°C and 200 MPa.

SEM was used to study the cavitation in crept specimen. Fig. 6.7(a) shows a low magnification SEM micrograph of cavities present in sample crept at 600ºC and 125 MPa. The necked area next to the fractured surface appears to have the higher density of cavity, while the cross section away from the fracture surface had limited cavitation. The extent of cavitation depends on the amount of local strain. Fig. 6.7(b) shows the variation of true local strain and Vickers microhardness of sample crept at 650ºC/80 MPa, and 600ºC/125 MPa, respectively. The fracture point is indicated as '0' which has the highest true strain of ~0.7 and lowest hardness of 56. Interestingly, sample crept at 650ºC/80 MPa had almost no true local strain at the weld and the base material. Thus, the deformation of was localized in the HAZ. The other HAZ that did not fracture has true localized strain of ~0.5. Similarly, sample crept at 600ºC/125 MPa had lowest microhardness values at the HAZ that fracture and other HAZ that did not fracture. The weld had the highest hardness value, similar to the one shown in Fig. 5. HAZ where the creep damage is concentrated and has high true strain undergoes true tertiary stage, while other parts on the gauge showing little true strain have not reached the tertiary creep stage. However, the HAZ section undergoing tertiary creep is so dominant that it becomes responsible to the final failure of the specimen.

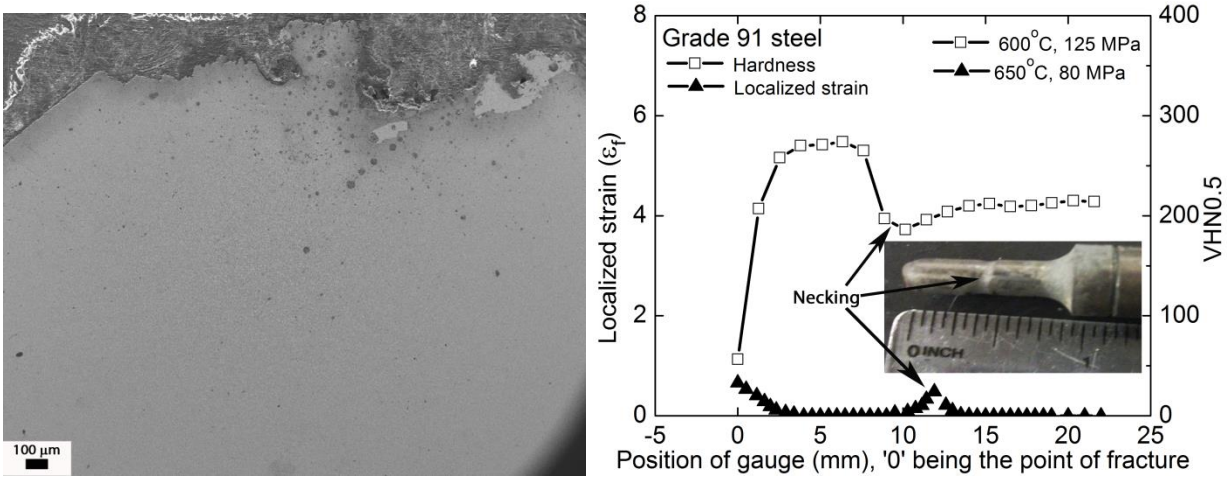

Fig. 6.7. (a) Low magnification SEM micrograph of cavities present in sample crept at 600ºC and 125 MPa, (b) variation of true local strain and microhardness with position in specimens fractured at 650ºC/80 MPa and 600ºC/125 MPa.

3.5. Creep rupture data analysis and life prediction

The relationship between minimum creep rate and rupture life is given by the Monkman-Grant equation [43]

$$\dot{\varepsilon}_m{}^m t_R = K_1, \tag{2}$$

where $\dot{\varepsilon}_m$ is the minimum creep rate, t_R the rupture time, m and K_1 are constants. The value of $K_1 = 0.07$ was obtained from straight line fit of the logarithmic relation deduced from Equation 6.2. Nabarro [44] noted that for better prediction of creep rupture life m needs to be less than 1.

In this study, the *m* was calculated to be 0.83. Thus, using the above relationship creep rupture life can be predicted based on the experimentally determined minimum creep rate.

Monkman and Grant [43] and Evans [45] found that the value of K_1 was 0.04 for monolithic ferritic steel and 0.08 for monolithic austenitic steel, and predicted that the K_1 to be less than n^{-1}. The stress exponents of welded creep sample were ~8, which is common in engineering alloys like Grade 91 steel. The inverse of the calculated stress exponent (*n*) was ~0.12. The fit in Fig. 8a resulted in K_1 to be 0.07. For a material to fail by complete necking, K_1 has to be equal to n^{-1} [45]. Thus, necking is not the dominant fracture mode in the creep rupture tests reported in this study.

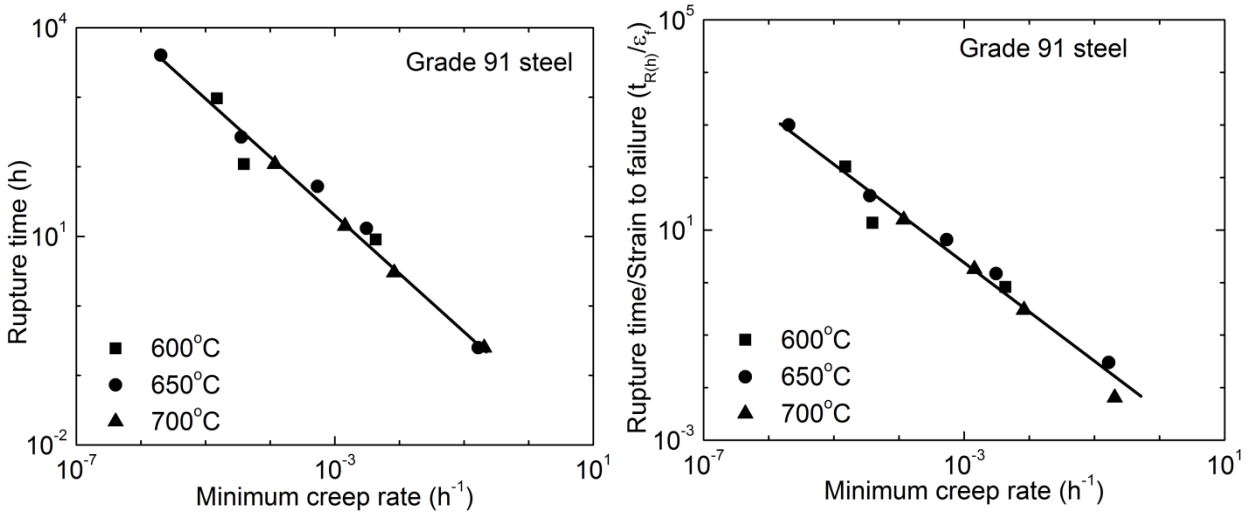

Fig. 6.8. (a) Monkman-Grant relation, and (b) modified Monkman-Grant relation.

With regards to engineering alloys like Grade 91 steel, Dobes *et al.* [46] modified the aforementioned Monkman-Grant relation to obtain better correlation of the rupture time with the minimum creep rate by an equation

$$\dot{\varepsilon}_m{}^{m'} \frac{t_R}{\varepsilon_f} = K_2, \tag{3}$$

where ε_f is the strain at fracture (based on elongation to fracture), K_2 and m' are constants. The value of $K_2 = 0.45$ was found from the fitting of logarithmic plot deduced from Equation 6.3, as shown in Fig. 8b. Eq. 6.3 was used to calculate the creep damage tolerance factor, λ. For $m' = 1$, λ is given by inverse of K_2 [47,48]. The creep damage tolerance factor is used as a measure to identify the creep rupture mode whose value for engineering alloys range from 1 to 20 [48]. For $\lambda = 1$, materials have low creep strain, and brittle fracture mode is detected as they fracture without any significant plastic deformation, while large values indicate that the material can withstand strain concentration without local cracking and the fracture is ductile [44,48]. Ashby and Dyson [48] suggested that λ in the range of 1.5 and 2.5 indicates that damage is due to the cavity growth resulting from combined effect of power law and diffusion creep. Incipient cavities grow by diffusion, but power law creep takes over as they become larger [41]. High λ value was attributed to the absence of intergranular cracks, absence of wedge shaped cracks, and the microstructural degradation like precipitate coarsening. Dominant creep damage mechanism is necking for λ higher than 2.5 [48], while coarsening of precipitates and subgrains, and

decrease in dislocation density are the dominant creep damage mechanism when λ is 5 or higher [48,49]. Creep damage tolerance λ of 1.5 was observed in MA957, an yttrium bearing oxide dispersion strengthened (ODS) ferritic alloy, which fractured with little evidence of neck formation [50]. In this study, creep damage tolerance factor of ~2.2 was observed. The λ of ~2.2 indicates that the creep damage is due to the cavity growth resulting from combined effect of power law and diffusion creep, necking and microstructural degradation. Coarsening of precipitates and subgrains which were observed in Grade 91 steel [8,9-11] can decrease the creep strength as they become less effective in disrupting the movement of mobile dislocations [6, 51]. Monolithic Grade 91 steel had creep damage tolerance of ~4, and the dominant failure mechanism was microstructural degradation with contribution from necking and void growth [7]. The welded Grade 91 steel had creep damage tolerance of ~2, meaning that the dominant failure mechanism is void growth with microstructural degradation without significant necking. This is illustrated in diagnostic diagram for creep failure as shown in Fig. 6.9. The figure shows that all the creep fracture data reported in this study fell on the microstructural degradation and void growth domain with lower fracture strain. Moreover, the creep rupture data of welded Grade 91 steel were compared with that of monolithic sample. The dominant creep fracture mechanism in precipitation strengthened monolithic Grade 91 steel was microstructural degradation with limited contribution from void growth, while welded Grade 91 steel with complex microstructure (as show in HAZ) exhibits void growth compounded by microstructural degradation – primarily at the heat affected zone. Parker et al. [17] reported the type IV cracking in welded Grade 91 steel as result of cavity nucleation and growth.

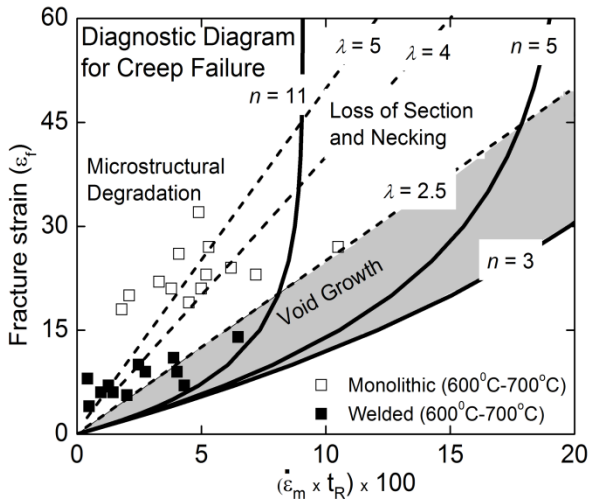

Fig. 6.9. A diagnostic diagram for creep failure of Grade 91 steel

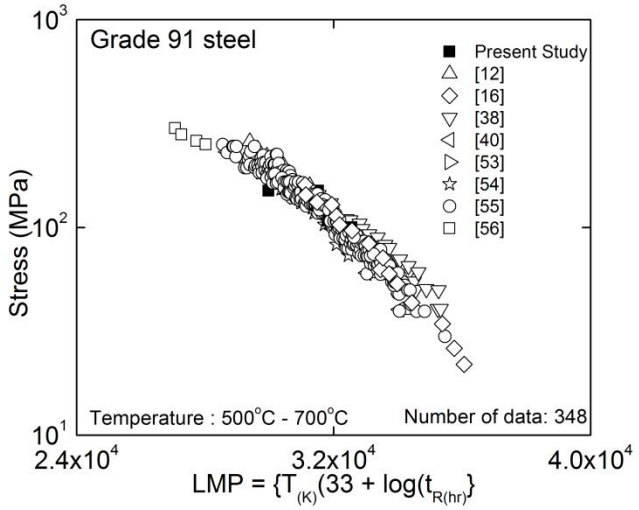

Fig. 6.10. Larson-Miller parameter plot of Grade 91 steel

Larson-Miller parameter (LMP) was used for predicting creep rupture life of welded Grade 91 steel. LMP can be expressed in terms of rupture time and temperature as

$$LMP = T(logt_R + C), \quad (4)$$

where T is the temperature (K), t_R the rupture time (hr), and C the Larson-Miller constant, typically taken as 33. LMP values of Grade 91 steel decrease with increased stress, and the data obtained in the present study remain within the ambit of the data band obtained from other studies, as shown in Fig. 6.10. A best fit polynomial equation for stress versus LMP plot, Fig. 6.10, was used to predict the creep life of Grade 91 steel in the 500-700°C temperature range. Table 6.2 lists the allowable creep stress predictions for Grade 91 steel. Thus, predicted creep life for 10^5 h rupture life is lower than the ones predicted for monolithic samples. Even though the Monkman-Grant relation and LMP can be used to predict rupture life, it does not provide us with insights of the creep failure mechanisms. These approaches are empirically based, so their use may not lead to the precise estimation of the creep rupture life.

Table 6.2. Creep strength prediction of Grade 91 steel by LMP

Temp (°C)	**Rupture life (h)**	**Monolithic: Allowable Stress (MPa)**	**Welded: Allowable stress (MPa)**
500	10^5	241	208
525	10^5	199	171
550	10^5	161	132
575	10^5	123	102
600	10^5	91	74
625	10^5	68	53
650	10^5	47	37
675	10^5	33	23
700	10^5	21	15

6.4. Conclusions

The creep rupture behavior of welded Grade 91 steel was studied in the temperature range of 600ºC to 700ºC and at stresses 50-200 MPa. The fractography of creep ruptured samples revealed transgranular failure mode with dimpled fractures surfaces. The creep rupture data was analyzed in terms of Monkman-Grant relation, modified Monkman-Grant relation and Larson-Miller parameter. The creep damage tolerance factor was used to identify cavity growth compounded by microstructural degradation as the dominant creep rupture mechanism.

References

[1] I. Charit, K. L. Murty, Structural materials issues for the next generation fission reactors, JOM 62 (9) (2010) 67-74.

[2] K. L. Murty, I. Charit, Structural materials for Gen-IV reactors: challenges and opportunities, J. Nucl. Mater. 383 (2008) 189-195.

[3] D. Rojas, 9-12% Cr heat resistant steels: alloy design, TEM characterization of microstructure evolution and creep response at 650ºC, Doctoral dissertation, Ruhr-University Bochum, Bochum, Germany, 2011.

[4] R. Vishwanathan, W. T. Bakker, Materials for boilers in ultra-supercritical power plants, ASME, Proceedings of 2000 International Joint Power Generation Conference, Miami Beach, Florida, July 23-26 (2000) 1-22.

[5] B. J. P. Buhre, R. Gupta, S. Richardson, A. Sharma, C. Spero, T. Wall, PF-Fired Supercitical Boilers: Operational Issues and Coal Quality Impacts, CCSD, March 2002.

[6] T. Shrestha, M. Basirat, I. Charit, G.P. Potirniche, K.K. Rink, J. Nucl. Mater. 423 (2012) 110-119.

[7] T. Shrestha, M. Basirat, I. Charit, G.P. Potirniche, K.K. Rink, Mater. Sci. Eng. A 565 (2013) 382-391.

[8] C. G. Panait, A. Zielinska-Lipiec, T. Koziel, A. Czyrska-Filemonowicz, A-F. Gourgues-Lorenzon, W. Bendick, Mater. Sci Eng A 527 (2010) 4062-4069.

[9] K. Sawada, H. Kushima, M. Tabuchi, K. Kimura, Mater. Sci. Eng. A 528 (2011) 5511-5518.

[10] V. Sklenicka, K. Kucharova, M. Svoboda, L. Kloc, J. Bursik, A. Kroupa: Mater. Charact. 51 (2003) 35-48.

[11] J. Hald, Int. J. Pressure Vessels Piping 85 (2008) 30-37.

[12] K. Laha, K.S. Chandravathi, P. Parameswaran, K. Bhanu Sankara Rao, and S.L. Mannan, Metall. Mater. Trans. A 38 (2007) 58-68.

[13] P. Mayr, Evolution of microstructure and mechanical properties of the heat affected zone in B-containing 9% chromium steels, Doctoral dissertation, Graz University of Technology, Austria, 2007.

[14] S. Spigarelli and E. Quadrini, Mater. Design, 23 (2002) 547-552.

[15] S. K. Albert, M. Matsui, T. Wanatabe, H. Hongo, K. Kubo, M. Tabuchi, Int. J Press. Vessel, 80 (2003) 405-413.

[16] M. Yaguchi, T. Ogata, and T. Sakai, Int. J Press. Vess. Pip., 87 (2010) 357-364.

[17] J. Parker, Int. J Press. Vess. Pip., (2012) Dec. 22, 1-12.

[18] Y. Li, Y. Monma, H. Hongo, M. Tabuchi, J Nucl. Mater. 4005 (2010) 44-49.

[19] M. L. Santella, S. S. Babu, R. W. Swindeman, E. D. Specht, In-situ characterization of austenite to martensite decomposition in 9Cr-1Mo-V steel welds, Proc. Austenite Formation & Decomposition Symposium, TMS, Nov. 09-12, 2003, Chicago, IL USA.
[20] V. T. Paul, S. Saroja, P. Hariharan, A. Rajadurai, and M. Vijayalakshmi, J Mater Sci 42 (2007) 5400-5713.
[21] S. J. Sanderson, (1983) In: A. K. Khare (ed) Proceedings of conference on ferritic steels for high-temperature applications. Warrendale, PA, 1981. ASM Metals Park, p 85
[22] M. Vijayalakshmi, S. Saroja, V. T. Paul, R. Mythili, V. S. Raghunathan, Metall Trans 30A (1999) pp. 161
[23] R. Kishore, R.N. Singh, T. K., Sinha B. P. Kashyap, J Nucl. Mater 195 (1992) pp. 198
[24] O. Grong, In: Metallurgical modelling of welding, 2nd edn. (1997), The Institute Of Materials, London, UK, pp. 28
[25] Y. You and R. Shiue, J Mater. Sci. Lett. 20 (2001) 1429-1432.
[26] B. Arivazhagan, R. Prabhu, S. K. Albert, M. Kamaraj, and S. Sundaresen, J Mater. Eng. Perf. 18(8) (2009) 999-1004
[27] G.E. Dieter, Mechanical Metallurgy, 3rd ed., McGraw-Hill, Boston, MA, 1986.
[28] M. Turski, A. H. Sherry, P.J. Bouchard, P.J. Withers, J. Neutron Res. 12(1-3) (2004) 45-49.
[29] P. J. Bouchard, P. J. Withers, S. A. McDonald, R. K. Heenan, Acta Mater. 52(1) (2004) 23-34.
[30] S. K. Albert, M. Matsui, H. Hongo, T. Watanabe, K. Kubo, M. Tabuchi, Int. J. Press. Vess. Pip. 81 (2004) 221–234.
[31] D. Li, K. Shinozaki, Sci. Technol. Weld. Join. 10(5) (2005) 544–549.
[32] T. Watanabe, M. Yamazaki, H. Hongo, M. Tabuchi, T. Tanabe, Int. J. Press. Vess. Pip. 81 (2004) 279–284.
[33] A. R. Pyzalla, Internal stresses in engineering materials, in: W. Reimers, A.R. Pyazalla, A. Schreyer, H. Clemens (Eds.), Neutrons and Synchrotron Radiation in Engineering Materials Science, Wiley-VCH, Weinheim, 2008, pp. 21-56.
[34] H. Dai, J.A. Francis, H.J. Stone, H.K.D.H Bhadeshia, P.J.Withers, Met. Mater. Trans. A 39 (2008) 3070-3078.
[35] E. Barker, Mater. Sci. Eng. 84 (1986) 49-64.
[36] S.A. David, T.Debroy, Sci. 257 (1992) 497-502.
[37] M. Regev, S. Berger, B.Z. Weiss, Weld. J. 75 (1996) 261s-268s.
[38] T. Sato, K. Tamura, Advances in Materials Technology for Fossil Power Plants: Proceedings of the 5th International Conference, Oct. 3-5, 2007, Marco Island, FL, USA, ASM Int., 2008, pp. 874-883.
[39] D. Dean, M. Hidekazu, Comput. Mater. Sci. 37 (2006) 209-219.
[40] M. Yamazaki, T. Watanabe, H. Hongo, M. Tabuchi, J Pow. Eng. Sys. 2(4) (2008) 1140-1149.
[41] A. C. F. Cocks, M.F. Ashby, Prog. Mater. Sci. 27 (1982) 189-244.
[42] H. Riedel, Fracture at High Temperatures, Springer-Verlag Berlin, Heidelberg, Germany, 1987, pp. 215-24.
[43] F. C. Monkman, N.J. Grant Proc. ASTM 56 (1956) 593-620.
[44] F.R.N. Nabarro, H. L. de Villiers, The Physics of Creep, Taylor & Francis, London, 1995, pp. 22-25.

[45] H. E. Evans: Mechanics of Creep Fracture, Elsevier Applied Science Publishers, New York, NY, 1984, pp. 18-22.
[46] F. Dobes, K. Milicka, Metal Sci. 10 (1976) 382-384.
[47] F.A. Leckie, D.R. Hayhurst, Acta Metall. 25 (1977) 1059-1070.
[48] M. F. Ashby, B.F. Dyson: in Advances in Fracture Research, Eds. S.R. Valluri et al. Vol. 1, Pergamon Press, Oxford, 1984, pp. 3-30.
[49] B. K. Choudhary, C. Phaniraj, B. Raj, Trans. Indian Inst. Met. 63 (2010) 675-680.
[50] B. Wilshire, H. Burt, Z. Metallkd. 96 (2005) 552-557.
[51] M. Basirat, T. Shrestha, G.P. Potirniche, I. Charit, K. Rink, Int. J. Plast. 37 (2012) 95-107.
[52] V.S. Srinivasan, B.K. Choudhary, M.D. Mathew, T. Jayakumar, Mater. High Temp. 29 (2012) 41-48.
[53] F. Masuyama, Int. J Press. Vess. Pip, 83 (2006) 819-825.
[54] S. J. Brett, D. J. Allen, L. W. Buchanan, The type IV creep strength of Grade 91 materials. In: Proceedings of the third international conference on integrity of high temperature welds. Institute of Materials; 2007, pp. 409-20.
[55] M. Tabuchi and Y. Takahashi, J Pres. Vess. Tech. 134 (2012) 031401-031401-6.
[56] F. Vivier, J. Besson, A. F. Gourgues, Y. Lejeail, Y. de Carlan, and S. Dubiez, in: Creep behavior and life prediction of ASME Gr. 91 steel welded joints for nuclear power plants, eds. Le Goff et al., Mines-Paris Tech, France, 2008, pp. 1-2.

Task 2: Testing of damage levels in aged pressure vessels with the Kr-85 leak rate method

2.1 Introduction

In this task small pressure vessels were manufactured by two welding techniques and their creep properties were estimated by measuring damage in the weld zone and by the leak rate measurement technique. Pressure vessels intended for thermal creep testing were machined from grade 91 alloy steel. Vessels were machined in two separate halves and then joined by inertia or TIG welding. Fabrication using the two different welding techniques was of interest since it is well-known that the orientation of the material microstructure is dependent on the fabrication process. More specifically, forging techniques produce microstructures that are aligned with the axis of the vessel as compared to the random microstructure observed in vessels machined from solid billets. Understanding the reliability of different weld processes and their effect on vessel integrity is also one of the major goals of this research. The hermetic integrity of inertia welds is of particular interest due to their relatively insensitivity to manufacturing process parameters (i.e. alignment, surface finish, cleanliness, etc.) compared to TIG welding techniques. The long-term behavior of these welds and their resistance cracking, corrosion, and other possible mechanisms of degradation is studied through microscopic inspection of random vessels that are periodically withdrawn from study, drained of high-pressure gases, and then sectioned for detailed metallurgical analysis.

2.2 Manufacturing of the inertia pressure vessels

A typical inertia welded pressure vessel is shown in Fig 2.1. Internal volumes in each half were formed by a simple boring process. Each vessel featured a specially-designed fill port through which gases could be introduced into the pressure vessels and then sealed using a ball weld process.

The internal geometry of the inertia-welded units differed from that of the TIG welded specimens due to the nature of the weld process. The TIG welded parts were bored to an internal diameter of 0.25” with a wall thickness of 0.564”. This relatively thick wall was necessary to ensure the specimens had an adequate safety factor given the fill pressure of 7000 psi (at 20°C) followed by thermal conditioning at 700°C. This extremely thick wall necessitated that the two halves joined by TIG welding be done in a tedious series of fillet welds preceded by the proper preheat treatment followed by adherence to the specified interpass and cooling temperatures.

Fig. 2.1. A typical pressure vessel manufactured from two halves cylinders by inertial welding technique.

The inertia welded specimens featured larger internal diameters in order to accommodate the weld. In inertia welding, a small amount of material termed the “weld curl” is displaced during the weld resulting in a slight shortening of the part. This shortening is commonly termed the weld “upset”. Some of this material is transported away from the weld externally while an equal amount is displaced internally. Therefore, during inertia welding, some material enters the internal cavity of the part thereby reducing the internal volume. In order to ensure the internal volume of the inertia-welded parts was not completely filled by weld upset material the vessels were bored to internal diameters of 0.628” and wall thickness was set at 0.375”. Thus the outside diameters of the inertia-welded and TIG welded vessel were equal at 1.378”. This is the maximum diameter that the scintillation crystal radiation detectors used in the research can accommodate.

Inertia welding was accomplished using an MTI Model 120 inertia welder fitted with a 3 in-diameter spindle tool and 11 in-outer diameter flywheel. During welding operations, the rotational inertia (one of the most important parameters in the inertia welding process) of the transmission, spindle, chuck, collet, backing plate, and flywheel assembly was approximately 11.725 lb/ft^2. Flywheel speed was set at 4500 rpm and flywheel force ranged from 26,137 lb to 28,010 lb, averaging about 27,500 lb. The resulting weld upset was typically 0.045”.

2.3 Hardness measurements

Inertia pressure vessel specimens were sectioned using a wire EDM process, polished and then acid-etched using HNO_3/H2O and HCL/H_2O solutions so the quality of the weld could be

examined and tested. Hardness values were measured using a Vickers indenter with a 500 gram load. Vickers Hardness values, HV, are noted in the cross-sectional views of the weld zones in the location they were measured, as shown in Fig. 2.2. In general, the quality of the inertia weld was found to be excellent.

Pressure vessels were first filled with a mixture of the Kr-85 and air (0.01% ^{85}Kr, molar basis) at very low pressures (2.0 mm Hg) followed by a high pressure (approximately 6000 to 7500 psi) mixture of argon and helium (80% Ar/20%He, molar basis). The weight of each pressure vessel was recorded after filling and an initial reading of the Kr-85 content was recorded. In this manner, leaks from the pressure vessel may be detected by mass loss (a gross or large leak check) or by reduction in Kr-85 greater than that expected by inherent radioactive decay. Leak detection by monitoring the reduction in Kr-85 content through gamma ray counting is considered the most sensitive leak detection technique available.

Hardness and microstructure were requested across the inertia weld zones of two specimens labeled 1 and 4. Hardness values were measured using a Vickers indenter with a 500 gram load. Vickers Hardness values, HV, are noted in cross section views of the weld zones in the locations where they were measured. Microstructure photos were taken at various noted locations across the weld zones. The etch solution used for general structure features was 10ml HNO_3, 20ml HCl and 30ml H_2O. The data are shown in the following figures.

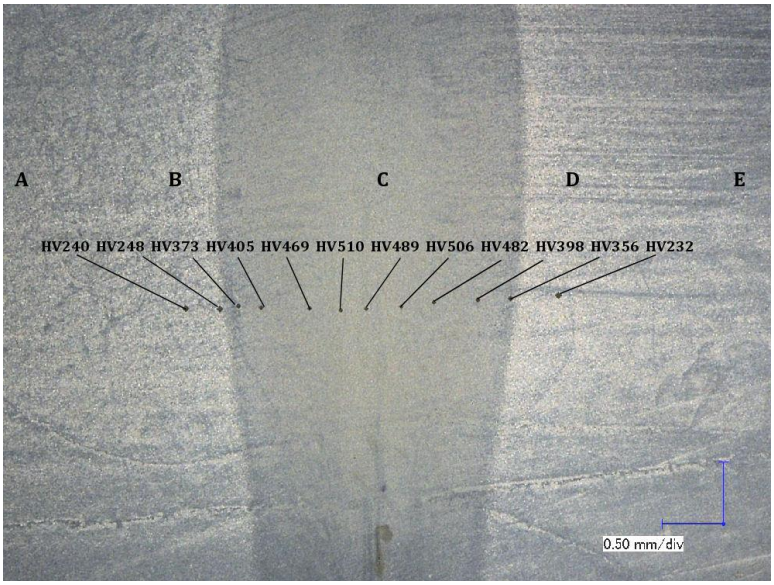

Fig. 2.2. Hardness values and microstructure photo locations for specimen 1.

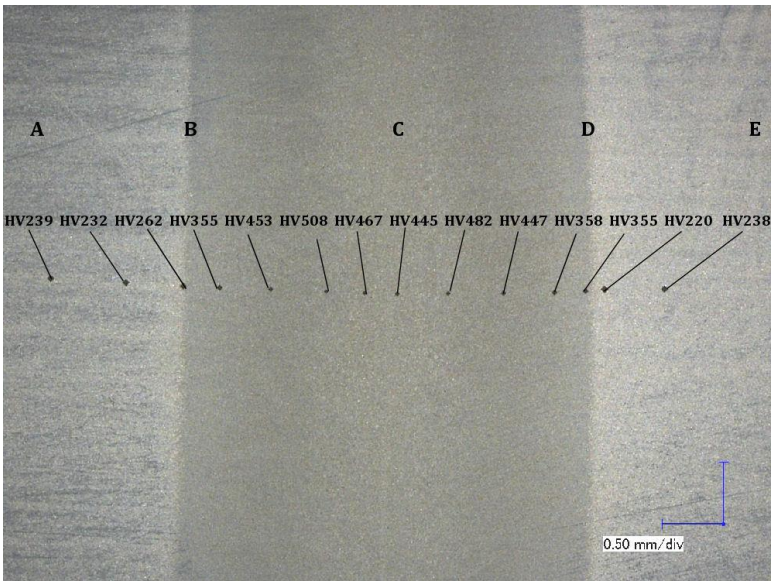

Fig. 2.3. Hardness values and microstructure photo locations for specimen 4.

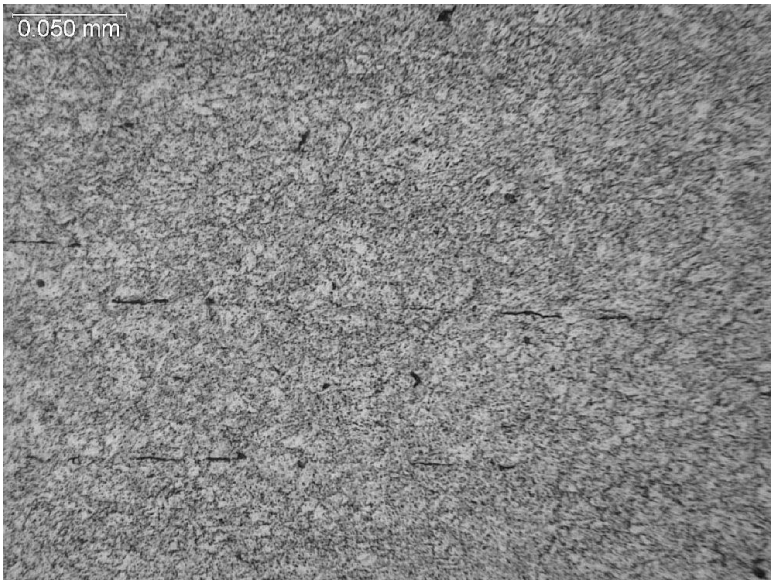

Fig. 2.4. Microstructure, location A, Fig. 2.1.

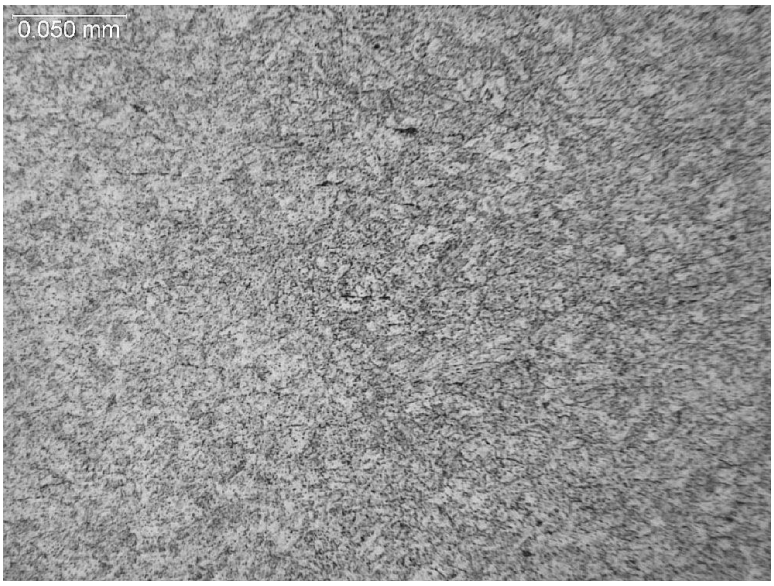

Fig. 2.5. Microstructure, location B, Fig. 2.1.

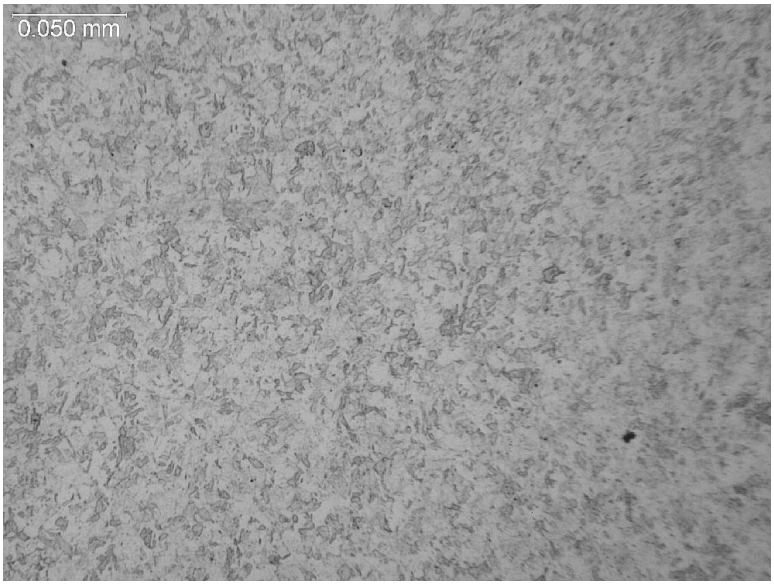

Fig. 2.6. Microstructure, location C, Fig. 2.1.

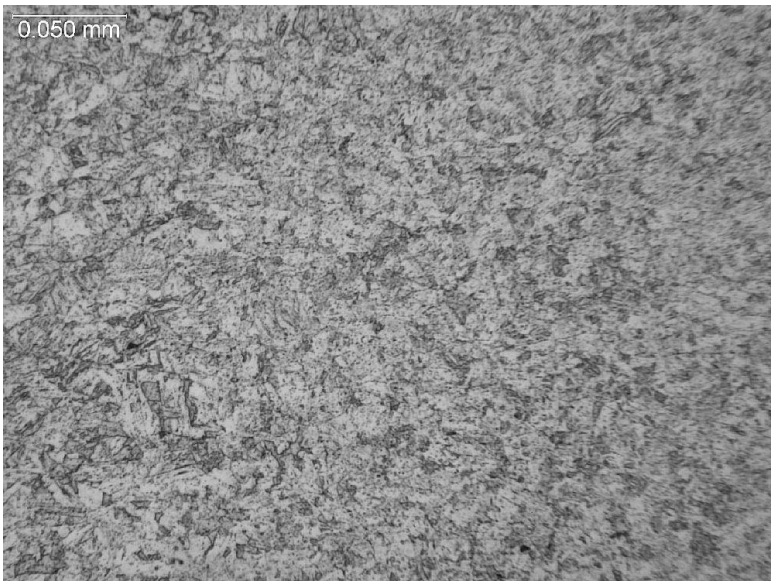

Fig. 2.7. Microstructure, location D, Fig. 2.1.

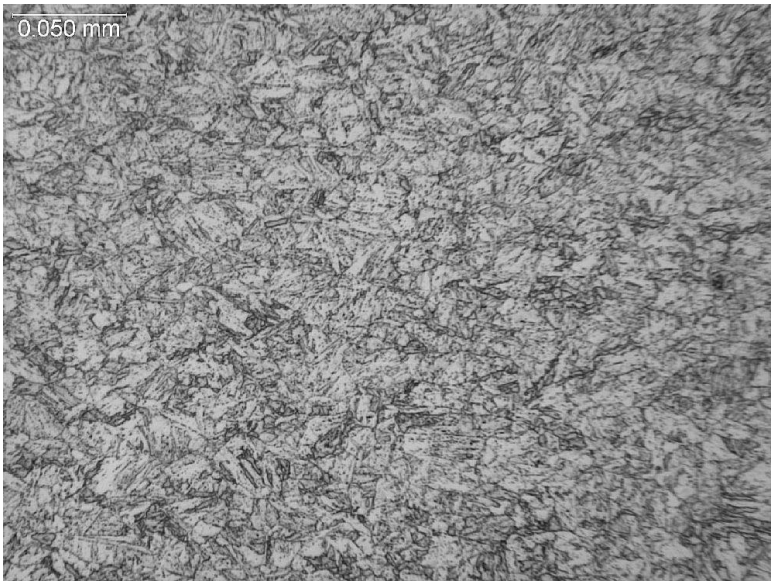

Fig. 2.8. Microstructure, location E, Fig. 2.1.

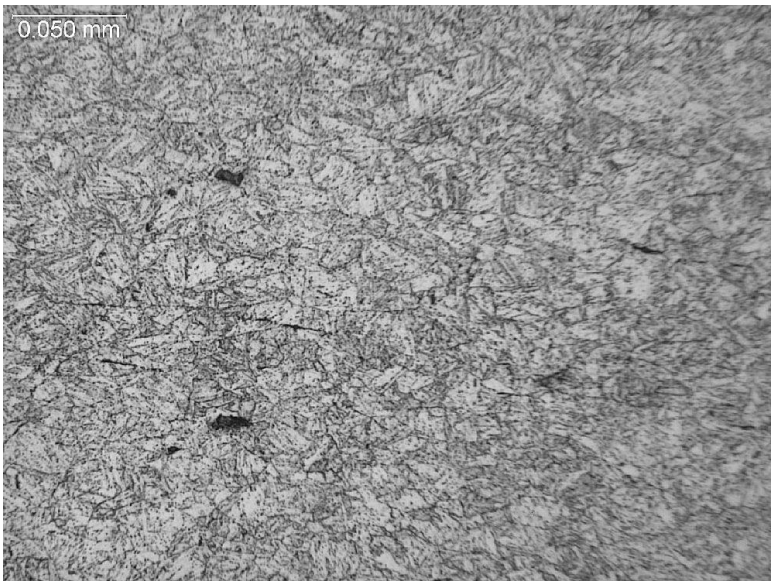

Fig. 2.8. Microstructure, location A, Fig. 2.2.

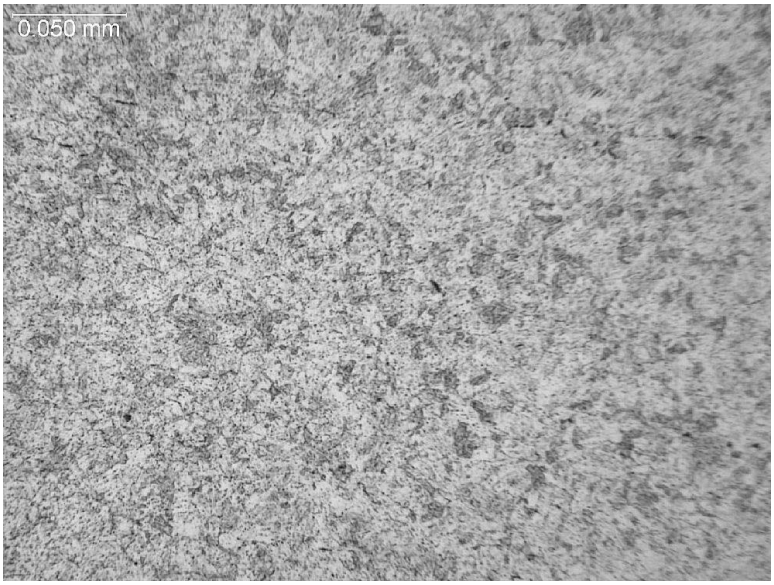

Fig. 2.10. Microstructure, location B, Fig. 2.2.

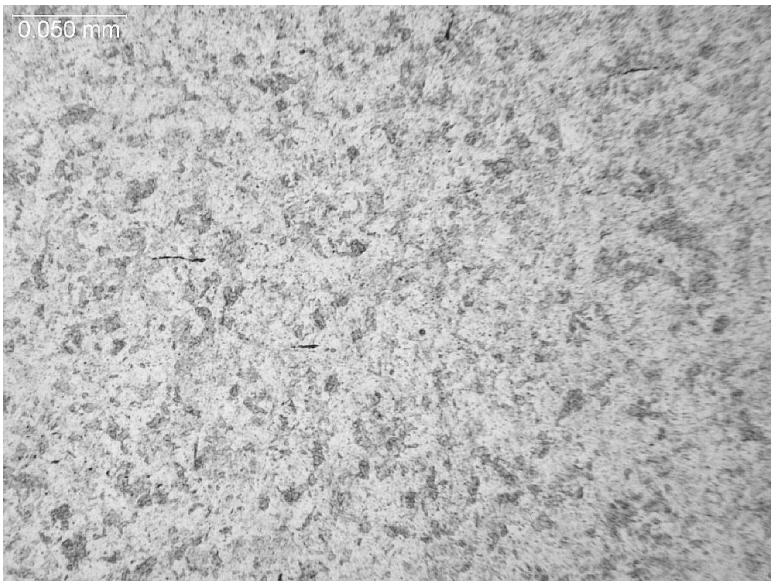

Fig. 2.11. Microstructure, location C, Fig. 2.2.

2.4. Kr-85 detection at damage sites in the weld region

In order to study the possible fractionalization of gases under long-term storage, the different pressure vessels were filled with a number of different gas mixtures at various initial pressures. These mixtures included pure helium, helium/argon, and nitrous oxide/argon/helium at different molar compositions and different pressures. In the case of fine leaks (< 1x10-7 atm cc/s) fundamental Knudesen diffusion theory predicts the preferential escape of low molecular weight gases at rates in excess of the higher molecular weight gases. It is of interest to understand if this effect is observed during the long-term storage of the gases in this study.

A significant aspect of this research involves the inclusion of a minute fraction (<0.001%, more basis) of the radioactive tracer gas krypton-85 (Kr-85) in all the gas mixtures. Since Kr-85 produces both gamma rays and beta particles in its radioactive decay process, the reduction in gamma ray activity in the pressure vessels as a function of time can be used to quantify the leak leak rate from the vessels. A reduction in gamma ray activity in excess of that expected due to the inherent radioactive decay of Kr-85 (10.76 year half-life) is an indication of a leak of gas from a vessel. Leak rate measurements obtained using Kr-85 are compared to those obtained by helium mass spectrometry (HMS) and direct measurements of vessel mass loss as a function of time. In many cases, the measured leak rates in this study are well beyond the capability of HMS using in this study (10-8 atm cc/s) and can only be measured using the Kr-85 technique - which is capable of detecting leak rates as low as 10-13 atm cc/s.

A novel aspect of this research involves using the products of Kr-85 decay to locate the extent of gas penetration within the pressure vessels walls, and the possible evolution of damage (cracks, voids, porosity, etc.) within the parent materials. Gaseous Kr-85 decays to form solid rubidium (Rb) as a decomposition product. Therefore, the identification of rubidium at levels in excess of baseline concentrations in the pressure vessel materials is direct evidence of the presence of Kr-85-containing gases at these locations. To locate rubidium, sectioned pressure vessels were studied using the energy dispersive spectroscopy (EDS) method.

EDS was used to characterize various elements present in the inner walls of prototype reactor pressure vessel. EDS study was done on a control sample that was not subjected to radioactive Kr-85, and a sample that was subjected to radioactive Kr-85. In samples subjected to radioactive Kr-85, non-radioactive Rb was detected in cracks. Radioactive Kr-85 gas used to fill the prototype pressure vessel decays to non-radioactive Rb over time. The Rb liquid exist as a thin film on the inner surface of the container. But since the inner surface of the vessel was ground and polished for microscopic studies, Rb was detected preferentially in the cracks. However, Rb was not detected in the cracks of the control sample that was not subjected to radioactive Kr-85. This study is quite promising, as there are very few studies in the literature to indicate the presence of Kr-85 in cracks at higher concentrations. The EDS study presents also a quantification of the amount of Kr-85 measured in cracks.

This study was undertaken to understand the chemistry around the crack in the internally pressurized (by Kr-85 gas) and heat treated prototype pressure vessel which were welded by Gas Tungsten Arc Welding (GTAW) and Inertia Welding (IW). Two prototype pressure vessels were made by GTAW and IW, respectively, and were subjected to a thermal treatment at 700 ^{o}C for 30 days after pressurizing inside space with Kr-85 at 8 psi. In theory, if the crack is there, Kr-85 will try to diffuse through the crack and in the process will decay to Rb isotopes. Therefore, one should be able to detect Rb in the crack. But if the crack allows gas leak, no Rb should be detected. In this study, the energy dispersive spectroscopy (EDS) in a scanning electron microscope (SEM) was used to accomplish the objectives.

The EDS technique was applied on a crack and the distribution of elements along the scanned line (the red-yellow line on the micrograph as shown in Fig. 2.12).

2.4.1. Line scan across the crack

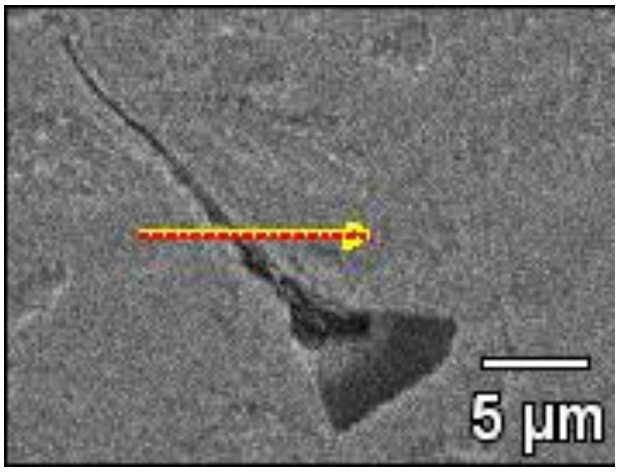

Fig. 2.12. A SEM picture of the crack in a GTAW specimen (the arrow indicates the EDS line scan direction and is transverse to the crack length at approximately 45^{o}).

The line scan profile of the elements along the scanned surface is shown in Fig. 2.13. The blue line indicated the increased Rb counts on the crack.

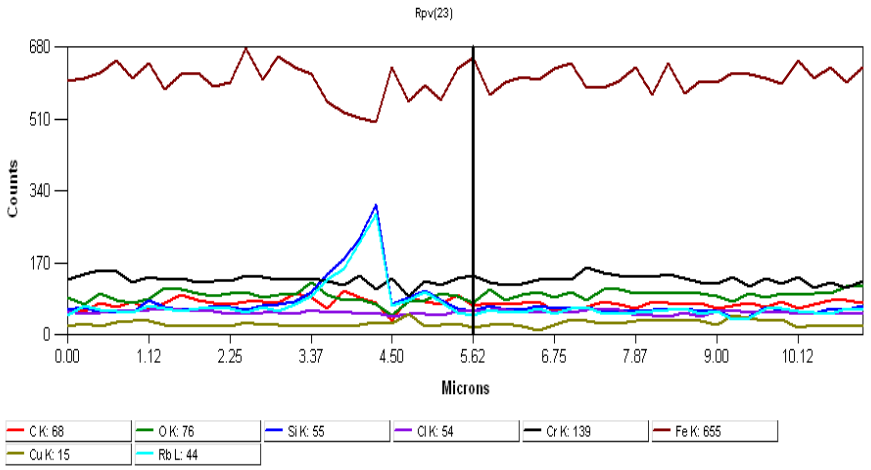

Fig. 2.13. The EDS composition profile across the crack in the GTAW specimen.

2.4.2. Line scan along the crack

A SEM micrograph (Fig. 2.14) of the same crack is shown but the arrow is along the length of the crack. Fig. 2.15 shows the EDS compositional profile of that line scan. Here also the peak coming from Rb is present.

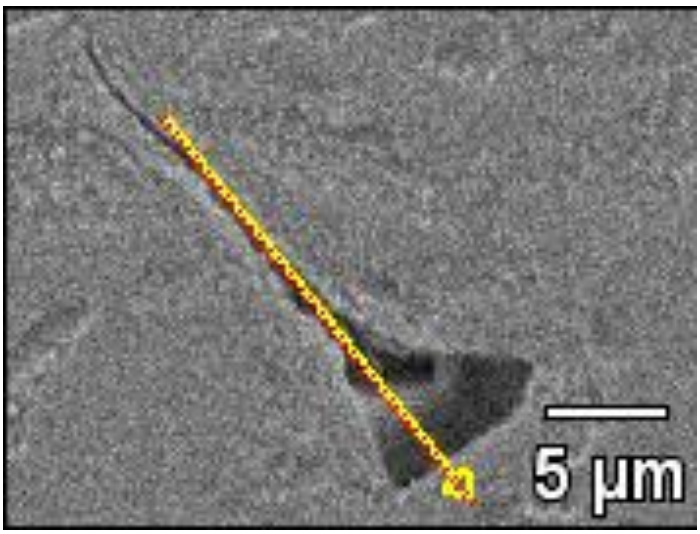

Fig. 2.14. A SEM picture of a crack in a GTAW specimen (the arrow indicates the EDS line scan direction).

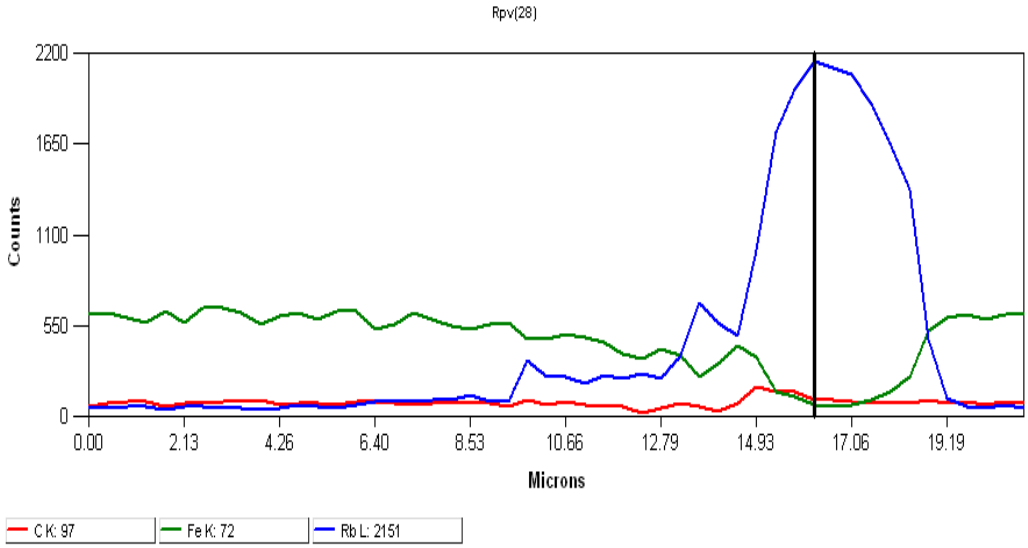

Fig. 2.15. The EDS composition profile along the crack in the GTAW specimen.

2.4.3. Elemental mapping of a crack in GTAWed and aged (700ºC and 30 days) Grade 91 steel

The EDS technique can show the distribution of individual elements around a particular region as compositional maps. Fig. 2.16 shows such a map from a GTAWed specimen which was aged at 700 ºC for 30 days.

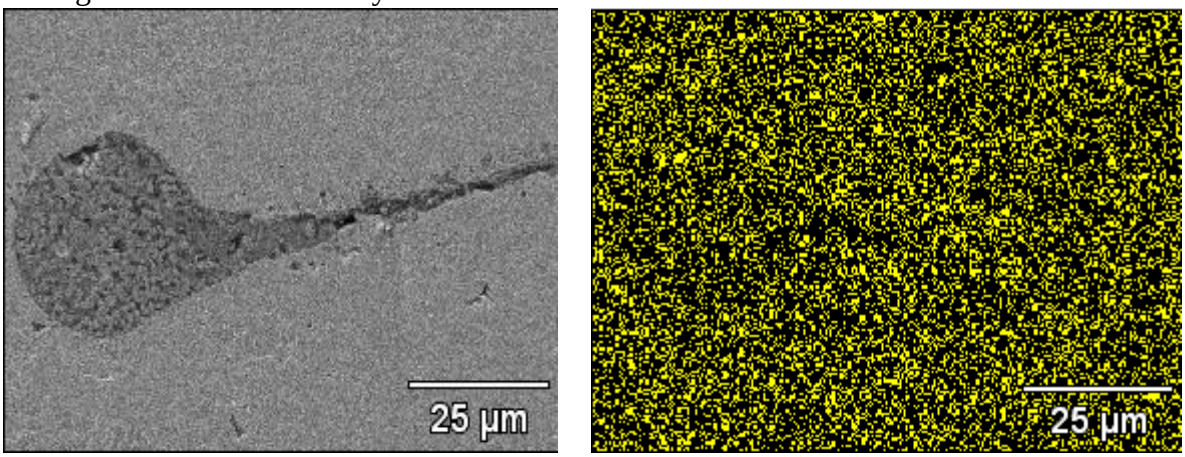

C

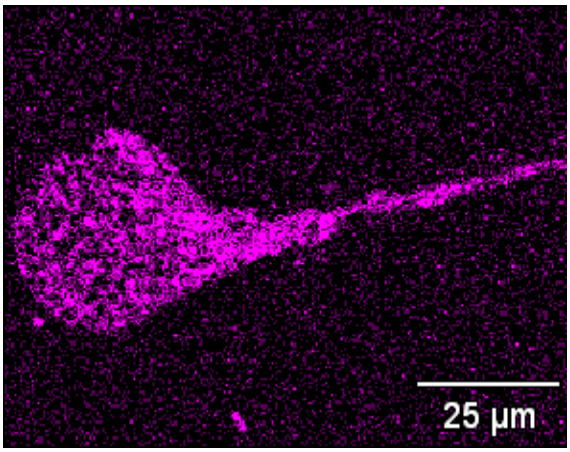

Si

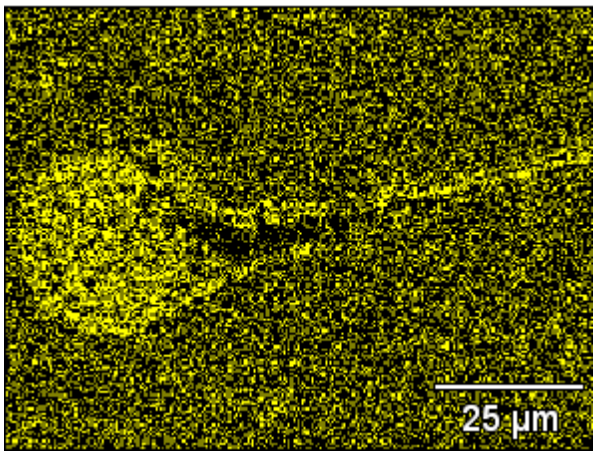

Cr

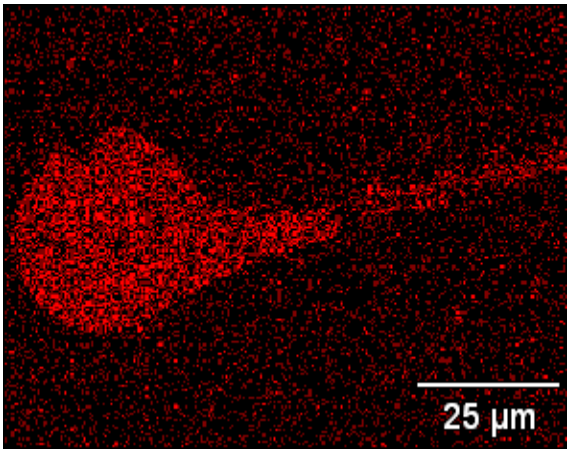

Mn

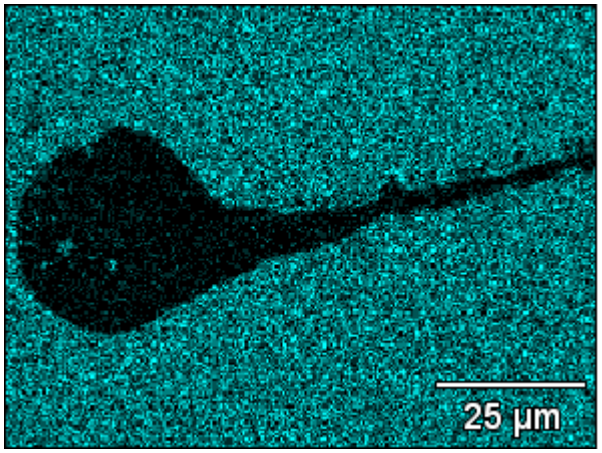

Fe

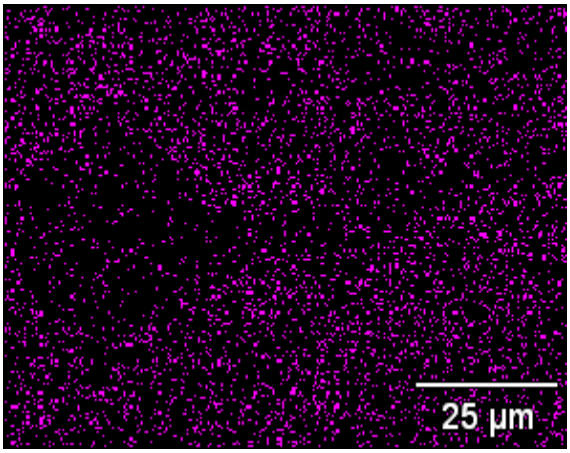

Cu

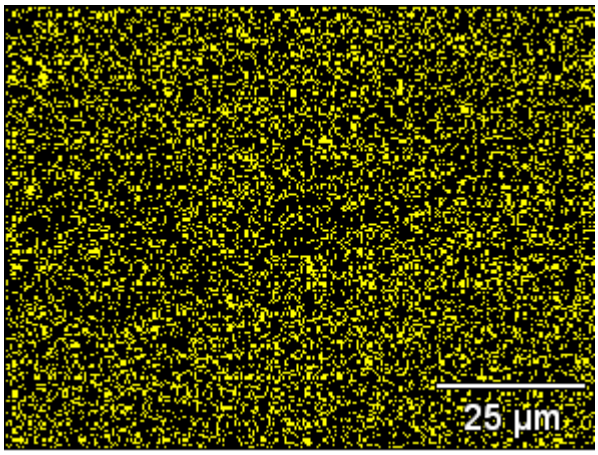

Mo

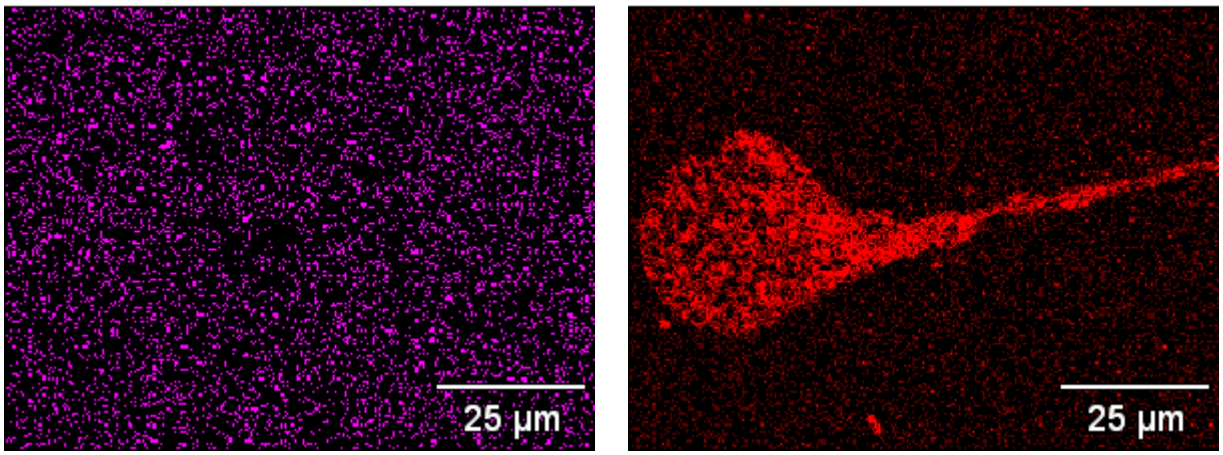

V **Rb**

Fig.. 2.16. The EDS compositional maps for various elements including Rb.

2.5. Inertia welded and aged (700ºC and 30 days) Grade 91 steel

The inertia welded specimen (a solid state weld) was found to be of better quality with no large crack present. However, one crack as shown in Fig. 2.17 was studied using the EDS technique. Here the EDS spectrum shown from a region on the crack. A small Rb peak can be seen in the EDS spectrum (Fig. 2.18), which corresponds to a spot in the crack shown in the micrograph (Fig. 2.17). However, when the EDS analysis was done much away from the crack, no Rb peak was revealed as shown in Fig. 2.19.

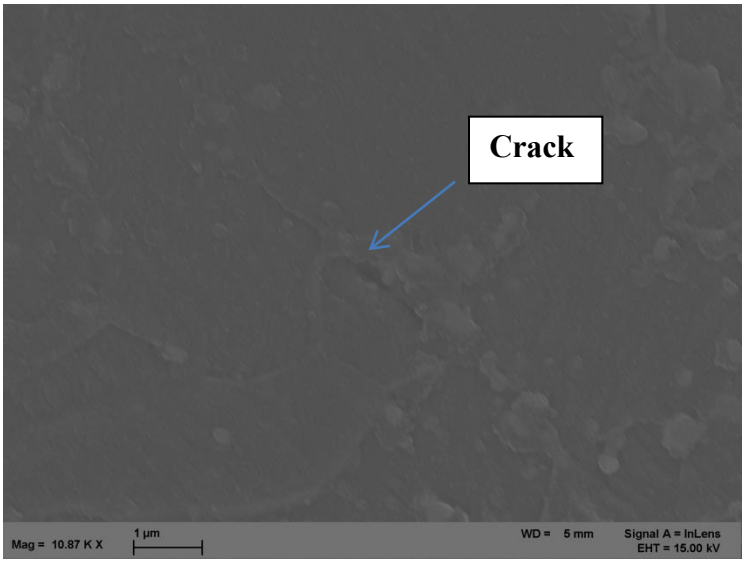

Fig. 2.17. SEM micrograph showing crack in inertia welded and aged sample

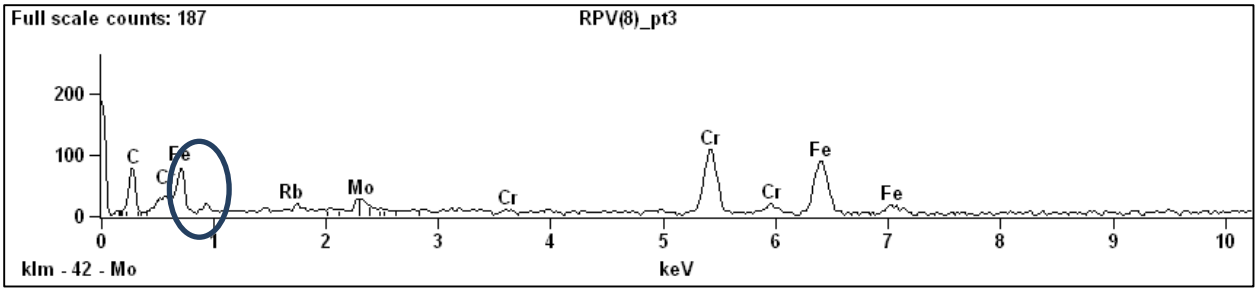

Figure 7. The EDS spectrum from a crack in the inertia welded and aged specimen.

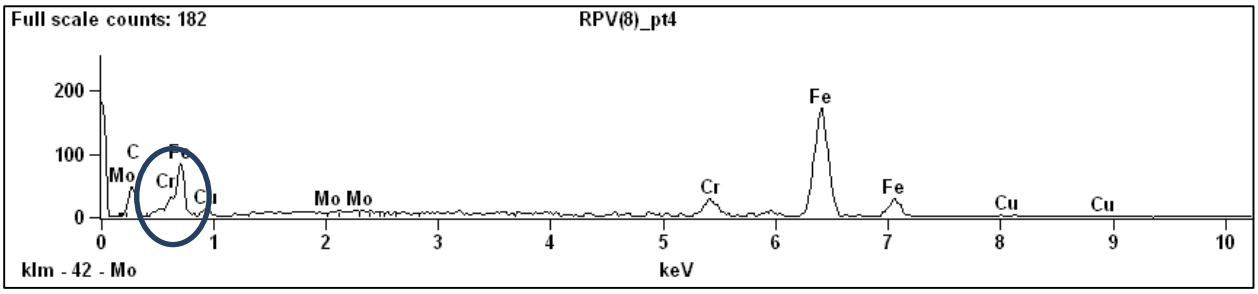

Fig. 2.18. The EDS spectrum of a region away from the crack in the inertia welded and aged specimen.

Radiation readings of the TIG and inertia-welded pressure vessels fabricated have been taken periodically. Results indicated that the reduction in gamma radiation, and therefore the activity of the gas contained within the vessels, over time continues to agree with the expected decay of Kr-85 over this time period. In other words, the leak rate from inertia welded pressure vessels appears to be certainly less than 1x10-10 atm cc/s and perhaps even lower. This indicates a good quality of the inertia welded in regard to the leak rates as a result of creep loading.

To measure such extremely fine leak rates, a novel calibration methodology to better understand the limit of detectibility of gamma radiation using our experimental instrumentation for our geometries and materials was developed. Generally speaking, the activity of an oil saturated with Kr-85 was first determined using the scintillation crystal detection equipment. The activity of the oil was determined on a mass basis in units of microcuries/gm of (vacuum pump) oil. Then known masses of the oil were carefully introduced in empty TIG and inertia welded specimens so the attenuation of the gamma ray signal due to the wall thickness of the different test vessels could be determined. As a result, the quantity of Kr-85 in a vessel can be known very accurately - much more accuratley than using other calibration techniqies. This has been very tedious work with many experiments necessary to refine the technique.

2.6. Conclusions

From this study, it was concluded that inertia welding is a much better welding technique compared to TIG welding for components that are intended to withstand creep conditions. The amount of damage in the inertia welded PVs is much lower compared with than observed in the

TIG welded vessels. Also, the leak rates from the TIG vessels were higher than those for inertial welded technique.

The Rb presence was observed mainly in the PVs filled with gas containing Kr-85. Rb is found in high concentrations in voids and cracks nucleated during the welding process in the heat-affected zone (HAZ) or as a result of the creep conditions. Rb is highly corrosive, and it is believed that it leads to an acceleration of the creep damage. Rb presence has been measured by atom count.

This study revealed that Rb can be found as a decay product of Kr-85 at the cracks. This technique can be used as a non-destructive evaluation method to assess the quality of the welds. However, it should be borne in mind that the EDS study is preliminary in nature. More in-depth studies will be required to substantiate the implication of these early findings.

Task 3: Constitutive model for creep damage in modified 9Cr-1Mo steels

3.1. Introduction

A micromechanical model is developed for the evaluation of creep deformation and rupture times of modified 9Cr-1Mo steel specimens. Creep deformation in metals is generally induced by the dislocation generation, motion, and annihilation. To evaluate the creep behavior of the modified 9Cr-1Mo steel the Orowan's equation was employed, which is valid for both glide and climb-controlled dislocation movement. The evolution of the dislocation density was modeled by considering the generation and annihilation of single and dipole dislocations. In addition to dislocation motion as a basis for creep deformation, there are several other factors which determine the creep resistance of this steel. Among these, the most significant are precipitate coarsening, solid solutions depletion, and void/crack nucleation and growth. The evolution of these mechanisms during creep deformation was accounted for by introducing specific continuum damage terms. Creep tests were also performed at several stress and temperature levels. The comparison of the numerical model results with the experimental data showed satisfactory agreement.

It is estimated that in the next 20 years the world demand for power supplies will increase by up to 50%. Thus, developing advanced energy resources becomes essential. The developed energy sources must be sustainable, environmental friendly and cost effective. Nuclear power meets these requirements for large scale power generation. The development of advanced nuclear power plants is followed under the Next Generation Nuclear Plant (NGNP) program. The NGNP program focuses on the development of the Very-High-Temperature Reactor (VHTR), which represents the next generation of the high temperature gas-cooled reactors. The VHTR is a helium-cooled, graphite-moderated reactor with a once-through uranium fuel cycle. The VHTR design specifications include higher operating temperatures, longer design life, and higher working pressures compared with previous reactor types, which make it necessary to consider new metallic alloys with improved creep properties for reactor pressure vessels and reactor internals. One such candidate material is modified 9Cr-1Mo steel.

Recently, several research studies have been performed to elucidate and model the creep behavior in metals. Preußner et al. [39] developed a dislocation density-based creep model, and the creep behavior of single fcc, bcc, and hcp crystals was studied using this model. Venkataramani et al. [50] developed a finite element crystal plasticity creep model and performed a parametric study to identify the primary microstructural parameters causing early crack initiation by load shedding in Ti-6242 during creep. They used the Schmid factor and the grain size and shape as the most critical parameters to prevent stress concentration and crack initiation.

Fischer and Svoboda [14] extended the Nabarro creep model to the general dislocation microstructure. At low stress levels the creep is controlled by the generation/annihilation of vacancies at dislocations jogs. They developed a model based on vacancy activity, dislocation microstructure and applied stress state, and simulation results were compared to experimental measurements of creep rates in P91 steel at low stresses and high temperatures. Oberson and Ankem [36] studied the creep deformation behavior of α-Ti–1.6 wt.% V. The formation of twinning at high strains was explained by dislocation pileups. Morra et al. [39] studied the precipitate coarsening in tempered SAE 52100 steel. It has been shown that the growth of

carbide precipitates is in correlation with the plastic strain evolution. Creep strength of as-cast and annealed Fe–Ni–Al alloy has been investigated by Muñoz et al. [33]. It has been shown that in the annealed alloy with less volume fraction of precipitates the creep strength decreases significantly while the ductility increases. Horstemeyer et al. [20] performed a review on the development and the use of internal state variable theory based on the Coleman and Gurtin thermodynamics formulations for dislocations, creep, and continuum damage mechanics.

The material of interest in this study is modified 9Cr-1Mo steel, and was developed in late 1970's for use in fossil fuel power plants, according to Swindeman et al. [40]. The main advantages of modified 9Cr-1Mo steel which make it a suitable candidate for VHTR structures are limited radiation hardening at higher temperature, lower shift in the Ductile-to-Brittle Transition Temperature (DBTT), low thermal expansion coefficient, and better void swelling resistance than austenitic steels. Furthermore, modified 9Cr-1Mo steel is a precipitate-hardened alloy with a stable microstructure. The mechanical behavior and chemical composition of the modified 9Cr-1Mo steel have been optimized in the recent years. This steel contains alloying elements such as Nb and V, which form fine and stable particles, and help to improve its creep strength.

The creep behavior of the 9Cr-1Mo steel has been studied by several researchers during the past years. Sklenicka et al. [44,45] suggested that the role of dislocation substructure is dominant for the creep behavior of 9Cr-1Mo steels. According to their study, carbide particles merely stabilize the substructure, while the dislocation structure and/or substructure development determine the creep behavior of the steel. Spigarelli et al. [46] concluded that the high values of the activation energy and the creep stress exponent indicate that in the high stress regime creep strain is controlled by dislocation movement and particle-dislocation interaction (Orowan by-pass and/or climb). Böck et al. [7] have performed an extensive research on the finite element modeling of the creep behavior of modified 9Cr-1Mo steel. Instead of using standard evolution laws for predicting long term creep, they proposed to utilize models which were based on microstructural variables. Artz and Wilkinson [2] proposed a dislocation based model for creep. The model is valid for local and general climb of dislocations regardless of the climb mechanisms. In this model the threshold stress is defined as the dislocation-particle attractive interaction. Creep models based on microstructure have also been proposed by several other authors [19,5,40,41]. The common theme of these models is that they employ multiple microstructural variables based on averaged microstructural quantities, such as the mobile dislocation density, static dislocation density, boundary dislocation density, subgrain radius, precipitate radius, precipitate concentration and glide energy.

Fujimitsu [17] studied the material degradation in modified 9Cr-1Mo steel welds during creep deformations. He proposed a new approach for the evaluation of creep degradation and life assessment in modified 9Cr-1Mo steel welds by the hardness measurement method. The uniaxial high-temperature creep behavior of the base metal and weldment of 9Cr1MoNbV steel was studied by Gaffard et al. [18]. They also investigated the type IV failure in the heat affected zone. Furthermore, a one-dimensional model based on a power law and the Monkman–Grant models were proposed for life time assessment of the weldment. Besson et al. [3] proposed a model which integrated the power-law creep, diffusional creep and a simple damage term for simulating the creep-failure behavior of the inter-critical heat affected zone. Fournier et al. [16] introduced a micromechanically based model considering the dislocation density and subgrain coarsening in order to predict the cyclic softening in the 9–12%Cr martensitic steels. The model shows a good consistency with the experiments for strain over 0.3%. Sauzay [47] studied the effect of

annihilation of low angle boundaries and the micro-grain coarsening during creep deformation of tempered martensite steel, and developed physically-based computations following the Read and Shockley model.

Several studies have been performed to evaluate the effect of precipitates on the creep behavior of 9Cr-1Mo steel. The type, size and volume fraction of precipitates in the modified 9Cr-1Mo steel were investigated by Chilukuru et al. [9]. They showed that V forms fine particles of M_2X, which may provide short term high creep strength, but the rapid coarsening of M_2X at the subgrain boundaries and Z-phase precipitation decrease the overall creep resistance. Kabadwal et al. [23] found that the primary creep stage of a specimen tempered at 500 ˚C was controlled by the mobile dislocation density reduction and is a recovery process, while for the specimens tempered at 800 ˚C, the primary creep is controlled by the increase in creep resistance due to the fine precipitation of VX. Also, it has been mentioned that the growth of $M_{23}C_6$ in the tertiary creep stage relates to the creep rate increase.

In addition to temperature and applied stress, there are several microstructural parameters which influence the creep behavior of materials. Continuum damage models have been widely used to simulate the material degradation due to microstructural evolution. During the past decades numerous continuum damage mechanics models coupling with plasticity, viscoplasticity, creep, and fatigue have been developed [1,4,8,13,28,34,52]. The tertiary creep stage of the modified 9Cr-1Mo steel is governed by several the microstructural processes which degrade the material. Ashby and Dyson explained the creep damage by the loss of internal and external sections, microstructure degradation, and gaseous environmental attack. Each category was found to contain several micro-mechanisms [11,31]. The effects of these factors have been considered in this model by employing creep damage terms.

In the current research, a dislocation-based creep model combined with a continuum-damage model was employed to simulate the creep behavior of modified 9Cr-1Mo steel. The Orowan's equation, relating creep rate with the density of mobile dislocations and their glide velocity, was employed as a foundation for the model. The evolution of dislocations was estimated based on a model proposed by Blum et al. [6]. The effects of precipitate coarsening, solid solution depletion and cavity nucleation were taken into account by including continuum damage terms into the Orowan's equation. In order to evaluate the effects of precipitate coarsening and solid solution depletion, the Orowan's formula was modified by the respective damage terms similarly to the procedure outlined by Semba et al. [42]. Another mechanism affecting creep strain in materials is void and crack formation. Yin et al. [53] modified the McLean et al. [30] formula by defining a term for cavity nucleation in 9Cr steels. In this research, a similar procedure was used, by adding a void formation term to the Orowan's equation, which makes it possible to evaluate the effect of void nucleation on creep strain rate.

3.2. Experimental procedure

The chemical composition and room temperature tensile properties of ASTM A387 Grade 91 CL2 steel investigated are shown in Tables 1 and 2, respectively. Hot rolled modified 9Cr-1Mo plates were received in a normalized condition at 1038 ºC for 240 minutes and tempered at 788 ºC for 43 minutes. The plate dimensions were 104 mm × 104 mm × 12.7 mm. Scanning and transmission electron microscopy (SEM and TEM) were performed to characterize the microstructural characteristics of the modified 9Cr-1Mo steel. Creep specimens with a gauge

length of 25.4 mm and gauge diameter of 6.35 mm were machined from the steel plates. The material has yield strength of 533 MPa, an ultimate tensile strength of 683 MPa and percentage elongation at fracture of 26% at room temperature. Creep tests were performed at several combinations of temperature (600, 650 and 700 ^{o}C) and stress (35-350 MPa) using an Applied Test Systems (ATS) lever arm (20:1) creep tester.

A microstructural study of the modified 9Cr-1Mo steel specimens has been performed using SEM in the secondary electron imaging mode and TEM. Furthermore, the energy dispersive spectroscopy (EDS) was used for the elemental analysis and precipitate characterization. A detailed description of the microstructure can be found elsewhere [43].

Table 1. Chemical composition (wt.%) of Grade 91 steel used in this study.

Elements	Nominal	Measured
Cr	8.00 - 9.50	8.55
Mo	0.85 - 1.05	0.88
V	0.18 - 0.25	0.21
Nb	0.06 - 0.10	0.08
C	0.08 - 0.12	0.1
Mn	0.30 - 0.60	0.51
Cu	0.4(max.)	0.18
Si	0.20 - 0.50	0.32
N	0.03 - 0.07	0.035
Ni	0.40(max.)	0.15
P	0.02(max.)	0.012
S	0.01(max.)	0.005
Ti	0.01(max.)	0.002
Al	0.02(max.)	0.007
Zr	0.01(max.)	0.001
Fe	Balance	Balance

Table 2. Mechanical properties of Grade 91 steel used.

Yield Strength (MPa)	Tensile Strength (MPa)	Elongation	
		Gage Length (mm)	%
533.60	683.27	50.80	26.0

3.3. Model description

3.3.1 Evolution and kinetics of dislocations

In crystalline materials in the power law regime creep generally occurs by dislocation glide and climb. In order to simulate the creep behavior of a material, it is necessary to distinguish between the controlling mechanisms of dislocations motion. There are different methods to analyze the mechanisms of dislocations motion in a material. Stress change test and in-situ observation of dislocation motion are two common methods for understanding the dislocations motion mechanisms. Terada et al. [49] have made an in-situ observation of dislocation motion in Fe-W and Fe-Mo solid solutions. Analysis of the video records of dislocation behavior in both Fe-W and Fe-Mo steels showed that the dislocation glide velocities were constant in both materials. It has also been observed that the dislocation dragged solute atmosphere with themselves. So, it can be concluded that the dislocations motion is viscous. According to this conclusion, the model proposed by Blum et al. [6] for the viscous glide of dislocation was utilized in this study. In this model the accumulation of creep deformation is linked to the dislocation generation, motion, and annihilation.

In the present model, the Orowan's equation is employed to compute the creep strain rate. Because the stress levels tested were above 60 MPa, the only mechanism considered is the power law creep. At stresses lower than this value, other mechanisms, such as the Nabarro-Herring Newtonian creep should also be taken into consideration. Orowan's equation relates the creep strain rate caused by dislocation motion to the density of mobile dislocations, Burgers vector and the glide velocity. Orowan's equation is valid for either glide or climb controlled motion of dislocations [38],

$$\dot{\varepsilon} = \frac{\rho_m b v_g}{M}, \tag{1}$$

where b is Burgers vector, M is the Taylor factor, v_g is the glide velocity and ρ_m is the density of the mobile dislocations. It is convenient to represent the total dislocation density in a material as the summation of the mobile and dipole dislocations.

$$\rho = \rho_m + \rho_{dip}, \tag{2}$$

where ρ is the total dislocation density and ρ_{dip} is the dislocation dipole density. The evolution of dislocations can be described in terms of the generation and annihilation of single and dipole dislocations. The subgrain formation and growth have not been taken into account in this study. It is assumed that all their effects are implicitly present in one of the curve-fitting parameters k_Λ which is introduced below. Future studies should focus on the modeling of the subgrain formation effect on creep deformation in Cr-Mo steels. The generation of single dislocations and the formation and annihilation of dipoles are modeled according to the Blum model as follows

$$\dot{\rho}_m = \dot{\rho}_{m,gen} - \dot{\rho}_{m,spon} - \dot{\rho}_{dip,gen}, \tag{3}$$

$$\dot{\rho}_{dip} = \dot{\rho}_{dip,gen} - \dot{\rho}_{dip,spon} - \dot{\rho}_{dip,c}. \quad (4)$$

Here, $\dot{\rho}_m$ is the rate of evolution of the mobile dislocations, $\dot{\rho}_{m,gen}$ is the rate of generation of mobile dislocations, $\dot{\rho}_{m,spon}$ is the rate of spontaneous annihilation of mobile dislocations, $\dot{\rho}_{dip}$ is the evolution rate of dipoles dislocations, $\dot{\rho}_{dip,gen}$ is the rate of generation of dipoles, $\dot{\rho}_{dip,spon}$ is the spontaneous annihilation of the dipoles, and $\dot{\rho}_{dip,c}$ is the climb annihilation of dipoles. The rate of generation of the mobile dislocations is defined as

$$\dot{\rho}_{m,gen} = \frac{M\dot{\varepsilon}}{b\Lambda}, \quad (5)$$

where M represents the Taylor factor, $\dot{\varepsilon}$ the creep strain rate, and Λ represents the total distance a dislocation glides and is proportional to the average spacing of total dislocation density as expressed by

$$\Lambda = k_\Lambda \rho^{-0.5}, \quad (6)$$

where k_Λ is a material parameter, which in the present model is assumed to be a function of temperature and stress. The magnitude of k_Λ will decrease with increasing temperature and stress. Two dislocations with Burgers vectors of opposite sign approaching each other on a slip plane within a distance smaller than a critical value, d_{dip}, will form a dipole. The average rate of annihilation of the mobile dislocations by forming dipoles on the active slip planes is defined as

$$\dot{\rho}_{m,ani} = \frac{4M\dot{\varepsilon}d_{dip}\rho_m}{b(n_g)} \quad (7)$$

In the above equation $\dot{\rho}_{m,ani}$ is the rate of annihilation of mobile dislocation spontaneously and by forming dipoles, in other words it is equal to the summation of the $\dot{\rho}_{m,spon}$ and $\dot{\rho}_{dip,gen}$. The term $(M/b)2d_{dip}\dot{\varepsilon}$ represents the change in time of the volume fraction single dislocations that can form dipoles. The term $1/(2n_g)$ is the average dislocation fraction with opposite Burgers vector sign, and n_g is the number of active slip planes [6]. The distance d_{dip} is the capturing dipole configuration distance for either two screw or edge dislocations of opposite sign, which approach each other to form a stable dipole. The parameter d_{dip} is a function of applied stress, and it varies between 12-16 nm for stress levels between 100-200 MPa. The annihilation distance of edge and screw dislocations are equal to y_e =4 *nm* and y_s = 50 *nm* respectively [16]. It can be observed that the parameter d_{dip} is within the range of edge and screw dislocation annihilation distances, and shows a good agreement with the experimental values.

$$d_{dip} = \frac{M}{8\pi(1-\nu)}\frac{Gb}{\sigma}. \quad (8)$$

In the above equation, G is the shear modulus and σ is the applied stress. Within a certain distance, d_{spon}, between the slip planes of the dipole dislocations, the dipoles will annihilate spontaneously and form point or agglomerate defects behind, Blum et al. [5]. The spontaneous dislocation annihilation rate is defined as

$$\dot{\rho}_{m,spon} = \frac{d_{spon}}{d_{dip}} \dot{\rho}_{m,ani} . \tag{9}$$

The dipole dislocations may draw near each other by climbing or cross slipping over the parallel slip planes in-between until their spacing reaches d_{spon}. Neglecting the subgrain formation, the process of annihilation of the dipoles represents the dynamic recovery. The rate of dipole annihilation climb or cross slip is assumed to be proportional with the climb velocity of dislocations,

$$\dot{\rho}_{dip,c} = \rho_{dip} \frac{4v_c}{(d_{dip} - d_{spon})} . \tag{10}$$

The climb velocity is the velocity with which edge dislocations move perpendicularly to the slip plane and can be defined as,

$$v_c = \frac{D\Omega\sigma_c}{bK_B T} , \tag{11}$$

$$\sigma_c + \frac{v_c}{B} = \frac{Gb}{2\pi(1-\nu)} \frac{2}{d_{spon} + d_{dip}} , \tag{12}$$

where Ω is the atomic volume, K_B is the Boltzmann constant, T is the temperature, D is the coefficient of self-diffusion, and the climb stress σ_c is found from Eq. (12). In this equation, B is the dislocation mobility term and defined as,

$$B = \frac{9\Omega D_{sol} K_B T}{M C_0 G^2 b^7 \varepsilon_a^2 \ln(\frac{r_2}{r_1})} . \tag{13}$$

The other mechanism which may annihilate dipole dislocations spontaneously is by passing a single dislocation near a dipole. The new single dislocation will annihilate with one side of the dipole. The remaining one will form a new single dislocation so that the single dislocation density will not change. The spontaneous rate of annihilation of dipoles is an athermal process, and is formulated as follows

$$\dot{\rho}_{dip,ani} = \frac{2M\dot{\varepsilon} d_{spon} \rho_{dip}}{b n_g} . \tag{14}$$

The kinetics of dislocation motion can be analyzed considering that the glide velocity of dislocations is a function of the effective stress, temperature, dislocation interactions, dislocation mobility, solute atom sizes, and the diffusion coefficient of solute atoms in the matrix. The effective applied stress is calculated from the applied external stress σ and the athermal stress component σ_i,

$$\sigma^* = \sigma - \sigma_i . \tag{15}$$

The athermal stress component resulting from the interdislocation interaction of both single dislocations and dipoles is

$$\sigma_i = \alpha MCGb\sqrt{\rho_m + c_{dip}\rho_{dip}} , \tag{16}$$

where α is a dislocation interaction constant, C is the inelastic deformation factor and c_{dip} is a weight factor. The glide velocity is directly proportional with the effective stress.

$$v_g = B\sigma^* , \tag{17}$$

here, D_{sol} is the solute atom diffusion coefficient in solvent atoms, C_0 is the solute concentration, r_1 and r_2 are the outer and inner cut-off radii of the dislocation stress field, and ε_a is the relative size misfit between solute and solvent atoms.

3.3.2 Formulation of creep damage

3.3.2.1 Solid solution depletion

Experiments in 9Cr-1Mo have indicated that the precipitation of Fe_2Mo Laves phase decreases creep resistance. The decrease in creep resistance is caused by the Mo depletion in the subgrain matrix during long term high temperature and stress exposure. Mo is added to the material to increase the creep resistance by solid solution strengthening mechanism. While the low volume fraction and the large size of the Laves phase (Fe_2Mo) could rarely help decrease the dislocations motion. The large size Laves phases at grain boundaries are the most likely source of cavity nucleation and the intergranular fracture because they are brittle in nature and have the tendency to absorb dislocations [27]. This mechanism is addressed in the next section concerning the damage evolution by void nucleation and crack formation. According to Kadoya, et al. [24] and Semba et al. [42], the damage caused by depletion of the Laves phase (D_s) is defined as

$$D_s = 1 - \frac{\bar{C}_t}{C_0}, \text{ where, } 0 < D_s < 1, \tag{18}$$

where C_0 is the initial concentration of solid solution, and $\bar{C}_t$ is their concentration at time *t*. In addition, the rate of change of D_s is

$$\dot{D}_s = K_s D_s^{1/3}(1-D_s), \tag{19}$$

with the constant K_s defined as

$$K_s = \left\lfloor 48\pi^2 (c_0 - \frac{c_e}{c_\beta})^{1/3} n^{2/3} D \right\rfloor. \tag{20}$$

Here, D is the diffusion coefficient of Mo in matrix, n the number of precipitate particles and c_β the concentration of solid solution in the precipitate of laves. Semba et al. [42] computed the values of c_0 and c_e using Thermo-Calc and found c_0 = 0.56 mol% and c_e = 0.33 mol%.

3.3.2.2 Precipitate particle coarsening

The precipitate coarsening in modified 9Cr-1Mo steel plays an important role in the creep resistance of this material. Nakajima et al. [35] studied the coarsening of $M_{23}C_6$ and MX precipitates in T91 steel during creep. They reported that the size of MX particles is smaller than that of $M_{23}C_6$, but the coarsening of $M_{23}C_6$ found on the subgrain boundaries and MX particles was consistent with the third power dependence of particle radius with activation energy similar to lattice diffusion. With the coarsening of the precipitates, the interparticle spacing between the precipitates increases. The increased interparticle spacing decreases the stress required for dislocations to climb over precipitates. Following Semba et al. [42], the damage caused by the coarsening of $M_{23}C_6$ precipitate particles is modeled as

$$D_P = 1 - \frac{P_0}{P_t}, \tag{21}$$

where P_0 is the initial particle diameter and P_t is the particle size at time *t*. The rate of precipitate particle coarsening is described by

$$\dot{D}_p = \frac{k_p}{3}(1-D_p)^4, \tag{22}$$

where k_p is the rate constant normalized by the third power of the initial particle size. As a result D_P varies between zero to one.

3.3.2.3 Void nucleation and crack formation

As was mentioned previously, creep damage in modified 9Cr-1Mo steel is governed by different mechanisms, with one of the most important one being void nucleation and cavity formation. Creep cavities and crack formation are generally controlled by grain-boundary sliding. Decohesion caused by the stress irregularities at grain boundaries will initiate cavities and cracks. The grain boundary interaction with the subgrains or second-phase particles will form possible crack nucleation sites [51]. In 9Cr-1Mo steel cavities usually nucleate at triple

junctions or at particles located on grain boundaries. It is observed that the major crack formation mechanism in this material is grain deformation. Moreover, as small inter-granular cavities coalesce, cavity growth increases, as observed by Gaffard et al. [18].

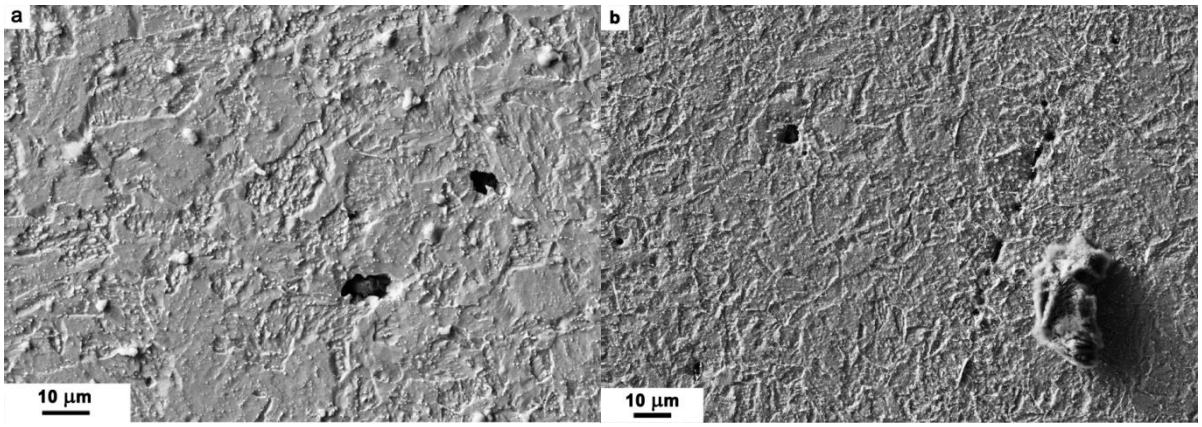

Fig. 1. Voids nucleated in after creep specimens at 650 ˚C and stress of 150 MPa.

Typical voids and possible wedge crack formation by coalescence of small cavities are shown in Fig. 1 for the creep damaged specimens at 650 °C and 150 MPa. These effects are accounted for by using a damage parameter D_N for the cavity nucleation and growth. There are several void growth, and void coalescence modeling approaches available such as Gurson's constitutive law or damage indicators developed by Fischer et al. [15]. In this work the formulation proposed by Yin et al. [53] has been chosen. In this model the rate of evolution of D_N is defined as,

$$D_N = A\dot{\varepsilon}\varepsilon^{0.9}, \tag{23}$$

where the material constant A is a function of temperature and stress. At large strains and high strain rates, the magnitude of D_N may be equal to or larger than one. This will cause a divergence in the computation at high stress and strain; therefore the magnitude of D_N should not reach one, thus $0 < D_N < 1$.

3.4. Results and discussion

Inserting the damage terms in the Orowan's equation (Eq. (1)), the formula for computing creep strain rate becomes

$$\dot{\varepsilon} = \frac{b \,.\, \rho_m \,.\, v_g}{M(1-D_s)(1-D_P)(1-D_N)}. \tag{24}$$

In general, different creep mechanisms may be divided into three categories: viscous creep, power-law creep and power-law break down creep. The current model was utilized to

simulate the creep behavior of the modified 9Cr-1Mo steel in power-law creep region. For the experiments conducted on the modified 9Cr-1Mo specimens at temperature levels equal to 600, 650 and 700 ˚C and stress levels over 80 MPa, the material follows the power low creep behavior. In this study, the numerical model was applied to the experimental data for temperatures from 600 to 700 ˚C and stress levels from 100 MPa to 200MPa. In the simulation procedure the engineering stress has been used. The computed results were compared with the experimental results, and they show a satisfactory match. Fig. 2 shows the comparison of creep strain rates predicted by the model with experimental data for the temperature of 650 ˚C and stresses of 150 MPa and 200 MPa. For the same temperature and stress levels, the creep strain variations with time are shown in Fig. 3. For crept specimens tested at stresses of 80 MPa and 100 MPa and temperature of 700 ˚C, the creep strain rates and creep strain versus time are shown in Figs. 4 and 5, respectively. Furthermore, the creep response for the stress levels of 150 MPa and 200 MPa at 700 ˚C was simulated, and the results are shown in Figs. 6 and 7, respectively. Figs. 8 and 9 show the creep behavior of the material at 600 ˚C, and applied stresses of 150 MPa and 200 MPa, respectively. The material parameters used in the model are shown in Tables 3 and 4.

As it was mentioned in section 4, in this model k_Λ is considered as an adjustable parameter. The parameter k_Λ has a significant effect in this model for simulating the creep rate for the first and second stage of creep. In order to find the k_Λ values, the simulations have been performed without the damage terms for the steady state creep stage. The values of k_Λ vary with temperature and applied stress. Fig. 10 shows the variation of k_Λ with the applied stress at different temperatures. At each temperature, by increasing the applied stress the value of k_Λ decreases. A similar conclusion can be drawn for the effect of temperature on the variation of k_Λ . At any stress level, the value of k_Λ will decrease with an increase in temperature. Future studies should focus on the physical relevance of k_Λ . The fitting procedure has been applied to k_Λ in each experiment, but as it was mentioned before, the variation of this parameter is inversely proportional with the increasing stress and temperature, thus it is possible to find an appropriate range with few experimental data available. The second major parameter is the term A in the damage caused by void nucleation and crack formation in Eq. (23). This parameter changes proportionally with stress and temperature, and it was fitted to all experimental data. Eq. (20) was used to determine K_s values for stress equal to 150 MPa and temperatures of 600 and 650 ˚C. Because of the lack of experimental values for the parameters in Eq. (20), the K_s parameter has been fitted to the rest of experiments. The parameter K_p has been fitted to all experiments.

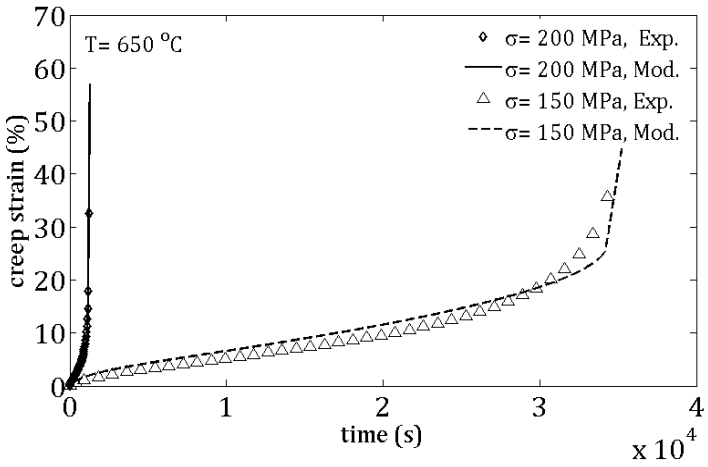

Fig. 3. Comparison between the model predictions and experimental data for the creep strains at 650 ˚C and stresses of 150 MPa and 200 MPa.

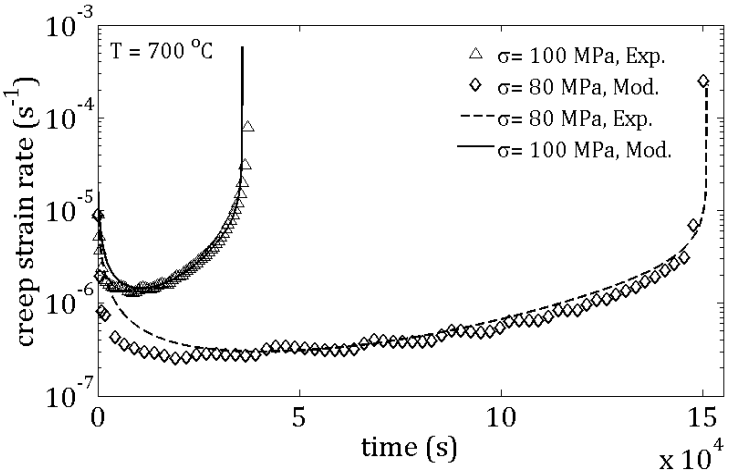

Fig. 4. Comparison between the model predictions and experimental data for the creep tests at 700 ˚C and stresses of 80 MPa and 100 MPa.

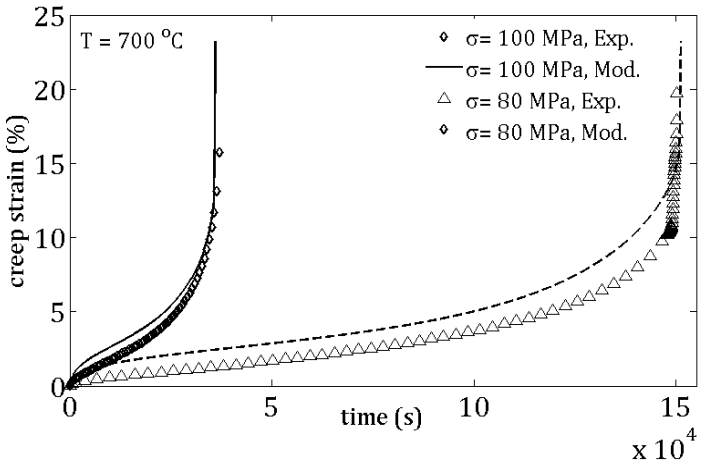

Fig. 5. Comparison between the model predictions and experimental data for the creep strains at 700 ˚C and stresses of 80 MPa and 100 MPa.

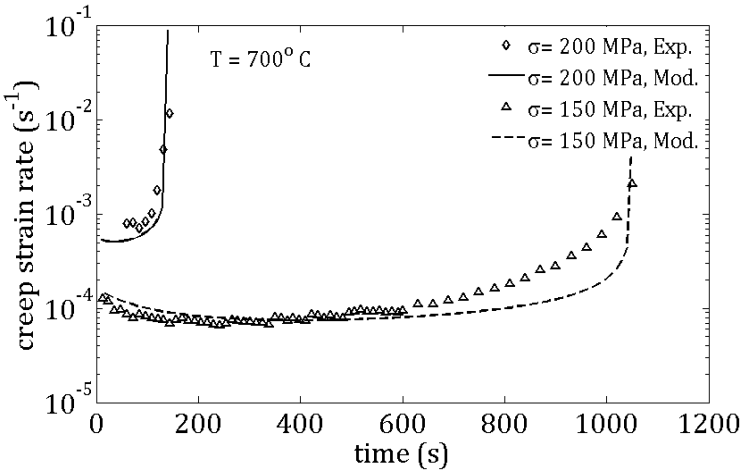

Fig. 6. Comparison between the model predictions and experimental data for the creep tests at 700 ˚C and stresses of 150 MPa and 200 MPa.

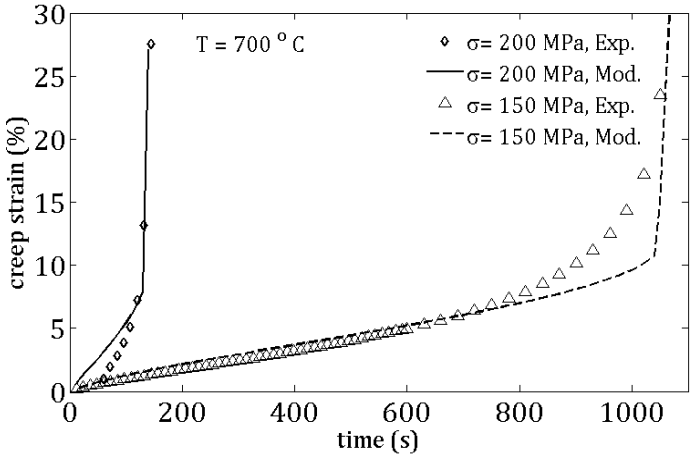

Fig. 7. Comparison between the model predictions and experimental data for the creep strains at 700 ˚C and stresses of 150 MPa and 200 MPa.

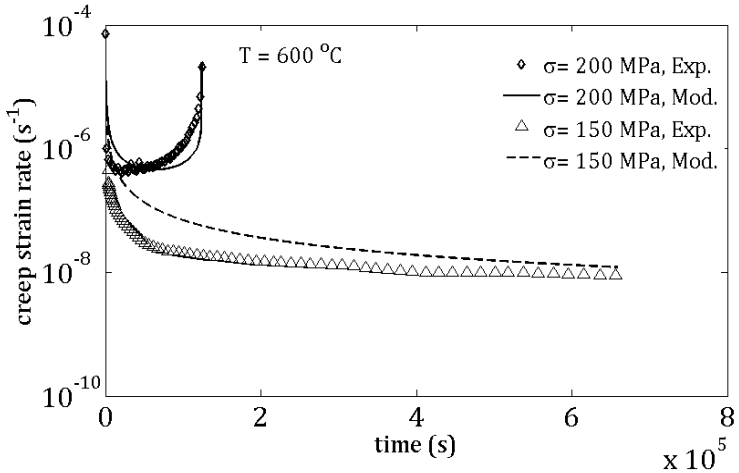

Fig. 8. Comparison between the model predictions and experimental data for the creep tests at 600 ˚C and stresses of 150 MPa and 200 MPa.

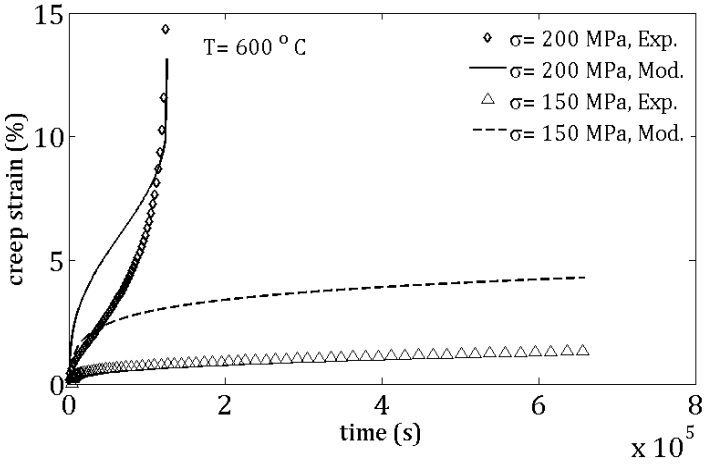

Fig. 9. Comparison between the model predictions and experimental data for the creep tests at 600 ˚C and stresses of 150 MPa and 200 MPa.

In the present model, dislocation density is a major parameter for computing creep strain rate. The model must be provided with a correct estimate of the initial dislocation density at each stress level, however measuring the dislocation density is not a trivial process. Thus, it is necessary to evaluate the sensitivity of the model to the initial values of dislocation density, and see how it affects the computed minimum creep rate. The dislocation density in the as-received material is known, and has been reported to be in order of 10^{14} m^{-2} by Fournier et al. [16], and Panait et al. [37]. The variation of the dislocation density is proportional to the second power of the applied stress. As it was mentioned, the dislocation density in current work is divided to mobile and dipole dislocation density. The initial value of dipole dislocation density is usually at least ten times less than that of mobile dislocations. Thus, only the effect of initial mobile dislocation density has been studied in this section.

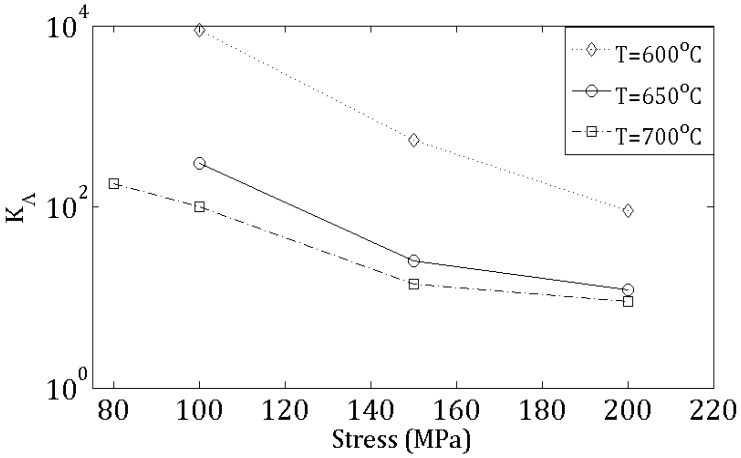

Fig. 10. Variations of the parameter k_{Λ} with the applied stress at temperatures of 600, 650 and 700 ˚C.

It is possible to consider a value for the initial dislocation density which best fits the experiments. Based on the value which has been chosen for the initial dislocation density at each stress level and the k_{Λ} value, the modeling result can be obtained.

Fig. 11 shows the creep strain rate versus time at 650 ˚C and 150 MPa for five different initial mobile dislocation densities at a fixed value of k_{Λ} . The initial mobile dislocation densities are 0.2×10^{14} m^{-2} ,0.6×10^{14} m^{-2} , 1.2×10^{14} m^{-2}, 1.6×10^{14} m^{-2}, and 2.2×10^{14} m^{-2}. As it can be observed, the curves have the same trend. For the initial mobile dislocation density equal to 0.2×10^{14} m^{-2}, the simulation results do not show a satisfactory correlation with the experimental results. For the other initial values the simulation results are close to the experiments, and this is particularly true for the initial densities of 0.6×10^{14} m^{-2} and 1.2×10^{14} m^{-2}.

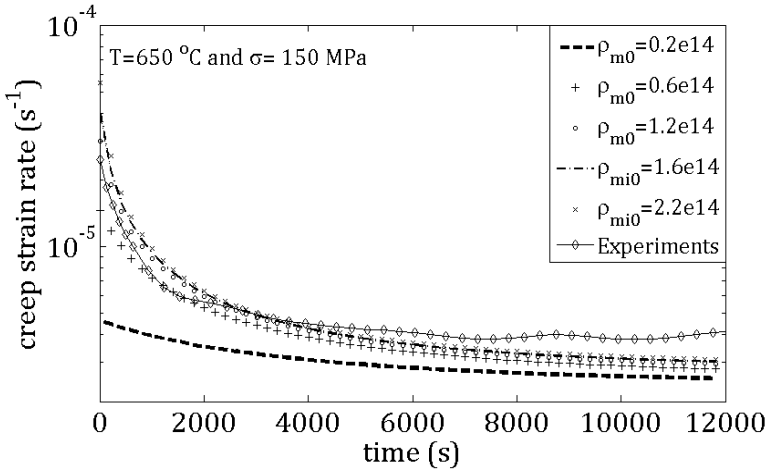

Fig. 11. Creep strain rate versus time for different values of initial dislocation densities for a creep test simulation at 150 MPa at 650 ˚C.

Fig. 12 shows the creep strain rate versus time at 700 ˚C and stress level of 150 MPa for different initial dislocation densities. Except for initial values equal to 0.2×10^{14} m^{-2} and 0.6×10^{14} m^{-2}, the simulation results are in good agreement with the experiments. Simulations have also been performed to investigate the effect of initial mobile dislocation densities for other loading cases. It can be concluded that the initial dislocation density has a significant effect on the simulation results, but it is not necessary to determine the exact value in order to produce good correlations with the experimental data. If an initial value is chosen in a domain near the dislocation density of the as-received material, the simulation results will converge to the same value.

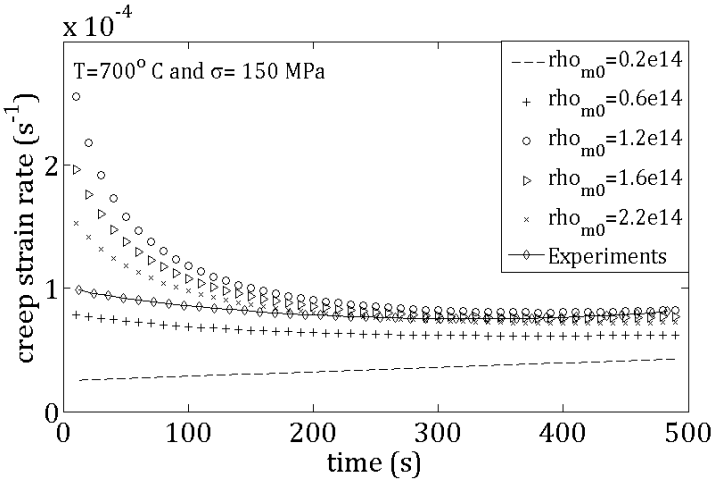

Fig. 12. Creep strain rate versus time for different values of initial dislocation densities for a creep test simulation at 150 MPa at 700 ˚C.

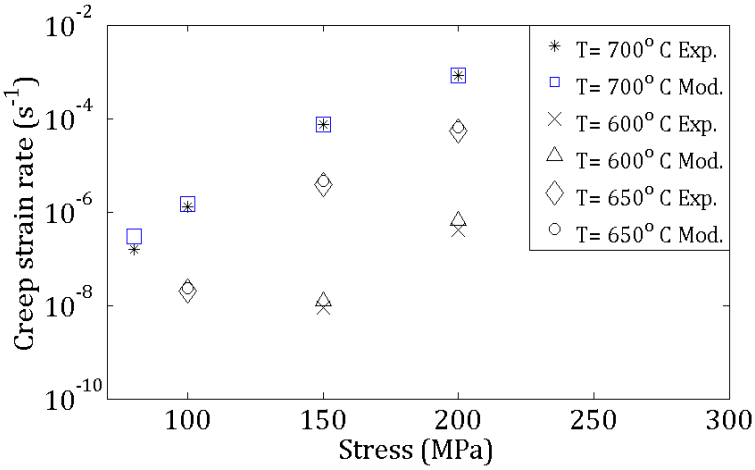

Fig. 13. Comparison between the model predictions and experimental data for the minimum creep strain rate versus applied stress at temperatures of 600, 650 and 700 ˚C.

In general, there are two different approaches to modeling creep behavior of materials. One is to simulate the three stages of the creep curve and the other is to evaluate the minimum creep rate. The advantage of the current model is that it makes both possible. In order to simplify the computing of the minimum creep rate, the model has the potential of turning all the damage terms off and predicting the minimum creep rate. Fig. 13 shows the minimum creep rates computed by the model and the comparison with experiments. In this figure, the minimum creep rate of the material at temperatures of 600, 650 and 700 ˚C and stresses of 80, 100, 150 and 200 MPa without considering the damage terms are shown. The model shows a good agreement with the experimental data.

3.5. Conclusions

This study addressed the creep behavior of the modified 9Cr-1Mo steel. By combining continuum damage terms with the Orowan's equation for creep deformation, a microstructure based model was developed. Viscous glide was considered as the main mechanism of deformation in the power-law creep region. A material parameter k_Λ in the formulation of mobile dislocation generation was considered as the only an adjustable constant, varying with both temperature and applied stress.

During creep deformation the material microstructure will degrade. The main microstructural degradations occurring in modified 9Cr-1Mo are coarsening of $M_{23}C_6$ precipitates, solid solution depletion and void and crack formation. In order to simulate the tertiary creep stage, the effect of these phenomena should be taken into account. A damage term has been defined for these microstructural changes. Three stages of creep deformation have been simulated utilizing the current model. Simulation results were compared with the experimental results for a temperature range of 600-700 ˚C and stress range of 80-200 MPa. The results obtained from the model are in a good agreement with the experimental data. As it was mentioned in this model the subgrain formation, coarsening, and also the grain boundary dislocations were neglected. The k_Λ parameter implicitly represents these effects of the aforementioned recovery processes. Future studies should focus on the physical aspects of the k_Λ parameter.

References

[1] Abu Al-Rub, R.K., Darabi, M.K., A thermodynamic framework for constitutive modeling of time- and rate-dependent materials. Part I: Theory. Int. J. Plasticity (2012), doi:10.1016/j.ijplas.2012.01.002

[2] Arzt, E., Wilkinson, D.S., 1986. Threshold stresses for dislocation climb over hard particles: The effect of an attractive interaction. Acta Metallurgica 34(10), 1893-1898.

[3] Besson, J. et al. 2009. Analysis of creep lifetime of a ASME Grade 91 welded pipe. Engineering Fracture Mechanics 76(10), 1460-1473.

[4] Bieler, T.R., Eisenlohr P., Roters, F., Kumar, D. Mason, D.E., Crimp M.A., and Raabe, D., 2009. The role of heterogeneous deformation on damage nucleation at grain boundaries in single phase metals. International Journal of Plasticity 25, 1655–1683.

[5] Blum, W., Eisenlohr, P., 2009. Dislocation mechanics of creep. Materials Science and Engineering A 510-511, 7-13.

[6] Blum, W., Eisenlohr, P., Breutinger, F., 2002. Understanding creep - a review. Metallurgical and Materials Transactions A 33, 291-303.

[7] Böck, N., Kager, F., 2005. Finite element simulation of the creep behaviour of 9% chromium steels based on micromechanical considerations. Materials Science & Technology 2005 Conference and Exhibition, Pittsburgh, PA, USA, 25-28 September 2005, 149-158.

[8] Brünig, M., Chyra, O., Albrecht, D., Driemeier, L., and Alves, M., 2008. A Ductile Damage Criterion at Various Stress Triaxialities. International Journal of Plasticity 24, 1731–1755.

[9] Chilukuru, H., Durst, K., Wadekar, S., Schwienheer, M.,Scholz, A., Berger, C., Mayer, K.H., Blum, W., 2009. Coarsening of precipitates and degradation of creep resistance in tempered martensite steels. Materials Science and Engineering A 510-511, 81-87.

[10] Courtney, T. H., 2000. Mechanical behavior of materials. McGraw-Hill series in material science and engineering, USA.

[11] Dyson, B., 2000. Use of CDM in materials modeling and component creep life prediction. Journal of Pressure Vessel Technology, Transactions of the ASME 122, 281-296.

[12] Ennis, P. J., Zielinska-Lipiec, A., Wachter, O., Czyrska-Filemonowicz, A., 1997. Microstructural stability and creep rupture strength of the martensitic steel P92 for advanced power plant. Acta Materialia 45, 4901-4907.

[13] Egner, H., and Skoczeń, B., 2010. Ductile damage development in two-phase metallic materials applied at cryogenic temperatures. International Journal of Plasticity 26, 488–506.

[14] Fischer, F.D., Svoboda, J., 2011. Chemically and mechanically driven creep due to generation and annihilation of vacancies with non-ideal sources and sinks. International Journal of Plasticity 27(9): 1384-1390.

[15] Fischer, F.D. et al., 1995. "Note on calibration of ductile failure damage indicators." International Journal of Fracture 73(4): 345–357.

[16] Fournier, B., Sauzay, M., Pineau, A. 2011. Micromechanical model of the high temperature cyclic behaviour of 9-12%Cr martensitic steels. International Journal of Plasticity 27, 1803-1816.

[17] Fujimitsu, M., 2006. Creep degradation in welds of Mod.9Cr-1Mo steel. International Journal of Pressure Vessels and Piping 83(11-12): 819-825.

[18] Gaffard, V., Gourgues-Lorenzon, A.F., Besson, J., 2005. High temperature creep flow and damage properties of 9Cr1MoNbV steels: Base metal and weldment. Nuclear Engineering and Design 235(24), 2547-2562.

[19] Ghoniem, N.M., Matthews, J.R., Amodeo, R.J., 1990. Dislocation model for creep in engineering materials. Res Mechanica 29, 197-219.

[20] Horstemeyer, M. F., Bammann, D. J., 2010. Historical review of internal state variable theory for inelasticity. International Journal of Plasticity 26(9): 1310-1334.

[21] Haney, E. M., Dalle, F., Sauzay, M., Vincent, L., Tournié, I., Allais, L., Fournier, B., 2009. Macroscopic results of long-term creep on a modified 9Cr–1Mo steel (T91). Materials Science and Engineering A 510-511, 99-103.

[22] Hollner S., Fournier B., Le Pendu J., Cozzika T., Tournié I., Brachet J. C., Pineau A., 2010. High-temperature mechanical properties improvement on modified 9Cr–1Mo martensitic steel through thermomechanical treatments. Journal of Nuclear Materials 405, 101-108.

[23] Kabadwal, A., Tamura, M., Shinozuka, K., Esaka, H., 2010. Recovery and precipitate analysis of 9 Pct Cr-1 Pct MoVNb steel during creep. Metallurgical and Materials Transactions A 41, 364-379.

[24] Kadoya, Y., Nishimura, N., Dyson, B. F., McLean, M., 1997. In: Earthman, J. C., and Mohamed, F. A., (Eds.) Proceeding of Creep and Fracture of Engineering Materials & Structures, The Minerals, Metals & Materials Society 1997, Warrendale, PA, United states, 343–352.

[25] Kang, G., Liu, Y., Ding, J., and Gao, Q., 2009. Uniaxial ratcheting and fatigue failure of tempered 42crmo steel: damage evolution and damage-coupled visco-plastic constitutive model. International Journal of Plasticity 25, 838–860.
[26] Klueh, R. L., Harris, R., 2001. High-Chromium ferritic and martensitic steels for nuclear applications. ASTM, West Conshohocken, PA, USA.
[27] Lee, Jae Seung et al. 2006. Causes of breakdown of creep strength in 9Cr–1.8W–0.5Mo–VNb steel. Materials Science and Engineering *A* 428(1–2), 270-275.
[28] Marotti de Sciarra, F., Hardening plasticity with nonlocal strain damage. Int. J. Plasticity (2012), doi:10.1016/j.ijplas.2012.01.009
[29] Masuyama, F., 2006. Creep degradation in welds of Mod.9Cr-1Mo steel. International Journal of Pressure Vessels and Piping 83, 819–825.
[30] McLean, M., Dyson, B. F., 2000. Modeling the effects of damage and microstructural evolution on the creep behavior of engineering alloys. Journal of Engineering Materials and Technology 122, 73-278.
[31] Miannay, D. P., 2001. Time-dependent fracture mechanics. Springer, New York, USA.
[32] Morra, P.V. et al. 2009. Precipitate coarsening-induced plasticity: Low temperature creep behaviour of tempered SAE 52100. International Journal of Plasticity 25(12): 2331-2348.
[33] Muñoz-Morris, M.A., Gutierrez-Urrutia, I., Morris, D. G., 2009. Influence of nanoprecipitates on the creep strength and ductility of a Fe–Ni–Al alloy. International Journal of Plasticity 25(6): 1011-1023.
[34] Murakami, S., Hayakawa, K., Liu, Y., 1998. Damage evolution and damage surface of elastic–plastic-damage materials under multiaxial loading. International Journal of Damage Mechanics 7, 103–128.
[35] Nakajima, T., Spigarelli, S., Evangelista, E., Endo, T. 2003. Strain Enhanced Growth of Precipitates during Creep of T91. Materials Transactions 44, 1802-1808.
[36] Oberson, P.G., Ankem S., 2009. The effect of time-dependent twinning on low temperature ($<0.25 * Tm$) creep of an alpha-titanium alloy. International Journal of Plasticity 25(5): 881-900.
[37] Panait, C. G., Zielińska-Lipieca, A. Z., Koziel, T., Czyrska-Filemonowicza, A., Gourgues-Lorenzonb, A. F., Bendickd, W., 2010. Evolution of dislocation density, size of subgrains and MX-type precipitates in a P91 steel during creep and during thermal ageing at 600 ◦ C for more than 100,000 h. Materials Science and Engineering A 527, 4062–4069.
[38] Poirier, J. P., 1985. Creep of crystals, high-temperature deformation processes in metals, ceramics, and minerals, Cambridge University Press, Cambridge.
[39] Preußner, J. et al. 2009. A dislocation density based material model to simulate the anisotropic creep behavior of single-phase and two-phase single crystals. International Journal of Plasticity 25(5): 973-994.
[40] Raj, S. V., 2002. Power-law and exponential creep in class M materials: Discrepancies in experimental observations and implications for creep modeling. Materials Science and Engineering A 322, 132-147.
[41] Raj, S. V., Iskovitz, Ilana, S., Freed, A., 1995. Modeling the role of dislocation substructure during class M and exponential creep. In: Unified Constitutive Laws of Plastic Deformation. Academic Press, San Diego, CA, USA, 343–439.
[42] Semba, H., Dyson, B. F., Mclean, M., 2005. Microstructural based creep modeling of a 9%Cr Martensitic steel. In: Shibli I. A., Holdsworth S. R., Merkling, G. (Eds.)

Proceeding of Creep and Fracture in High Temperature Components-Design and Life Assessment, 12-14 September 2005, London, UK, DEStech Publications Lancaster, PA, USA, 419–27.

[43] Shrestha T., et al. 2012. Creep deformation mechanisms in modified 9Cr–1Mo steel. Journal of Nuclear Materials 423, 110-119.

[44] Sklenička, V., Kuchařová, K., Svoboda, M., Kloc, L., Burši, J., Kroupa K. A., 2003. Long-term creep behavior of 9–12 Cr power plant steels. Materials Characterization 51, 35-48.

[45] Sklenička, V., Kuchařová, K., Dlouh, S, A., Krejci, J., 1994. Creep behaviour and microstructure of a 9%Cr steel In: Coutsouradis, D. Davidson, J. H., Ewald, J., Greenfield, P. (Eds.) Proceedings of the Conference on Materials for Advanced Power Engineering, Kluwer Academic Publishing, Dordrecht, Netherlands, 435–444.

[46] Spigarelli, S., Kloc, L., Bontempi, P., 1997. Analysis of creep curves in a 9Cr-1Mo modified steel by means of simple constitutive equations. Scripta Materialia 37, 399-404.

[47] Sauzay, M., 2009. Modelling of the evolution of micro-grain misorientations during creep of tempered martensite ferritic steels. Materials Science and Engineering A 510–511, 74-80.

[48] Swindeman, R. W., Santella, M. L., Maziasz, P. J., Robertsb , B. W., Coleman , k., 2004. Issues in replacing Cr–Mo steels and stainless steels with 9Cr–1Mo–V steel term. International Journal of Pressure Vessels and Piping 81, 507-512.

[49] Terada, D., Yoshida, F., Nakashima, H., Abe, H., & Kadoya, Y., 2002. In-situ Observation of Dislocation Motion and Its Mobility in Fe–Mo and Fe–W Solid Solutions at High Temperatures. ISIJ International 42, 1546-1552

[50] Venkataramani, G., Kirane, K., Ghosh, S., 2008. Microstructural parameters affecting creep induced load shedding in Ti-6242 by a size dependent crystal plasticity FE model. International Journal of Plasticity 24(3): 428-454.

[51] Viswanathan, R. 1989. Damage mechanisms and life assessment of high-temperature components. ASM International, Ohio, USA.

[52] Voyiadjis, G.Z., Kattan, P.I., 1992. A plasticity-damage theory for large deformation of solids 1: Theoretical formulation. International Journal of Engineering Science 30, 1089–1108.

[53] Yin, Y. F., Faulkner, R. G., 2008. Creep life predictions in 9% Cr Ferritic steels. In: Proceeding of International Conference on New Developments on Metallurgy and Applications of High Strength Steels (TMS). Buenos Aires, Argentina 2008, 283-296.

Task 4: Simulations of modified 9Cr-1Mo structures using polycrystal plasticity

4.1. Introduction

In this task a dislocation-based creep model combined with a continuum damage model for modified 9Cr-1Mo steels is developed and implemented in the finite element method. Modified 9Cr-1Mo steel is a candidate material for very high-temperature reactor (VHTR) pressure vessels. The material microstructure degrades during the welding process, hence the material creep resistance reduces during service. The evolution of dislocation structure has been considered as the driving creep mechanism in this material. The effect of void growth and crack formation, precipitate coarsening, and solid solution depletion were t considered as damage evolution phenomena. . The analytical model was been implemented in the commercial finite element code ABAQUS Standard as a User Material Subroutine (UMAT). Experimental creep tensile tests and finite element simulations of welded specimens manufactured from modified 9Cr-1Mo were performed. The creep behavior of testing specimens was simulated by taking into account the difference in the creep strength of materials in the in the heat affected zone (HAZ) and the base material. The tensile creep tests were performed at temperature range of 550-700 ˚C and stress level of 80-200 MPa. The model predicts well the creep behavior of welded specimens. Lastly, the show the applicability of the developed model, an analysis of a three-dimensional geometry subjected to creep loading was performed.

The Very High Temperature Reactor (VHTR) represents the next generation of high temperature gas-cooled nuclear reactors. VHTRs operate at temperature range of 450- 550° C and pressure range of 5-9 MPa. The design life of VHTR is 60+ years and its size is almost two times larger than that of the current gas-cooled reactors. In order to satisfy design conditions, it is necessary to employ a heat and radiation resistant material for the pressure vessel. The modified 9Cr-1Mo steel is a potential material for the VHTR pressure vessels. Manufacturing this type of large pressure vessel involves on-site ring forging and on-site joining. Welding is the preferred joining method. While welding is one of the most beneficial advantageous joining methods, it however exposes the components to high temperatures which may result in the degradation of the material microstructure. Although 9Cr-1Mo steel exhibits a excellent heat resistance property, it is not excluded from microstructural degradation during the welding process. Therefore, for applications such as pressure vessels for VHTRs, it is crucial to investigate the creep resistance of 9Cr-1Mo steel welded joints. The creep behavior of welded joints of 9Cr-1Mo steel has been previously studied by [1,3,7,8,9,16,17,18,19].

Dislocations restructuring is the main mechanism that drives creep deformation in modified 9Cr-1Mo steel. The dislocation restructuring results from dislocation and dipole generation and annihilation, as well as dislocation glide and climb. The macroscopic effect of these microstructural changes is the resulting creep strain rate. In addition to deformation related to changes in dislocation density, other degradation phenomena leading to creep in 9Cr-1Mo steel include microstructural changes of solid solutions, precipitates, grain boundaries, and subgrains. For example, the depletion of Mo particles in the subgrain matrix under long term thermo-mechanical loading decreases the creep resistance. Moreover, $M_{23}C_6$ and MX precipitates coarsening increases the interparticle spacing between the precipitates, leading to enhanced dislocation mobility. Consequently, dislocations require less energy to climb over

precipitates [3]. Void nucleation and crack formation is one of the most important damage mechanisms in 9Cr-1Mo steel. Cavities usually nucleate at triple junctions or at the particles located at grain boundaries. Grain deformation and cavity coalesce are the main crack formation mechanism in 9Cr-1Mo [7,10,11].

The primary goals of this research are to propose a unified elastic-viscoplastic constitutive model for the creep analysis of modified 9Cr-1Mo steel in a format that can be implemented in the finite element method. The microstructural creep model combined with a continuum damage mechanics model was first developed and presented in [2]. However, in that study the model was implemented as a one-dimensional material-point simulator code, and was successfully applied only to homogenous specimens made of the base metal (BM) of modified 9Cr-1Mo. The motivation of this research was the need for a numerical model implemented in the finite element analysis to analyze three-dimensional geometries of non-homogenous materials (i.e. welded specimens) subjected to complicated loading cases. To achieve these goals, the afore-mentioned model was modified and implemented by means of a semi-implicit integration scheme. The time integration algorithm was implemented in ABAQUS by developing a User Material Subroutine (UMAT). In order to check the accuracy and stability of the model, several case studies of elastic-viscoplastic deformations of single element under uniaxial tensile loading have been studied. The implemented model was used to predict the creep deformation and resistance of welded joints of modified 9Cr-1Mo steel.

4.2. Constitutive Model

4.2.1. Elasticity and creep constitutive equation

According to the classical theory of plasticity for any infinitesimal inelastic deformation the accumulated strain is modeled here as the summation of the elastic and creep strains,

$$\varepsilon_{ij} = \varepsilon_{ij}^{el} + \varepsilon_{ij}^{cr} \quad (1)$$

and in the rate form

$$\dot{\varepsilon}_{ij} = \dot{\varepsilon}_{ij}^{el} + \dot{\varepsilon}_{ij}^{cr} \quad (2)$$

The creep strain rate is considered a function of equivalent stress, temperature and some internal state variables,

$$\dot{\varepsilon} = \dot{\varepsilon}(\bar{\sigma}, T, \xi) \quad (3)$$

where the equivalent stress is computed as

$$\bar{\sigma} = \sqrt{\frac{3}{2} S_{ij} : S_{ij}}, \; Where \; S_{ij} = \sigma_{ij} - \frac{1}{3}\delta_{ij}\sigma_{kk} \quad (4)$$

The evolution of the state variables has the same format as that of the creep strain as

$$\dot{\xi}_a = q_a(\bar{\sigma}, T, \xi) \tag{5}$$

In the present model, internal variables refer to the dislocation density, solid solutions, precipitate size, and other strengthening mechanisms terms. These strengthening mechanisms could induce isotropic hardening in the material. This isotropic hardening resistance evolves during a thermally activated deformation process such as creep. In a rate-dependent inelastic deformation, the rate of evolution of the internal variables can also be expressed by the internal variables rate equations $\dot{\xi}_a$. Here, $\dot{\xi}_a$ is defined by some functions q_a which depend on σ, T, ξ. The elastic response of the material is modeled by the linear isotropic elastic equation. The linear isotropic elastic stress strain equation is valid for creep deformation and it has been defined in equation 2.

$$\sigma_{ij} = 2G\varepsilon_{ij}^{el} + \lambda \delta_{ij}\varepsilon_{kk} \tag{6}$$

where, G is the shear modulus and λ is Lame' Coefficient.

A continuum damage creep model has been developed in a previous work [2]. A simplified version of the mentioned model has been employed here to analyze the creep behavior of the modified 9Cr-1Mo steel. In the original model the density of the dipole dislocations was taken into account. By performing numerous simulations on the original model, it was observed that neglecting the dipole dislocations density reduces the number of equations in the model significantly, while it doesn't change the simulation results considerably. Starting from the equations presented in [2], the Orowan's equation for creep modified for damage was employed to evaluate the creep strain rate in the media

$$\dot{\bar{\varepsilon}}^{cr} = \frac{\rho_m b B_{visc}}{M\, D}(\bar{\sigma} - \alpha MCGb\sqrt{\rho_m}) \tag{7}$$

In this equation ρ_m is the mobile dislocation density, b is the burger's vector, α is a dislocation interaction constant, M is the Taylor factor, C is the inelastic deformation factor (C has been considered equal to *0.2* in this research), and B_{visc} is the dislocation mobility term. For simplicity, the following notation is made $K_1 = \alpha MCGb$. The term D represents the damage caused by precipitate coarsening, depletion of solid solutions, and void and crack formation. The dislocation mobility term is defined according to [4] as

$$B_{visc} = \frac{9\Omega D_{sol} K_B T}{MC_0 G^2 b^7 \varepsilon_a^2 \ln(\frac{r_2}{r_1})} \tag{8}$$

where Ω is the atomic volume (which has been considered equal to b^3), K_B is the Boltzmann constant, T is the temperature, D_{sol} is the solute atom diffusion coefficient in solvent atoms, C_0 is the solute concentration, r_1 and r_2 are the outer and inner cut-off radii of the dislocation stress field, and ε_a, is the relative size misfit between solute and solvent atoms. The rate of evolution of

mobile dislocations density is defined as the difference between the rate of generation of mobile dislocations ($\dot{\rho}_{m,gen}$), and the rate of annihilation of mobile dislocations density

$$(\dot{\rho}_{m,ani}), \dot{\rho}_m = \dot{\rho}_{m,gen} - \dot{\rho}_{m,ani} \tag{9}$$

The rate of generation of the mobile dislocation density is

$$\dot{\rho}_{m,gen} = \frac{\rho_m B_{visc} \sqrt{\rho_m}}{k_\Lambda D} (\bar{\sigma} - K_1 \sqrt{\rho_m}) \tag{10}$$

where k_Λ is a material parameter, and is a function of temperature and equivalent stress. The rate of annihiliation of the mobile dislocationsis modeled as

$$\dot{\rho}_{m,ani} = \frac{4M\dot{\varepsilon} d_{dip} \rho_m}{b n_g} \tag{11}$$

The rate of annihiiation of mobile dislocation is equal to the summation of the densities of dislocations which annihiliate spontaneously and those which form dipoles. It is a function of strain rate, mobile dislocations density, burger's vector, Taylor factor and the number of active slip planes n_g . Replacing the $\dot{\varepsilon}$ in equation (11) by its value from equation (7) and the rate of annihilation of mobile dislocations could be expressed as,

$$\dot{\rho}_{m,ani} = \frac{4 d_{dip} \rho^2{}_m B_{visc}}{n_g D} (\bar{\sigma} - K_1 \sqrt{\rho_m}) \tag{12}$$

two mobile disliocations with opposite sings approach eachother, at a certain distance they will form dipoles and produce sessile dislocations. This distance is d_{dip} called, the dipole formation distance and has been defined as

$$d_{dip} = \frac{M}{8\pi(1-\nu)} \frac{Gb}{\bar{\sigma}} \tag{13}$$

In this equation ν is the Poisson's ratio. Replacing d_{dip} in equation (12), the rate of annihilation of mobile dislocations will be,

$$\dot{\rho}_{m,ani} = \frac{4MbG\rho^2{}_m B_{visc}}{2\pi(1-\nu) n_g D \bar{\sigma}} (\bar{\sigma} - K_1 \sqrt{\rho_m}) \tag{14}$$

4.2.2. Damage constitutive equations

The material microstructures will degrade during high temperature exposure. In other words, the strengthening mechanisms that have been used to increase the creep resistance of materials will become less effective during creep loading. The main strengthening mechanisms in modified 9Cr-1Mo steel are work hardening, solid solution strengthening, precipitation hardening, and grain boundary strengthening. It has been shown by several researchers that the Mo particles deplete in the subgrain matrix under long term thermo-mechanical loading [5,13,14]. Moreover, the precipitate coarsening ($M_{23}C_6$ and MX) in modified 9Cr-1Mo increases the interparticle spacing between the precipitates. Solid solutions depletion and precipitate coarsening increase the dislocations mobility. Consequently dislocations require less energy to move [3]. Furthermore, void nucleation and crack formation is one of the most important creep damage mechanisms in 9Cr-1Mo steel. The cavities usually nucleate at triple junctions or at the particles located on grain boundaries. Grain deformation and cavity coalesce are the main crack formation mechanisms in 9Cr-1Mo steel.

Mo is added to 9Cr-1Mo steel to induce solid solution strengthening. During creep loading the Mo particles deplete in the subgrain matrix and form precipitation of Fe_2Mo Laves phase. It has been shown by experiments that Fe_2Mo precipitates with low volume fraction and larger size could not effectively block dislocations motions. These large size Laves phases (Fe_2Mo) are a source for dislocations absorbent, and they are brittle phases. These inopportune properties will lead to a reduction of the creep resistance of modified 9Cr-1Mo. [11]

Equations (15-16) show the damage caused by solid solution depletion and its corresponding rate, respectively is the solid solution depletion term is a function of the initial and current solid solution concentrations, C_0 and C_t

$$D_s = 1 - \frac{\bar{C}_t}{C_0} \tag{15}$$

$$\dot{D}_S = K_S D_S^{1/3}(1 - D_S) \tag{16}$$

where, K_S is the material parameter.

Another important damage mechanism in 9Cr-1Mo steel is caused by the coarsening of $M_{23}C_6$ and MX precipitates. The coarsening of precipitates increases the interparticle spacing and consequently the easier motion of dislocations which means less creep resistance. This damage and damage rate of accounting for the precipitate coarsening written as

$$D_P = 1 - \frac{P_0}{P_t} \tag{17}$$

$$\dot{D}_p = k_p(1 - D_p)^4 \tag{18}$$

where P_0 and P_t are the initial and current size of the precipitates, and k_P is the material parameter.

A leading failure mechanism during creep deformation of modified 9Cr-1Mo is crack incubation and growth. Microstructural stress concentrations are responsible for grain boundary sliding leading to the formation of creep cavities and creep crack formation. Creep crack

formation and growth has been extensively studied in literatures. In this research a modified Kachanov damage model has been employed for the crack-driven creep damage. Simply, creep damage is expressed as a function of creep exposure time (t), creep rupture time ($t_{rupture}$), and a material parameter B and is a function of stress. The creep rupture time can be obtained from experiments. The creep rupture time for 9Cr-1Mo steel is shown in Fig. 1. To summarize the crack-driven damage is modeled as

$$D_N = 1-(1-\frac{t}{t_{rupture}})^{1/(1+B)} \tag{19}$$

For simplicity, the total damage in the material caused by solid solution depletion, precipitate coarsening and crack formation is denoted as D, and is defined as

$$D = D(D_S, D_P, D_N) = (1-D_S)(1-D_P)(1-D_N) \tag{20}$$

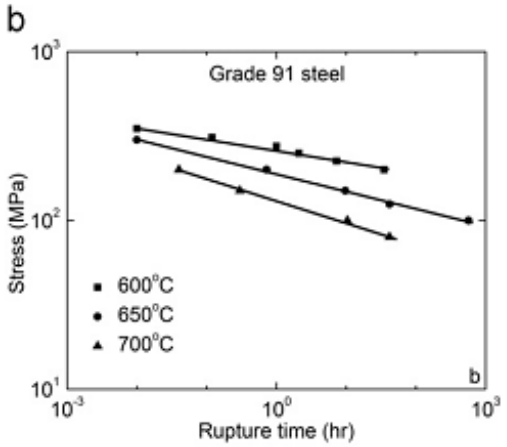

Fig.. 1. True stress versus creep rupture time for Grade 91 steel specimens.

4.2.3. Numerical Integration

In order to be able to simulate three-dimensional geometries or components made of different materials one has to use the finite element method. The analytical model presented in the previous section was implemented in the finite element code ABAQUS Standard as a User Material (UMAT) subroutine. . Creep deformation is a history-dependent process. In order to solve the set of differential equations representing the constitutive model, it is necessary to discretize these equations and integrate them over time. First, the governing equations for the equivalent stress are presented.

The strain decomposition rule should be valid at any time increment (n) for any increment of trial strain,

$$\varepsilon_{ij,n+1}^{el} = \varepsilon_{ij,n}^{el} + (\Delta\varepsilon_{ij}^{tr} - \Delta\varepsilon_{ij}^{cr}) \tag{21}$$

Replacing equation (21) in equation (2) and performing and after some re-arrangement, the stress in predictor-corrector form easily obtain as

$$\sigma_{ij} = \sigma_{ij}^{tr} - 2G\Delta\varepsilon_{ij}^{cr} . \tag{22}$$

From the classical theory of isotropic plasticity, it is possible to express the components of creep strain rate in the direction of stress as

$$\dot{\varepsilon}_{ij}^{cr} = \lambda S_{ij} = \frac{3}{2}\dot{\bar{\varepsilon}}^{cr}\frac{S_{ij}}{\bar{\sigma}}, where\ \lambda = \frac{3\dot{\bar{\varepsilon}}^{cr}}{2\bar{\sigma}} . \tag{23}$$

where λ is the creep strain multiplier. From the previous equation, multiplying by time increment Δt,

$$\Delta\varepsilon_{ij}^{cr} = \frac{3}{2}\Delta\dot{\bar{\varepsilon}}\frac{S_{ij}}{\bar{\sigma}}\Delta t = \frac{3}{2}\Delta\bar{\varepsilon}^{cr}\frac{S_{ij}}{\bar{\sigma}} = \mathbf{n}\Delta\bar{\varepsilon}^{cr} . \tag{24}$$

Here, $\mathbf{n}$ is the unit vector normal to the yield surface, and the above equation represents the normality rule. It can be shown that $\mathbf{n} = \frac{3}{2}\frac{S_{ij}}{\bar{\sigma}}$. With some algebra it is possible to rewrite equation (22) in the equivalent stress format [6].

$$\bar{\sigma} - \bar{\sigma}^{tr} + 3G\Delta\bar{\varepsilon}^{cr} = 0 \tag{25}$$

Equation (25) is the governing equation for the equivalent creep stress, while the trial stress σ^{tr} is calculated using equation (6). In addition to the creep strain, another state variable considered in this model is the density of mobile dislocations ρ_m .Replacing equations (10) and (14) in equation (9) rate of change of mobile dislocation density becomes

$$\dot{\rho}_m = g(\bar{\sigma}, \rho_m, D) = \frac{\rho_m B_{visc}(\bar{\sigma} - K_1\sqrt{\rho_m})}{D}\left(\frac{\sqrt{\rho_m}}{K_\Lambda} - \frac{4d_{dip}\rho_m}{n_g}\right) \tag{26}$$

The integration of the damage term is done using an explicit scheme

$$D_{n+1} = D_n + \dot{D}_n\Delta t \tag{27}$$

The following equations show the discretized form of equations (25) and (26)

$$F(\bar{\sigma}_{n+1}, \rho_{m_{n+1}}, D_n) = \bar{\sigma}_{n+1} - \bar{\sigma}_{n+1}^{Tr} + 3Gf(\bar{\sigma}_{n+1}, \rho_{m_{n+1}}, D_n) = 0 \tag{28}$$

$$G(\bar{\sigma}_{n+1}, \rho_{m_{n+1}}, D_n) = \rho_{m_{n+1}} - \rho_{m_n} + g(\bar{\sigma}_{n+1}, \rho_{m_{n+1}}, D_n) = 0 \tag{29}$$

To solve the above system of equations, the Newton-Raphson (N-R) method combined with a backline search algorithm was used. The Jacobian matrix needed in the N-R method was

computed numerically, however, analytical form could also be obtained. At the end of each time step, the damage terms have been explicitly updated The N-R method gives the increments in equivalent stress and dislocation density

$$\begin{pmatrix} \Delta\bar{\sigma}_{n+1} \\ \Delta\rho_{m_{n+1}} \end{pmatrix} = -\begin{pmatrix} \dfrac{\partial F}{\partial\bar{\sigma}_{n+1}} & \dfrac{\partial F}{\partial\rho_{m_{n+1}}} \\ \dfrac{\partial G}{\partial\bar{\sigma}_{n+1}} & \dfrac{\partial G}{\partial\rho_{m_{n+1}}} \end{pmatrix}^{-1} \begin{pmatrix} F(\bar{\sigma}_n, \rho_m, D_{T_{n-1}}) \\ G(\bar{\sigma}_n, \rho_{m_n}, D_{T_{n-1}}) \end{pmatrix}$$

(30**)**

and the $\bar{\sigma}_{n+1}$, and $\rho_{m_{n+1}}$ will be updated using $\bar{\sigma}_{n+1} = \bar{\sigma}_n + \Delta\bar{\sigma}_{n+1}$, and $\rho_{m_{n+1}} = \rho_{m_n} + \Delta\rho_{m_{n+1}}$.

After that, the damage term D_n updated with equation (27) Introducing the updated variables and D_n in equation (31), the $\dot{\bar{\varepsilon}}^{cr}_{n+1}$ will be found and consequently the $\Delta\bar{\varepsilon}^{cr}$

$$\dot{\bar{\varepsilon}}^{cr}_{n+1} = f(\bar{\sigma}_{n+1}, \rho_{m_{n+1}}, D_n) = \frac{\rho_{m_{n+1}} bB_{visc}}{M\, D_n}(\bar{\sigma}_{n+1} - \alpha MCGb\sqrt{\rho_{m_{n+1}}}) \qquad \textbf{(}31\textbf{)}$$

Substituting the equivalent increment of creep strain ($\Delta\bar{\varepsilon}^{cr}$) in equation (23), the components of creep strain tensor will be obtainable. Once the strain increment and strain tensors components are obtained the stress increment and stress tensor components will be obtain using equation (32),

$$\sigma_{ij_{n+1}} = \mathbf{C}^{el}(\Delta\varepsilon^{tr}_{ij_{n+1}ij_{n+1}} - \Delta\varepsilon^{cr}_{ij}) + \sigma_{ij_n}. \qquad (32\textbf{)}$$

The updated stress, state variables and a tangent stiffness matrix are returned to ABAQUS by the UMAT. To update the tangent stiffness matrix, the elastic stiffness matrix ($\mathbf{C}^{el}$) was, which is a common approach in finite element simulation of creep deformations.

4.3. Experimental Method and Properties of Welded Material

Creep experiments were conducted on welded specimens at temperatures between 550˚C and 700˚C and stress levels between 80 and 200 MPa by using an Applied Test Systems (ATS) lever arm (20:1) creep tester. Welded specimens were been made of ASTM A387 Grade 91 CL2 steel (Grade 91) steel. The specimens were machined out of as-received plates and were given around cross-section with a diameter of 12.7 mm and gage length of 45 mm. The chemical composition of Grade 91 steel is shown in Table 1.

The as-received plates were delivered from hot rolled Grade 91, in normalized and tempered condition (i.e., austenitized at 1038 K for 240 minute, followed by air cooling, and tempered at 789 K for 43 minute). The original dimensions of the as-received Grade 91 plate were 104 mm×104 mm×12.7 mm. The mechanical properties of the material are shown in Table 2. In order to make the specimens, plates were cut into halves and tapered for double V welding joints, as shown in Fig. 3. In this figure Long, Trans, and TT are the longitudinal, the transversal

and the through-thickness directions, respectively. The Metrode 2.4 mm diameter 9CrMoV-N TIG filler wire, which is well known for low residual stresses, was used for welding. The plates were preheated at 260^{o}C before welding. To prevent overheating, the steel plates were placed on an aluminum plate during welding. The welding was completed in three successive passes with a current of 130 A, and voltage of 15 V. The post weld heat treatment (PWHT) was conducted at 750^{o}C for 2 hr.

As it was mentioned earlier, the microstructure of the welding heat affected zone will undergo changes due to the temperature gradient during welding. The microstructure of the as-welded and post-weld heat-treated specimens exhibits three different zones, i.e. the unaffected base material, the heat affected zone and the weld material. A typical heat affected zone presents two distinct microstructures: the fine grain heat affected zone (FGHAZ), and the coarse grain heat affected zone (CGHAZ). It has been widely reported that type IV cracks initiate at heat affected zone. This is caused by non-uniform structure of the heat affected zone. The non-uniform structure of HAZ is caused by the partial transformation of austenite into martensite, the presence of retained austenite, the formation of delta-ferrite, and differential migration of interstitial and precipitate forming elements through the heat affected zone which creates a complex microstructure prone to failure.

The hardness of Grade 91 steel in the as-received and PWHT condition has been measured by using a Vickers microhardness tester. The hardness of the as-welded material increased across the weld but decreased in the HAZ, as shown in Fig. 2a. As-welded specimen had a maximum hardness of 474 VHN in the weld, while HAZ exhibited the lowest hardness of 200 VHN. The base material had a hardness of approximately 225 VHN. The HAZ was symmetric on either side of the weld. The hardness profile of specimen PWHT at 750^{o}C for 2 hours was similar to the as-welded specimen, but the hardness magnitudes were lower. The maximum hardness of 304 VHN was observed at the weld, while the lowest hardness of 174 VHN was observed at HAZ. There have been correlations the hardness of steels with the yield stress. The yield stress profile of as-welded and PWHT specimen is similar to the hardness profile, as observed in Fig. 2b.

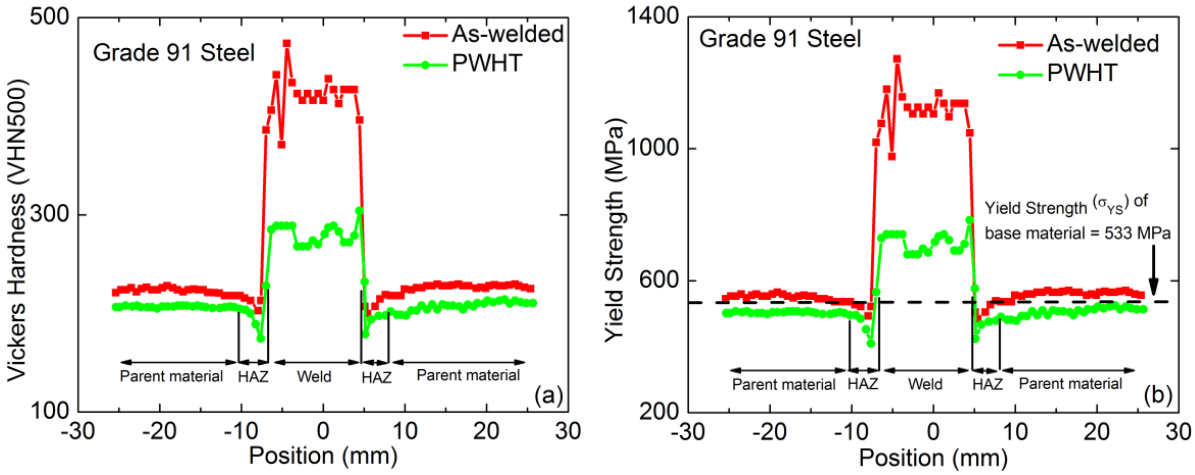

Fig. 2- Vickers microhardness (a) and yield strength profile (b) of welded Grade 91 steel. Position '0' indicates the center of the weld.

4.4. Results

In order to perform a finite element analysis on the welded specimen it is necessary to provide the material parameters for each distinct region of the specimen. In general, it is acceptable to divide the specimen into three regions, the BM, FGHAZ (HAZ II), CGHAZ (HAZ I) and the welded material (WM).

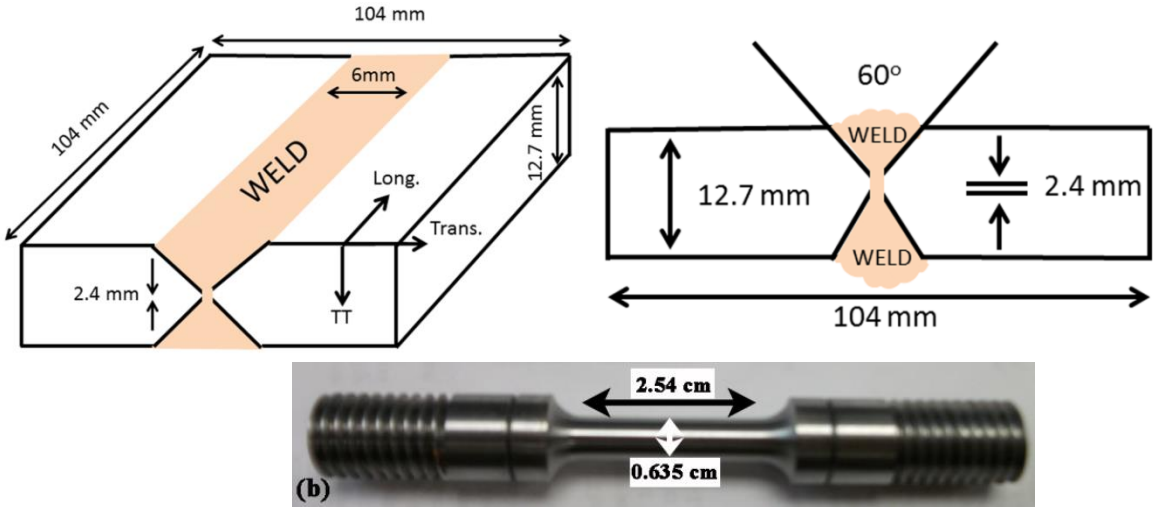

Fig. 3- (a) Schematic representation of the double V-butt welded plate and (b) specimen used for creep testing. The specimen is cut from the plate, and the central portion of the specimen matches the weld zone.

Although the HAZ microstructure changes gradually from the WM to the BM, in this study, for simplicity the HAZ was considered as divided into two homogeneous parts (HAZ I and HAZ II). Gaffard, et al. [7] showed that the WM and BM demonstrate similar steady state creep behaviors. Hence, in the finite element model the same material properties were considered for BM and the WM regions.

Simulations were performed on a model with three materials, the BM and HAZ, the HAZ segment was divided to HAZ I and HAZ II. Fig. 4 shows the schematic sketch of each segments of the welded specimen. Given such a configuration of the specimen, the steady state creep rate is computed using the following equation

$$\dot{\varepsilon}_{SS} l_T = l_{BM}\dot{\varepsilon}_{BM} + l_{WM}\dot{\varepsilon}_{WM} + l_{HAZ}\dot{\varepsilon}_{HAZ} \tag{33}$$

where, $\dot{\varepsilon}_{SS}$, $\dot{\varepsilon}_{BM}$, $\dot{\varepsilon}_{WM}$ and $\dot{\varepsilon}_{HAZ}$ are the steady state creep strain rates of the welded specimen (SS), BM, WM, and HAZ respectively. l_T (=45 mm) is the total gage length of the specimen, l_{BM}, l_{WM} ($l_{BM} + l_{WM}$ = 39 mm) represent the length of BM, WM zones, and l_{HAZ} (= 6 mm) is the length of HAZ zone. If the steady state creep test data for both welded specimen and BM are available, the material properties for HAZ can be obtained. Considering the same material properties for the steady state creep rate of the welded specimen in the WM and BM, and replacing the parameters in equation (33) one can find the material properties for the HAZ as

$$\dot{\varepsilon}_{HAZ} = \frac{\dot{\varepsilon}_{SS} l_T - (l_{BM} + l_{WM})\dot{\varepsilon}_{BM}}{l_{HAZ}}. \tag{34}$$

As discussed before, the model requires a number of material parameters. Some of these parameters are a function of temperature and applied stress, while others are independent of stress and temperature. The material properties independent of the loading conditions are $b = 2.47e{-}10\,m$, $M = 3$, $ng = 5$, $\alpha = .02$, and $C_0 = .056$. Two key material parameters for the second stage creep are k_Λ and ρ_m. While it is not straight forward how to measure the dislocation density ρ_m, it has been showed by [2] that, in this model if the initial dislocation density is in a realistic range (=0.2 e14 to 2 e14 m^{-2}), the final results will converge to the same value.

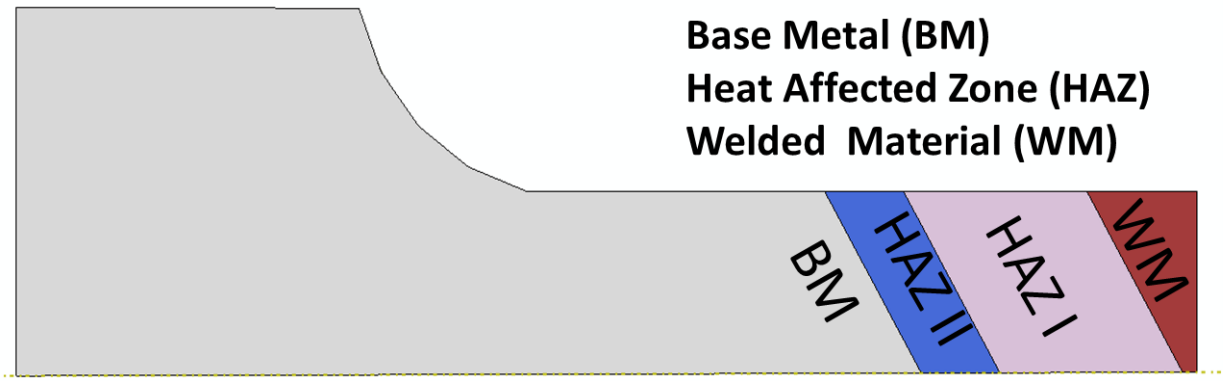

Fig.4 Schematic representation of the welded specimen, showing the Base Metal (BM), Heat Affected Zone I and II (HAZ I and II), and the Welded Material (WM).

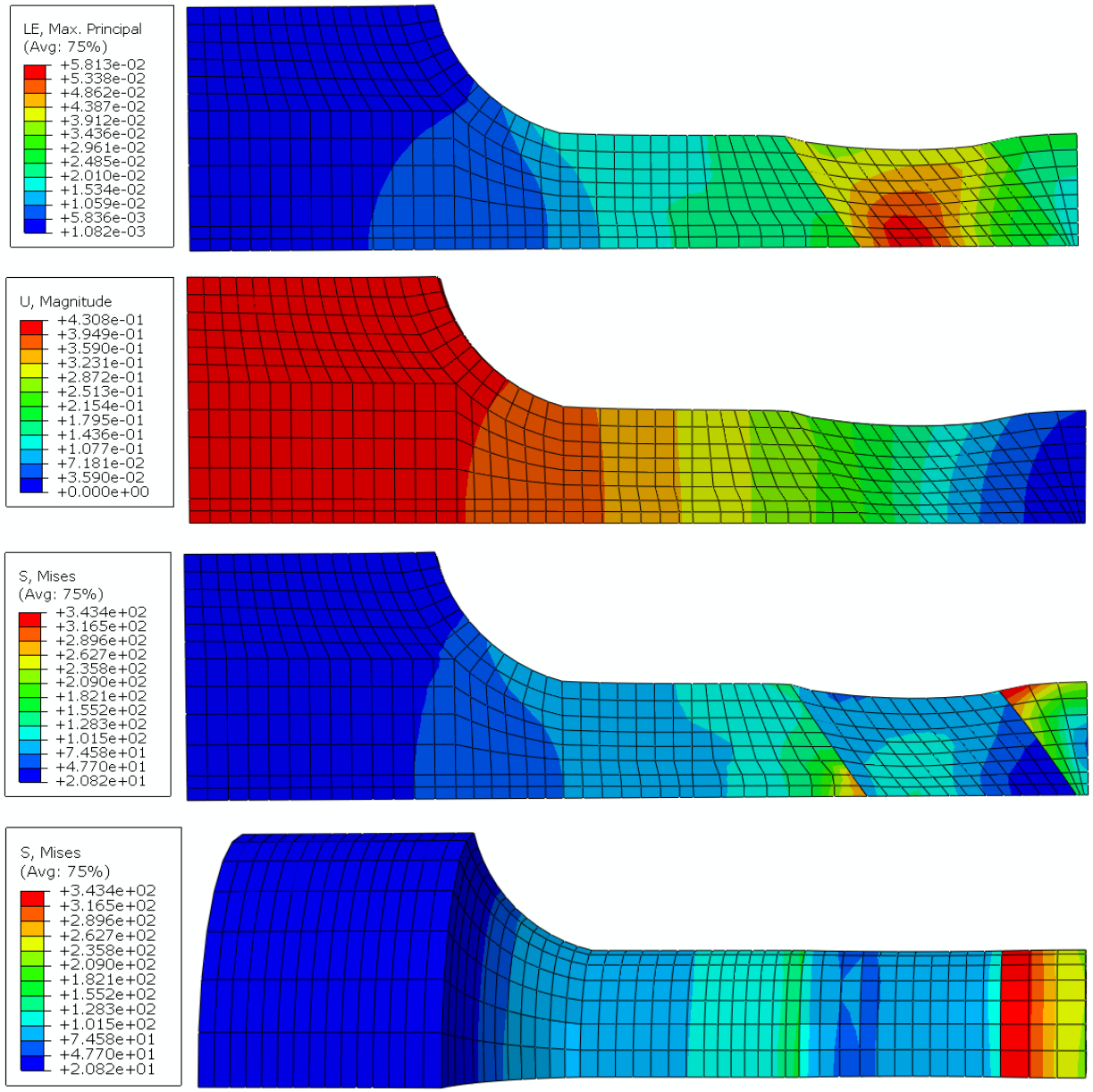

Fig.5- Finite element simulations form an applied stress of 200 MPa and 600˚C: (a) maximum principle strain, (b) von-Mises stress in the cross section of the specimen, (c) displacement along the axis of the specimen, and (d) the stress distribution at the surface of the specimen.

The values for k_{Λ} may be determined by performing simulation for minimum creep rate in the welded and BM specimens, and by employing equation (33). Furthermore, $t_{rupture}$ for different loading conditions has been obtained from Fig. 1 and our experiments. Values for the remaining material parameters that have been used in this research are indicated in Table 3.

The finite element simulations have been performed in Abaqus for a range of stress and temperature. Figs. 5a-d show the displacement along the axis of the specimen, the maximum

principle strain, and the von-Mises stress on a cross-section and at the surface of the specimen. Fig. 6 shows the comparison of the experimental result to the model simulation for 100 MPa and 600˚C. Fig. 6a shows the rate of creep strain versus time and Fig. 6b shows the true creep strain versus time.

The simulation and experimental results comparison for 150 MPa at 600˚C have been showed in Fig. 7. Again, Fig. 7a is the creep strain rate versus time and Fig. 7b is the true creep strain versus time. For specimen crept at 200 MPa and 600˚C figures (8a and 8b) respectively show the creep strain rate versus time and the true creep strain versus time. The comparison of the modeling versus experiments at 650˚C and applied stresses of 100 MPa, as well as 125 MPa and 200 MPa have been showed in Fig. 9 and 11 respectively. Finally, Fig. 12a-b show the comparison of creep strain rate versus time and true creep strain versus time at 700˚C and applied stress of 100 MPa.

The main goal of developing this numerical model was to enable us to simulate the creep deformations in complex geometries. The model was applied to study the creep in a pipe made of 9Cr steel connected to a flange of Inconel X625. The creep deformation and stress distribution in this joint have been showed in Fig. 13.

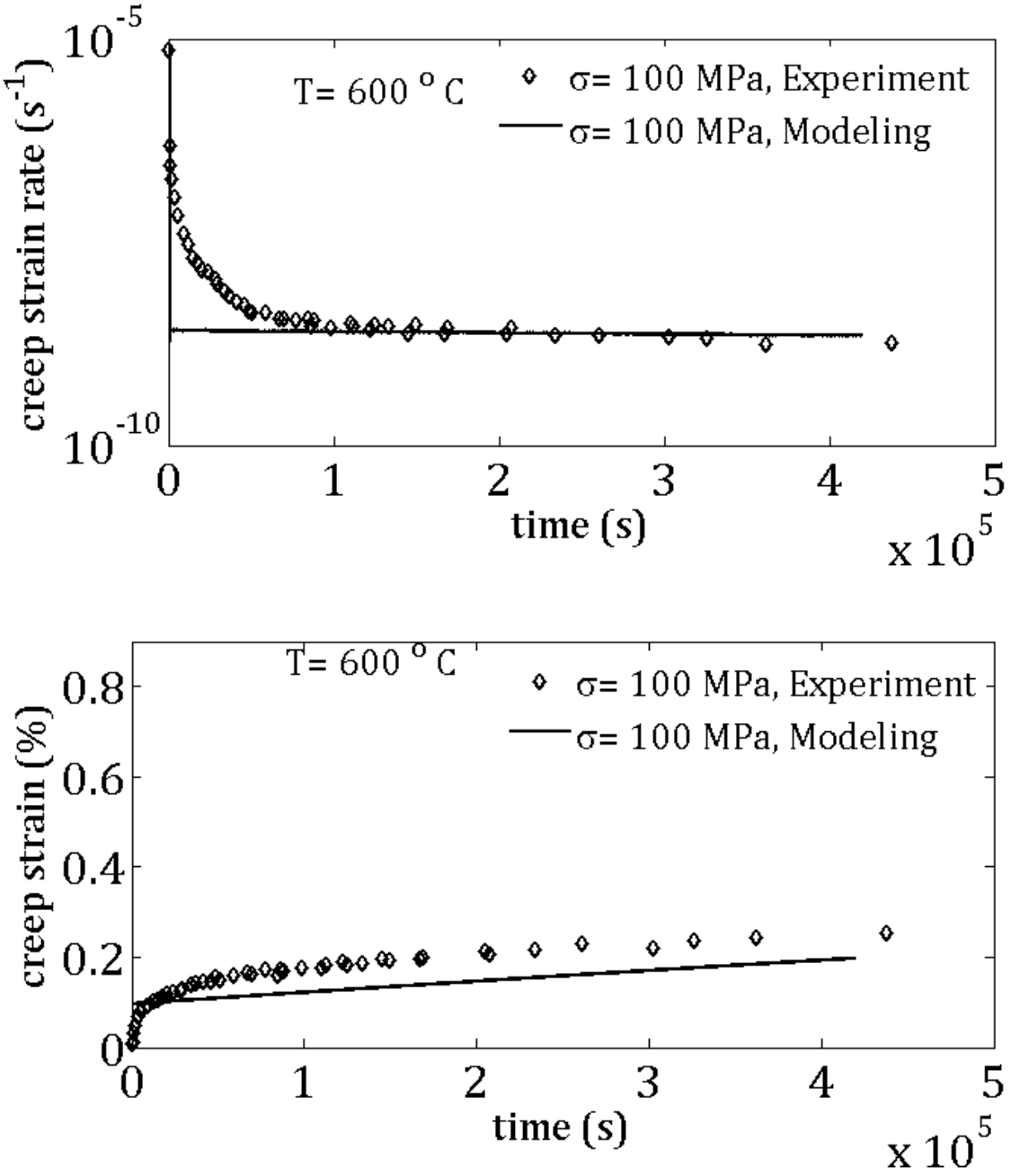

Fig.6 Creep results from experiments and FEA simulation for 100 MPa and 600˚C, (a) true creep strain versus time, (b) creep strain rate versus time.

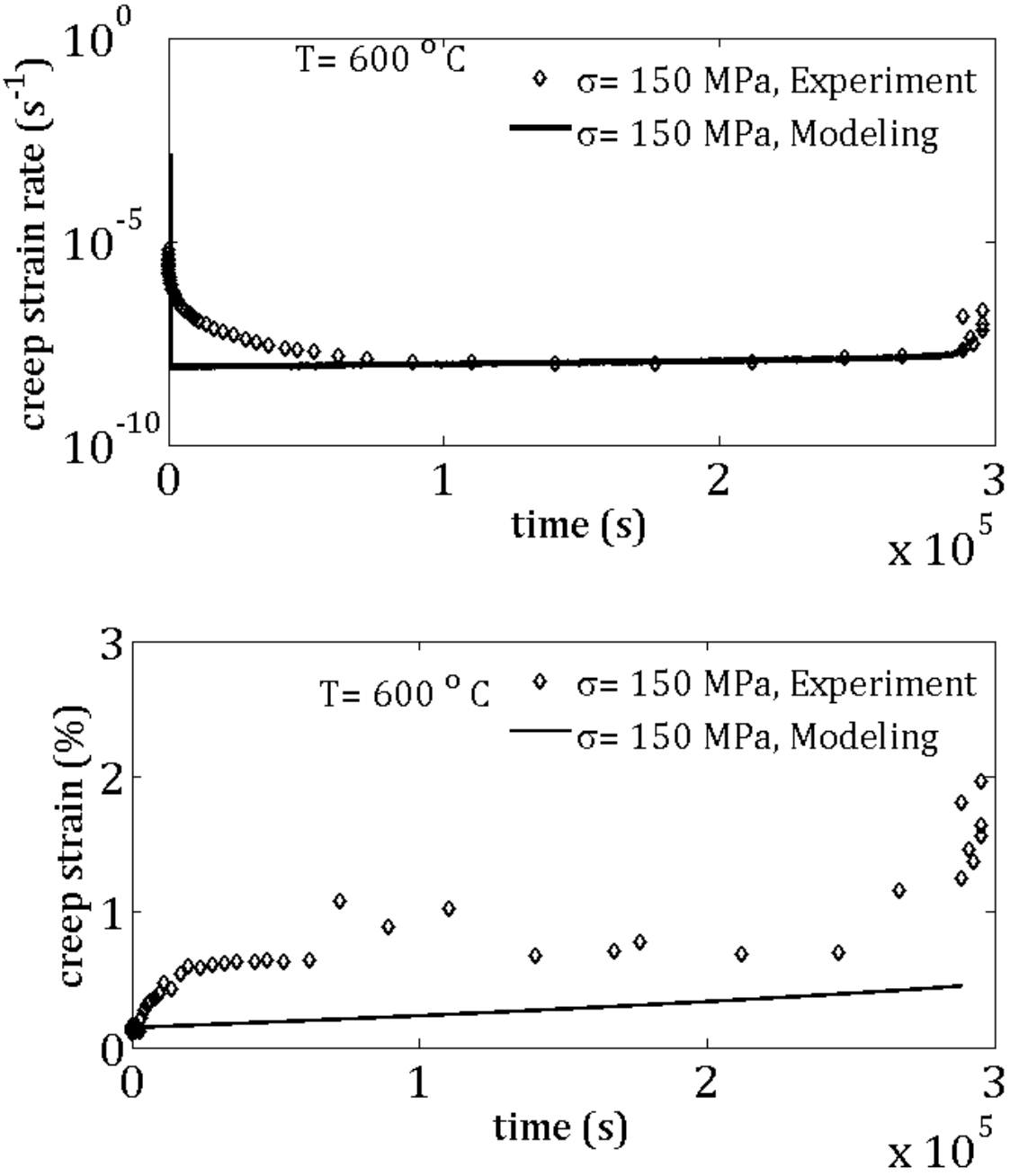

Fig.7 Creep results from experiments and FEA simulation for 150 MPa and 600˚C, (a) true creep strain versus time, (b) creep strain rate versus time.

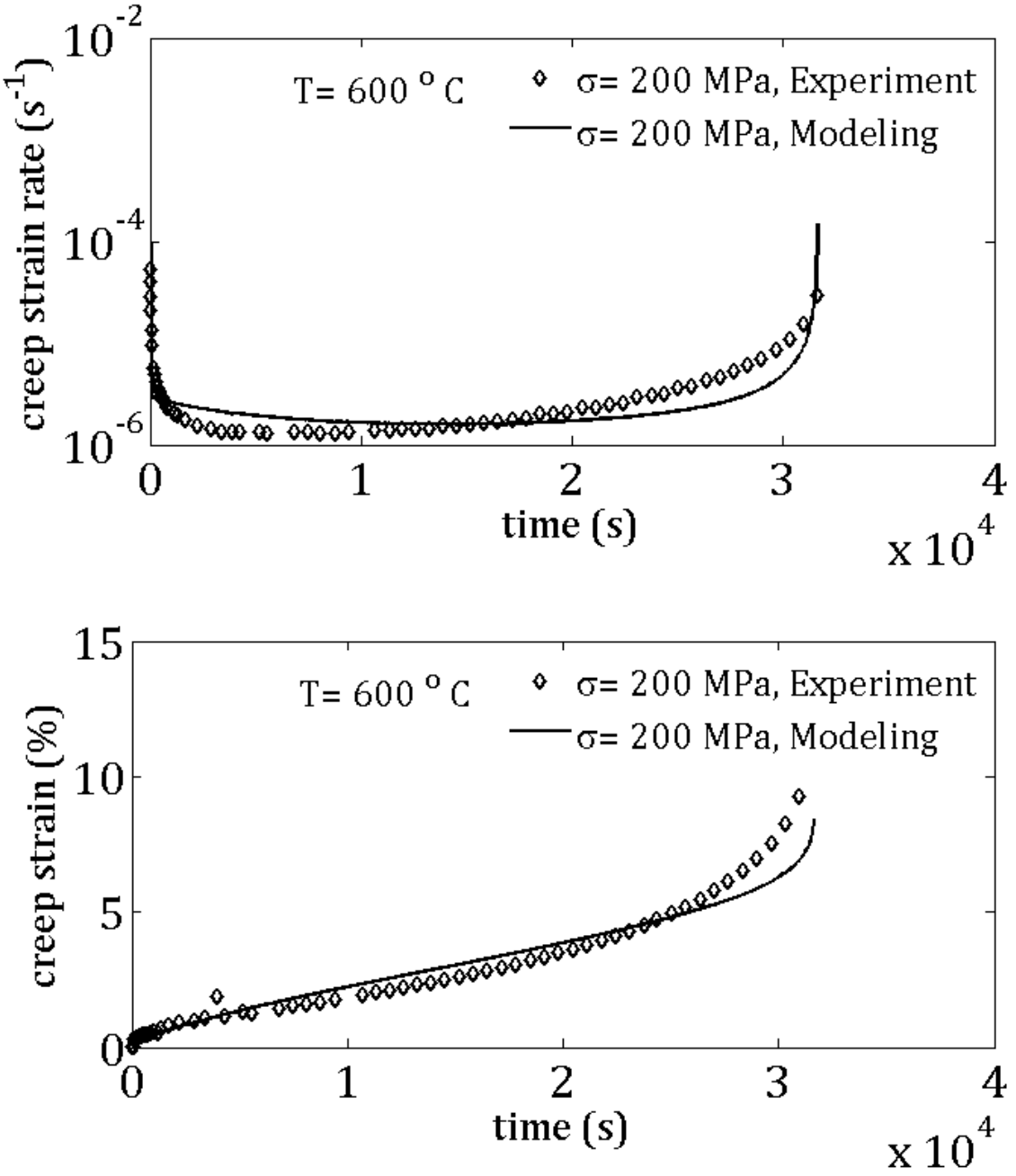

Fig.8 Creep results from experiments and FEA simulation for 200 MPa and 600˚C, (a) true creep strain versus time, (b) creep strain rate versus time.

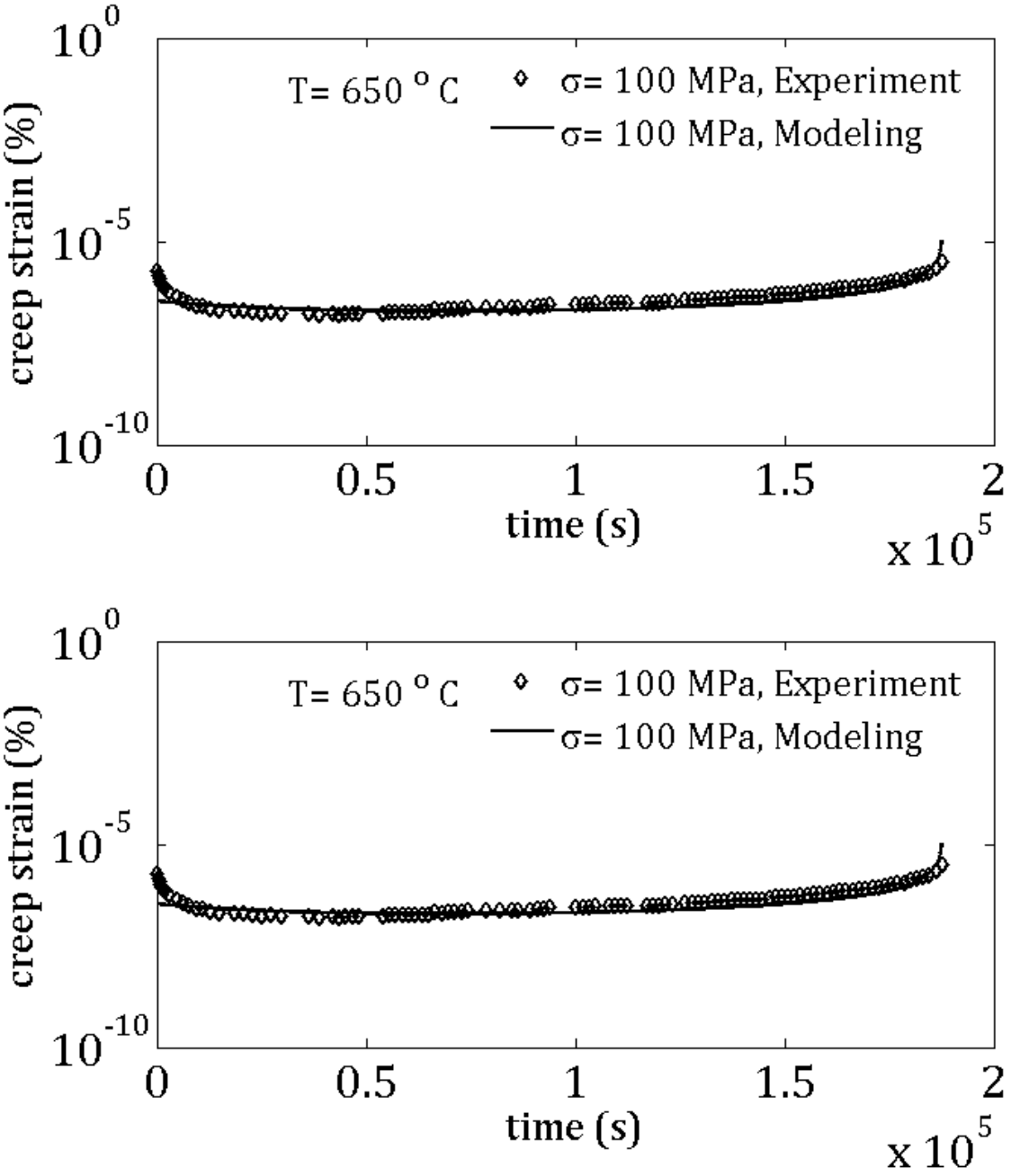

Fig.9 Creep results from experiments and FEA simulation for 100 MPa and 650˚C, (a) true creep strain versus time, (b) creep strain rate versus time.

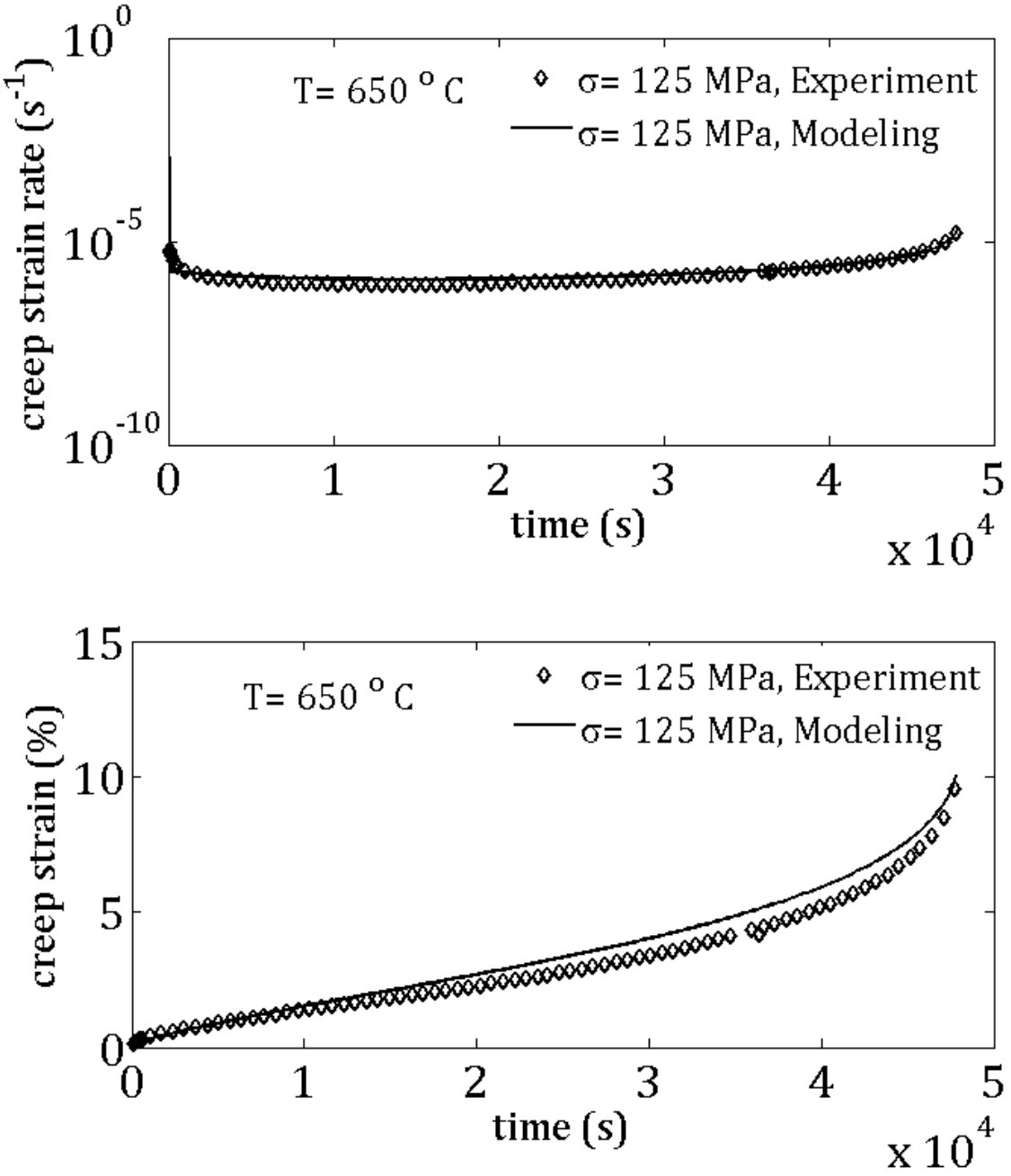

Fig.10 Creep results from experiments and FEA simulation for 125 MPa and 650˚C, (a) true creep strain versus time, (b) creep strain rate versus time.

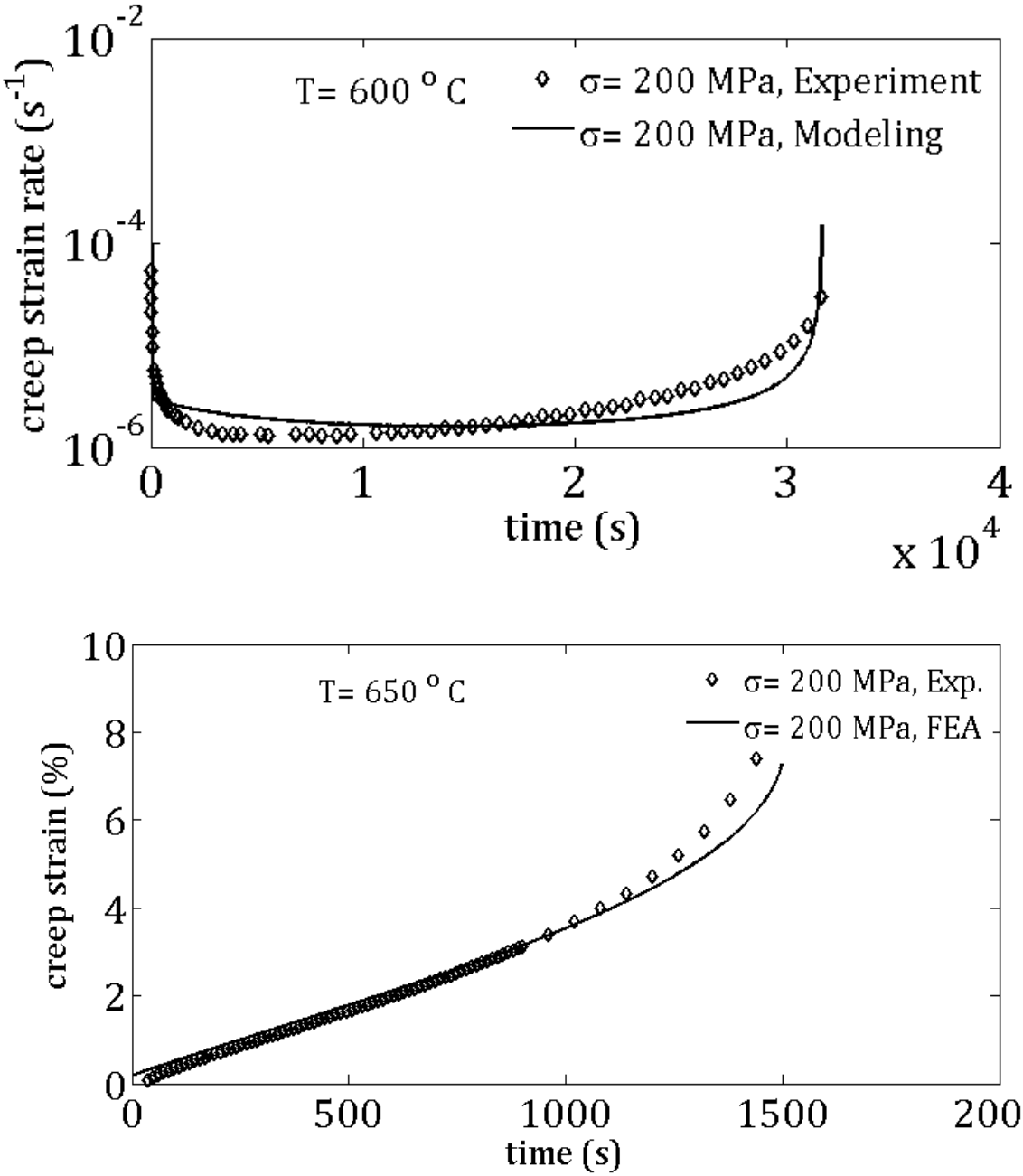

Fig.11 Creep results from experiments and FEA simulation for 200 MPa and 650˚C, (a) true creep strain versus time, (b) creep strain rate versus time.

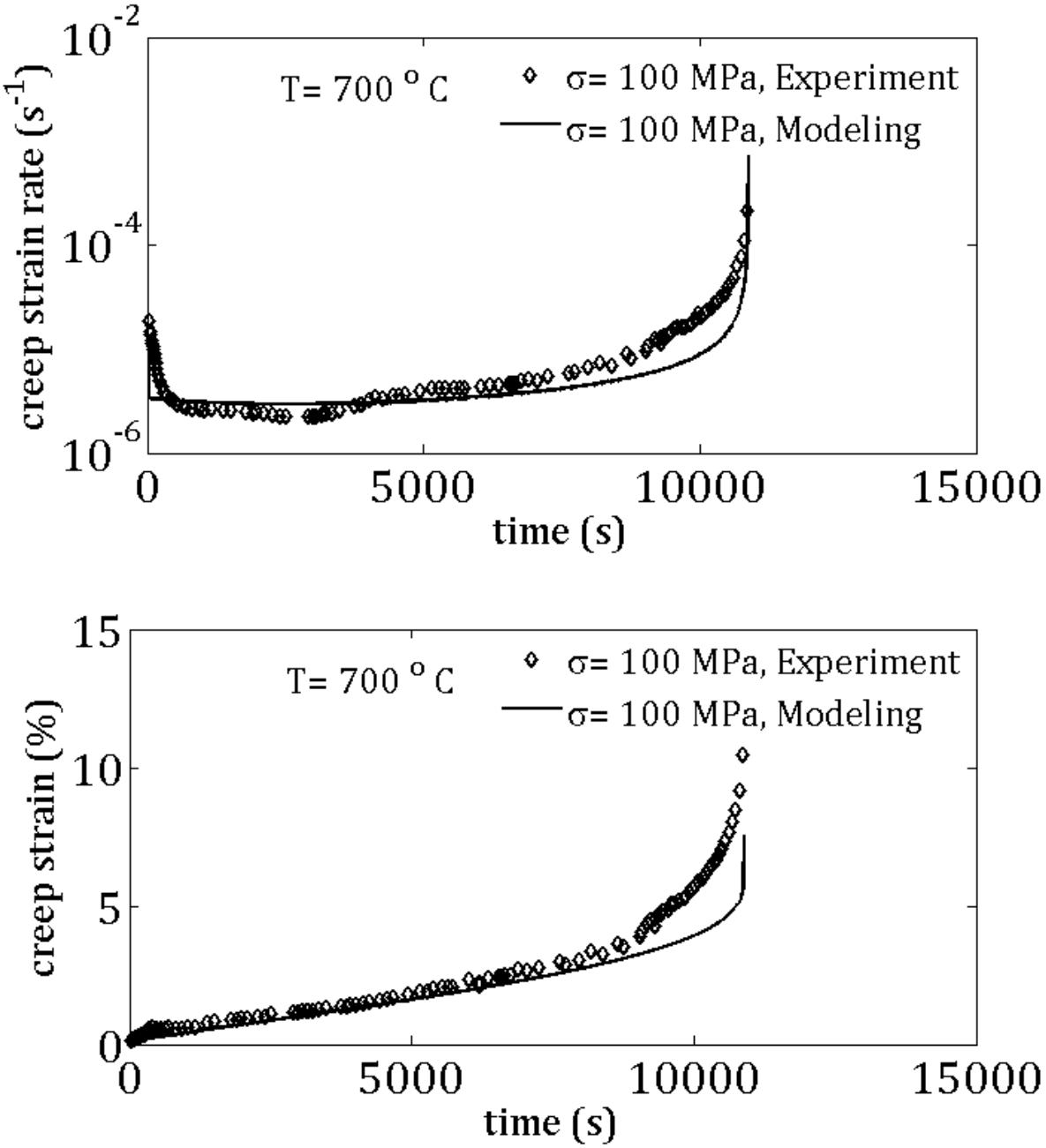

Fig.12 Creep results from experiments and FEA simulation for 100 MPa and 700˚C, (a) true creep strain versus time, (b) creep strain rate versus time.

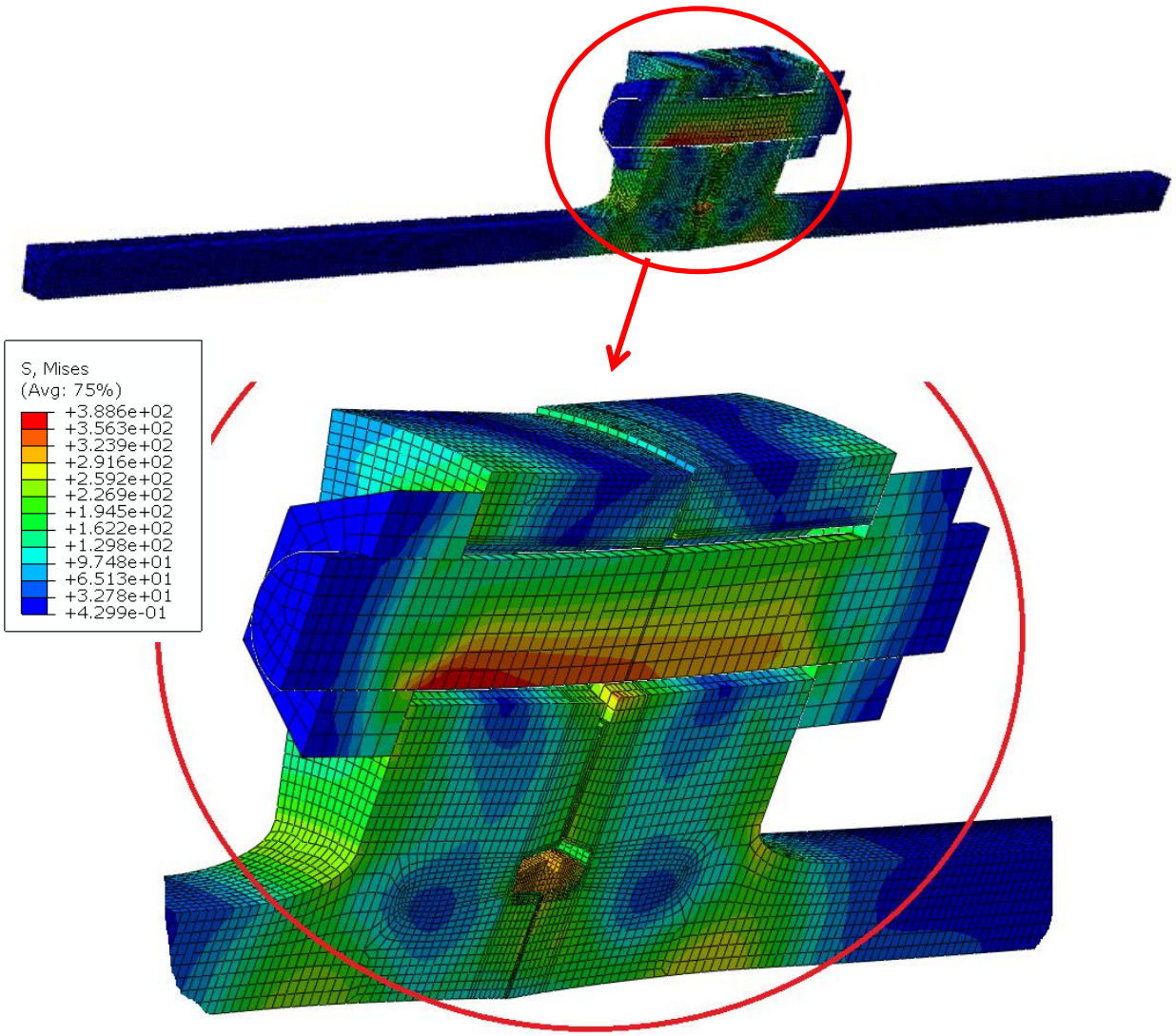

Fig.13 Creep stress distribution in a 9Cr-1Mo steel pipe connected to an Inconel X625 flange under thermomechanical loading. The operating temperature and pressure are 575˚C and 17 MPa internal pressure.

4.5. Conclusions

A unified elastic-viscoplastic constitutive model for creep analysis of modified 9Cr-1Mo has been developed. The model considered the dislocation density evolution as the main creep mechanism in this material. In order to predict the third stage of creep several damage terms were included. The model has been implemented in a User Material Subroutine for ABAQUS by using a semi-implicit numerical integration scheme. Creep tests have been conducted on welded and non-welded specimens made of modified 9Cr-1Mo steel. The creep tests were simulated in ABAQUS utilizing the developed numerical model. The modeling creep results show good correlations with the experimental results for the temperature range of 600-700 C and stress

range of 80 to 200 MPa. The model can be applied to study creep deformation and failure in three-dimensional complex geometries.

References

[1] Auerkari, P., S. Holmström, J. Veivo, and J. Salonen. 2007. "Creep Damage and Expected Creep Life for Welded 9–11% Cr Steels." *Development of and Integrity Issues with New High Temperature High Strength Steels* 84 (1–2) (January): 69–74. doi:10.1016/j.ijpvp.2006.09.011.

[2] Basirat, M., T. Shrestha, G.P. Potirniche, I. Charit, and K. Rink. 2012. "A Study of the Creep Behavior of Modified 9Cr–1Mo Steel Using Continuum-damage Modeling." *International Journal of Plasticity* 37 (0) (October): 95–107. doi:10.1016/j.ijplas.2012.04.004.

[3] Besson, J., S. Leclercq, V. Gaffard, and A.-F. Gourgues-Lorenzon. 2009. "Analysis of Creep Lifetime of a ASME Grade 91 Welded Pipe." *Engineering Fracture Mechanics* 76 (10) (July): 1460–1473. doi:10.1016/j.engfracmech.2008.12.007.

[4] Blum, W., P. Eisenlohr, and F. Breutinger. 2002. "Understanding Creep—a Review." *Metallurgical and Materials Transactions A* 33 (2) (February 1): 291–303. doi:10.1007/s11661-002-0090-9.

[5] Chilukuru H., Durst K. 2009. "Coarsening of Precipitates and Degradation of Creep Resistance in Tempered Martensite Steels." *Mater. Sci. Eng. A Materials Science and Engineering A* 510-511 (C): 81–87. /z-wcorg/.

[6] Dunne, Fionn. 2007. *Introduction to Computational Plasticity*. Oxford; New York: Oxford University Press.

[7] Gaffard, V., A.F. Gourgues-Lorenzon, and J. Besson. 2005. "High Temperature Creep Flow and Damage Properties of 9Cr1MoNbV Steels: Base Metal and Weldment." *Nuclear Engineering and Design* 235 (24) (December): 2547–2562. doi:10.1016/j.nucengdes.2005.07.001.

[8] Hyde, T. H., and A. Tang. 1998. "Creep Analysis and Life Assessment Using Cross-weld Specimens." *International Materials Reviews* 43 (6): 221–242. doi:10.1179/095066098790105609.

[9] Hyde, T.H., M. Saber, and W. Sun. 2010. "Creep Crack Growth Data and Prediction for a P91 Weld at 650 °C." *International Journal of Pressure Vessels and Piping* 87 (12) (December): 721–729. doi:10.1016/j.ijpvp.2010.09.002.

[10] Laha, K., K.S. Chandravathi, P. Parameswaran, and K. Bhanu Sankara Rao. 2009. "Type IV Cracking Susceptibility in Weld Joints of Different Grades of Cr-Mo Ferritic Steel." *Metallurgical and Materials Transactions A* 40 (2) (February 1): 386–397. doi:10.1007/s11661-008-9724-x.

[11] Lee, Hyeong-Yeon, Jong-Bum Kim, Woo-Gon Kim, and Jae-Han Lee. 2010. "Creep-fatigue Crack Behaviour of a Mod. 9Cr-1Mo Steel Structure with Weldments." *Transactions of the Indian Institute of Metals* 63 (2-3) (April 1): 245–250. doi:10.1007/s12666-010-0033-x.

[12] Lemaître, J. 1990. *Mechanics of Solid Materials*. Cambridge: Cambridge University Press.

[13] Morra, P.V., S. Radelaar, M. Yandouzi, J. Chen, and A.J. Böttger. 2009. “Precipitate Coarsening-induced Plasticity: Low Temperature Creep Behaviour of Tempered SAE 52100.” *International Journal of Plasticity* 25 (12) (December): 2331–2348. doi:10.1016/j.ijplas.2009.03.002.

[14] Muñoz-Morris, M.A., I. Gutierrez-Urrutia, and D.G. Morris. 2009. “Influence of Nanoprecipitates on the Creep Strength and Ductility of a Fe–Ni–Al Alloy.” *International Journal of Plasticity* 25 (6) (June): 1011–1023. doi:10.1016/j.ijplas.2008.09.006.

[15] Naumenko, K. D. 2007. *Modeling of Creep for Structural Analysis*. Berlin; New York: Springer.

[16] Spigarelli, S., and E. Quadrini. 2002. “Analysis of the Creep Behaviour of Modified P91 (9Cr–1Mo–NbV) Welds.” *Materials & Design* 23 (6) (September): 547–552. doi:10.1016/S0261-3069(02)00026-2.

[17] Watanabe, Takashi, Masaaki Tabuchi, Masayoshi Yamazaki, Hiromichi Hongo, and Tatsuhiko Tanabe. 2006. “Creep Damage Evaluation of 9Cr–1Mo–V–Nb Steel Welded Joints Showing Type IV Fracture.” *International Journal of Pressure Vessels and Piping* 83 (1) (January): 63–71. doi:10.1016/j.ijpvp.2005.09.004.

[18] Yaghi, A H, T H Hyde, A A Becker, and W Sun. 2008. “Finite Element Simulation of Welding and Residual Stresses in a P91 Steel Pipe Incorporating Solid-state Phase Transformation and Post-weld Heat Treatment.” *The Journal of Strain Analysis for Engineering Design* 43 (5) (May 1): 275–293. doi:10.1243/03093247JSA372.

[19] Yaguchi, Masatsugu, Takashi Ogata, and Takayuki Sakai. 2010. “Creep Strength of High Chromium Steels Welded Parts Under Multiaxial Stress Conditions.” *International Journal of Pressure Vessels and Piping* 87 (6): 357–364. doi:10.1016/j.ijpvp.2010.03.018.

Task 5: Creep fracture simulations using FEM and strip yield modeling

5.1. Numerical strip-yield modeling for the creep fracture in Cr-Mo steels

5.1.1. Introduction

A numerical strip-yield model was developed to simulate creep crack incubation in heat-resistant steels. The model is based on a formulation proposed by Newman (ASTM STP 748, pp. 53-84, 1981) for fatigue crack growth under variable amplitude loading. The time evolution of the plastic deformation ahead of a crack loaded in tension is modeled using the Norton law for secondary creep stage, while the primary and tertiary creep stages are neglected. The model assumes a pre-existing crack in a specimen, and models the behavior of the material prior to the beginning of crack propagation due to creep loading. The evolution with time of the crack-tip plastic zone, crack-tip opening displacement and yield strength in the plastic zone are computed at constant temperature for center crack panels. Comparison with two previous strip-yield models and experimental data is performed, and good correlation is obtained for several Cr-Mo-V steels. This approach to modeling creep crack incubation has the potential to be applied to other types of cracked specimens under constant or variable amplitude loading.

Heat-resistant alloys are used extensively in coal-fired power plants, as gas turbine materials for gas-fired power plants, or as reactor internals for nuclear power plants. With ever increasing requirements imposed on structural materials operating at high temperatures, there is a growing need to predict the service life and reliability of components experiencing creep fracture and creep-fatigue damage. Components operating at high temperatures may develop cracks which can incubate and grow under large local creep strains, even though the nominal applied stresses or strains are low. Strip-yield modeling (SYM), as a numerical method to simulate crack growth under constant or variable amplitude loading, was proposed primarily for the modeling of fatigue crack growth in aerospace alloys, and is based on the Dugdale model [1]. Even though numerous SYMs have been developed for fatigue crack growth, there are very few that focused on creep-fracture or creep-fatigue problems. Vitek [2] originally proposed an analytical SYM based on the Bilby-Cotterell and Swinden model [3] for the dislocation distribution at the crack tip in a center-crack panel of infinite width. The incubation period of the crack embedded in the creeping material was modeled by formulating the time evolution of the plastic zone development and density of edge dislocations in front of the crack tip. He also modeled the evolution of the yield stress near the crack tip with time. Ewing [4] developed another analytical model for the creep crack incubation and growth based on the SYM approach. The material was assumed isotropic hardening, and Norton equation was used for the creep behavior in the secondary stage, while the first and tertiary stages were neglected in his model. In order to predict the onset of crack growth, Ewing used a critical crack-opening displacement (CTOD) criterion. In his work, Ewing demonstrated that the crack incubation and failure time of a specimen can be correlated with the applied stress intensity factor *K*. Ewing compared his model predictions with the experimental data obtained by Batte [5] and Haigh [6,7]. Other researchers have simulated creep crack incubation and growth, and they used either the finite element method [8-11] or analytical formulations [12-15].

Experimental studies of crack nucleation and growth in heat resistant steels are numerous. Haigh [6-7] performed creep crack growth tests under both stationary and variable loading on three different Cr-Mo-V alloys using wedge-opening-load (WOL) specimens. He measured crack opening displacements versus time, and correlated the rate of CTOD increase with the increment in crack length. A thorough review of the creep behavior in Cr-Mo-V steels is presented by Haigh in [7]. Haigh et al. [16] also studied the influence of oxidation on creep crack growth during high cycle fatigue. They found that oxidation plays a significant role in the creep crack growth, while the loading frequency is more marked in air compared with vacuum. Several other experimental studies were performed on Cr-Mo-V alloys [17-20].

The failure process by creep crack growth in steels consists of crack incubation and growth. The goal of this project was to apply a numerical SYM to study the time evolution of the crack tip parameters during creep crack incubation in Cr-Mo-V steels. The model is based on the formulation of the crack opening displacement and plastic zone at the crack tip in an isotropic elastic – perfectly plastic material. For simplicity, the creep behavior is assumed to be described by a Norton power law. The criterion used for the transition from a non-propagating to a propagating crack is the critical CTOD, as used also by several other authors [2,4,19,21]. Model predictions are compared with results of two other SYMs [2,4], and good agreement is obtained. Comparison with experimental data from the Haigh study [6] is performed, and good correlation of the evolution of the crack opening displacement with time is also obtained.

5.1.2. Analytical strip-yield model and numerical implementation

Considering a center crack of length *2a* embedded in panel of width *2b* and loaded under a constant tensile stress *S*, the resulting crack-tip plastic zone size is ρ, as shown in Fig. 1. According to the Dugdale model [1], the elastic-plastic problem can be solved by considering the superposition of two elastic solutions for the embedded crack in a finite width panel, as shown in Fig. 2. Fig. 2a shows the specimen under the remotely applied load *S*. According to Tada et al. [22], the mode I stress intensity factor K_I for this configuration is

$$K_{IS} = S\sqrt{\pi d}\sqrt{sec\frac{\pi d}{2b}} \tag{1}$$

where $d = a + \rho$ is the fictitious crack length, and the secant term in the above equation becomes one for an infinite width plate. Fig. 2b shows the same specimen loaded with the flow stress σ caused by the yielding in the crack-tip plastic zone for the fictitious crack of length *2d*. K_I in this case is given by

$$K_{I\sigma} = \frac{2\sigma}{\pi}\sqrt{\pi d}\left(\frac{\pi}{2} - sin^{-1}\frac{a}{d}\right)F(a,d) \tag{2}$$

where the geometrical factor *F* due to the finite width of the specimen is

$$F(a,d)=\left[\frac{\frac{\pi}{2}-\sin^{-1}\left(\frac{\sin\frac{\pi a}{2b}}{\sin\frac{\pi d}{2b}}\right)}{\frac{\pi}{2}-\sin^{-1}\frac{a}{d}}\right]\sqrt{\sec\frac{\pi d}{2b}} \tag{3}$$

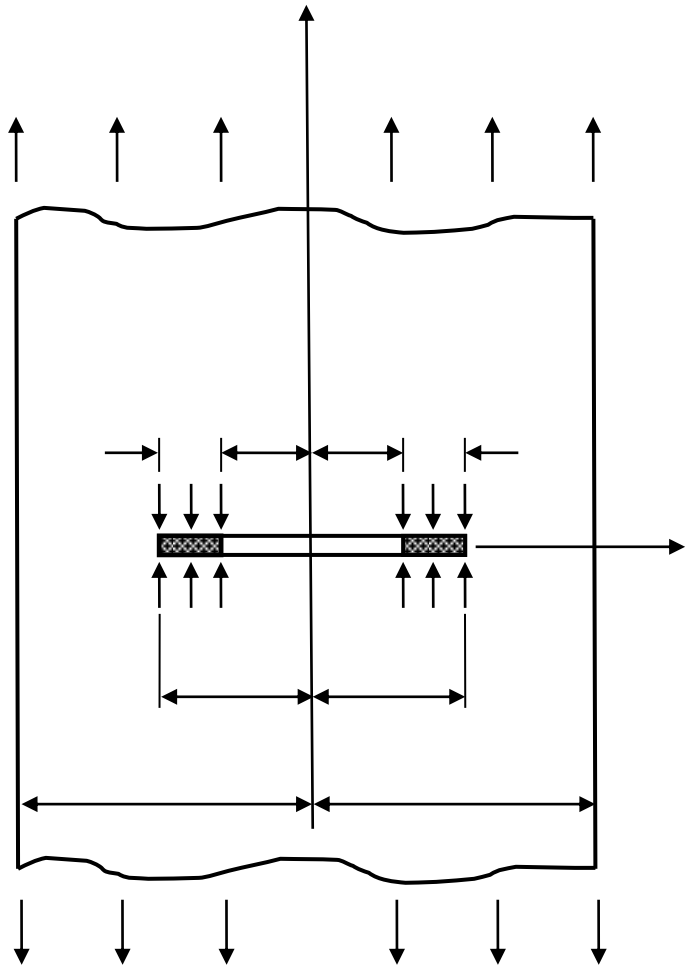

Fig. 1. Schematic of the strip-yield model for a finite width center-crack panel.

For an infinite width specimen, *F(a,d)* = 1. As the superposition of the two stress intensity factors is performed, the stress at *x* = *d* must have a finite value, thus the total stress intensity at this point should be zero

$$K_{IS} + K_{I\sigma} = 0 \tag{4}$$

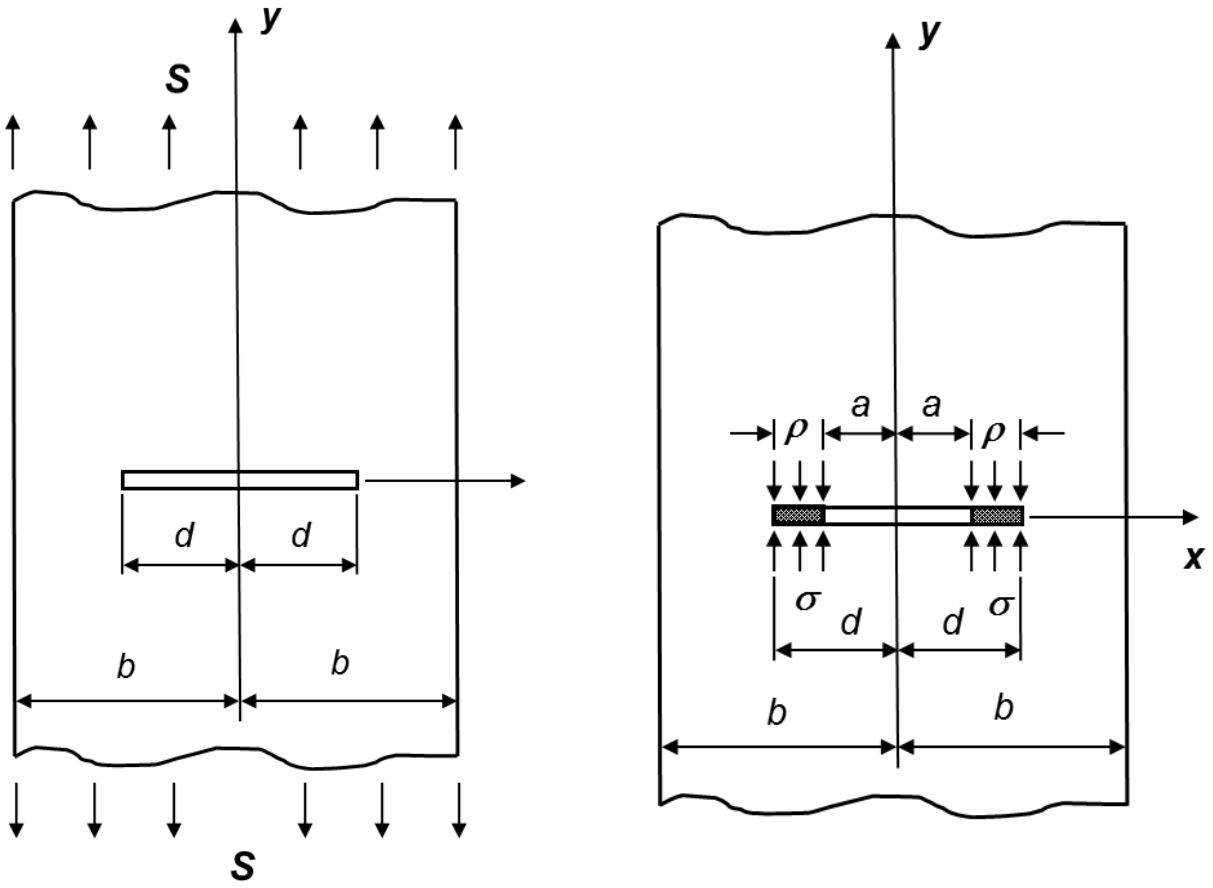

(a) (b)

Fig. 2. Superposition principle for two elastic solutions using: (a) the remotely applied load, and (b) the local stresses in the crack-tip plastic zone.

Solving for the plastic zone size from the above equation, it results that

$$\rho = \frac{2b}{\pi} sin^{-1}\left(sin\frac{\pi a}{2b} sin\frac{\pi S}{2\sigma} \right) - a \tag{5}$$

where the stress $\sigma = \alpha\sigma_0$ is the flow stress in the plastic zone adjusted by the constraint factor α to account for the stress state, with $\alpha = 1$ for plane stress, and $\alpha = 3$ for plane strain. Since this is a fracture study, the load applied to the specimen is a monotonic tensile stress, and the crack does not experience compressive loads. However, future developments that will involve fatigue loads with alternating tensile-compressive loading cycles should take into account that for compressive loads the constraint factor is customarily chosen as $\alpha = 1$.

To formulate the numerical model for the center crack panel, the crack opening displacements (CODs) must be computed at the maximum loading. To calculate the CODs, a discretization into a certain number of elements was performed for the entire crack plane, which

is illustrated in Fig. 3. The crack-tip plastic zone was divided into 10 elements, numbered from $j = 1$ to $j = 10$. The smallest element is placed at the crack tip ($x = a$), and the width of the plastic zone elements increases for elements located farther from the crack tip. The widths of the plastic zone elements normalized with the plastic zone size varied from $2w/\rho = 0.01$ (for $x = a$) to $2w/\rho = 0.3$ (for $x = d$). The elements widths in the plastic zone used in this study are the ones listed by Newman [23]. The physical crack plane is discretized with elements numbered from $j = 11$ to $j = n$.

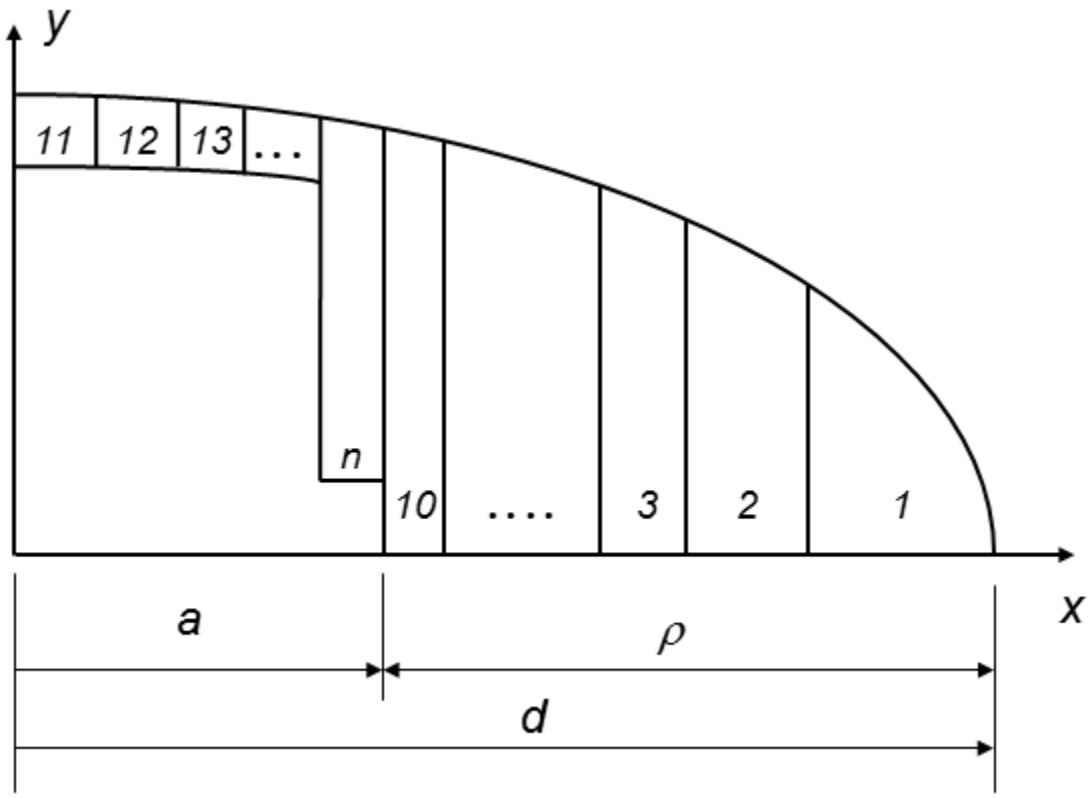

Fig. 3. Meshing of the crack plane.

For a generic element j located in the plastic zone and shown in Fig. 4, the crack-surface displacement is V_j, and the element length is L_j. The element has a width $2w_j$, and is subjected to a compressive stress $\sigma_j = -\alpha\sigma_0$. Then, for an arbitrary element i located at $x = x_i$, the crack-surface displacement V_i caused by the remotely applied stress S and the local stress σ_j acting on each element j can be written according to [22,23]

$$V_i = Sf\left(x_i\right) + \sum_{j=1}^{n} \sigma_j g\left(x_i, x_j\right) \tag{6}$$

where the functions f and g for a center crack in finite width panel are defined as follows

$$f\left(x_i\right)=\frac{2}{E'}\left[\left(d^2-x_i^{\,2}\right)sec\frac{\pi d}{2b}\right]^{1/2} \tag{7}$$

$$g\left(x_i,x_j\right)=G\left(x_i,x_j\right)+G\left(x_i,-x_j\right) \tag{8}$$

and

$$G\left(x_i,x_j\right)=\frac{2\sigma_j}{\pi E'}\left[\left(b_2-x_i\right)cosh^{-1}\frac{d^2-b_2x_i}{d\left|x_i-b_2\right|}-\left(b_1-x_i\right)cosh^{-1}\frac{d^2-b_1x_i}{d\left|x_i-b_1\right|}+\left(sin^{-1}\frac{b_2}{d}-sin^{-1}\frac{b_1}{d}\right)\sqrt{d^2-x_i^{\,2}}\right]\cdot F\left(b_1,b_2,d\right) \tag{9}$$

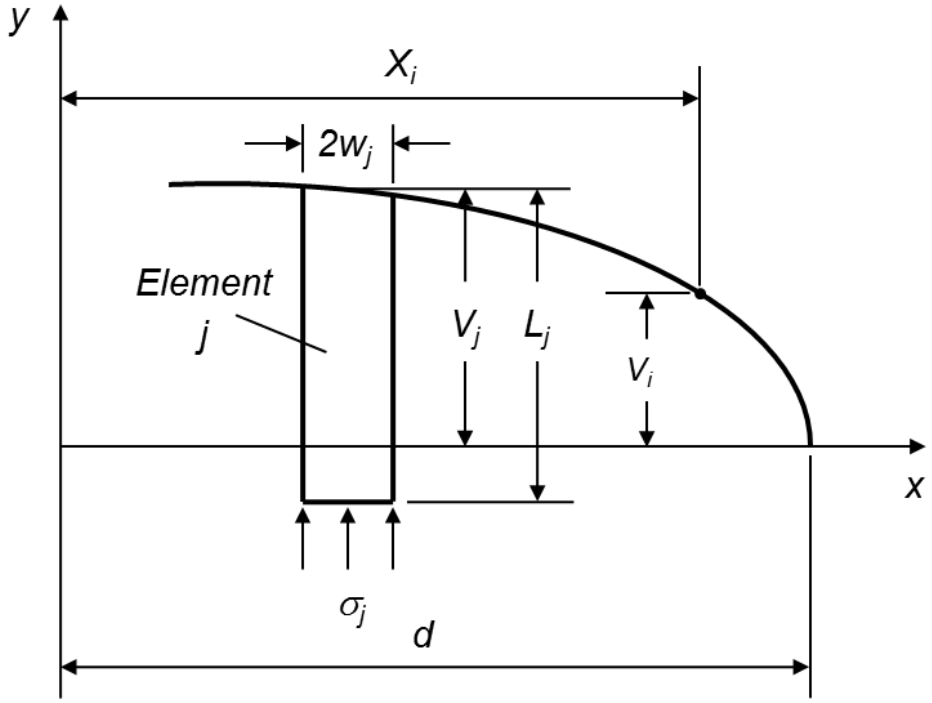

Fig. 4. Definition of crack-surface displacements.

The geometrical factor $F(b_1,b_2,d)$ for a finite width panel is

$$F\left(b_1,b_2,d\right)=\left[\frac{\sin^{-1}\left(\frac{\sin\frac{\pi b_2}{2b}}{\sin\frac{\pi d}{2b}}\right)-\sin^{-1}\left(\frac{\sin\frac{\pi b_1}{2b}}{\sin\frac{\pi d}{2b}}\right)}{\sin^{-1}\frac{b_2}{d}-\sin^{-1}\frac{b_1}{d}}\right]\sqrt{\sec\frac{\pi d}{2b}} \tag{10}$$

where $b_2=x_j+w_j$ and $b_1=x_j-w_j$, while for an infinite width plate $F(b_1,b_2,d)$ = 1, and

$$E'=\begin{cases}E & \text{for plane stress}\\ \dfrac{E}{1-\upsilon^2} & \text{for plane strain}\end{cases} \tag{12}$$

with E being the modulus of elasticity, and υ the Poisson ration.

Ewing [4] introduced the idea that creep deformation at the crack tip is experienced by an element of a certain length (λ), which can be considered a material constant. For instance, the length of the crack tip element λ can be related to the grain size of the material, thus it is independent of the crack length, or it can be assumed related to the plastic zone size, in which case it is dependent on the crack length. Here it is assumed that the length of the crack tip element is a material constant independent of the crack length. Assuming, for brevity, that the CTOD is denoted ϕ, from the discretization of the crack plane explained above it results that

$$V_{10}=\phi \tag{13}$$

Assuming for the creep behavior of the material a power law of the form

$$\dot{\varepsilon}_s=A\left(\frac{\sigma_0}{G}\right)^m \tag{14}$$

where ε_s is the creep strain for the secondary creep stage, A and m are material constants, G is the shear modulus, and σ_0 is the flow stress loading the crack-tip element. Then, the time rate of change of the *CTOD* becomes

$$\dot{\phi}=\dot{\varepsilon}_s\lambda \tag{15}$$

In this study, the external load S is constant, thus the crack is always open, as opposed to a fatigue loading process, whereas the crack may experience some closure for a portion of the loading cycle. It results that the contribution to the crack surface displacements from the local

stresses σ_j is given only by the elements in the plastic zone, j = 1,2,…10, which results in the following equation

$$\phi = Sf\left(a\right) - \frac{\sigma_0}{\pi E'} \sum_{j=1}^{10} g\left(a, x_j\right) \tag{16}$$

Two other equations can be derived as

$$d = sec^{-1}\left(sin\frac{\pi S}{2\sigma_0} \right) \tag{17}$$

$$\dot{\phi} = \lambda A \left(\frac{\sigma_0}{G} \right)^m \tag{18}$$

where Eq. (17) results directly from Eq. (5), and Eq. (18) is obtained from Eqs. (13)-(15).

The system of Eqs. (16)-(18), with ϕ, σ_0 and d as unknowns, was integrated using an explicit procedure. Assuming that the variables of interest are known at time k, for a time step $\Delta t = t_{k+1} - t_k$, the updated variables at time $k+1$ are

$$\dot{\phi} = \lambda A \left(\frac{\sigma_{0k}}{G} \right)^m \tag{19}$$

$$\phi_{k+1} = \phi_k + \dot{\phi} \cdot \Delta t \tag{20}$$

$$\sigma_{0k+1} = \frac{Sf_k\left(a\right) - \phi_{k+1}}{\sum_{j=1}^{10} g_k\left(a, x_j\right)} \tag{21}$$

$$d_{k+1} = sec^{-1}\left(sin\frac{\pi S}{2\sigma_{0k+1}} \right) \tag{22}$$

$$f_{k+1} = f\left(a, d_{k+1}\right) \tag{23}$$

$$g_{k+1} = g\left(a, d_{k+1}\right) \tag{24}$$

Because the numerical implementation used an explicit scheme, the influence of the time step on the model results was studied, and the results are shown in Fig. 5. Several time steps were considered in the analysis, ranging from $\Delta t = 10^{-3}$ h to Δt = 10 h. The crack opening displacement versus time was plotted, and the results were almost identical for all time steps considered. Similar results were also obtained for the plastic zone size and relaxation of the yield strength with time.

5.1.3. Results

This section presents a comparison between the present model's predictions and results from other SYMs, as well as comparisons with experimental data. Typical evolutions of the CTOD, ρ, and σ_0 with time are illustrated in Fig. 6. For this simulation, the specimens is assumed in plane stress, the crack length is a = 1 mm, and the flow stress is σ_0 = 600 MPa. The constants in the creep law are A = 21 h^{-1} and m = 3, while λ = 100 μm. Also, the assumption is made that the flow stress is the same for the entire crack-tip plastic zone. It can be observed that, while the flow stress in the plastic zone σ_0 decreases from 600 MPa to 265 MPa, the CTOD increases from 1.8 μm to approximately 6 μm, and the plastic zone size ρ increases from 1.2 mm to 3.9 mm.

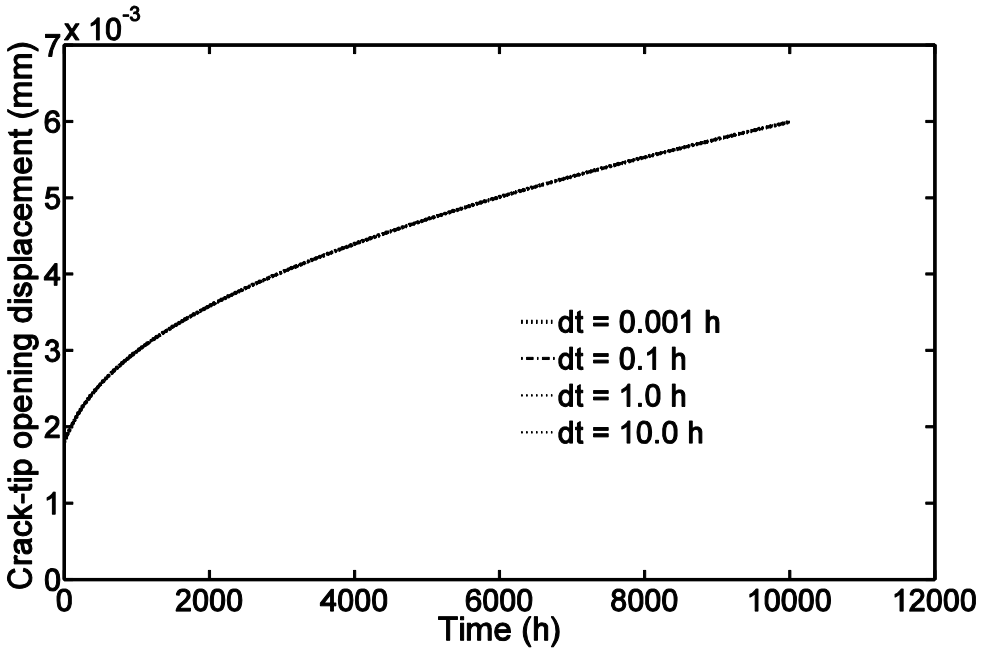

Fig. 5. Influence of time step size on the evolution of the crack-tip opening displacement.

Table 1 shows a comparison between the model results and the experimental data of creep crack incubation obtained by Batte [5]. The material used in the experiments was a bainitic Cr-Mo-V rotor steel, and the creep tests were performed at 550°C. The detailed alloy concentration, heat treatment and properties are given in the paper of Ewing. Batte used a double-edge notched specimen. However, Ewing considered in his model the case of a center crack in an infinite plane in plane stress, thus he used the stress intensity factor $K = \sigma\sqrt{\pi a}$, instead of $K = 1.12\sigma\sqrt{\pi a}$. He also did not correct for the finite edges of the specimens. Ewing performed simulations using the Vitek model, and used the same configuration of a crack in an infinite plane. In this study, the same crack case as the one used by Ewing was considered, because the goal was to compare the predictions of this model with those of the other two SYMs. Only the secondary creep strain effects are taken into consideration, and the creep law is presented in Eq. (14). The creep law constants for this material, as specified by Ewing, are A = 21 h^{-1} and m = 3. The shear modulus is G = 56.2 GPa, and λ = 100 μm was kept constant for all simulations. Batte tested several specimens with different crack lengths and applied stress values, as listed in

Table1. The incubation period t_i is defined from experiments, and the three models predict the critical *CTOD* at the end of t_i.

Table 1. Creep crack incubation results for a bainitic rotor steel. Comparison between experimental results (Batte, 1975), and the predictions of the present model and the strip-yield models of Vitek (1977) and Ewing (1978).

Experiment (Batte)			**Vitek Model**		**Ewing Model**		**Present model**	
Applied stress S (MPa)	Crack length a mm)	Incubation time t_i (hr.)	Yield stress σ_{oi}/G	CTOD (μm)	Yield stress σ_{oi}/G	CTOD (μm)	Yield stress σ_{oi}/G	CTOD (μm)
221.9	1.0	50	2.50	1.67	3.38	1.18	3.08	1.54
193.8	1.3	40	2.79	1.56	3.81	1.11	3.61	1.40
177.0	1.6	80	3.10	1.89	4.25	1.34	3.63	1.65
148.9	2.2	70	3.55	1.78	4.89	1.27	4.37	1.58
122.5	3.2	150	4.21	2.11	5.82	1.52	4.66	1.75
177.0	1.0	200	2.07	1.66	2.75	1.20	4.03	0.95
132.0	6.0	40	8.35	2.7	11.7	1.33	5.61	2.90
132.0	4.0	75	5.61	2.36	7.80	1.94	5.11	2.10
Average			4.02	1.96	5.55	1.36	4.26	1.73

Table 2. Creep law constants and ultimate tensile strengths for the three materials in the Haigh (1975) experiments.

Material	**A (h^{-1})**	**m**	**U.T.S (MPa) at 550°C**
1%Cr-Mo-V(1) at 550°C	$1.4 \cdot 10^{22}$	10.4	375
1/2%Cr-Mo-V(2) at 550°C	$1.4 \cdot 10^{22}$	10.3	330
1%Cr-Mo-V(1) at 550°C	$1.4 \cdot 10^{22}$	11.3	453

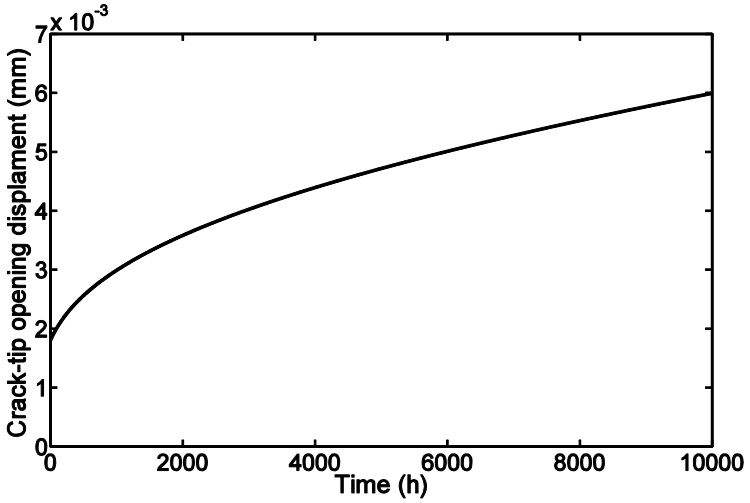

(a)

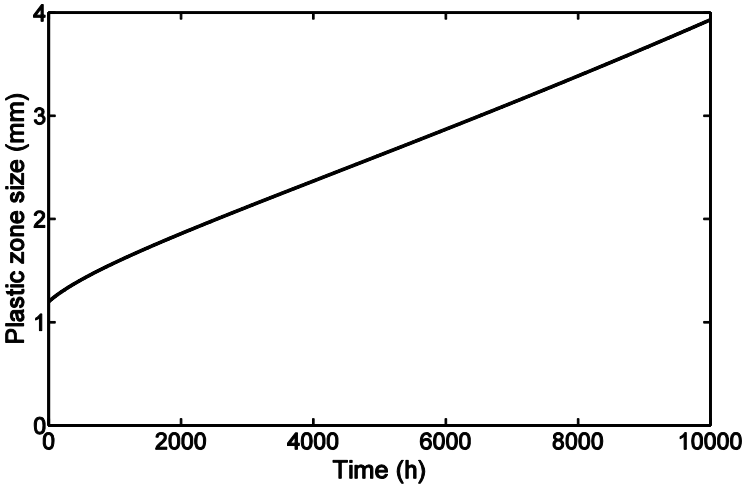

(b)

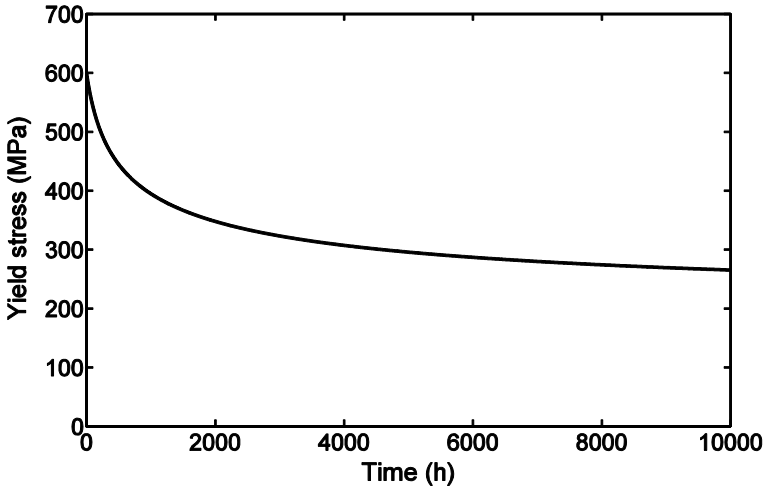

(c)

Fig. 6. Variation of the crack-tip parameters with time during a typical creep process: (a) crack-tip opening displacement, (b) plastic zone size, and (c) yield strength at the crack tip.

The average critical *CTOD* predicted with the Vitek model is 1.96 μm, while the prediction of the Ewing model is 1.36 μm, and the present model predicts a value of 1.73 μm. Even though there is a consistent difference between the predictions of the three models for different specimens, the present model can be considered satisfactory regarding the critical *CTOD* data. A comparison of the yield strength normalized by G at the end of t_i is also performed. The models predict values that do not deviate much from each other, i.e. 4.02 (Vitek), 5.55 (Ewing) and 4.26 (present model). Next, a comparison with the experimental data obtained by Haigh [6] was performed for three Cr-Mo-V steels used in turbine casings. Two of the tested materials (Material 1 and Material 3) were 1%Cr-Mo-V with different heat treatment, and the third was ½Cr-Mo-V (Material 2). Details regarding their exact composition, heat treatment and properties are given in the Haigh paper. All creep tests were performed at 550°C. The tensile strength of these materials is given in Table 2, along with the constants used for the creep law in Eq. (14). The creep constants were obtained by curve-fitting the creep strain versus time data presented by Haigh. The curve-fits are shown in Fig. 7. Ewing presented a comparison between his model, the Vitek model and the experimental results of Haigh only for Material 1. In this research, the comparison is extended to Materials 2 and 3. In the present model, the ultimate tensile strength (U.T.S.) was considered equal to the flow stress, as no information on hardening was presented by Haigh. Moreover, the Ewing model also considered the flow stress as the U.T.S., thus for consistency, the same assumption was made in this study. The same values for the constant λ were chosen as in the Ewing study, i.e. λ = 35 μm and λ = 350 μm. For consistency, the specimens were center-crack panels of infinite width in plane stress, similar to the ones analyzed by Ewing. Tables 3-6 indicate the applied stress and crack length for each of the materials analyzed.

Table 3. Comparison between experimental results and model predictions for Material 1(1%Cr-Mo-V) for a constant λ = 35 μm.

λ = 35 μm		**Experiment (Haigh 1975)**		**Present model**		**Vitek Model**		**Ewing Model**	
Applied stress S (MPa)	Crack length a (mm)	Incubation time t_i (hr.)	Measured CTOD (μm)	CTOD (μm)	Yield stress σ_{oi} (MPa)	CTOD (μm)	Yield stress σ_{oi} (MPa)	CTOD (μm)	Yield stress σ_{oi} (MPa)
172.5	32.0	750	230	144.0	209	103	232.0	90.8	246.3
181.5	35.0	180	270	152.7	229	102	263.9	91.3	282.6
221.9	34.4	14	180	284.0	241	110	362.9	100.4	392.2

Table 3 shows the results for Material 1, whereas the experimental results are compared with the predictions of the three SYMs. The incubation times, as measured from experiments, are given for each stress and crack length case. Given a value for t_i, the SYMs predict the critical CTOD.

The CTOD was also measured by Haigh, and is presented in each table. Tables 3 and 4 show that, for both λ = 35 μm and λ = 350 μm, the present model consistently calculates larger critical CTODs than the models of Ewing and Vitek. The predictions of the present model are also closer to the experimental values measured by Haigh. The constant λ = 350 μm gives CTOD values closer to the experimental data compared with the values predicted using λ = 35 μm. The predicted flow stress at the end of the incubation period σ_{0i} is also compared between the three models. From Tables 3 and 4, it can be observed that the present model predicts σ_{0i} values similar to those predicted by the Ewing and Vitek models for lower applied stresses of S = 172 and S = 181 MPa, while for the large applied stress of S = 222 MPa, the present model predicts a significantly lower value of σ_{0i} compared with the other two SYMs.

Table 4. Comparison between experimental results and model predictions for Material 1(1%Cr-Mo-V) for a constant λ = 350 μm.

λ = 350 μm		**Experiment (Haigh 1975)**		**Present model**		**Vitek Model**		**Ewing Model**	
Applied stress S (MPa)	Crack length a (mm)	Incubation time t_i (hr.)	Measured CTOD (μm)	CTOD (μm)	Yield stress σ_{oi} (MPa)	CTOD (μm)	Yield stress σ_{oi} (MPa)	CTOD (μm)	Yield stress σ_{oi} (MPa)
172.5	32.0	750	230	223	185	137	203.4	90.8	211.0
181.5	35.0	180	270	206	205	140	226.1	91.3	236.5
221.9	34.4	14	180	298	238	149	302.1	100.4	299.2

Table 5. Comparison between experimental results and model predictions for Material 2(½%Cr-Mo-V).

Experiment (Haigh 1975)				**Present model**			
				λ = 35 μm		**λ = 350 μm**	
Applied stress S (MPa)	Crack length a (mm)	Incubation time t_i (hr.)	Measured CTOD (μm)	CTOD (μm)	Yield stress σ_{oi} (MPa)	CTOD (μm)	Yield stress σ_{oi} (MPa)
131.7	35	550	105	90	185	124	158
147.9	35	250	125	113	194	142	176
181.5	35	130	120	245	196	267	192
133.7	41	30	90	98	196	104	190
124.4	42	18	200	84	196	87	192

Table 6. Comparison between experimental results and model predictions for Material 3(1%Cr-Mo-V).

Experiment (Haigh 1975)				**Present model**			
				λ = 35 μm		**λ = 350 μm**	
Applied stress S (MPa)	Crack length a (mm)	Incubation time t_i (hr.)	Measured CTOD (μm)	CTOD (μm)	Yield stress σ_{oi} (MPa)	CTOD (μm)	Yield stress σ_{oi} (MPa)
181.52	35	40	30	69	379	86	320
134.46	35	200	20 to 30	44	318	55	266
155.97	42	4	20 to 50	53	423	60	373

Table 5 shows the comparison between the present model predictions and the experimental data of Haigh for Material 2. The experiments were performed on specimens with several crack lengths ranging between a = 35 mm and a = 42 mm, and stress levels between S = 131 MPa and S = 181 MPa. In general, the present model predicts the critical CTOD reasonably well. The larger discrepancies between the experiment and model are recorded for the case of the large applied stress of S = 181 MPa, or for the case of the large crack length of a = 42 mm. Table 6 shows the comparison between the data from Haigh's experiments and the present model for Material 3, considering λ = 35 μm and λ = 350 μm. In general, the model reasonably predicts the value of the critical CTOD given the incubation times t_i. Some of the discrepancies may probably be attributed to experimental uncertainties in accurately measuring the critical CTOD. As it can be observed from Tables 3-6, there is a significant decrease in the flow stress in the plastic zone, thus it can be assumed that large scale yielding conditions prevail during the creep crack incubation, and at the onset of the crack growth phase. The accumulation of creep damage around the crack tip and the large increase in the plastic zone, combined with a significant decrease in the flow stress indicates that the critical CTOD is a suitable measure that can be used to predict the initiation time t_i.

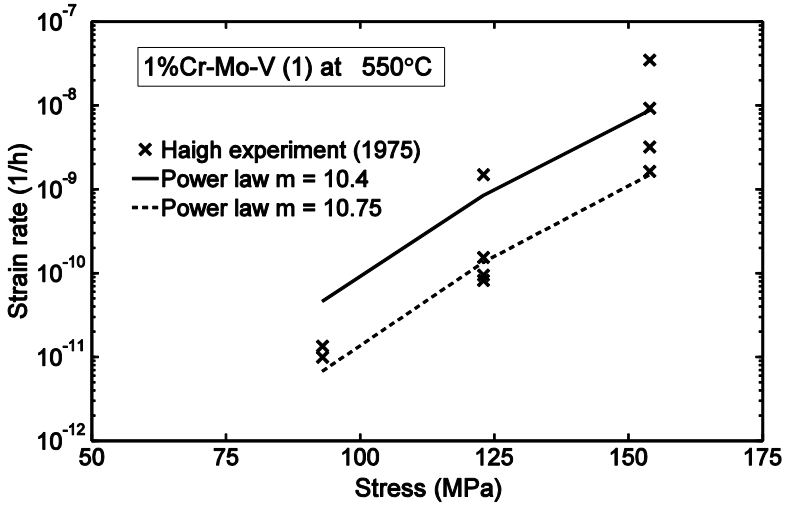

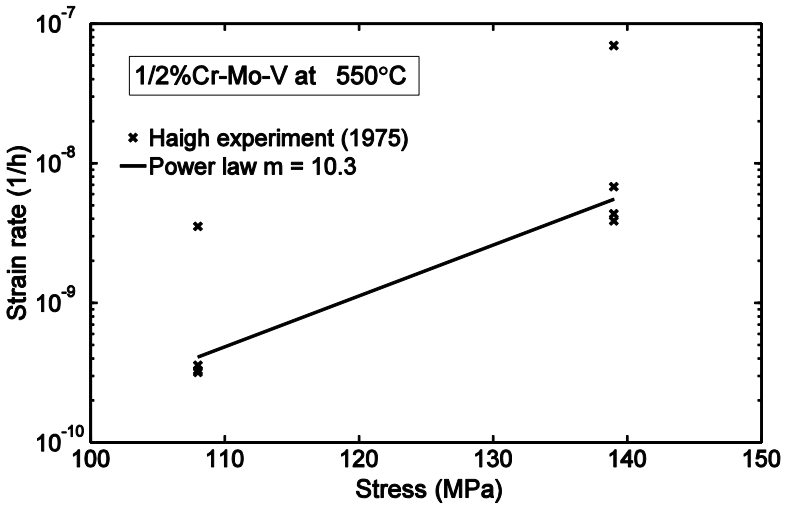

(b)

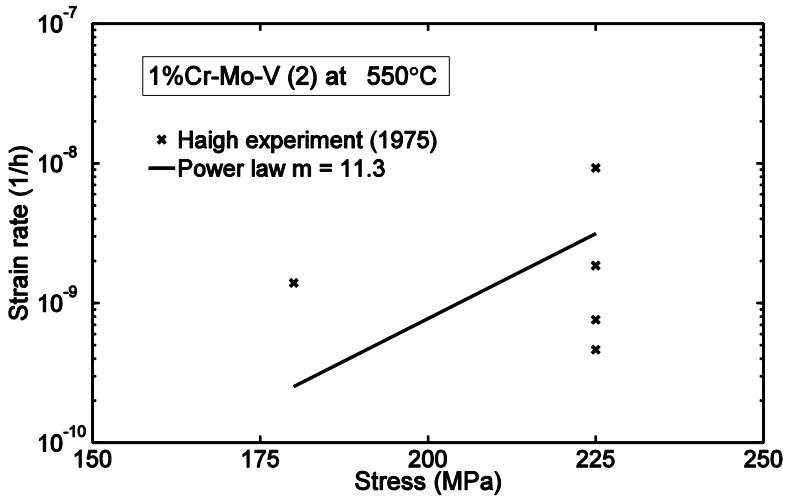

(c)

Fig. 7. Curve-fit to obtain the creep power law constants for: (a) Material 1 – 1%Cr-Mo-V(1), (b) Material 2 – 1/2%Cr-Mo-V, and (c) Material 3 – 1%Cr-Mo-V(2).

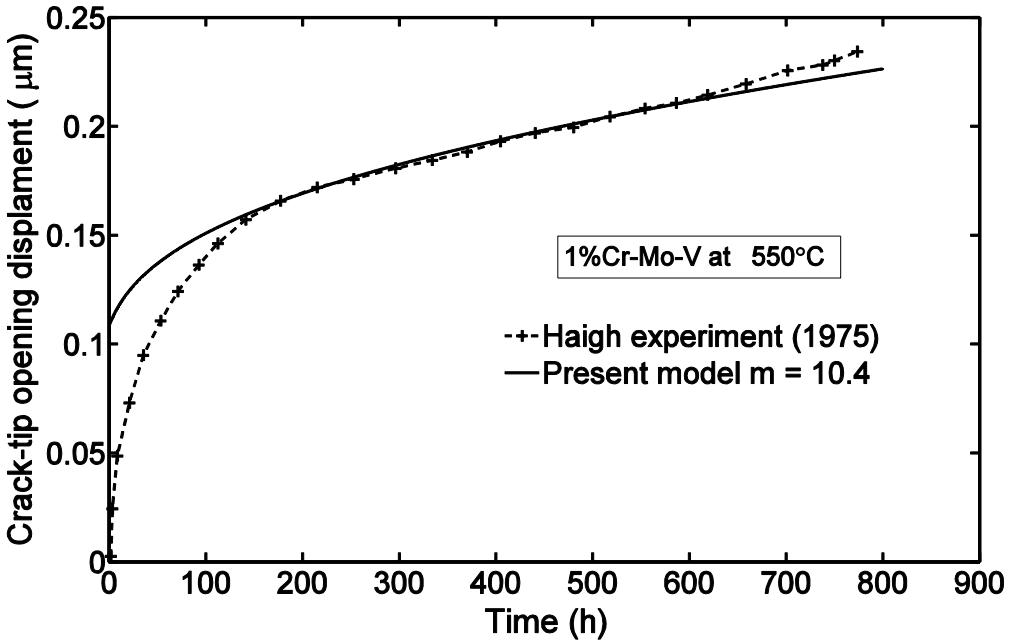

Fig. 8. Comparison between the experimental results and modeling predictions for the evolution of the crack-tip opening displacement for 1%Cr-Mo-V steel tested at 550ºC.

A comparison between experiment and modeling results for the evolution of the CTOD during the incubation time for Material 1 is shown in Fig. 8. In this case, the crack length was a = 32 mm and the applied stress S = 172 MPa. From this comparison, it can be observed that for the large majority of the incubation time, the model predicts well the evolution of the CTOD for the first 800 hours, however there is a discrepancy between the experiment and modeling results for the first 100 hours.

The slight mismatch toward the end of the CTOD curve is due to the fact that, after t = 750 hours, in the experiment the crack starts growing, marking the end of the incubation time. This phenomenon is not captured in the present model. Vitek also presented the variation of the CTOD with time for the same material, crack length and applied stress, but did not compare his model results with the experiment of Haigh. Vitek used a power exponent of m = 10 in his model. Fig. 9 shows the comparison of the CTOD evolution with time for the present model and the Vitek model.

The present model shows a slight discrepancy with the Vitek data when a creep power exponent of m = 10 is used, however the two models show excellent agreement when a value of m = 10.75 is used in the present model. Given the scatter in the experimental data, and that the value of m = 10.75 does not produce a significant difference in the power law curve-fit compared with m = 10, or m = 10.4, as illustrated in Fig. 7a, the comparison between the two models can be considered adequate.

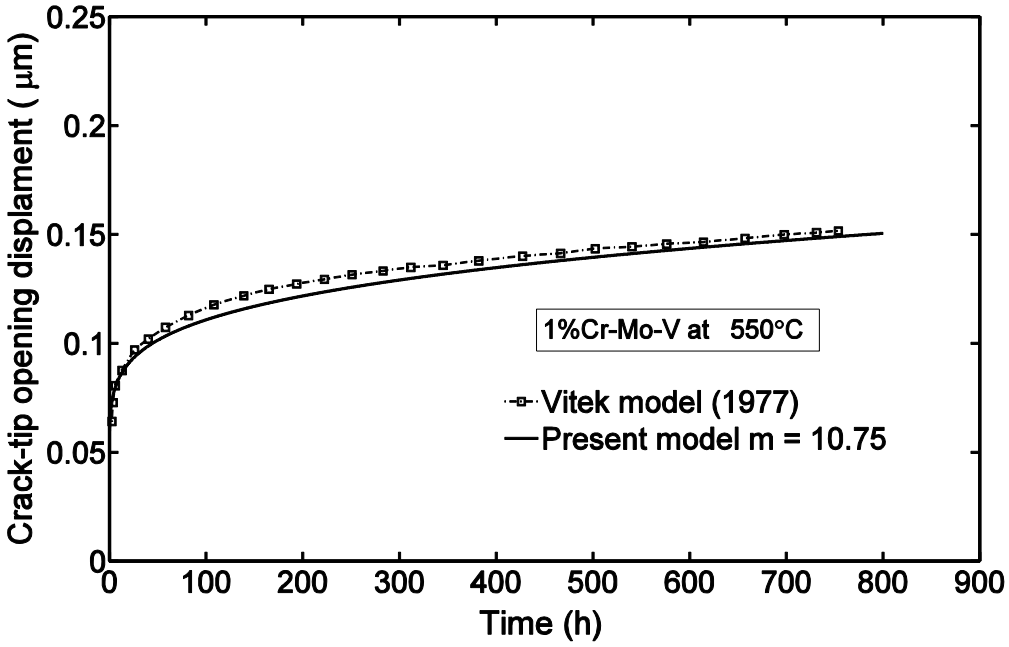

Fig. 9. Comparison between the present model and the Vitek (1977) model prediction for the evolution of the crack tip opening displacement for 1%Cr-Mo-V steel tested at 550ºC.

5.1.4. Conclusions

A strip-yield model was adapted for the computation of creep crack incubation periods in cracked components. The method uses a critical crack-tip opening displacement (CTOD) approach, but other methods can be easily implemented in the model, such as *K*-based or *C**-based laws for crack incubation. Given the large scale yielding condition prevailing at the crack tip during creep deformation, the critical CTOD was used as a crack incubation criterion. The creep behavior accounts only for secondary stage effects, while it neglects the primary and the tertiary stages. Future developments should consider these effects as well, for a more realistic simulation of the creep crack incubation and growth processes. The versatility of this methodology is that it can easily be adapted to other crack geometries. Moreover this approach can be modified to include more detailed models for the creep deformation and damage in the plastic zone, thus resulting in more realistic models for controlling the crack incubation or crack growth processes. The model predicts the time dependent variation of the CTOD, crack-tip plastic zone sizes and flow stress in the plastic zone. In general, the model presented in this research gives crack incubation times in agreement with the predictions provided by two other strip-yield models. Also, the model results compare well with experimental data for critical CTOD.

References

[1] Dugdale, D.S., "Yielding of steel sheets containing slits," J. Mech. Phys. Solids, Vol. 8, 1960, pp. 100-104

[2] Vitek, V., "A theory of the initiation of creep crack growth," Int. J. Fracture, Vol 13, 1977, pp. 39-50
[3] Bilby, B.A., Cottrell, A.H., Smith, E., Swinden, K.H., "Plastic yielding from sharp notches," P. Roy. Soc. Lond. A, Vol. 279, 1964, pp. 1-9
[4] Ewing, D.J.F., "Strip yield models of creep crack incubation," Int. J. Fracture, Vol. 14, 1978, pp. 101-117
[5] Batte, A.D., "The initiation and growth of creep cracks in 1%CrMoV rotor forging material," private communication to D.J.F. Ewing, 1975
[6] Haigh, J.R., "The mechanisms of macroscopic high temperature crack growth. Part I: Experiments on tempered Cr-Mo-V steels," Mater. Sci. Eng., Vol. 20, 1975, pp. 213-223
[7] Haigh, J.R., "The mechanisms of macroscopic high temperature crack growth. Part II: Reviews and re-analysis of previous work," Mater. Sci. Eng., Vol. 20, 1975, pp. 225-235
[8] Tvergaard, V., "Analysis of creep crack growth by grain boundary cavitation," Int. J. Fracture, Vol. 31, 1986, pp. 183-209
[9] Tvergaard, V., "Effect of microstructure degradation on creep crack growth," Int. J. Fracture, Vol. 42, 1990, pp. 145-155
[10] Davies, C.M., O'Dowd, N.P., Nikbin, K.M., Webster, G.A., "An analytical and computational study of crack initiation under transient creep conditions," Int. J. Solids Struct., Vol. 44, 2007, pp. 1823-1843
[11] Yatomi, M., O'Dowd, N.P.; Nikbin, K.M.; Webster, G.A., "Theoretical and numerical modelling of creep crack growth in a carbon-manganese steel," Eng. Fract. Mech., Vol. 73, 2006, pp. 1158-1175
[12] Nikbin, K.M., Smith, D.J., Webster, G.A., "Prediction of creep crack growth from uniaxial creep data P. Roy. Soc. Lond. A Mat., Vol. 396, 1984, pp. 183-197
[13] Nishida, K., Nikbin, K.M., Webster, G.A., "Influence of net section damage on creep crack growth," J. Strain Anal. Eng. Design, Vol. 24, 1989, pp. 75-82
[14] Smith, D.J., Webster G.A., "Esimates of the C* parameter for crack growth in creeping materials," *Elastic-plastic fracture: Second Symposium, Volume I – Inelastic Crack Analysis, ASTM STP 803*, C.F. Shih, J.P. Gudas, Eds., ASTM International, West Conshohocken, PA, 1983, pp. 654-674
[15] Wasmer, K., Nikbin, K.M., Webster, G.A., "Influence of reference stress formulae on creep and creep-fatigue crack initiation and growth prediction in plate components," Int. J. Pres.Ves. Pip., Vol. 87, 2010, pp. 447-456
[16] Haigh, J.R., Skelton, R.P., Richards, C.E., "Oxidation-assisted crack growth during high cycle fatigue of a 1%Cr-Mo-V steel at 550," Mater. Sci. Engng., Vol. 26, 1976, pp. 167-174
[17] Siverns, M.J.; Price, A.T., "Crack propagation under creep conditions in a quenched 2¼ chromium 1 molybdenum steel," Int. J. Fracture, Vol. 9, 1973, pp. 199-207
[18] Barker, E. Lloyd, G.J.; Pilkington, R., "Creep fracture of a 9 Cr-1Mo steel," Mater. Sci. Eng., Vol. 84, 1986, pp. 49-64
[19] Piques, R., Molinie, E., Pineau, A., "Comparison between two assessment methods for defects in the creep range," Fatigue Fract. Engng. Mater. Stuct., Vol. 14, 1991, pp. 871-885
[20] Piques, R., Molinie, E., Pineau, A., "Creep and creep-fatigue cracking behaviour of two structural steels," Nuclear Engineering and Design, Vol. 153, 1995, pp. 223-233
[21] Ainsworth, R.A., "The initiation of creep crack growth," J. Solids Struct., Vol. 18, 1982, pp. 873-881

[22] Tada, H., Paris, P.C., Irwin, G.R., *The stress analysis of cracks handbook*, The AMSE Press, New York, 2000

[23] Newman, J.C. Jr., "A crack-closure model for predicting fatigue crack growth under aircraft spectrum loading," *Methods and models for predicting fatigue crack growth under random loading, ASPM STP 748,* J.B. Chang, C.M. Hudson, Eds ASTM International, West Conshohocken, PA, 1981, pp.53-84

5.2. Finite element modeling of creep fracture

5.2.1. Introduction

In the present research a numerical model for studying the creep fracture behavior of Grade 91 steel has been developed. Creep crack incubation in Cr-Mo steels has been studied. In order to predict creep crack growth under thermal and mechanical loading, a finite element model has been developed for the creep deformation and damage. The model considered the evolution of the dislocation density as the main creep deformation mechanism. Furthermore, the effect of void growth and crack nucleation has been taken into account in the damage formulation. In order to be able to measure and study the crack tip plastic zone during creep the afore-mentioned model has been combined with a linear kinematic hardening model. The model was implemented as a User Material subroutine (UMAT) in Abaqus Standard. Crack-tip opening displacement (CTOD), crack tip plastic zone sizes, and material relaxation in the crack tip plastic zone were simulated. Creep crack incubation times were predicted based on a critical CTOD criterion.

5.2.2. Constitutive equations for creep and plasticity

In this chapter the constitutive model for the coupled plasticity creep model has been explained. Accumulated strain is modeled here as the summation of the elastic, plastic and creep strains,

$$\varepsilon_{ij} = \varepsilon_{ij}^{el} + \varepsilon_{ij}^{pl} + \varepsilon_{ij}^{cr} \tag{135}$$

and in the rate form

$$\dot{\varepsilon}_{ij} = \dot{\varepsilon}_{ij}^{el} + \dot{\varepsilon}_{ij}^{pl} + \dot{\varepsilon}_{ij}^{cr} \tag{2}$$

The creep strain rate is considered a function of equivalent stress, temperature and some internal state variables,

$$\dot{\varepsilon} = \dot{\varepsilon}(\bar{\sigma}, T, \xi) \tag{36}$$

where the equivalent stress is computed as

$$\bar{\sigma} = \sqrt{\frac{3}{2} S_{ij} : S_{ij}}, Where\, S_{ij} = \sigma_{ij} - \frac{1}{3}\delta_{ij}\sigma_{kk} \tag{4}$$

The evolution of the state variables has the same format as that of the creep strain as

$$\dot{\xi}_a = q_a(\bar{\sigma}, T, \xi, \alpha)$$

(37)

In the present model, internal variables refer to the dislocation density, solid solutions, precipitate size, and other strengthening mechanisms terms. These strengthening mechanisms could induce isotropic hardening in the material. This isotropic hardening resistance evolves during a thermally activated deformation process such as creep. In a rate-dependent inelastic deformation, the rate of evolution of the internal variables can also be expressed by the internal variables rate equations $\dot{\xi}_a$. Here, $\dot{\xi}_a$ is defined by some functions q_a which depend on σ, T, ξ, α .The parameter α represents the Prager-Ziegler kinematic hardening. The elastic response of the material is modeled by the linear isotropic elastic equation. The linear isotropic elastic stress strain equation is valid for creep deformation and it has been defined as

$$\sigma_{ij} = 2G\varepsilon_{ij}^{el} + \lambda \delta_{ij}\varepsilon_{kk} \tag{6}$$

where G is the shear modulus and λ is Lame' Coefficient. A continuum damage creep model has been developed in a previous work [1]. A simplified version of the mentioned model has been employed here to analyze the creep behavior of the modified 9Cr-1Mo steel. In the original model the density of the dipole dislocations was taken into account. By performing numerous simulations on the original model, it was observed that neglecting the dipole dislocations density reduces the number of equations in the model significantly, while it doesn't change the simulation results considerably. Starting from the equations presented in [1], the Orowan's equation for creep modified for damage was employed to evaluate the creep strain rate in the media

$$\dot{\bar{\varepsilon}}^{cr} = \frac{\rho_m b B_{visc}}{M D}(\bar{\sigma} - \alpha MCGb\sqrt{\rho_m}) \tag{7}$$

In this equation ρ_m is the mobile dislocation density, b is the burger's vector, α is a dislocation interaction constant, M is the Taylor factor, C is the inelastic deformation factor (C has been considered equal to *0.2* in this research), and B_{visc} is the dislocation mobility term.. For simplicity, the following notation is made $K_1 = \alpha MCGb$. The term D represents the damage caused by precipitate coarsening, depletion of solid solutions, and void and crack formation. The dislocation mobility term is defined according to [2] as

$$B_{visc} = \frac{9\Omega D_{sol} K_B T}{M C_0 G^2 b^7 \varepsilon_a^2 \ln(\frac{r_2}{r_1})} \tag{8}$$

where Ω is the atomic volume (which has been considered equal to b^3), K_B is the Boltzmann constant, T is the temperature, D_{sol} is the solute atom diffusion coefficient in solvent atoms, C_0 is the solute concentration, r_1 and r_2 are the outer and inner cut-off radii of the dislocation stress field, and ε_a, is the relative size misfit between solute and solvent atoms. The rate of evolution

of mobile dislocations density is defined as the difference between the rate of generation of mobile dislocations ($\dot{\rho}_{m,gen}$), and the rate of annihilation of mobile dislocations density ($\dot{\rho}_{m,ani}$),

$$\dot{\rho}_m = \dot{\rho}_{m,gen} - \dot{\rho}_{m,ani} \tag{9}$$

The rate of generation of the mobile dislocation density is

$$\dot{\rho}_{m,gen} = \frac{\rho_m B_{visc} \sqrt{\rho_m}}{k_\Lambda D} (\bar{\sigma} - K_1 \sqrt{\rho_m}) \tag{10}$$

where k_Λ is a material parameter, and is a function of temperature and equivalent stress. The rate of annihiliation of the mobile dislocationsis modeled as

$$\dot{\rho}_{m,ani} = \frac{4M\dot{\varepsilon} d_{dip} \rho_m}{b n_g} \tag{11}$$

The rate of annihiiation of mobile dislocation is equal to the summation of the densities of dislocations which annihiliate spontaneously and those which form dipoles. It is a function of strain rate, mobile dislocations density, burger's vector, Taylor factor and the number of active slip planes n_g. Replacing the $\dot{\varepsilon}$ the rate of annihilation of mobile dislocations could be expressed as,

$$\dot{\rho}_{m,ani} = \frac{4 d_{dip} \rho^2{}_m B_{visc}}{n_g D} (\bar{\sigma} - K_1 \sqrt{\rho_m}) \tag{12}$$

two mobile disliocations with opposite sings approach eachother, at a certain distance they will form dipoles and produce sessile dislocations. This distance is d_{dip} called, the dipole formation distance and has been defined as

$$d_{dip} = \frac{M}{8\pi(1-\nu)} \frac{Gb}{\bar{\sigma}} \tag{13}$$

In this equation ν is the Poisson's ratio. Replacing d_{dip}, the rate of annihilation of mobile dislocations will be,

$$\dot{\rho}_{m,ani} = \frac{4MbG\rho^2{}_m B_{visc}}{2\pi(1-\nu) n_g D \bar{\sigma}} (\bar{\sigma} - K_1 \sqrt{\rho_m}) \tag{14}$$

5.2.3. Constitutive equations for creep damage

The material microstructures will degrade during high temperature exposure. In other words, the strengthening mechanisms that have been used to increase the creep resistance of materials will become less effective during creep loading. The main strengthening mechanisms in modified 9Cr-1Mo steel are work hardening, solid solution strengthening, precipitation hardening, and grain boundary strengthening. It has been shown by several researchers that the Mo particles deplete in the subgrain matrix under long term thermo-mechanical loading [3,6,7]. Moreover, the precipitate coarsening ($M_{23}C_6$ and MX) in modified 9Cr-1Mo increases the interparticle spacing between the precipitates. Solid solutions depletion and precipitate coarsening increase the dislocations mobility. Consequently dislocations require less energy to move [3]. Furthermore, void nucleation and crack formation is one of the most important creep damage mechanisms in 9Cr-1Mo steel. The cavities usually nucleate at triple junctions or at the particles located on grain boundaries. Grain deformation and cavity coalesce are the main crack formation mechanisms in 9Cr-1Mo steel.

Mo is added to 9Cr-1Mo steel to induce solid solution strengthening. During creep loading the Mo particles deplete in the subgrain matrix and form precipitation of Fe_2Mo Laves phase. It has been shown by experiments that Fe_2Mo precipitates with low volume fraction and larger size could not effectively block dislocations motions. These large size Laves phases (Fe_2Mo) are a source for dislocations absorbent, and they are brittle phases. These inopportune properties will lead to a reduction of the creep resistance of modified 9Cr-1Mo..

Equations (15-16) show the damage caused by solid solution depletion and its corresponding rate, respectively is the solid solution depletion term is a function of the initial and current solid solution concentrations, C_0 and C_t

$$D_s = 1 - \frac{\bar{C}_t}{C_0} \tag{15}$$

$$\dot{D}_S = K_S D_S^{1/3}(1 - D_S) \tag{16}$$

where, K_S is the material parameter.

Another important damage mechanism in 9Cr-1Mo steel is caused by the coarsening of $M_{23}C_6$ and MX precipitates. The coarsening of precipitates increases the interparticle spacing and consequently the easier motion of dislocations which means less creep resistance. This damage and damage rate of accounting for the precipitate coarsening written as

$$D_P = 1 - \frac{P_0}{P_t} \tag{17}$$

$$\dot{D}_p = k_p(1 - D_p)^4 \tag{18}$$

where P_0 and P_t are the initial and current size of the precipitates, and k_p is the material parameter.

A leading failure mechanism during creep deformation of modified 9Cr-1Mo is crack incubation and growth. Microstructural stress concentrations are responsible for grain boundary sliding leading to the formation of creep cavities and creep crack formation. Creep crack formation and growth has been extensively studied in literatures [5]. In this work a modified Kachanov damage model has been employed for the crack-driven creep damage. Simply, creep damage is expressed as a function of creep exposure time (t), creep rupture time ($t_{rupture}$), and a

material parameter B and is a function of stress. The creep rupture time can be obtained from experiments. The creep rupture time for 9Cr-1Mo steel is shown in Fig. 1. To summarize the crack-driven damage is modeled as

$$D_N = 1-(1-\frac{t}{t_{rupture}})^{1/(1+B)} \tag{19}$$

For simplicity, the total damage in the material caused by solid solution depletion, precipitate coarsening and crack formation is denoted as D, and is defined as

$$D = D(D_S, D_P, D_N) = (1-D_S)(1-D_P)(1-D_N) \tag{20}$$

In order to be able to simulate three-dimensional geometries or components made of different materials one has to use the finite element method. The analytical model presented in the previous section was implemented in the finite element code ABAQUS Standard as a User Material (UMAT) subroutine. Creep deformation is a history-dependent process. In order to solve the set of differential equations representing the constitutive model, it is necessary to discretize these equations and integrate them over time.

5.2.4. Results

The developed UMAT has been used to study the crack deformations in Cr-Mo steels. A center crack in a plate was simulated. The geometry has been generated and meshed in ANSYS APDL. The crack file was exported to Abaqus, by using a FORTRAN code and in an input file format. The plate is under uniform uniaxial tension. The symmetric condition has been applied to the model so a quarter of the model was studied. Fig. 10 shows the geometry the mesh and the boundary conditions applied to the crack. A quarter of crack was simulated. The symmetry boundary conditions were applied to the nodes on the X and Y axis and the other side of the plate was restricted from moving in Z direction.

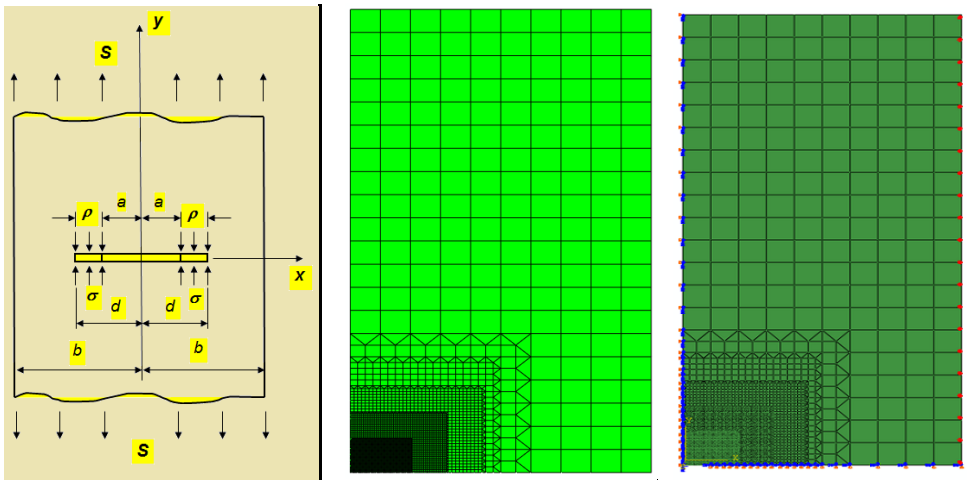

(a) (b) (c)

Fig. 10. (a) Middle-tension specimes with a center crack loaded in tension; (a) finite elemen mesh for one fourth of the specimen shown in (a) taking advantage of the symmetry, and (c) boundary conditions for the finite element study.

Fig. 11 shows the crack mouth opening at different time increments. The deformation scale has been increased to better visualize the creep crack mouth opening.

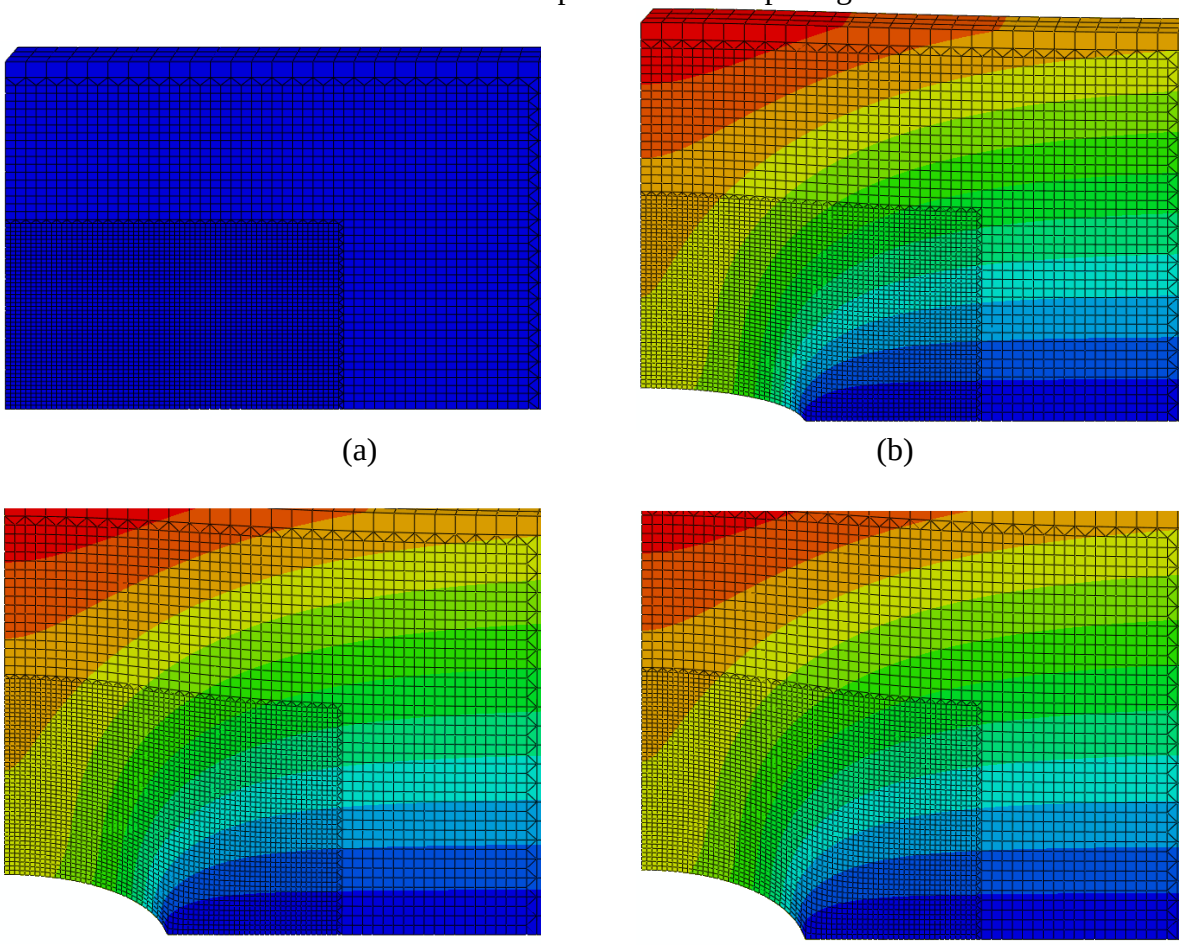

(a) (b)

(c) (d)

Fig. 11. Creep crack deformation after (a) 0 , (b) 12000, (c) 124,000, and (d) 250,000 seconds. Magnification factor used for displacements was 10 times.

Fig. 12 shows the crack tip opening for a plate with a 1 mm center crack under a tensile load equal to 221 MPa. Figs. 13 and 14 show the stress versus time in the plate and at the crack zone.

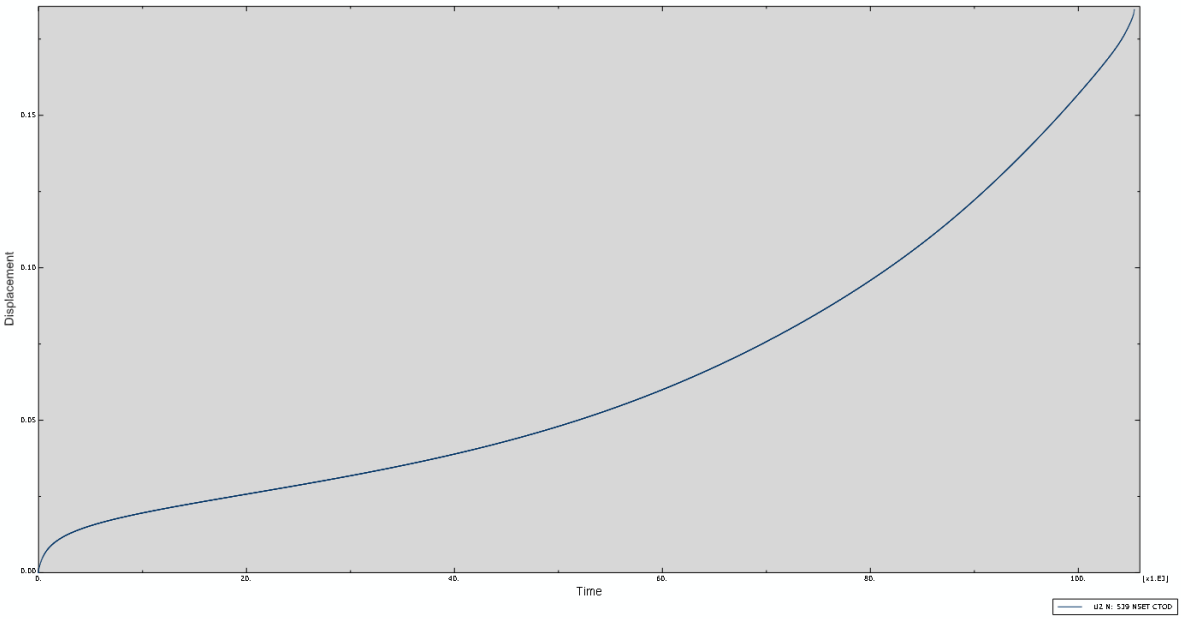

Fig. 12. Crack tip opening displacement (CTOD) versus time during creep deformation.

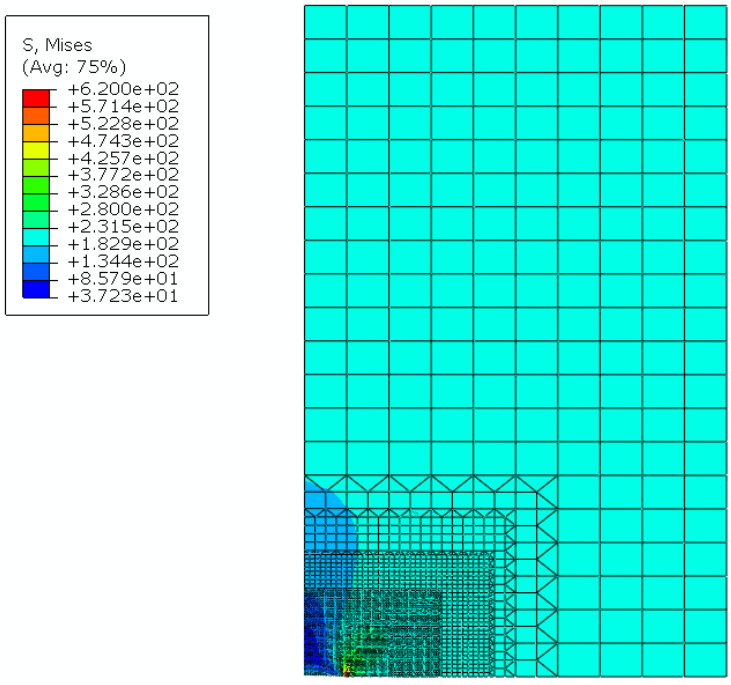

Fig. 13. Crack tip plastic zone during creep deformation.

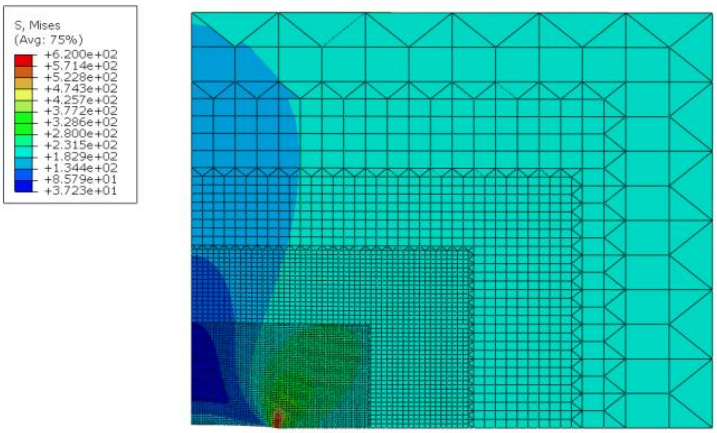

Fig. 14. Zoomed-in image of the plastic deformation at the crack tip during creep deformation.

As it was discussed in the formulation part the evolution of the dislocations during creep has been considered as the main mechanism for the creep deformation. Fig. 15 shows the mobile dislocation evolution versus time at the crack tip. The dislocation density drops by 30 % at the crack tip.

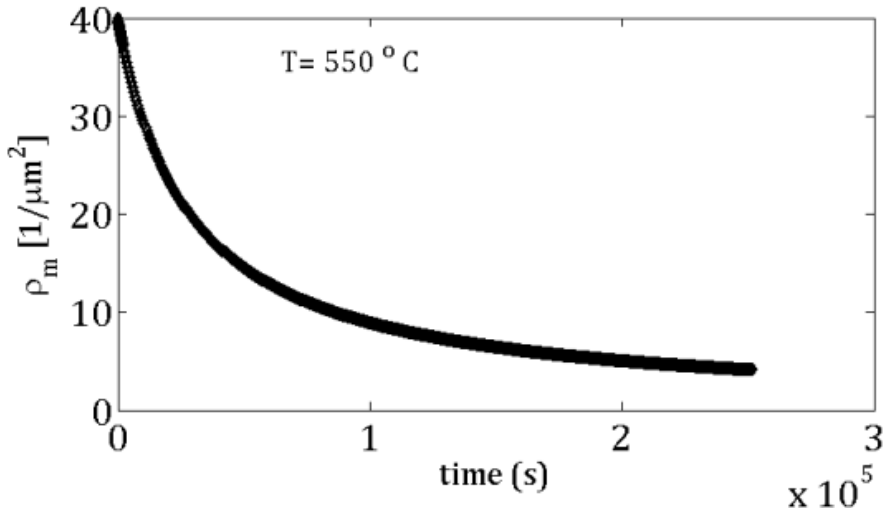

Fig. 15. The evolution of the mobile dislocation density versus time at the crack tip.

Figs. 16-18 show the variations of the stress versus the distance from crack tip axes at the different time steps. As it was expected at further distance from crack tip the stress is lower and the maximum stress locates at the crack tip. It also could be seen that at the further distances from crack tip the stress remains steady.

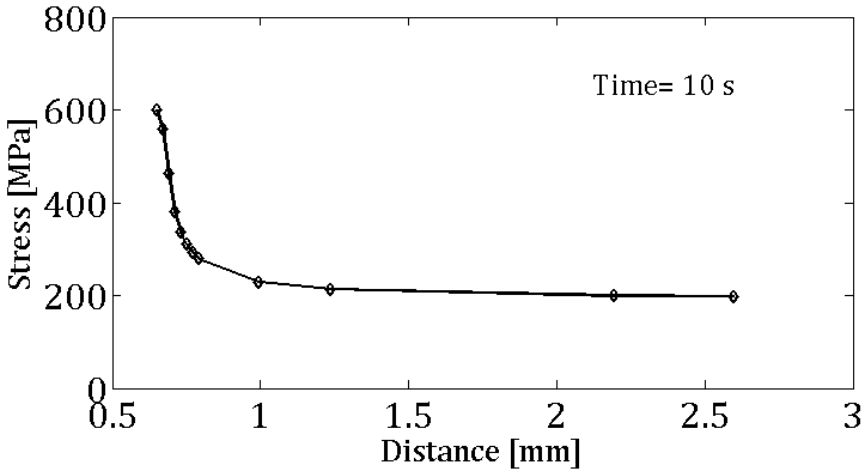

Fig. 16.Stress variations ahead of the crack tip at time equal to 10 seconds.

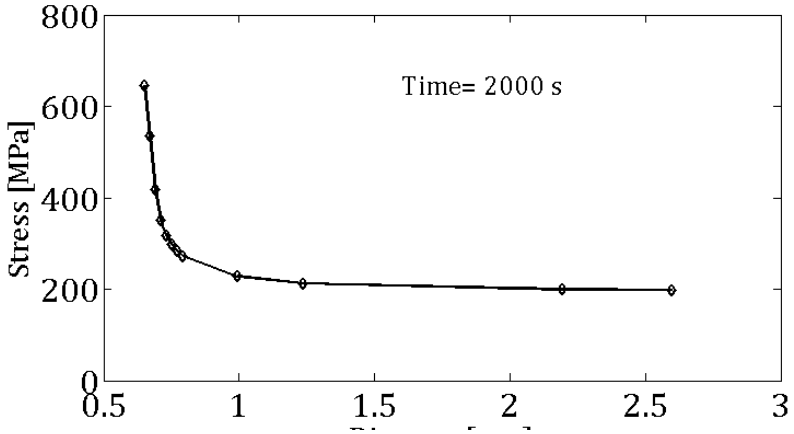

Fig. 17. Stress variations ahead of the crack tip at time equal to 2000 seconds.

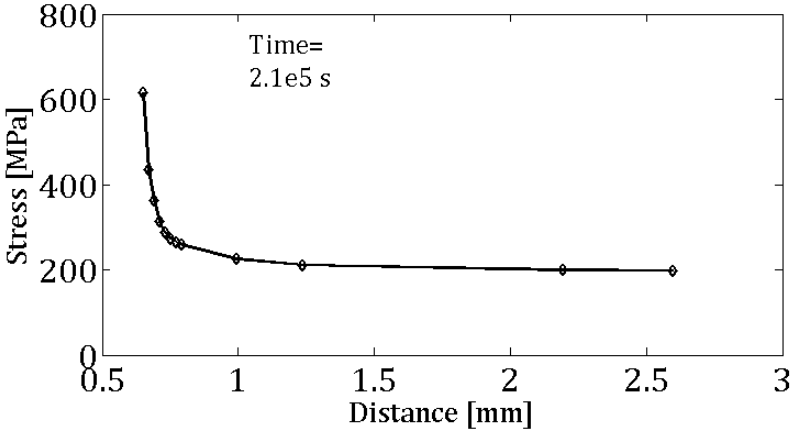

Fig. 18. Stress variations ahead of the crack tip at time equal to 215000 seconds.

5.2.5. Conclusions

A finite element model was developed to simulate the creep deformation at the crack tip of a crack embedded in a Grade 91 steel specimes. The model combined plasticity and creep constitutive modeling. Both the plasticity and creep integration schemes are implicit procedures. Simulations of crack incubation were performed, and crack-tip parameters were characterized. The density of mobile dislocation at the crack tip decreased with the time elapsed during the creep loading, indicating a relaxation of the yield stress at the crack tip. In addition, it was found that the crack-tip stress decreases with the distance from the crack tip. Moreover, the crack tip plastic zone increases in size with more creep loading applied to the fractured specimens. These results confirm the strip-yield model result presented in the prevous section. The model can be used to predict crack incubation in Grade 91 steels.

References

[1] Basirat, M., Shrestha, T., Potirniche, G.P., Charit, I., Rink, K., 2012. A study of the creep behavior of modified 9Cr–1Mo steel using continuum-damage modeling. Int. J. Plast. 37, 95–107.

[2] Blum, W., Eisenlohr, P., Breutinger, F., 2002. Understanding creep—a review. Met. Mater. Trans. 33, 291–303.

[3] Chilukuru H., D.K., 2009. Coarsening of precipitates and degradation of creep resistance in tempered martensite steels. Mater Sci Eng Mater. Sci. Eng. 510-511, 81–87.

[4] Dunne, F., 2007. Introduction to computational plasticity. Oxford University Press, Oxford; New York.

[5] Lemaître, J., 1990. Mechanics of solid materials. Cambridge University Press, Cambridge.

[6] Morra, P.V., Radelaar, S., Yandouzi, M., Chen, J., Böttger, A.J., 2009. Precipitate coarsening-induced plasticity: Low temperature creep behaviour of tempered SAE 52100. Int. J. Plast. 25, 2331–2348.

[7] Muñoz-Morris, M.A., Gutierrez-Urrutia, I., Morris, D.G., 2009. Influence of nanoprecipitates on the creep strength and ductility of a Fe–Ni–Al alloy. Int. J. Plast. 25, 1011–1023.

Task 6: Design of a device for damage detection using leak method

6.1. Introduction

Kr-85 content is commonly measured using gamma detectors that employ thallium-doped Sodium Iodide (NaI) crystals. These crystals are often manufactured using a Bridgman process and are formed in a wide variety of geometries depending on the nature of a specific application. In general, they take the shape of: (1) a flat surface, (2) a well-shaped geometry, or (3) a tunnel. Flat crystals are most convenient for checking the gamma emission from rather large devices, while well crystals offer very high counting efficiencies for relatively small devices. Tunnel crystals, on the other hand, are applicable to high-volume manufacturing processes in which components to be checked may pass-through the crystal at a high rate with minimum physical interaction.

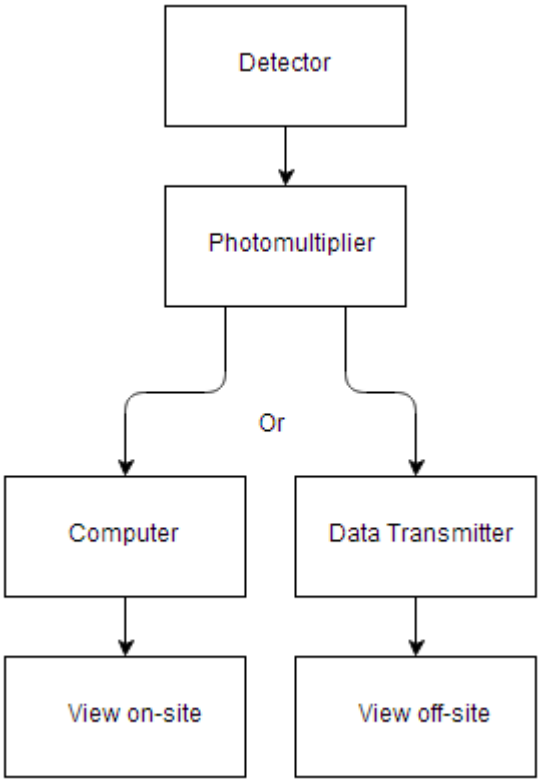

Fig. 1. Scintillation counter configuration

Regardless of the geometry the crystal, development of a NaI based radiation detector includes the necessity to encase and protect the crystal component to minimize physical interaction between the crystal and any environment in which will be operating. NaI scintillation crystals are both hydroscopic and easily fractured, either event leading to component failure and either incorrect or no detection capability. Typically, NaI crystals are sealed in thin, highly-polished (for reflectivity of the photons emitted by the crystal) aluminum packages. Current

development is underway to formulate a complete and cost effective crystal casing for the purpose of reducing the potential for hydroscopic based failure of the NaI scintillation crystal. Furthermore, the design of these packages must include an optical "light pipe" leading to a photomultiplier tube so that the photon emission from the NaI crystal may be quantified and recorded with proper means while maintaining a hermetic seal throughout the parts working life.

6.2. Description of the Kr-85 detector design

Our research indicated that small packages can be manufactured using low temperature co-fired ceramics (LTCC) which exhibit high degrees of hermeticity (with leak rates less than 10^{-10} atm cc/s). At the same time, conventional electrical interconnections (or "vias") can also be incorporated into LTCC products which also exhibit hermetic properties. This enables the possibility of manufacturing a new type of packaging for NaI scintillation detectors. Particularly intriguing is the possibility of producing scintillation detectors that could be place within pressure vessels, or possibly within the walls of pressure vessels and other containers, so that the emission process from a radioactive tracer can be monitored.

The scintillation detector consists of four primary components and one soldered interface depicted in Fig 2. The components are as follows: a scintillation crystal, a protective housing, a light pipe, and a photomultiplier. LTCC containers featuring small volumes with silvered walls can be manufactured and tested to quantify its hermetic properties. Following the results from testing, the containers will be designed to incorporate small NaI crystals and appropriate light pipes for transmission of light to small photo-detectors. These two basic components of a novel gamma detection system can be fabricated. A cross-section of the complete system is shown in Fig. 2.

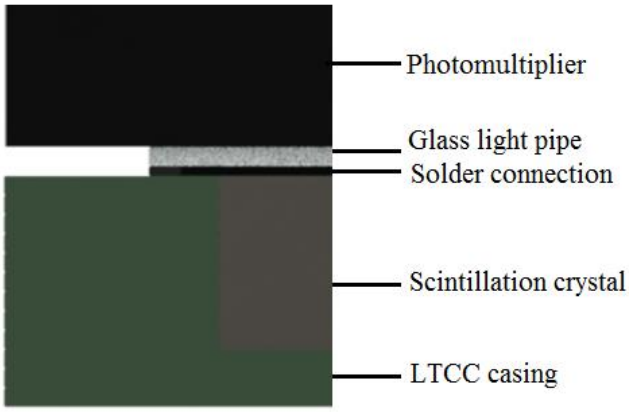

Fig. 2. Detector profile

Low temperature co-fired ceramic technology has been commonly employed in development of micro-electronic boards utilizing multilayered ceramics. [1] The potential for scalability and modification in further design coupled with easy installation of the interface between the scintillator and its accompanying photomultiplier makes LTCC an ideal candidate for continued development in hermetic packaging.

The current LTCC casing design is scaled to the size of commercially available scintillation crystals for the purpose of developing a low cost prototype. With the ability to grow custom sized scintillation crystals, the end product can easily be scaled to maintain acceptable cost for each and any different application. The diameter of a small commercially available cylindrical crystal is approximately 16mm with a similar height. As the driving dimension, the LTCC layers must be designed with an end goal of sustaining a cavity with enough volume to incorporate the crystal and enough excess material to maintain structural integrity on a small scale.

The material used for creating layered ceramics is DuPont 951 green tape which consists of a sintered ceramic with an organic binder. During the firing process, the organic binder is evaporated and the material shrinks to its final size as dictated in DuPont's material properties database. The cavity must therefore be initially oversized (approximately 18.5mm diameter) to incorporate potential shrinkage during firing, and allowing the crystal to fit in the finished ceramic. [2]

NaI (Tl) scintillation crystals can be either purchased from commercially available material or grown in a lab. The crystal can be manufactured by utilizing the "Pulling-down" method in a furnace [3]. Initially, the materials are placed in a crucible, brought to melting temperature (around 700 ºC) and slowly lowered into a cooling chamber of the furnace where it slowly crystalizes. Due to the hydroscopic nature of the NaI (Tl) crystal, special care must be taken to ensure an absolute minimum amount of moisture is exposed to the crystal during its growth. Additionally, other potential radioactive contaminates such as ^{40}K, must be controlled to ensure proper crystal calibration can be achieved post growth [3,4].

The desired geometry associated with the LTCC portion of the detector is dictated by available scintillation crystals and photomultipliers and can be scaled through the use of a CNC pneumatic punch machine coupled with AutoCAD as the supporting software. The design was created by laying out the template in AutoCAD as depicted in the Fig. 3. Fig. 3a depicts the entire punch profile template set up for punching individual LTCC detector housing layers and Fig 3.b depicts an enlarged version of the individual housing profiles.

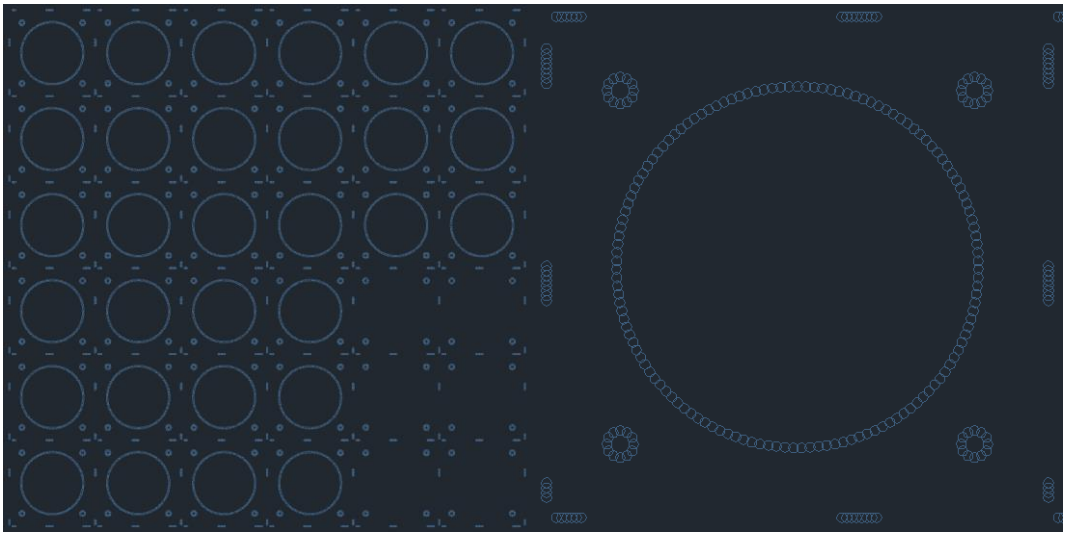

Fig. 3. AutoCAD punch template

From the AutoCAD drawing, the files are converted to an .MWD format using appropriate conversion software and uploaded into the punch device command controller. The .MWD format identifies the center point of each individual circle from the AutoCAD file and logs it as a coordinate to initiate a punching operation. By overlapping circles in the Cad file, larger holes geometric shapes can be punched from the DuPont tape with approximate dimensions. Fig. 4 shows the resultant geometry formed in this manner.

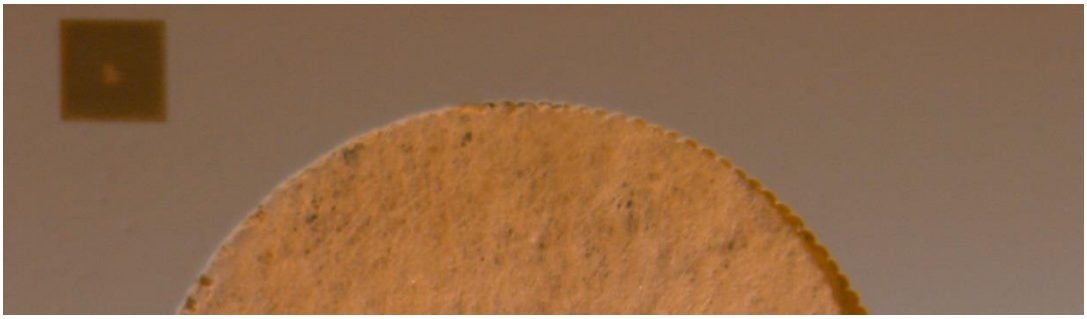

Fig. 4. LTCC post punching operation

As depicted above in Fig. 4, the edges of the large circle take on a jagged orientation where each individual punch operation can be clearly identified. The size of the jagged protrusions can be reduced by increasing the overlap from each punch operation which in turn increases the number of punches that must be performed to complete the part as well as the length of time for the total operation.

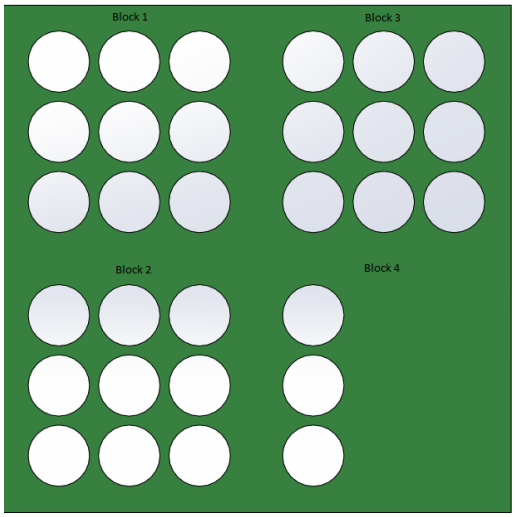

Fig. 5. DuPont 951 tape cutout

Once the part has been punched properly, the next step in construction is to cut out each individual part and stack them in an appropriately sized jig. Once stacked, the layers must be laminated in a heated press as per the tape's design specifications.[2] For a part such as this one,

three separate lamination steps must be undertaken in order to ensure full and proper lamination occurs. Each layer containing a large circular cavity must be laminated together with care to ensure that not too much pressure is applied and the design is warped. During this lamination step, damage can easily be caused by the application of too much force as the material tends to deform easily. This leads to uneven deformation of the central cavity and a significant decrease in the diameter of the cavity. Secondly the base layers which contain no cavity must be laminated together separately. If they are laminated with the primary layers, no applied force will act on the area underneath the cavity hole resulting in improper lamination of the base layers and a potential for part failure. Following this step, the cavity layers and the base layers must be laminated together.

A common issue with this stems from the applied force's interaction with the central location of each layer piece. Since the base layers are solid and the cavity layers have a large hole in the center, an uneven applied load results in "bubbling" of the central cavity. This not only leads to potential part failure but also decreases the internal volume of the part. Unless this is mitigated, the scintillation crystal will be unable to fit properly inside the LTCC cavity. One effective method of fixing this issue utilizes a sacrificial material to act as a compressing body in the internal cavity as shown in Fig. 6a. In this case a slug from the original hole cut out was formed. This provides similar the same thickness and similar compressive characteristics as the remaining material. The pictures in Fig. 6b and Fig. 6c show that very little damage has been observed in the LTCC part in comparison to the damage sustained from using no sacrificial material as depicted in Figs. 6d and 6e. Although hard to see from the Figs. 6b and 6d show the interior of the cavity where 6d exhibits a large bulge and 6b shows a compression indentation from the slug shown in Fig. 6a. Likewise, Figs. 6c and 6e show the underside of the part, where damage is substantially greater in 6e.

(a) (b)

(c)

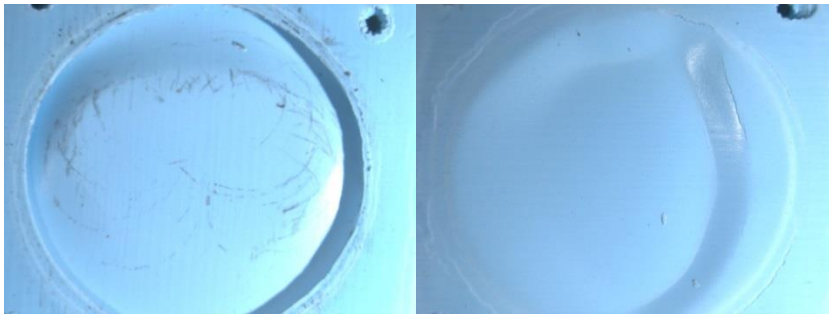

(d) (e)

Fig 6. LTCC slug present: (A), Slug sample interior: (B), Slug sample base: (C), No slug sample interior (D), No slug sample base: (D)

Once the parts have been laminated, it must be fired in a box oven at approximately 1000 C to be given the final form of the ceramic. During the firing process, the organic binder present in the DuPont tape is evaporated and expelled from the part, resulting in a slight decrease in the part size and allowing the sintering process to be completed. The LTCC will leave the box oven as a hardened ceramic part that is essentially comprised of one solid singular layer of material. At this point, the LTCC has been completely finished and any further operations to the part are to facilitate the bonding process between the light pipe and the LTCC upper surface.

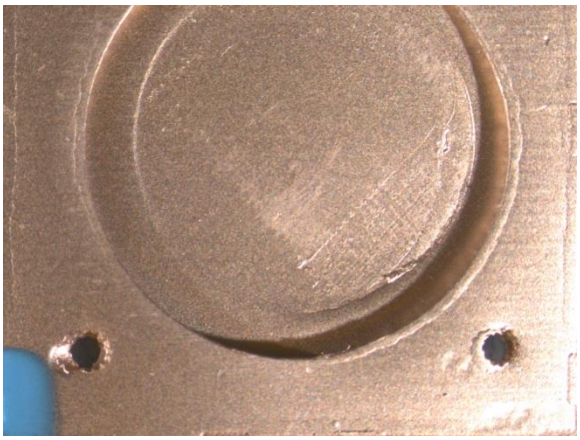

Fig 7. Metallization of LTCC structure

The next step in the detector's assembly is to coat the surface of both the glass light pipe and the LTCC in a thin metallic compound. This is achieved through sputter metal deposition and results in a well bonded thin metal film coating on the surface of both parts. [BARLOW] The sputter deposition process consists of two metallization phases and a photoresist/etchant phase to form the final geometry. Initially the LTCC and glass are coated with a thin layer of Ti (500 Å) called a "seed layer." The "seed layer" forms a strong adhesive bond with the substrate and allows for deposition of a conductive layer. The primary metallization surface is created with the deposition of Cu at approximately 1000 Å thickness. The copper metal provides ideal soldering properties for adhesion of glass lid to ceramic. Fig. 7 shows the LTCC substrate fully

coated with Ti and Cu and ready for the soldering phase. The left lower corner in the figure remains uncoated due to the presence of a holding clip to keep the LTCC snugly in place.

The blanket coating of sputtered metal effectively eliminates the potential for photons to pass through the glass light-pipe by creating a layer of metal along one side and must be refined to work properly. The use of photo-resist and multiple chemical etchants can be applied to remove metal from specific the desired view port in the center of the glass lid. The photo chemistry requires 6 steps to remove metal from any desired locations as dictated by the design. The glass is evenly coated with a photo-resistant material, covered with a pre-designed photomask, exposed to U/V light to chemically alter the photoresist at any locations not protected by the photomask, placed in a developer to remove the U/V exposed photoresist, and chemically etched to remove metal at specific locations. Once completed, the glass/metal wafer is placed in an automated dicing saw where it its outer dimensions are cut to shape.

Incorporating a transparent lid requires the selection of a suitable adhesion method and lid material selection. Scintillation crystals allow for a wide range of glass material for use due released photons operating at a wavelength in the visible spectrum. However, metal deposition on the surface of the glass is required to initiate the solder bond between glass lid and ceramic casing. Therefore a glass substrate suitable for metal sputter deposition must be used. For bonding glass to ceramic, the application of a low temperature solder is required to ensure that no thermal damage to the crystal occurs. Low temperature solder is punch formed into a shape slightly smaller to the upper ceramic layer, sandwiched between glass lid and ceramic base, and evenly heated to solder flow conditions. A solder pre-form can be created with the same punch equipment that is used for manipulation of the LTCC, making scalability and modification to solder/LTCC design easy to incorporate in an industrial setting. Solder joints have been utilized for hermetic packaging in many operations and are ideal for this application due to ease of use, versatility of design, and low cost.

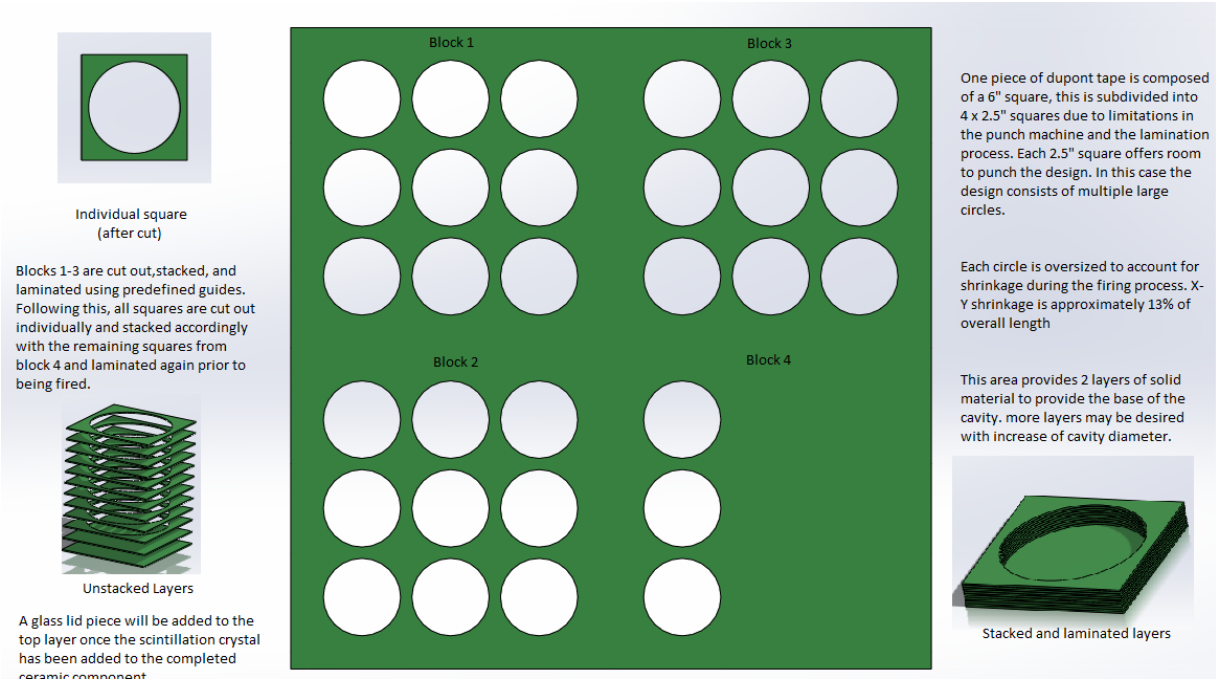

Fig. 8. LTCC Multilayered casing for scintillation crystal.

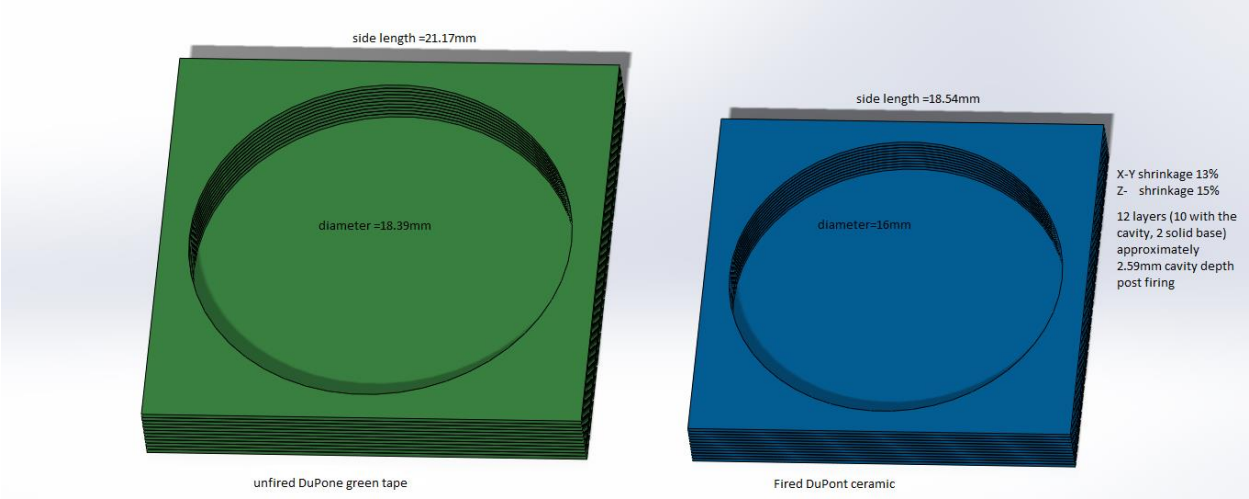

Fig. 9. Stacked layers of LTCC.

References

[1] Barlow, Fred D., Elshabini, Aicha. "*Ceramic Interconnect Technology Handbook",* Boca Raton: CRC/Taylor & Francis, 2007.

[2] DuPont Microcircuit Materials, "951 Green Tape™: Thick Film Composition,"MCM951datasheet, 2001 [Revised Sep. 2003].

[3] Imagawa, Kyoshira, Et. Al., "NaI Scintillation Detector," Horiba Technical Reports. Readout English Ed. 9.

[4] http://www.horiba.com/uploads/media/RE09-18-098_03.pdf

Appendix: Publications and presentations as a result of this research

1) Published and submitted peer-reviewed refereed journal publications:

Shrestha, T., Basirat, M., Charit, I., Potirniche, G.P, Rink, K.K. Creep rupture behavior of Grade 91 steel, *Materials Science and Engineering A*, vol. 565, pp. 382-391, 2013

Potirniche, G.P. A numerical strip-yield model for the creep crack incubation in steels, *Journal of the ASTM International*, Selected technical papers STP 1546, vol. 38, pp. 197-214, 2012

Basirat, M., Shrestha,T., Potirniche, G.P., Charit, I., Rink, K. A study of the creep behavior of modified 9Cr-1Mo steel using continuum-damage modeling, *International Journal of Plasticity*, vol. 37, pp. 95-107, 2012

Shrestha, T., Basirat, M., Charit, I., Potirniche, G.P, Rink, K.K., Sahaym, U. Creep deformation mechanisms in modified 9Cr-1Mo steel, *Journal of Nuclear Materials*, vol. 423, pp. 110-119, 2012

Shrestha, T., Basirat, M., Charit, I., Potirniche, G.P., Rink, K. Creep studies of modified 9Cr-1Mo steel for very high temperature reactor pressure vessel applications, *Ceramic Transactions, Advances in Materials Science for Environmental and Nuclear Technology II*, vol. 227, pp. 231-240, 2011

T. Shrestha, S.F. Alsagabi, I. Charit, G. P. Potirniche, and Michael V. Glazoff. Effect of Heat Treatment on the Mechanical Properties of Modified 9Cr-1Mo Steel, submitted to *Metallurgical and Materials Transactions A* (2013).

Basirat*, M., Shrestha, T., Potirniche, G.P., Charit, I., Finite Element Analysis of Creep and Damage in Modified 9Cr-1Mo Steel Weldments, submitted to the *Journal of Nuclear Materials* (2013)

1) Peer-reviewed refereed journal publications currently in preparation:

T. Shrestha, M. Basirat, S. Alsagabi, I. Charit and G.P. Potirniche, Creep Rupture Behavior of Welded Grade 91 Steel, to be submitted to *Nuclear Engineering and Design* (2013)

T. Shrestha, I. Charit and G. Potirniche, Residual Stress Measurement by Neutron Diffraction in Modified 9Cr-1Mo Steel Weldments, to be submitted to *Materials & Desig*n (2013).

Basirat, M., Shrestha, T., Potirniche, G.P., Charit, I., Fracture simulations in modified 9Cr-1Mo welded steels using a combined plasticity-creep constitutive model, to be submitted to *the International Journal of Fracture* (2014)

2) Published conference proceedings:

Wuthrich ,Z., Shrestha,T., Charit,I., Rink,K., Basirat,M., Potirniche, G.P. Studies of the effects of heat treatment on hardness and creep behavior for a modified 9Cr-1Mo Steel, *ASME 2011 International Mechanical Engineering Congress & Exposition*, on CD, Denver Co, Nov. 11-17, 2011

Basirat, M. , Shrestha, T., Potirniche, G.P., Charit, I., Rink, K. Creep Damage Analysis in Welded Joints of Modified 9Cr-1Mo Steel, *American Nuclear Society (ANS) meeting*, November 11-15, 2012, San Diego, CA, paper submitted

3) Presentations at meetings and conferences:

Basirat, M., Potirniche, G.P., Shrishta, T., Charit, I., Wuthrich, Z. Dislocation-Based Continuum-Damage Modeling of Creep Behavior of Heat-Resistant 9Cr-1Mo Steel, *ASME 2011 International Mechanical Engineering Congress & Exposition*, Denver, CO, Nov. 11-17, 2011

Basirat, M., Potirniche, G.P, Shrestha, T., Charit, I. and Rink,K. A dislocation based CDM model for estimating the creep rupture time of the modified 9Cr-1Mo steel for the VHTR, *TMS 2011*, San Diego, CA, Feb. 27-Mar. 3, 2011

T. Shrestha, M. Basirat, Z. Wuthrich**,** I. Charit, and G. Potirniche, Creep Characteristics of a Grade 91 Steel, *Materials for the Nuclear Renaissance II*, TMS Annual Meeting, Feb. 28 - Mar. 3, 2011, San Diego, USA.

T. Shrestha, M. Basirat, I. Charit, G. Potirniche, K. Rink, and U. Sahaym, Creep Deformation Mechanisms in Grade 91 Steel," *Mechanical Performance of Materials for Current and Advanced Nuclear Reactors*, TMS Annual Meeting, Orlando, Florida, March 11-15, 2012.

Basirat, M., Shreshta, T. Potirniche, G.P., Charit, I. Finite element simulations and experimental testing of creep fracture in welded 9Cr-1Mo steels, *ASME 2013 International Mechanical Engineering Congress & Exposition*, San Diego, CA, Nov. 15-21, 2013

Basirat, M., Shreshta, T. Potirniche, G.P., Charit, I. A study of creep crack incubation in heat resistant steels using finite element method and strip-yield modeling, *ASME 2013 International Mechanical Engineering Congress & Exposition*, San Diego, CA, Nov. 15-21, 2013